Global Compilation and Analysis of Fault Zone Permeability

Jacek Scibek

Department of Earth and Planetary Sciences

McGill University, Montreal

April, 2019

A thesis submitted to McGill University in partial fulfillment of the requirements of the degree of Doctor of Philosophy

The 5 years of hard, often tedious, academic labour and the resulting articles and thesis are dedicated entirely to the people who have been, or will be, affected by natural disasters related to fault ruptures. My insignificant scientific contribution, in this case the organization and clarification of the trends in rock permeability-properties, some observations, and the database collected, perhaps may help others find the information more efficiently as they work on the problem of fluid flow in faults at depth.

Jacek Scibek

Table of Contents

LIST OF TABLES ix

LIST OF FIGURES xi

ABSTRACT xvii

RÉSUMÉ xviii

ACKNOWLEDGEMENTS xx

CONTRIBUTIONS OF AUTHORS xxii

1 Introduction 1

1.1 Observations of fluid involvement in brittle fault zones 1

1.2 Research Objectives 3

2 Methodology 5

2.1 Thesis organization 5

2.2 Data sources for statistical analysis 6

2.3 The scale of hydraulic tests on fault rocks 6

2.4 Description of field study site 9

3 Multidisciplinary database of permeability of fault zones and surrounding protolith rocks at world-wide sites 11

3.1 Abstract 11

3.2 Background and summary 12

3.3 Methods 15

3.3.1 Dataset review process 15

3.3.2 Data sources 17

3.3.3 Permeability summaries 25

3.3.4 Geologic categories 26

3.4 Technical validation 29

3.4.1 Matrix permeability uncertainty 29

3.4.2 Bulk permeability uncertainty 30
3.4.3 Permeability ratios 31
3.5 References 32
4 The biases and trends in fault zone hydrogeology conceptual models: global compilation and categorical data analysis 44
4.1 Abstract 44
4.2 Introduction 45
4.3 Methods 46
4.3.1 Data sources 46
4.3.2 Data sources used in statistical analysis 47
4.3.3 Data sources reviewed but not used in statistical analysis 48
4.4 Data synthesis and fault zone attribute counting 49
4.4.1 Observation method categories 49
4.4.2 Geoscience discipline categories 50
4.4.3 Lithology categories 52
4.5 Categorical data analysis with Chi-Square test 52
4.5.1 Hypotheses tested 52
4.5.2 Statistical methods 52
4.6 Results 54
4.6.1 Hypothesis 1 test (simplified fault zone permeability structure vs. observation method) 54
4.6.2 Hypothesis 2 test (simplified fault zone permeability structure vs. geoscience discipline) 56
4.6.3 Hypothesis 3 test (simplified fault zone permeability structure vs. lithology): 58
4.6.4 Hypothesis 4 test (as in Hypothesis 2 but for sedimentary and crystalline rocks separately) 59
4.6.5 Estimating the proportion of fault conduits from long transportation tunnels 61

4.7 Discussion 64
4.7.1 Biases in observing the fault zone permeability structure 64
4.7.2 Estimating the proportion of faults that are conduits 66
4.8 References 68
5 The permeability of fault zones in the upper continental crust 79
5.1 Abstract 79
5.2 Introduction 79
5.3 Methods 80
5.3.1 Permeability data sources 80
5.3.2 Permeability-depth curves 82
5.3.3 Permeability ratios 83
5.3.4 Bulk permeability estimates for fault zones from tunnel inflows 84
5.3.5 Fault bulk permeability at EGS and HDR sites 85
5.3.6 Regional seismicity-depth distributions 85
5.4 Results 86
5.4.1 Statistics of conduit behavior of fault damage zones 86
5.4.2 Depth distribution of fault damage zone bulk permeability 88
5.4.3 Bulk permeability ratio (contrast) 88
5.5 Discussion of processes 90
5.6 Conclusions 92
5.7 References 93
6 The bulk permeability of fault rocks and protoliths: Insights from statistical analysis 115
6.1 Abstract 115
6.2 Introduction 116
6.3 Methods 118
6.3.1 Permeability datasets by lithologic category 118
6.4 Statistical analysis 121

6.5 Results 123

6.5.1 Descriptive statistics and distributions 123

6.5.2 Regression results for permeability-depth trends 126

6.5.3 Regression results for fault damage zone-protolith pairs for bulk permeability of macro-fractured rocks from in-situ tests 126

6.6 Discussion 131

6.6.1 Possible reasons for correlation between damage-zone and protolith permeability 131

6.6.2 Comparing the permeability ratios and inferring the magnitude of fault conduit and barrier 132

6.6.3 On the importance of permeability-depth distribution 134

6.7 Transient variations in fault-zone permeability 138

6.8 Estimating the global crustal permeability distribution 140

6.9 Conclusions 142

6.10 References 143

7 Fault zone permeability structure in Precambrian metapelitic gneiss and pegmatite, hosting uranium mineralization under the eastern Athabasca Basin, Canada 156

7.1 Introduction 156

7.2 Regional geology and structure 157

7.3 Protoliths 159

7.3.1 Metapelites 159

7.3.2 Metaquartzites 160

7.3.3 Pegmatitic melts and intrusions in metasediments 161

7.4 Gryphon fault zone and deposit 162

7.4.1 Fault core zone and fault rocks 164

7.4.2 Fault damage zone 166

7.5 Rock alteration zones 169

7.5.1 Paleo-weathering and regolith ... 169
7.5.2 Alteration assemblages by temperature and fluid type ... 171
7.5.3 Chlorite, illite, tourmaline ... 172
7.5.4 Sericite texture of mica alteration (phengite, paragonite) ... 172
7.5.5 Argillic alteration (e.g. kaolinite) ... 173
7.6 Permeability testing methods ... 174
7.6.1 Probe tip seal on rock ... 174
7.6.2 Potential effects of drilling damage on sample surface ... 177
7.6.3 Constant flow rate test ... 178
7.6.4 Unsteady gas flow test (pressure-decay test) ... 181
7.7 Evaluation of consistency of results for samples ... 186
7.7.1 Water saturation of drillcore samples ... 186
7.7.2 Heterogeneity of sample spots ... 187
7.8 Results ... 190
7.8.1 Site-wide statistics ... 190
7.8.2 Expected pressure sensitivity of the protoliths ... 191
7.8.3 Expected pressure sensitivity of fault rocks ... 192
7.8.4 Fault rocks ... 195
7.8.5 Transects across the fault zone ... 200
7.8.6 Rock alteration and permeability changes ... 202
7.8.7 Hydrothermal desilicification and silicification ... 203
7.8.8 Episyenite zones ... 204
7.8.9 Transmissivity of Gryphon fault zone ... 208
7.8.10 Conceptual model of permeability structure ... 211
7.9 Conclusions ... 215
7.10 References: ... 216
8 Conclusion and summary ... 241

9 References 243
Appendix 1 250
9.1 Data records 250
9.2 Dataset table 250
9.2.1 Dataset number, site name, and location information: 250
9.2.2 Lithologic and structural information summary: 252
9.2.3 Permeability test methods and result categories: 252
9.2.4 Depth of tested zone relative to the ground surface: 253
9.2.5 Depth of tested zone relative to the top of metamorphic or plutonic basement rock: 253
9.2.6 Elevation of tested zone relative to mean sea level: 254
9.2.7 Confining pressure and effective depth (matrix samples only): 254
9.2.8 Permeability values: 255
9.2.9 Ratios of permeability values: 255
9.3 References table: 256
Appendix 2 257
10 Supporting information for article in Chapter 5 257
10.1 Additional estimates of bulk permeability of fault zones from groundwater inflow rates to tunnels 258
10.2 Summary of bulk permeability of fault zones at EGS/HDR/rock laboratory sites .262
10.3 Regional seismicity-depth distributions 279
Appendix 2 281
11 Permeability of drillcore samples at Gryphon site 281

LIST OF TABLES

Table 3-1 Data sources for inputs to the database, with dataset counts. 17

Table 3-2 List of sites for inputs to database section "Active faults and faulting processes". 21

Table 3-3 List of sites for inputs to database section "Geothermal reservoirs". 22

Table 3-4 List of sites for inputs to database section "Radioactive waste repositories". 23

Table 3-5 List of sites for inputs to database section "Groundwater resources and contamination". .. 23

Table 3-6 List of sites for inputs to database section "Petroleum reservoirs and faulting processes". 24

Table 3-7 List of sites for inputs to database section "Engineering projects". 25

Table 4-1 (a) Counts of fault study sites reviewed and used in statistical analysis from five geoscience disciplines. (b) Counts of fault sites reviewed from geothermal and geophysical data sources but not used in statistical analysis. 47

Table 4-2 Fault zone permeability structure model counts by categories of observation method: contingency table of observed, expected frequencies, and calculated Chi-square terms and standardized Pearson residuals. The categories of observation method table columns are: A - drill core and outcrop samples, B - borehole interval hydraulic tests (packer, slug), C - borehole interval large hydraulic tests (pump or injection), D - hydraulic head or pressure differences across fault, E - water chemistry, temperature, natural tracers, F - tunnel inflow or drawdown. 54

Table 4-3 Fault zone permeability structure model counts by categories of geoscience discipline: contingency table of observed, expected frequencies, and calculated Chi-square terms and standardized Pearson residuals. A - Structural geology, B - Hydrogeology, C - Tunnel Engineering, D - Mining and Dams, E - Hydrocarbon Reservoirs 56

Table 4-4 Comparing the frequencies of occurrence of data within lithological categories. The table shows the counts of fault zone simplified permeability structures, and the counts of fault zone sites within geoscience disciplines that have the specified lithology of protolith. A - Structural geology, B - Hydrogeology, C - Tunnel Engineering, D - Mining and Dams 58

Table 4-5 Comparing the frequencies of occurrence of permeability structures for three geoscience disciplines (Structural Geology, Hydrogeology, Tunnel Engineering) separately for the crystalline rocks (metamorphic and igneous), and for the sedimentary rocks. 60

Table 4-6 Summary of proportions (%) of fault conduits relative to the total number of major fault zones crossed in tunnels and drilled at research sites. Lithology listed in order of % occurrence in tunnel: G=granitic, GN=gneiss, S=sedimentary, S-L=limestone, M-S=metasedimentary, VS=volcanic sediments, tuffs, VB=basalt, andesite, VD=intrusive dikes. 62

Table 6-1 Fault-zone permeability data by lithologic category. 119

Table 6-2 Descriptive statistics for bulk permeability of fault damage zones and protolith,) by lithologic category. [a] 125

Table 6-3 Results of linear regression on log values of bulk permeability from fault damage zone and protolith. 127

Table 6-4 Matrix permeability of protolith and bulk permeabilities of protolith and fault damage zones from various metamorphic and igneous rock types. Permeability values shown as $\log_{10}$(permeability in m^2) 137

Table 7-1 Typical b values calculated with Equation 10 and 11. 185

Table 7-2 Porosity and matrix permeability of metasedimentary, granitic, and fault rocks from geoscientific literature review. Values are at shallow crustal depths <1km in most cases, outcrops, and tested at low effective confining pressures (as noted). 198

Table 7-3 Estimation of permeability thickness of components of fault zone, by lithological-alteration-structural categories of rocks. 209

Table 7-4 Estimation of permeability thickness in fault damage zone, fault core, protolith, and strongly altered protolith. 210

Table 10-1 Box plot statistics for permeability values from Table S1 257

Table 10-2 Box plot statistics for permeability values from Table S2 258

Table 10-3 Bulk permeability of fault zones calculated from groundwater inflow rates to selected tunnels. 259

Table 10-4 Enhanced fracture and fault zone permeability at EGS/HDR sites. 278

Table 10-5 List of regions and datasets and references. 279

Table 10-6 Earthquake counts at depth intervals for regional seismicity-depth histograms. 280

Table 11-1 Comparing the permeability of drillcore samples tested on October 5, 2016 after owen-drying at Wheeler River site, and the same samples tested previously in 2016 (air dried in ambient storage conditions or partly saturated for some samples). 283

LIST OF FIGURES

Figure 1-1 Three main objectives of the research and the five research articles in the thesis. 4

Figure 2-1 (a) World-wide locations of test sites of fault zone permeability shown with different symbols for bulk permeability at depth (in-situ by drilling or tunneling), and matrix permeability (at outcrops). In smaller maps in lower panels the test sites are separated by data source category. (b) Locations along geographic longitude and in-situ depth intervals permeability tests in fault zones. Elevation is relative to mean sea level of in-situ permeability test intervals in drillholes or tunnels. The topographic profile is plotted from elevations of the test sites, and is not a global average elevation. The sea floor elevation at oceanic sites is also indicated, with an added conceptual sketch of ocean floor (not actual transect). 7

Figure 2-2 (a) The regional structure of the eastern portion of Athabasca Basin, Canada (inset map on lower right), uranium deposits along major faults near the unconformity surface (structure details after Thomas et al. 2014 of Cameco Corp.; regional geology simplified from Jeanneret et al. 2016), (b) geologic map of the Wheeler River exploration area (Denison Mines Ltd. 2018), with a cross-section A-A' indicated from Gryphon and Phoenix deposit. 10

Figure 3-1 Schematic diagram of the permeability data compilation and review process: (a) search and review of publications (map of the world showing the locations of test sites in this study), (b) hydrogeology & structure at site scale (sketch based on Soultz-sous-Forêts geothermal site, modified after Vidal and Genter 2018), (c) fault zone structure and permeability domains (fault zone sketch modified after Vidal et al. 2015, and fault zone domains terminology after Caine et al. 1996), (d) permeability test scale (matrix, bulk (drillhole fracture model modified after Sausse et al. 2008), (e) summary of permeability values in database, (f) technical validation.... 16

Figure 3-2 (a) World-wide locations of test sites of fault zone permeability shown with different symbols for bulk permeability at depth (in-situ by drilling or tunneling), and matrix permeability (at outcrops). In smaller maps in lower panels the test sites are separated by data source category: (b) active faults and faulting processes, (c) geothermal reservoirs, (d) radioactive waste repository studies, (e) groundwater resources and contaminated sites, (f) petroleum reservoirs and faults in sedimentary rocks, (g) engineering projects. 18

Figure 3-3 World-wide locations along geographic longitude and in-situ depth intervals permeability tests in fault zones. All sites are projected on one section and plotted along longitude. (a) Elevation relative to mean sea level of in-situ permeability test intervals in drillholes or tunnels. The topographic profile is plotted from elevations of the sites, and is not a global average elevation. The sea floor elevation at oceanic sites is also indicated, with an added conceptual sketch of ocean floor (not actual transect). (b) Depth of in-situ bulk permeability test intervals and lithologic category of protolith in tested fault zone. The depths are below ground surface for land sites and below sea floor for oceanic sites. (c) Outcrops of fault zones plotted at 0 depth, and the effective depths that correspond to the confining differential pressures of matrix permeability tests on some fault rock samples. 27

Figure 4-1 Locations of reviewed fault zone study sites categorized by (a) geoscience discipline of data source, (b) simplified conceptual model of fault zone permeability structure. 51

Figure 4-2 Summary histograms for the simplified fault zone permeability structures in observation method categories: (a) histograms relative frequencies by observation method, and (b) comparing the observed to expected frequencies of fault zone simplified permeability structures using the calculated Person Residuals from Chi-Square analysis of categorical data. 55

Figure 4-3 Summary histograms for the simplified fault zone permeability structures in geoscience discipline categories: (a) histograms of relative frequencies by geoscience discipline, and (b) comparing the observed to expected frequencies of fault zone simplified permeability structures using the calculated Person Residuals from Chi-Square analysis of categorical data. 57

Figure 4-4 Comparing the (a) histograms of fault zone simplified permeability structures by lithology categories, and, (b) proportion of sample sites that have the dominant lithology in sedimentary or crystalline rocks in subsets of data by geoscience discipline. 59

Figure 4-5 Comparing the proportions of barrier, conduit and barrier-conduit faults in the main lithological categories: (a) crystalline rocks, (b) sedimentary rocks. 60

Figure 4-6 Global proportions and trends with depth of conduits in major fault zones (a) counted along long tunnels and representing several large research sites (Table 6 data summary), and, (b) estimates based on the global database of fault zone study sites from five geoscience disciplines (Table 1) and graphical description of fault zone permeability structural styles (Caine et al. 1996) included in our simplified categories. 67

Figure 5-1 Fault zone permeability distributions (boxplots) for specific lithologies and fault zone structural domains. (a) Matrix permeability of fault damage zone, protolith, and fault core at outcrops (from low-pressure tests) and of fault core rocks at near in situ pressures. (b) Bulk permeability estimated from in situ tests in drillholes, comparing the fault damage zone, protolith, and fault core. The fault permeability architectural units (after Caine et al. 1996) are coloured to match the shading of boxplots in (a) and (b) for easier reference: fault core is dark grey, damage zone is light grey, and protolith is white. Fault core data are from coarse siliciclastic rocks and plutonic and metamorphic rocks only. Boxplot center lines show the medians and box limits the 25th and 75th percentiles; whiskers extend 1.5 times the interquartile range; outliers are represented by empty circles; crosses represent sample means. (c) Permeability ratio of fault damage zone to protolith, by lithological categories. The bulk permeability ratios can be compared to the corresponding data distributions for each lithologic category in part (b). Matrix permeability ratio shown only for siliciclastic coarse rocks (such as sandstones) at fault outcrop sites (upper portion of c). 87

Figure 5-2 Logarithms of bulk permeability of fault damage zones, for different lithologic categories, plotted against depth below ground surface (or below sea floor surface) at a mid-point of tested *in situ* interval. The depth scale is logarithmic in the upper panels (a, b), and arithmetic in the lower panels (c, d). The lower plots are otherwise identical to the upper plots. In (a) or (c), the bulk permeability of fault damage zones is shown as representative points (one per dataset), the modified geothermal-metamorphic curve approximates the average permeability of the protolith, and the damaged-crust curve is an approximate upper bound of the bulk permeability of fault zones. In (b) or (d), the points represent the logarithms of ratio of bulk permeability (fault damage zone / protolith) for each dataset, and the ratio curve is the difference of log permeability values of the two curves in (a) and (c). 89

Figure 5-3 Comparison of the bulk permeability ratio (fault damage zone / protolith) to seismicity-depth distributions for 18 regions represented in the fault zone permeability data set, showing that fault permeability is most different from protolith in the uppermost crust above seismogenic depths. (a) Bulk permeability ratios at fault zone sites compared to the post- to pre-stimulation permeability ratios (magnitude of permeability enhancement) for 21 EGS/HDR projects; the permeability ratio curve from Figure 2b is plotted as a dashed line. (b) Seismicity-depth distribution from selected regions represented in the permeability data set. 91

Figure 6-1 Locations of test sites in fault zones from the database of Scibek et al. (2019 submitted - a) and digital maps of major faults: (a) western USA - Quaternary faults in green shade (USGS 2006) and other faults in grey (USGS 2016), (b) Japan - active faults from (GSJ 2012), (c) cumulative frequency of in situ hydraulic tests with depth. Fault outcrop locations are at 0 depth. 117

Figure 6-2 Summary of log values of bulk and matrix permeability of fault damage zone and protolith for datasets from plutonic & metamorphic rocks, volcanic rocks, and sedimentary rocks. (a) Histograms comparing bulk and matrix permeability in damage zone (upper panels) and protolith (lower panels). (b) Histograms of ratio of bulk permeabilities (fault damage zone/protolith). (c) Boxplots of bulk permeability distributions with depth: quartiles, median, minimum, and maximum, and individual data points where n<5. 124

Figure 6-3 Regression lines and scatterplots of log bulk permeability values vs. depth by lithological categories. (a) Damage zone permeability vs. depth, (b) protolith permeability vs. depth, and (c) data distributions as probability-density functions compared to normal distributions............... 128

Figure 6-4 Regression lines and scatterplots of log bulk permeability values by lithological categories. (a) Regression of log10 (kFDZ) on log10 (kProtolith), (b) regression of residual kFDZ on residual kProtolith after removing depth trends, and (c) data distributions as probability-density functions compared to normal distributions.. 129

Figure 6-5 (a) Residuals from regression of k_{FDZ} on $k_{\mathrm{Protolith}}$ as a function of $k_{\mathrm{Protolith}}$, with lines drawn to indicate the trend of decreasing variance with increasing $k_{\mathrm{Protolith}}$, (b) squared residuals as a function of $k_{\mathrm{Protolith}}$ and the decreasing trend in variance that indicates heteroscedasticity, and (c) ratio of permeabilities $\log(k_{\mathrm{FDZ}}/k_{\mathrm{Protolith}})$ as a function of $k_{\mathrm{Protolith}}$. 130

Figure 6-6 Bulk permeability of damage zone vs. protolith in (a) plutonic and metamorphic rocks, (b) volcanic rocks, (c) carbonates and mudrocks, (d) coarse siliciclastic rocks, and (e) damage zone matrix permeability for various rock types. Fault core matrix permeability for (f) mudrocks, carbonates, and metamorphic rocks and (g) coarse siliciclastic coarse rocks. (h) Comparing the magnitude of fault conduit and barrier behavior on plot of fault vs. protolith bulk permeability from this study, showing permeability data envelopes from (a) to (g). The permeability ratio labelled on the diagonal scale. The shaded region in (h) is for deformation bands (after Ballas et al. 2015) and a few fault cores from the database in this study... 133

Figure 6-7 Comparison between *in situ* permeability data and the geothermal-metamorphic data used by Manning and Ingebritsen (1999). (a) Damage zone permeability, (b) protolith permeability at the same sites, and (c) the same as (a) but plotted on an arithmetic depth scale. The graphs in the two upper panels are plotted with logarithmic depth scales to clarify the data distribution at shallow depths. Curves are the geothermal-metamorphic curve (thick black dashed line) of Manning and Ingebritsen (1999) and the modified geothermal-metamorphic curve at depths <1 km (see Chapter 4).. 136

Figure 6-8 Schematic workflow for incorporating statistical results from this study into a digital crust model. (a) Simplified classification of fault zone hydraulic models, (b) fault damage zone vs. protolith scaling ratios by rock type, (c) permeability vs. depth trends and bounds, (d) digital crust implementation in EarthCube. 141

Figure 7-1 The geology and structure from Gryphon to Phoenix deposit at Wheeler River site, (a) cross-section of the Athabasca Basin and the upper portion of basement rock, and (b) structure of the Gryphon fault zone. 163

Figure 7-2 (a) Fault gouge with breccia in Offset Faults (WR-668D2, ≈ 620m), (b) strand of Offset Fault core with fine breccia (WR-687, 558m), (c) damage zone in graphitic metapelite with slickensides of cm-scale displacement shears, (d) fault breccia in G-Fault, (e) dravite+kaolinite+illite altered fault breccia and gouge in weakly altered metapelite (WR-690), (f) clay-altered cemented breccia and cataclasite (WR-688D1, ≈ 306.5m), (g) fault breccia from older cataclasite in clay-altered metapelite in G fault, (h) cemented fault breccia in linkage faults, redox fronts (reddish) and clay alteration (white-grey), hosting uranium mineralization (black). 167

Figure 7-3 Mapped alteration zones at the Gryphon fault zone and uranium deposit, from regular 3m interval sampling of drillcore and short-wave infrared spectrometry (SRK Consulting 2015b, SRK Consulting Inc. & RPA Inc. 2018). 170

Figure 7-4 Epoxy resin seal ring at test spots on dry drillcore surfaces and surface roughness under about 10x magnification: (a) pelitic gneiss, (b) desilicified and clay altered gneiss, (c) silicified pegmatitic rock with <0.1mm wide fractures and microfractures, (d) apparatus schematic and example of field site setup with prepared pelite pieces in drillhole WR-665. 176

Figure 7-5 (a) Section through drillcore sample showing probe tip seal geometry, (b) flow lines and pressure equipotential lines with probe tip outer to inner seal radius ratio of 4 (after Tartakovsky et al. 2000), (c) example of gas exit pattern on altered gneiss sample in two different spots (spot 1 has more connected pores than spot 2). 180

Figure 7-6 (a) Example of pressure-decay permeameter time-series for a test in rock of low permeability at initial pressure about 350 kPa above the sample (after Persofff and Hulen 2001), (b) unconfined sample probe pressure-decay curves from several tests in this study for rocks of different permeabilities, (c) pressure-decay curve selected segment (between square points), and compared to analytical solution in thick orange line for one reservoir permeameter test (Kaczmarek 2008), (d) plot of transformed pressure vs. transformed time for a small segment of pressure-decay curve. 183

Figure 7-7 Comparing the matrix permeability log values of various samples from the Gryphon fault zone: (a) pressure-decay vs. steady-state gas flow tested on the same samples, (b) samples at ambient moisture content vs. the same samples oven dried, (c) comparing permeabilities at multiple spots on one drillcore piece and the median value, tested on different rock types and sorted by permeability median value, (d) scatter in results of about 1200 tests graphed as permeability vs. log of change in pressure over time in the analysed segment of the pressure-decay curve. 189

Figure 7-8 Summary statistics of matrix permeability by rock lithology and alteration categories, at the Gryphon fault zone and deposit. 190

Figure 7-9 G-Fault in Gryphon fault zone, permeability testing in WR-668-D2 and -D3 drillholes: (a) matrix permeability transect of both drillholes and a simplified structural log for -D3 hole, (b) interpreted simplified structural features of the fault core and damage zone, overlayed on the photographic mosaic of the drillcore from -D3 hole, and examples of test spots on fault rocks. 197

Figure 7-10 Permeability transect across the Gryphon fault zone along drillhole WR-665 and WR-668-D2, shown in rotated cross-section. 202

Figure 7-11 Permeability transect for different categories of permeable samples (by lithology, alteration, fracturing), across the Gryphon fault zone along drillhole WR-665 and WR-668-D2, shown in rotated cross-section. 206

Figure 7-12 Permeability transect for different categories of permeable samples (by lithology, alteration, fracturing), across the Gryphon fault zone along drillhole WR-507 and WR-671, shown in rotated cross-section. 207

Figure 7-13 Permeability distribution in Gryphon fault zone, separated into components (a) fault core and protolith, (b) fractured damage zone, (c) strongly altered porous rock in the damage zone or in the protolith (strong porosity enhancing alteration component to permeability), (d) permeability data for transect across the MTL (Wibberley and Shimamoto 2003), (e) permeability transect through Nojima fault zone (Lockner et al. 2009), (f) fault zone geometry, drillholes, and transect sketches. 214

ABSTRACT

Fault zones are a ubiquitous part of the of the Earth's brittle crust, influencing a wide range of processes including hydrothermal circulation, ore deposition, crustal strength, and seismicity. However, despite the large amount of drilling and *in situ* hydraulic testing worldwide, there are no comprehensive summary statistics and analyses of fault permeability. The objective of my PhD research was to develop an improved understanding of fault zone permeability at the crustal scale through data analysis and field research.

The initial statistical analysis was done to investigate the biases and trends in observations in fault zones in various geoscience disciplines. The revised database is 429 datasets (at 364 locations), and it enabled a more complete statistical description of trends and distributions of the permeability with depth, and between different rock types. The permeability ratio (fault zone / protolith) is used as a metric to describe crustal permeability variation. The average of this ratio value varies from +2 to +3 orders of magnitude over the 10 km depth range. The maximum ratio value occurs at shallow depths, between 1 and 3 km.

From the bulk permeabilities, mostly from *in situ* drillhole tests, the depth-distribution of permeability was synthesized. In the upper few kilometres of the crust, fault zones serve as fluid conduits (bulk permeability >10^{-17} m^2 threshold). The distribution of world-wide fault permeability values, when compared to the geothermal-metamorphic curve that represents the trend for time-averaged metamorphic fluid fluxes, is consistent with the trend over depth in fault zone permeability. This finding implies that fault zones control and serve as large-scale fluid conduits through the metamorphic crust in tectonically active regions at least.

Another important and new result was a significant and relatively good correlation (r^2 = 0.5 to 0.8) between the bulk permeability of the fault zone (mostly the damage zone) and the surrounding protolith in most rock types considered here, but not in coarse siliciclastic rocks. This empirical relationship may be used to predict the permeability of fault zones from the permeability of the protoliths and depth in the brittle crust, in the absence of other data.

The thesis also includes original field-based research (Gryphon uranium deposit). A wide (>350 m) fault zone was tested for matrix permeability in drillcore (>700 drillcore samples). The fractured fault damage zone accounts for most of the transmissivity (67%), but the enhanced porosity from rock alteration acts to magnify the conduit of the damage zone. The ability to separate the permeability and transmissivity into components within highly heterogeneous fault zone is a step forward in better understanding the permeability structure

of faults, but it requires a large number of tests, such as presented here. My results suggests that present-day permeability of fault zones, where adequately "preserved", offer direct insights into past fluid flow and paleo-permeability.

RÉSUMÉ

Les zones de failles sont omniprésentes dans la croûte fragile de la Terre, exerçant une influence sur un large éventail de processus, dont la circulation hydrothermale, la formation de gisements de minerai, la résistance de la croûte et la sismicité. Malgré de nombreux forages et essais hydrauliques *in situ* dans le monde entier, il n'existe pas de statistiques sommaires ou d'analyses exhaustives sur la perméabilité des failles. L'objectif de mes travaux de doctorat était d'établir une meilleure compréhension de la perméabilité des zones de faille à l'échelle de la croûte terrestre par l'analyse des données et des travaux de recherche sur le terrain.

Une première analyse statistique se penche sur les biais et tendances dans les observations sur les zones de faille dans diverses disciplines géoscientifiques. La nouvelle base de données passe ainsi à 429 ensembles de données (sur 364 emplacements) et permet une description statistique plus complète des tendances et de la répartition de la perméabilité en fonction de la profondeur et pour différents types de roches. Le rapport de perméabilités (zone de faille/protolithe) est utilisé comme mesure de la variabilité de la perméabilité de la croûte. La moyenne de ce rapport varie sur de 2 à 3 ordres de grandeur sur les 10 km de profondeur de la croûte fragile. La valeur maximum de ce rapport est observée à faible profondeur, entre 1 km et 3 km.

Une synthèse de la distribution de la perméabilité en fonction de la profondeur est produite à partir de perméabilités globales obtenues principalement d'essais de forage *in situ*. Dans les quelques kilomètres supérieurs de la croûte, les zones de faille servent de conduits pour l'écoulement des fluides (perméabilité globale $>10^{-17}$ m^2). La distribution des valeurs de perméabilité des failles à l'échelle mondiale, comparée à la courbe géothermique-métamorphique qui représente la tendance des flux de fluides métamorphiques à moyenne temporelle, concorde avec la tendance de la perméabilité des zones de faille en fonction de la profondeur. Elle ne concorde pas avec la seule perméabilité du protolithe, qui définit aussi une tendance décroissante en fonction de la profondeur. Cette constatation indique que les zones de faille servent de conduits à grande échelle pour l'écoulement des fluides à travers la croûte métamorphique à tout le moins dans les régions tectoniquement actives.

Un autre nouveau résultat important est la présence d'une corrélation significative et relativement bonne ($r^2 = 0,5\text{-}0,8$) entre la perméabilité globale des zones de faille (des zones endommagées principalement) et des protolithes environnants dans la plupart des types de roches considérés, mais non dans les roches silicoclastiques à grains grossiers. Cette relation empirique peut être utilisée pour prédire la perméabilité de zones de faille à partir de la perméabilité des protolithes et de la profondeur dans la croûte fragile, en l'absence d'autres données.

La thèse présente également les résultats de travaux de terrain originaux (le gisement d'uranium de Gryphon). Des essais sur des carottes de forage (>700 échantillons) ont été réalisés pour déterminer la perméabilité matricielle dans une large zone de faille (>350 m). La zone endommagée fissurée de la faille explique la majeure partie de la transmissivité (67 %). Cette augmentation de la porosité due à l'altération de la roche a pour effet d'amplifier le comportement de conduit de la zone endommagée. La capacité de séparer en différents composants la perméabilité et la transmissivité à l'intérieur d'une zone de faille très hétérogène constitue une avancée vers une meilleure compréhension de la structure de perméabilité des failles, mais nécessite un grand nombre d'essais, à l'instar de ce qui est présenté ici. Mes résultats donnent à penser que la perméabilité actuelle des zones de faille, là où elle est bien « préservée », ouvre une fenêtre directe sur l'écoulement passé de fluides et la paléoperméabilité.

ACKNOWLEDGEMENTS

This research was funded by a grant from *Fonds de Recherche du Québec – Nature et technologies* (FRQNT) to Jeffrey McKenzie at McGill University. Other funding was provided by Tom Gleeson, now at University of Victoria. This research would not be possible without the force of scientific nature of Tom Gleeson, and editorial involvement in countless revisions of the papers for the many journals that we submitted to. The same goes for Jeffrey McKenzie, who spent time on this and approving this research (and funding) going forward, no matter what ideas I had and where my field work took me. Without the freedom of thought and action, none of this work would happen, because it had to be multidisciplinary and broad in scope. Scholarships were received from:

- IAH Scholarship 2017 (Canadian chapter) - Dr. Diana Allen, President,
- Robert Wares Fellowship in 2017, and
- 2018 Graduate Mobility Award from McGill University for research trip to Japan.

From 2016 to 2019, special acknowledgement and thanks goes to the on-going scientific and peer-review support from Steve Ingebritsen of USGS, the co-author of two of my papers in this thesis. My work on permeability-depth trends follows directly from published research by Steve Ingebritsen in 2010 and 1999. At the USGS, internal review of the journal paper on "The bulk permeability of fault rocks and protolith in Earth's brittle crust: Insights from statistical analysis of the first global database" was done in great detail by Jonathan Caine. The same paper was peer-reviewed in one of its forms by N. Farrell (University of Aberdeen) and R. Holdsworth (Durham University), who took the time for journal review. In 2016-2017, Michael Manga of University of California is thanked for participating in our discussions of processes that might control permeability in fault zones.

In the second paper, "The biases and trends in fault zone hydrogeology conceptual models: global compilation and categorical data analysis", Andreas Hartmann took time to write suggestions that clarified the presentation of statistical methods. During my data compilation, I visited ETHZ Zurich and I thank Peter Achtziger-Zupancic and Simon Loew for their time to discuss. Much of this research was inspired by observations and data from tunnels. Thanks to the Japan Atomic Energy Agency (JAEA) hydrogeologists at the Mizunami Site, Japan, for explaining the fault permeability structure there, and other useful discussions about faults and fractures and permeability by Dr. Ishii at Horonobe research site, Hokkaido, Japan. I learned a lot at the JpGU conference in Chiba from many of the posters and presentations about fault outcrops and permeability.

The initial permeameter setup idea was taken from the published literature on this topic, and also from my discussions and viewing of the manual probe used by Dr. Koki Kashiwaya, at Kyoto University, in tests on tunnels walls at the Mizunami underground laboratory, a JAEA facility in Japan.

The last part and the largest single part of the thesis, could not be possible without generous help from Denison Mines company who allowed me access to the Wheeler Camp, and drillcore samples, vehicles, nitrogen gas container supplied by the drilling contractor, lodging at the camp, food, transport to Wheeler Camp from Montreal. As part of the project, I provided my assistance to performing packer tests (injection tests) on newly drilled holes during the 2016 summer and 2017 winter seasons (thanks to Peter Longo for giving me the project), and geotechnical core logging on site. Clark Gamelin, the project geology manager on site, provided countless support on site in his busy schedule, cross-sections, and access to mineralized drillcore and most other drillcore. Thanks to Clark Gamelin, Yongxing Liu and Dale Verran of Denison Mines for helpful comments and corrections to the initial draft of text about the geology of the Gryphon deposit.

At McGill University, I thank Jeanne Paquette for teaching me the basics of mineralogy that I needed for my papers later, Yajing Liu for the earthquake seismology course that I sat in, huge thanks to Christie Rowe for the crustal rheology course and parts of other courses that I attempted to attend in between my field work drilling faults in the Athabasca Basin. Although I did not use my fault rock samples yet in the XRD, I am thankful for the experience of learning how this testing method works in the lab. Christie Rowe also suggested, on review of one of my papers in 2016, that the protolith and the fault damage zone might be both controlled by the same controlling processes, thus causing the scaling of permeability (the ratio of it). That idea was tested and used in the discussion in the journal paper later.

CONTRIBUTIONS OF AUTHORS

There are five articles written for scientific journals and I am the lead and primary author on all of them. The co-authors and their contributions are listed below. The co-authors were not involved in data collection, data entry, analysis, figure drafting, and text was originally written by me. The co-authors participated in internal review and editorial text changes. Particular scientific effort and many text edits were done on two articles by Steve Ingebritsen of the US Geological Survey, a co-author on two of the articles.

- Article #1 is in Chapter 3, was submitted and passed the first review in the journal Scientific Data. I am the only author on this paper.
- Article #2 is in Chapter 4, was already published in the journal of Geofluids in 2016. The co-authors were Tom Gleeson and Jeffrey M. McKenzie.
- Article #3 is in Chapter 5. The paper was submitted to a succession of various journals over the 2 years, and recently underwent a review at the Geophysical Research Letters journal. Tom Gleeson and Steve Ingebritsen were the lead scientific methods co-authors, and Jeffrey McKenzie the contributing co-author.
- Article #4 in Chapter 6 was recently submitted and reviewed at the Journal of Geophysical Research Solid Earth. The co-authors are Tom Gleeson, Steve Ingebritsen, and Jeffrey M. McKenzie.
- Article #5 is in Chapter 7 and is in the submission process to a journal. The co-authors, for editorial and internal review comments are Tom Gleeson and Jeffrey McKenzie. I was responsible for the entire test program, industry connections, all methods, apparatus design and testing, data analysis, and a complete draft writing.

The co-author affiliations are:

- Jeffrey McKenzie is at Earth and Planetary Sciences, McGill University, Montreal, Quebec, Canada
- Tom Gleeson is at Civil Engineering / School of Earth and Ocean Sciences, University of Victoria, Victoria, BC, Canada
- Steve Ingebritsen is at U.S. Geological Survey, Menlo Park, California, USA

CHAPTER 1

1 Introduction

1.1 Observations of fluid involvement in brittle fault zones

The permeability of rocks and sediments, and the structural features in the Earth's crust are central to solving problems of pore fluid flow both at present day and over geological time scales. The permeability contrasts in fault zones are important in coupled fluid-geomechanical models of faults (Chester and Logan 1986, Rice 1992, Sibson 2000, Yamashita and Tsutsumi 2018). According to review papers published over the past 100 years, the hydrogeological effects on fluid flow (e.g. barriers and conduits) have been observed at faults feeding thermal springs, in petroleum reservoirs, mines, tunnels, and dam foundations (Bryan 1919, Meinzer 1923, Louderback 1950, Snow 1965, Seeburger 1981). The evidence of enhanced permeability over geological time has been inferred from fractures and mineral veins (Newhouse 1942, Sibson 1981, Kerrich 1986), and similarities to the localization of active hydrothermal flow systems (Curewitz and Karson 1997, Rowland and Simmons 2012). My research follows the terminology for a fault zone's hydro-structural units that emerged from research in structural geology: fault core, damage zone, and the surrounding protolith or host rock (Chester and Logan 1986, Scholz and Anders 1994, Caine et al. 1996).

Brittle faults are structural discontinuities in the Earth's brittle crust, that offset the rocks and geology on either side of the fault. The shear displacement is locally concentrated along central deformation zones ("fault core" zone), along principal slip surfaces, and distributed heterogeneously in smaller faults and fractures in the wider "damage zone" (Chester and Logan 1986, Scholz and Anders 1994, Caine et al. 1996). The fault rocks within a fault core may include gouges and breccias (variably cemented) from cataclasis and brecciation, cataclasites from exhumed from larger depths, and ductile sheared mylonitic rocks (Engelder 1974, Sibson 1977, Woodcock and Mort 2008). In general, the damage zone ends and the protolith begins where the background frequency (spacing or distribution) of macroscopic fractures no longer decreases away from the fault core (Evans 1988, Savage and Brodsky 2011, Choi et al. 2016), and similarly for microfractures (Mitchell and Faulkner 2012), although blocks of protolith may exist in the damage zone. The protolith may also contains natural fractures from macroscopic to microscopic (Snow 1970, Seeburger and Zoback 1982). In this thesis, the bulk permeability data are derived from fault zones at the scale of meters to 100's of meters, and from macroscopic fractures that cut the porous rock matrix that contains discontinuities and pores microscopic scale.

A variety of fault geometries are seen in outcrops of crystalline metamorphic and plutonic rocks, and can be categorized by their inferred paleo-hydraulic behaviours (Scholz and Anders 1994, Caine et al. 1996). Mapping and outcrop testing of petrophysical properties, including permeability, and fracture distributions revealed different styles of heterogeneity and linkages to processes (Faulkner et al. 2010, Matonti et al. 2012, Johri et al. 2014). In large and heterogeneous fault zones, where multiple anastomosing faults (and their fault rocks) may exist, the permeability distribution is difficult to characterize, both in the rock matrix and in the bulk properties.

Some of the earliest *in situ* quantitative estimates of bulk fault permeability of fractures are from engineering projects (Snow 1965), but the most targeted hydraulic tests in fault zones have been done in fault-hosted geothermal reservoirs (Kassoy and Zebib 1978, Bodvarson and Benson 1982).

The role of faults in the flow system depends primarily on local geology. For example, in volcanic rocks with interlayered aquifer-aquitard units, the role of faults as conduits or barriers is uncertain and inferred from the combined geophysical, geochemical, and hydrogeological interpretations (Stimac et al. 2008, Pope et al. 2016). In higher porosity rocks in sedimentary basins, the problem of fault seals and compartmentalization of petroleum reservoirs (Jolley et al. 2010), resulted in studies of outcrops as analogues for fault permeability distributions at depth (Shipton et al. 2002, Flodin 2003, Michie and Haines 2016).

Despite the large amount of drilling and *in situ* hydraulic testing worldwide, there are no comprehensive summary statistics of fault permeability. Previous reviews included relatively few results at depths < 5km, with a discussion on the deepest scientific drilling projects or model-derived permeability estimates (Manning and Ingebritsen 1999, Townend and Zoback 2000, Stober and Bucher 2007, Ingebritsen and Manning 2010). Larger data compilations from bulk permeability tests in fractured metamorphic and plutonic rocks (upper 2km depth) presented useful trends but did not focus on fault zones or the permeability contrasts between faults and protoliths (Ranjram et al. 2015, Achtziger-Zupancic et al. 2017). In published global permeability maps for the upper 100 m of the continental crust (Gleeson et al. 2011), the effects of faults on aquifer properties is not accounted for. With a growing number of measurements, data compilation becomes difficult, while the geoscience specialization can lead to certain biases in data collection at different scales of measurement.

1.2 Research Objectives

The research project has three objectives, as described in Figure 1-1 and outlined here:
1) The first objective was to count and map the inferred simplified fault permeability structures at various locations and regions. This means counting where and how the fault permeability is measured and how it is represented and with what model. The permeability "structure" or conceptual models of permeability patterns across fault zones, had to be simplified to categories such as barrier, barrier-conduit, conduit.
2) The second objective is the comparison of permeability in fault zones from different test methods and scale of measurement. For example, the observations may include change in hydraulic head across a fault, fluid flow, gas seeps, aquifer tests, fracture mapping. Some observations are of natural conditions and some observations are of induced changes during testing or tunnel excavation. The scale of measurement describes the volume of rock tested hydraulically, or participating in the flow system.
3) The third objective was a quantitative, statistical description of the permeability distribution in fault zones world-wide in any available data (mostly in damage zones, and a relatively few measurements in fault core zones only). Integrated in this study is a discussion of processes that may control fault permeability at depth. The statistical approach allows to compare the fault zone permeability at different depths, and rock types, and fault types. I aimed to develop useful empirical relationships, from regression analysis, that could be used to predict the permeability of fault zones from the permeability of the protoliths and depth in the brittle crust.

The last part of the project was a relatively large field project to map the permeability of a fault zone the Wheeler River project (Paper 5 in the thesis). The scientific questions were to characterise the "components" of permeability that correspond to the main fault zone permeability and structural zones (fault damage zone, fault core, protolith). The studied fault is presently not considered to be active, due to lack of evidence for recent displacement or macro-seismic activity. The uranium deposit and the hydrothermal alteration, and fault rocks, have remarkably preserved permeability in the rock matrix and give evidence for the distribution of paleo-permeability. The permeability test results of this study are the compared with other well known active faults. A practical method was developed for testing drillcore samples directly at a mineral exploration site, over a wide range of matrix and small fracture (channelized) permeability, and to collect a large number of permeability measurements rapidly and at low cost.

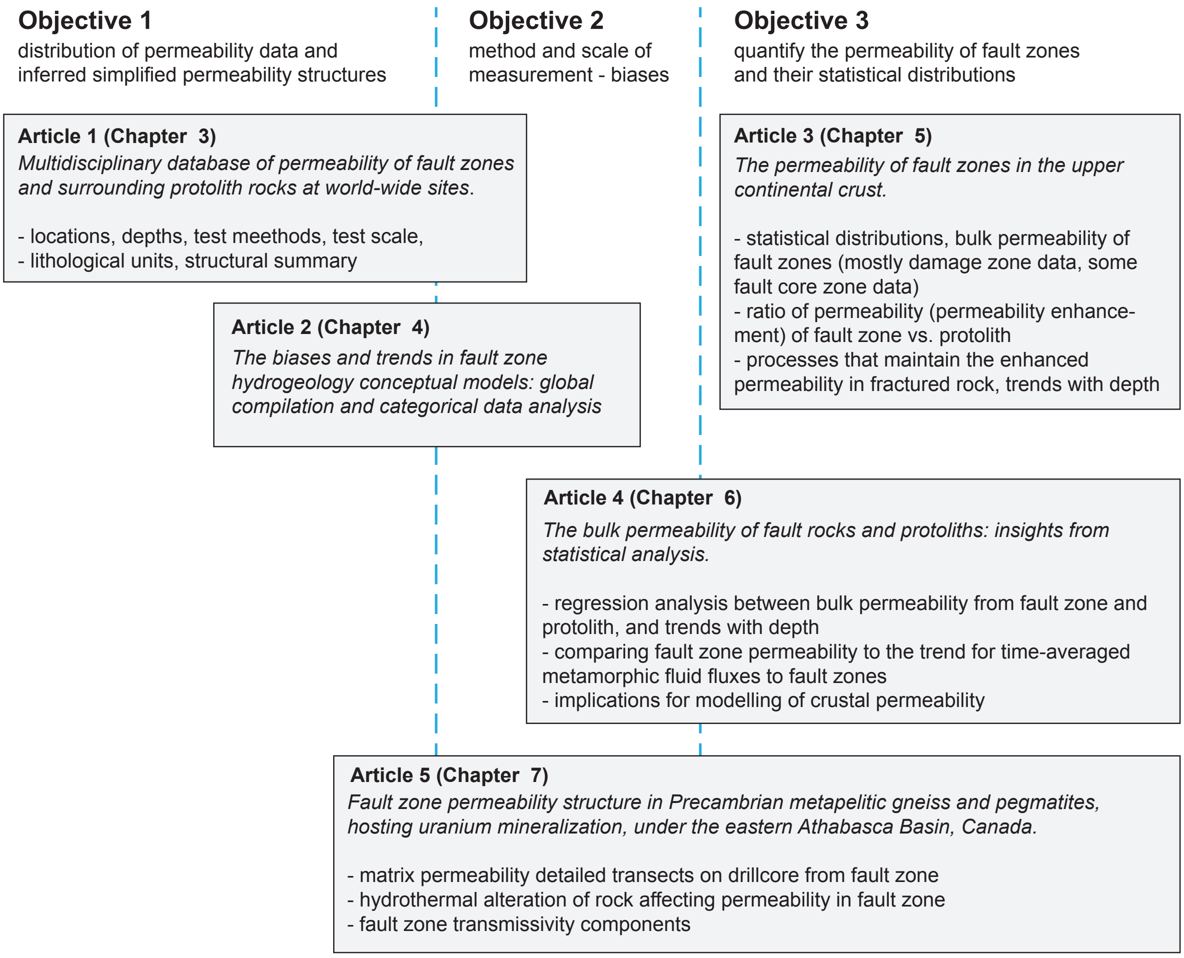

Figure 1-1 Three main objectives of the research and the five research articles in the thesis.

CHAPTER 2

2 Methodology

2.1 Thesis organization

This thesis is presented in the manuscript (article) style, where each article forms a chapter of this thesis. Each article contains an abstract, introduction with a comprehensive review of geoscientific literature (in support of that article), methods, results and discussion, conclusions, and references. The text of original articles was not edited, but the font was changed to match the thesis document style. The tables are also formatted to the common font and fitted to pages. The figure images are only sized to fit to thesis pages. There is a brief introductory text that has been added before ach article abstract, to link the article to the rest of the thesis.

- Chapter 2, provides an overview of the methods used in this research, to avoid repetition, because in each article (chapter) there are detailed descriptions of methods, with relevant references.
- Chapter 3, "Multidisciplinary database of permeability of fault zones and surrounding protolith rocks at world-wide sites", has the 1st article in the logical series, on the subject of the multi-disciplinary database.
- Chapter 4, "The biases and trends in fault zone hydrogeology conceptual models: global compilation and categorical data analysis", has the 2nd paper, is on the topic of biases in observations of fault zone hydrogeology, and presents statistical results (categorical data analysis).
- Chapter 5, "The permeability of fault zones in the upper continental crust", has the 3rd paper about the permeability trends with depth and processes controlling it. There is Appendix 1 with supplementary information (tables, descriptions of larger spreadsheeet tables).
- Chapter 6, "The bulk permeability of fault rocks and protoliths: Insights from statistical analysis", has the 4th paper that presents the results of regression analysis on permeability datasets from fault zones.

- Chapter 7, "Fault zone permeability structure in Precambrian metapelitic gneiss and pegmatites, hosting uranium mineralization, under the eastern Athabasca Basin, Canada", contains the 5th paper, about the permeability testing at my field site.
- Chapter 8 has the summary and conclusions.
- References after chapter 8 are for the introductory chapters 2 and 3 of the thesis.

2.2 Data sources for statistical analysis

In this study I used 429 datasets of permeability data from tests in fault zones at 364 locations world-wide (Figure 2-1). The scope of the work is global and multidisciplinary. There was no limit placed on data quantity or sources. In total, over 10000 publications were searched and more than 3000 used, as references for data (permeability, structure, geology) on fault zones that were then summarized or entered to the database. The various permeability data sources, often isolated from each other in the geoscientific literature, that contributed to this work (taken from Chapter 3).

2.3 The scale of hydraulic tests on fault rocks

An important aspect of the thesis is the careful separation of permeability data at two different test scales for most of the world-wide permeability tests. After a careful review, I applied the terms "matrix" permeability to refer to cohesive rock or incohesive fault gouge at outcrop or drillcore sample scale, that excludes macroscopic open fractures and joints, and "bulk" permeability for the total (or equivalent porous medium) permeability of some rock volume that contains the rock matrix blocks and the macroscopic fracture networks between the blocks. The main difference is that bulk permeability tests both the macroscopic fracture networks and the rock matrix, while the matrix permeability tests only the rock matrix and very small macroscopic fractures or parts of them, and microfractures. The terms are widely used in geothermal and hydrogeological research (e.g. Atomic Energy Control Board 1986, National Research Council 1996, Fisher 1998, Mitchell and Faulkner 2012). The matrix permeability of crystalline rocks is 2 to 4 orders of magnitude smaller than the bulk permeability of the same naturally fractured rocks (Brace 1980). At this scale of flow paths are pore networks in clastic rocks, and a range of small fractures of small length that do not cross the whole drillcore sample, and micro-fractures at mineral grain boundaries and intra-grain (Bossart and Mazurek 1991).

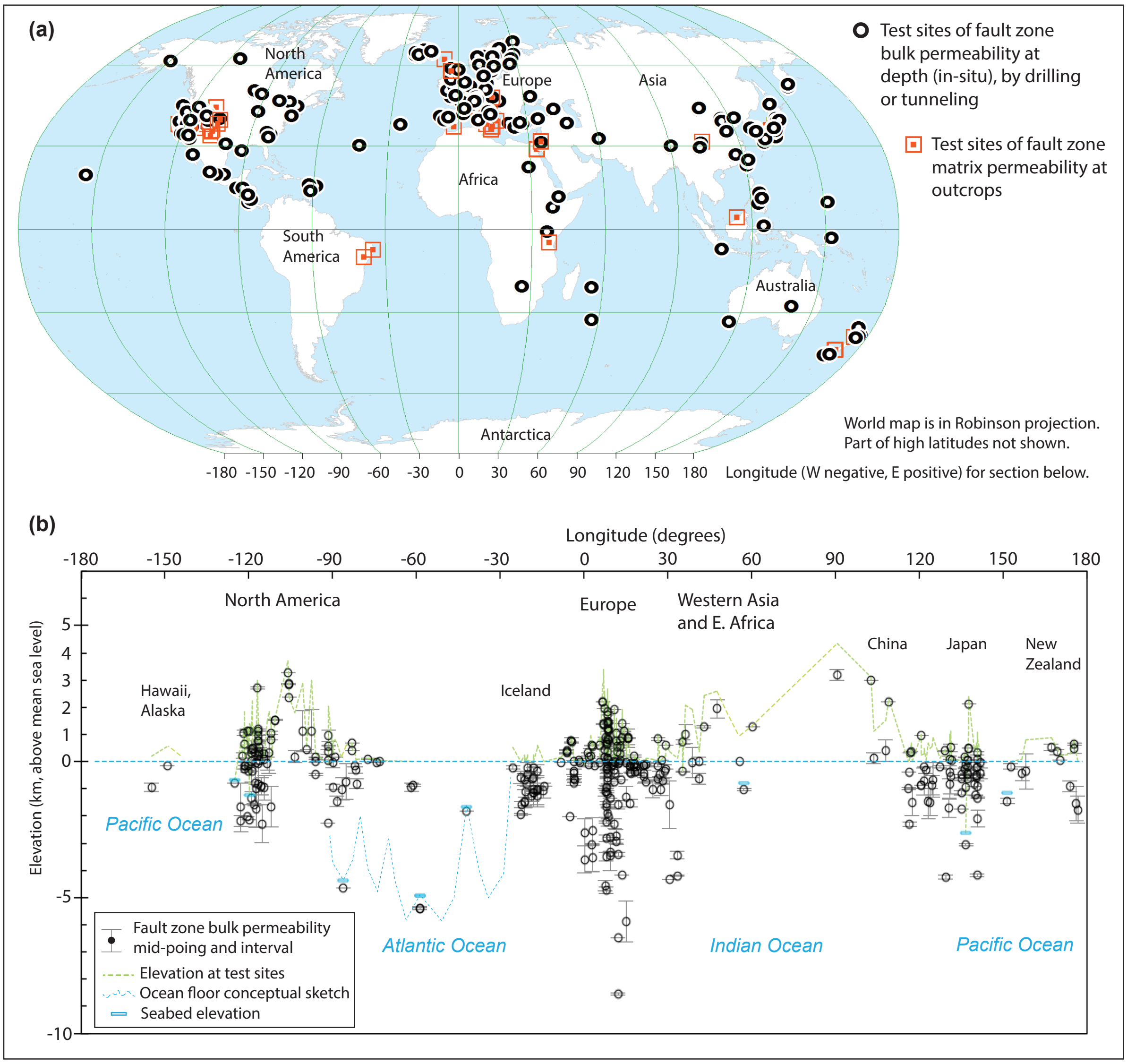

Figure 2-1 (a) World-wide locations of test sites of fault zone permeability shown with different symbols for bulk permeability at depth (in-situ by drilling or tunneling), and matrix permeability (at outcrops). In smaller maps in lower panels the test sites are separated by data source category. (b) Locations along geographic longitude and in-situ depth intervals permeability tests in fault zones. Elevation is relative to mean sea level of in-situ permeability test intervals in drillholes or tunnels. The topographic profile is plotted from elevations of the test sites, and is not a global average elevation. The sea floor elevation at oceanic sites is also indicated, with an added conceptual sketch of ocean floor (not actual transect).

The most prolific data were from in-situ permeability tests at bulk permeability scale, and these were used for most of the statistical analysis and results. The bulk permeability of fault is measured using a variety of methods (e.g. Becker et al 1994, Stober and Bucher 2007, Karasaki et al. 2014, Kitagawa and Kano 2016, Rutqvist 2017), including:

- water discharge tests from specific intervals in drillholes (e.g. "pump tests"),

- water injection tests or transient pressure perturbations in specific intervals of drillholes that were isolated by inflatable packers or other methods (e.g. "packer tests", drill-stem tests (DST), "slug tests", etc.),
- water flow logging from discrete zones in drillholes using flowmeter probes.

In underground tunnels, the groundwater discharge rates from fault zones and the protolith can be compared and the fault zone bulk permeability estimated (e.g. Masset and Loew 2010). Other large-scale measurements of heat flow, hydraulic head or pressure gradients across fault zones, and thermal water up-flow and discharge can be analysed and modelled to estimate the bulk permeability of conduits in fault zones (e.g. review in Bense et al. 2013). Other models of paleo-permeability evolution can be calibrated to geochemical data from rock samples or whole fault outcrops, giving a range of bulk permeabilities of the ancient flow system (e.g. Manning and Ingebritsen 1999, Howald et al. 2017). In this thesis, the emphasis in the statistical analysis is on *in-situ* tests in drillholes and tunnels, with minor contribution from calibrated or well-constrained fluid flow models using permeability at present time at exploited fault-hosted geothermal reservoirs (i.e. not paleo-permeability).

The matrix data are not used in the analysis of permeability with depth because of the small scale of measurements (not including larger fracture networks) and the uncertainty and poor constraints on the irreversible effects of compaction of porous samples at simulated effective depths. This issue is reviewed and discussed in more detail in Chapter 7. The number of datasets and study sites was also much smaller than for the *in-situ* (drilled) test sites.

The matrix permeabilities of fault rocks and in damage zones from the world-wide compilation of published data were summarized with descriptive statistics. The matrix permeability is measured at confining pressures in the laboratory on drillcore samples (Evans et al. 1997, Lockner et al. 2009), on samples taken from outcrops (Wibberley and Shimamoto 2003), or on cored from walls of underground excavations (Wenning et al. 2018). In relatively permeable rocks and sediments, the fault zones can be measured in ambient pressures directly on rock outcrops exposed at ground surface (Balsamo and Storti 2010, Okubo 2012). A few authors of previous publications have also attempted to measure matrix permeability at thin-section (microscopic) scale, and to upscale the results from microfractures to the outcrop (e.g. Gomila et al. 2016), although the microfracture connectivity is known to be weak at sample scale (Zoback and Byerlee 1975).

The matrix permeability along fault zone transects is useful in mapping the permeability patterns and to give some estimate of the bulk permeability and transmissivity of whole fault zone to fluid flow at present time. In this research project, at a field site described in the next section and in Chapter 7, the drillcore samples were tested using a N_2 gas permeameter probe in unconfined ambient air pressure conditions.

2.4 Description of field study site

The field site used in Chapter 7 is located at the Wheeler River project, and focusses on the Gryphon deposit (Figure 2-2). According to Denison Mines, the Wheeler River is the largest undeveloped uranium project in the infrastructure rich eastern portion of the Athabasca Basin region, in northern Saskatchewan (Denison Mines 2018). The Gryphon deposit and fault zone is a wide (>350m) fault zone, mainly with reverse slip since the Proterozoic, parallel to regional metasedimentary strata and structure of fold and thrust belt related to the Trans Hudson Orogeny around 1860 to 1775Ma (Bickford et al. 1990, Tran 2001). The steeply dipping and overturned folds in the orogen have been eroded and truncated to the unconformity surface (Annesley et al. 2005, Jeanneret et al. 2016). The protoliths are metapelites, pegmatite-rich metapelites, pegmatites, and pervasively silicified "metaquartzites". The fault zone is located below about 500m of Athabasca Group sandstones, but fault structures extend from the basement into the sedimentary strata, and possibly to the ground surface, but any outcrops are covered by glacial deposits. In the thesis, I also make references to protoliths and their permeabilities at the Olkiluoto research site in Finland, because of very similar geologic units and structures (Tuisku and Karki 2010).

Lastly, I compared the matrix permeability distribution of the inferred "preserved" permeability structure from >700 Ma age at the Gryphon fault zone with published data from two large active fault zones in Japan: the Median Tectonic Line (MTL), in Mie prefecture (Wibberley and Shimamoto 2003, Shigematsu et al. 2012), and Nojima fault, on Awaji Island, Hyogo prefecture (Ito et al. 2000, Mizoguchi et al. 2008). I selected the data from Japan because of my familiarity with that area, high quality of data, good data availability, and some similarities between the size and structure of the Gryphon fault zone and the MTL in cross-section.

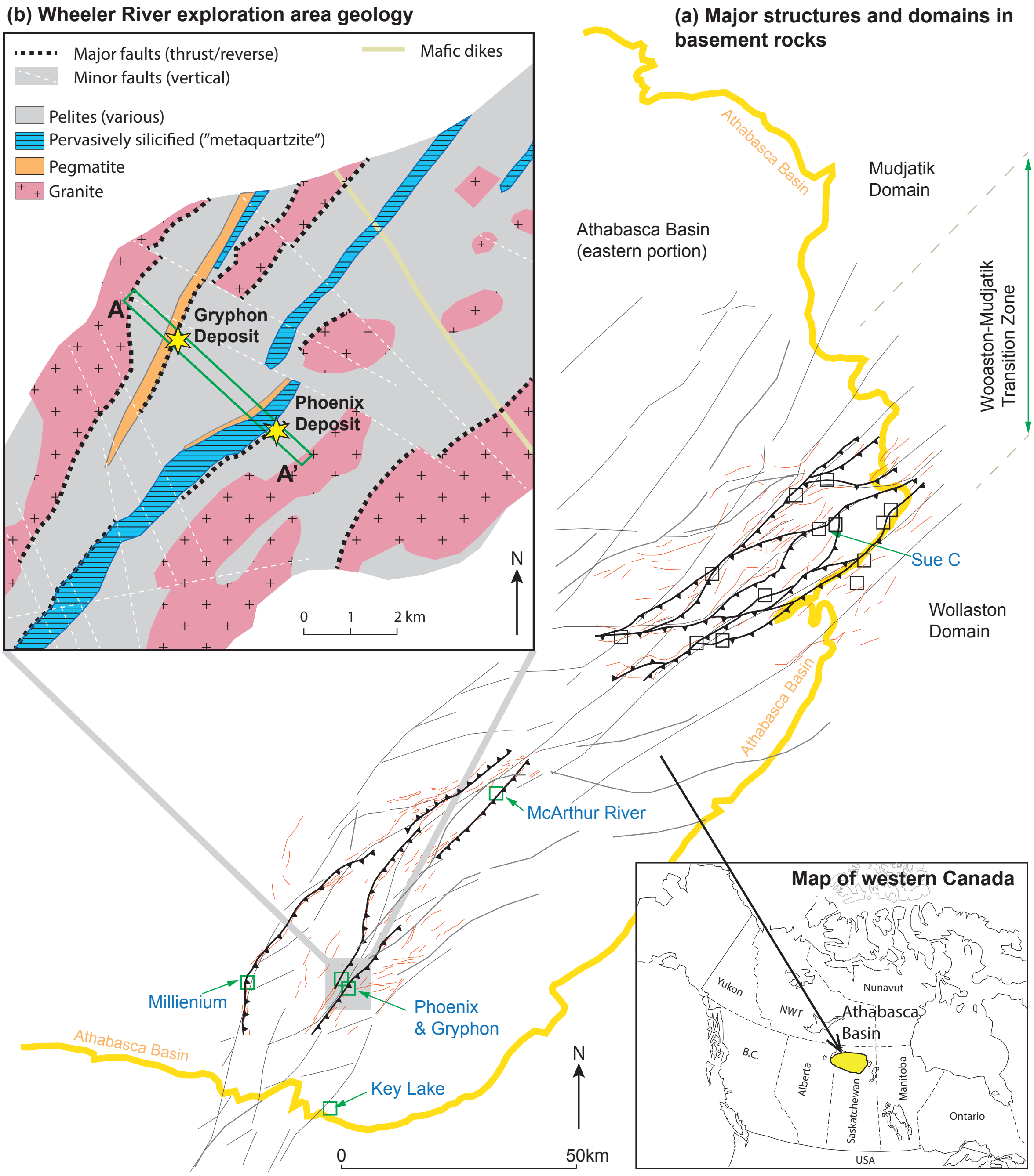

Figure 2-2 (a) The regional structure of the eastern portion of Athabasca Basin, Canada (inset map on lower right), uranium deposits along major faults near the unconformity surface (structure details after Thomas et al. 2014 of Cameco Corp.; regional geology simplified from Jeanneret et al. 2016), (b) geologic map of the Wheeler River exploration area (Denison Mines Ltd. 2018), with a cross-section A-A' indicated from Gryphon and Phoenix deposit.

CHAPTER 3

3 Multidisciplinary database of permeability of fault zones and surrounding protolith rocks at world-wide sites

In this article I describe the methods for a world-wide data review and the format and contents of the resulting database. These datasets are later used in statistical analysis and description in Chapters 3 to 6. The article was written in "Data Descriptor" format, as required by the journal *Scientific Data*. It does not contain any discussion or interpretations, or analyses, except brief literature review and listings of data sources. This article does not contain a conclusions section. The "Data Records" description is in **Appendix 1** of this thesis, although it appears inside the article in the publication format.

3.1 Abstract

The permeability properties of rocks and sediments, and the structural features in the Earth's crust are central to solving problems of pore fluid flow at present and over geological time scales. This data descriptor is for a world-wide database that contains summarized permeability estimates for 429 datasets, from tests in fault zones at 364 locations. The review covered over 9500 research items from multidisciplinary data sources. The main categories of data sources are studies of active faults and faulting processes, geothermal exploration, radioactive waste repository, groundwater resources, petroleum reservoirs, engineering projects). The objectives of this data compilation are to stimulate cross-disciplinary data sharing and communication on the topic of fault zone hydrogeology, to enable further statistical analysis and more informed inputs to models using crustal-permeability as parameters, and to compare the magnitudes of bulk and matrix permeability in different structural domains of fault zones.

3.2 Background and summary

The permeability property of rocks and sediments, and the structural features in the Earth's crust is central to solving problems of pore fluid flow at present and over geological time scales. The hydrogeological effects on fluid flow (e.g. barriers and conduits) have been observed at faults feeding thermal springs, in petroleum reservoirs, mines, tunnels, and dam foundations - according to the review papers published in the past 100 years (Bryan 1919, Meinzer 1923, Louderback 1950, Snow 1965, Seeburger 1981). The evidence of enhanced permeability over geological time has been inferred from fractures and mineral veins (Newhouse 1942, Sibson 1981, Kerrich 1986), and similarities to the localization of active hydrothermal flow systems (Curewitz and Karson 1997, Rowland and Simmons 2012). This article follows the terminology for fault zone's hydro-structural units that emerged from research in structural geology: fault core, damage zone, and the surrounding protolith or host rock (Chester and Logan 1986, Scholz and Anders 1994, Caine et al. 1996). Continued mapping and outcrop testing of petrophysical properties, including permeability, and fracture distributions revealed different styles of heterogeneity and linkages to processes (Faulkner et al. 2010, Matonti et al. 2012, Johri et al. 2014). Some of the earliest in-situ quantitative estimates of bulk fault permeability of fractures have been made at engineering projects (Snow 1965), but the most targeted hydraulic tests in fault zones have been done in fault-hosted geothermal reservoirs (Kassoy and Zebib 1978, Bodvarson and Benson 1982). At any location, the role of faults in the flow system depends on local geology. For example, in volcanic rocks with interlayered aquifer-aquitard units, the role of faults as conduits or barriers is uncertain and inferred from the combined geophysical, geochemical, and hydrogeological interpretations (Stimac et al. 2008, Pope et al. 2016). In higher porosity rocks in sedimentary basins, the problem of fault seals and compartmentalization of petroleum reservoirs (Jolley et al. 2010), resulted in studies of outcrops as analogues for fault permeability distributions at depth (Shipton et al. 2002, Flodin 2003, Michie and Haines 2016).

The data descriptor is for a compiled database of summarized permeability estimates for 429 datasets, from tests in fault zones, at 364 locations world-wide. The review spanned five years and 9500 research items such as journal papers, reports, conference proceedings. World-wide there are various permeability data sources, often isolated from each other in the geoscientific literature, that contributed to this data compilation:

- permeability of faults as parameter in geomechanical models of crustal-scale active faults (Rice 1992, Haneberg et al. 1999, Gratier et al. 2003, Yamashita and Tsutsumi 2018),
- permeability testing in outcrops exhumed from seismogenic depths (Evans et al. 1997, Wibberley and Shimamoto 2003, Lockner et al. 2009, Walker et al. 2010),
- fracture-aperture based estimates of fault paleo-permeability (Hashimoto et al. 2009, Gomila et al. 2016),
- permeability testing in outcrops of sediments poorly lithified rocks (Sigda et al. 1999, Okubo 2012, Balsamo and Storti 2013),
- in-situ hydraulic testing in recently active fault zones on continents (Ito et al. 2000, Doan et al. 2006, Karasaki et al. 2012, Xue et al. 2013, Matsumoto and Shigematsu 2018), and accretionary prisms near seduction zones (Saffer 2015),
- deep scientific drilling in metamorphic crust of recently low tectonic activity (Juhlin and Sandstedt 1989, NEDRA 1992, Huenges et al. 1997),
- permeability of fault zones inferred from the rate of migration of seismicity along faults (Nur and Booker 1972, Shapiro et al. 1999, Miller et al. 2004, Okada et al. 2015), and from other induced-seismicity cases (Talwani et al. 2007),
- permeability parameters in models of hydrothermal ore deposit formation (Ingebritsen and Appold 2012, Cox 2016), or fault zones in metamorphic complexes (Gottardi et al. 2013),
- geothermal exploration and production in naturally faulted reservoirs (Goko 2000, Sausse et al. 2006), and enhanced geothermal reservoirs in faulted rocks (Evans et al. 2005, Ladner and Häring 2009),
- thermal spring conduits along faults (Sorey and Lewis 1976, Lopez and Smith 1996, Gudmundsson et al. 2002, Muraoka et al. 2006),
- regional heat flow and permeability of the faulted crust (Manning and Ingebritsen 1999, Saar and Manga 2004, Saffer 2015),

- hydrogeological studies on radioactive waste storage repositories in faulted Precambrian shields (Bossart et al. 2001, Vaittinen et al. 2011), faulted mudrocks (Marschall et al. 2003, Ishii 2015), or faulted tuffs (Sweetkind and Drake 2007),
- hydrogeology of fault zones in long tunnels (Maréchal 1998, Ganerød et al. 2008, Masset and Loew 2010, Seebeck et al. 2014),
- assessment of groundwater resources in fractured and faulted crystalline basement rocks (Carlsson and Olsson 1977, Mäkelä 2012, Roques et al. 2014),
- petroleum reservoirs in sedimentary rocks, with fault barrier-conduit effects (Antonellini and Aydin 1994, Fisher and Knipe 2001),
- groundwater flow in faulted sedimentary basins (Person et al. 1996, Bense et al. 2013, Cilona et al. 2015).

The sampling and scale of permeability tests is important between the rock matrix permeability can be 2 to 4 orders of magnitude smaller than the bulk properties of the macroscopic fracture networks in low-porosity rocks (Brace 1980, Brace 1984, Clausser 1992, Schulze-Makuch et al. 1999). The relative effect of macroscopic fractures becoming more important in rocks of lower porosity and larger density (Lamur et al. 2017). In this compilation, the matrix permeability refers to tests on small (few cm size) rock samples or rock outcrop spots (Lockner et al. 2009, Mitchell and Faulkner 2012, Morrow et al. 2014), but does not include macroscopic fracture networks. The bulk permeability here refers to an estimate of permeability from in-situ hydraulic tests at length scales of meters to 100's meters that includes connected macroscopic fracture networks (e.g. Zoback and Hickman 1982, Caine and Tomusiak 2003).

Previous reviews included relatively few results at depths <5km, with a discussion on the deepest scientific drilling projects or model-derived permeability estimates (Manning and Ingebritsen 1999, Townend and Zoback 2000, Stober and Bucher 2007, Ingebritsen and Manning 2010). Larger data compilations from bulk permeability tests in fractured metamorphic and plutonic rocks (upper 2km depth) presented useful trends but did not focus on fault zones or the permeability contrasts between faults and protoliths (Ranjram et al. 2015, Achtziger-Zupancic et al. 2017). In the published world-wide average permeability maps of groundwater aquifers in the upper 100m of the continental crust (Gleeson et al. 2011), the effects of faults on aquifer properties were not yet taken into account.

The compilation and description of these permeability data has several objectives:

- First, this work aims to stimulate cross-disciplinary data sharing and communication. With a growing number of measurements, data compilation becomes difficult, while the geoscience specialization can lead to certain biases in data collection at different scales of measurement (Scibek et al. 2016). The multidisciplinary data search was important because most authors in particular geoscientific specialization do not reference works from outside of their field of study, thus creating rather limited reference links that tend to be re-used by subsequent authors.
- Second, this database - or the raw data in the reviewed reference works - can be used for statistical analysis of crustal-permeability trends with depth.
- The third objective is to compare the magnitudes of bulk and matrix permeability in fault damage zone, fault core, and the protolith, where the data are available. The matrix permeability, and its confining pressure-dependency on rock samples, has been reported and discussed extensively. This data compilation contains summaries of matrix permeability datasets, but most of the data are from in-situ test sites (drilled or tunnelled) and the corresponding bulk permeability estimates of fractured rocks.

3.3 Methods

3.3.1 Dataset review process

The concept of "systematic review" and meta-analysis is used many scientific fields (Moher et al. 2009), and here it was adapted to hydrogeological data that are both qualitative and quantitative. The search was comprehensive, using multiple databases, and then searching and reviewing all references listed in every publication found in the database, on the topic of fault zone permeability. The full search of reference lists in all publications was ultimately more systematic and complete, compared to the searches through academic journal or institutional report databases because the titles and keywords were moderately to poorly useful in locating the permeability datasets or supporting documents. The review process is described in Figure 3-1.

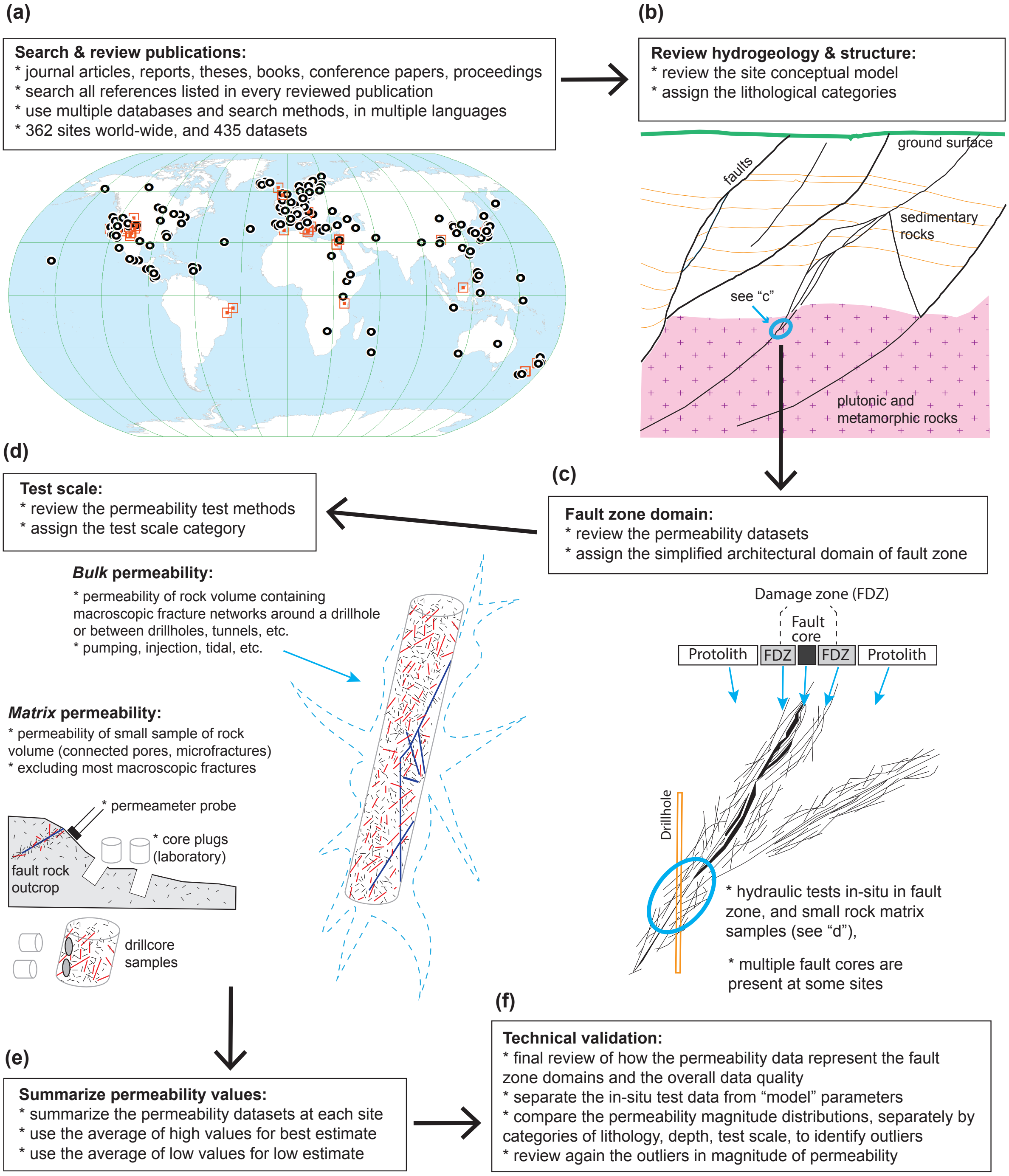

Figure 3-1 Schematic diagram of the permeability data compilation and review process: (a) search and review of publications (map of the world showing the locations of test sites in this study), (b) hydrogeology & structure at site scale (sketch based on Soultz-sous-Forêts geothermal site, modified after Vidal and Genter 2018), (c) fault zone structure and permeability domains (fault zone sketch modified after Vidal et al. 2015, and fault zone domains terminology after Caine et al. 1996), (d) permeability test scale (matrix, bulk (drillhole fracture model modified after Sausse et al. 2008), (e) summary of permeability values in database, (f) technical validation.

The first and still on-going step was a search for relevant publications. For each study location, the hydrogeological conceptual model was reviewed, geological structures summarized, the lithological category assigned, and the type of data available noted in the database. Next, the review focussed on the permeability data in relation to the fault structure. The datasets were separated according to the simplified fault zone domains. The permeability test scale was reviewed and assigned to either matrix or bulk category. The reviewed data were summarized for each dataset at each site. (see the following section about "Permeability summaries"). In the technical validation, each dataset was re-examined on the overall data quality and how it represented the fault zone domains. The magnitude of permeability distributions were compared in for all sites world-wide to identify outliers. This was done separately (in data subsets) by categories of lithology, depth, and test scale. The data outliers were reviewed again to confirm the values. The statistical work is in preparation for publication separately.

3.3.2 Data sources

The data sources are organized in six sections, defined loosely by the objectives and motivations of the studies, although many of the studies were multi-disciplinary (Table 3-1). The locations of in-situ and outcrop test sites are shown in Figure 3-2, and the depth and elevation distribution is plotted along longitude in Figure 3-3a.

Table 3-1 Data sources for inputs to the database, with dataset counts.

Database section	Reviewed datasets in database	# Datasets after review	Downhole in-situ bulk permeability	Outcrop only
Active faults and faulting processes	107	85	51	34
Geothermal reservoirs	164	136	136	0
Radioactive waste repositories	79	77	74	3
Water resources and contaminated sites	20	18	14	4
Petroleum reservoirs and faulting processes	61	41	12	29
Engineering projects	77	72	70	2
Totals	508	429	357	72

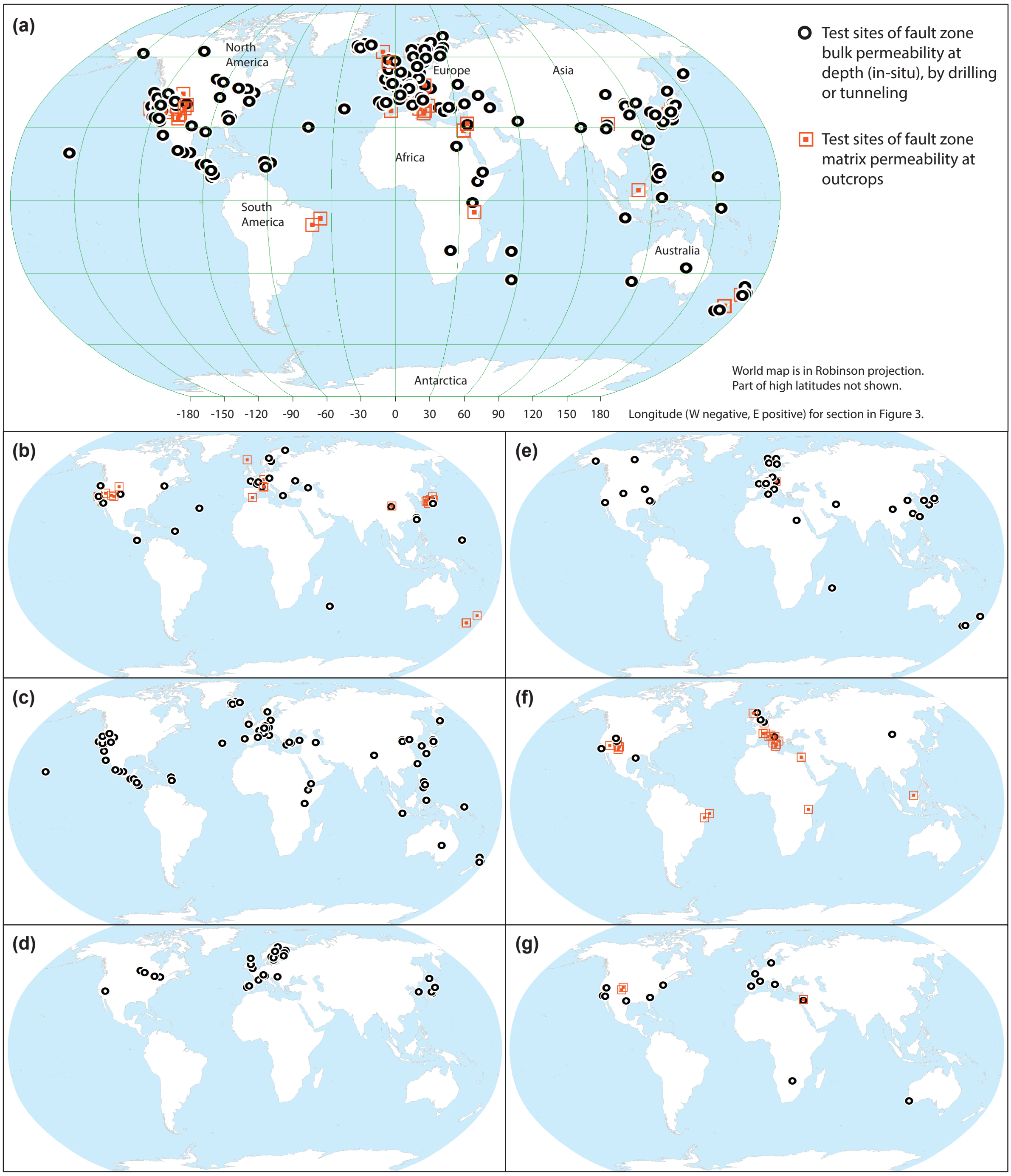

Figure 3-2 (a) World-wide locations of test sites of fault zone permeability shown with different symbols for bulk permeability at depth (in-situ by drilling or tunneling), and matrix permeability (at outcrops). In smaller maps in lower panels the test sites are separated by data source category: (b) active faults and faulting processes, (c) geothermal reservoirs, (d) radioactive waste repository studies, (e) groundwater resources and contaminated sites, (f) petroleum reservoirs and faults in sedimentary rocks, (g) engineering projects.

Active faults and faulting processes:

Approximately 2500 research items were reviewed at 110 locations, from structural and hydrogeological studies. Representative fault zone permeability values were entered for 85 datasets (Table 3-2). Excluded are permeability estimates for sites that could not be reviewed sufficiently or that could not be found. The database contains several estimates of paleo-permeability from fault outcrop mineralogy and geometry, but those were also clearly separated from the in-situ test results.

Geothermal reservoirs:

I reviewed the published data from 240 locations, and categorized 164 reservoirs as dominated by fracture permeability related to faults. We found bulk permeability estimates for 136 reservoirs (Table 3-3). Particularly useful sources of geothermal data were: UNU-GTP (United Nations Geothermal Training Programme) in Iceland, GRC (Geothermal Resources Council) database, and Stanford University Geothermal Workshops. The review and permeability summaries were also done for EGS (Enhanced Geothermal System) and HDR (Hot Dry Rock) sites. The enhanced permeability of faults after pressure injection ("fault stimulation") were stored separately from the values "before stimulation" (natural conditions). In many geothermal fields, the numerical models provide a good summary of site-wide bulk permeability, because the models are calibrated to in-situ hydraulic tests. In some cases were not able to review the original in-situ data, only the site-wide models. The notes in the database indicate the data source and in-situ test methods and/or models.

Radioactive waste repository studies:

The hydrogeological investigations motivated by test sites for nuclear waste disposal (Table 3-4), generally located in low-porosity fractured and faulted metamorphic, plutonic, and volcanic rocks, are a good data source (77 datasets). The reports containing the data are searchable through the INIS Repository database of the International Atomic Energy Agency (IAEA) and from national agencies such as Nagra (Switzerland), SKB (Sweden), Posiva Oy (Finland), and the USGS and U.S. Department of Energy, as well as national laboratories (United States), JAEA (Japan), AECL (Canada). Selected results have also been published previously in scientific journals.

Groundwater resources and contaminated sites:

Aquifer models average large volumes of material and in a few cases obtain estimates of fault zone conductance or hydraulic conductivity for groundwater flow across the fault, calibrating to observed hydraulic head distributions around the fault zone. Statistical studies on well yield correlations with fault zones were not useful because the well yield could not readily be converted to permeability, and because the datasets were regional and not site-specific. Of the hundreds of aquifer studies reviewed, only 18 datasets were used as representative of fault permeability structures (Table 3-5).

Petroleum reservoirs and faults in sedimentary rocks:

Many permeability measurements are done routinely by the petroleum industry, and the search results were from publically available articles and reports only. There are 61 published datasets on permeability of fault rocks in sedimentary basins and were able to use 41 of these. The data are largely from outcrop transects (29 sites). In 12 of the datasets, the matrix permeability values were reported from drilled cores from depth, and in a few cases permeability values were tested in-situ using hydraulic methods (Table 3-6).

Engineering projects:

This section relies upon reports and papers on hydraulic tests and observations in long tunnels, mines, and dams constructed in various lithologies and at depths up to 1.5 km. 72 datasets were used. Groundwater inflow to tunnels from fault zones can provide estimates of transmissivity and bulk permeability. The values can be compared to results of other in-situ hydraulic tests at the same sites (Table 3-7).

Table 3-2 List of sites for inputs to database section "Active faults and faulting processes".

Dataset #	Site Name	Country
1	Jorgillo fault	Chile
2, 3	Wenchuan, Yingxiu-Beichuan faults	China
4	Faroe Islands fault zones	Denmark
5, 6, 9	LSBB galeries lab, Ploemeur, Coaraze	France
7, 8, 12	fault outcrops in Rhine Graben, Bersezio faults	France
10, 11	Auriat, Sancerre-Couy drillholes	France
13, 14	Aigion and Pirgaki faults	Greece
15, 16	KTB	Germany
18, 19	Hanaore fault, Iida-Matsukawa fault	Japan
20 to 22	Median Tectonic Line sites, Matsusaka-Iitaka (ITA) obs.	Japan
23, 24	Nojima fault	Japan
25, 26	Shimanto accret. complex (Okitsu, Mugi outcrops)	Japan
27 to 31	Neodani (at Kinbara, Midori), Usukidani, Nishiyama, Tsugawa faults	Japan
32, 33	Atotsugawa fault, Tottori-ken Seibu EQ fault	Japan
34, 35	Taranaki Rift, Alpine fault drilling/outcrops	New Zealand
36, 37	Chelungpu, Pingshi faults	Taiwan (Rep. China)
38 to 40	SG-3 Kola, SG-8 Krovoy Rog, Tyrnauz	Russia & Ukraine
41	Carboneras fault	Spain
42, 43	Gravberg-1, COSC	Sweden
44 to 47	San Andreas (Cajon Pass, Cienaga Valley, SAFOD)	USA (California)
47 to 53	San Andreas fault system (Logan quarry, Big Pines, Golden Gate, Dry Lk, Hi Vista, Pinyon Flat obs.)	USA (California)
54, 55	Wildcat fault, Silver Creek fault	USA (California)
56	Elkhorn fault	USA (Colorado)
57	Stillwater fault (Dixie Valley)	USA (Nevada)
58 to 59	White Canyon, Spring and Sage Flat Hollow sites	USA (Utah)
60	Champlain Thrust	USA (Vermont)
61	East Fork thrust fault	USA (Wyoming)
Ocean drilling sites:		
62 to 66	Middle Valley, Barbados N. Ridge, Costa Rica Rift	(Atlantic Ocean)
67, 68, 69	Nankai Trough, Woodlark Basin	(Pacific Ocean)
70	SW Indian Ridge (Atlantis II FZ)	(Indian Ocean)
71, 72	Mid-Atlantic Ridge	(Atlantic Ocean)

Table 3-3 List of sites for inputs to database section "Geothermal reservoirs".

Dataset #	Site Name	Country
73	Habanero	Australia
74 to 79	Tianjin, Lishuiqiao, Xiongxian, Silapu, Zhangzhou, Yangbajing	China
80	Miravalles	Costa Rica
81, 82	Ahuachapan, Berlin	El Salvador
83, 84	Aluto-Langano, Dubti	Ethiopia
85, 86	Soultz-sous-Forêts, Rittershoffen	France
87	Bouillante (Guadeloupe Island)	France
88	Le Mayet de Montagne	France
89 to 93	Landau, Urach-3, Waldshut-T., Bad Teinach, Unterhaching,	Germany
94 to 96	Falkenberg, Groß Schönebeck, Bruchsal	Germany
97	Milos	Greece
98	Zunil	Guatemala
99	Platanares	Hoduras
100 to 102	Krafla, Namafjall (Bjarnaflag), Theistarekir	Iceland (North)
103 to 105	Nesjavellir, Hellisheidi, Ölfus-Bakki	Iceland (SW)
106 to 108	Svartsengi, Reykjanes, Ellidaar	Iceland (SW)
109 to 116	Botn, Glerardalur, Laugaland (Daelustod), Thelamork, Hjalteyri, Hamar, Laugerengi, Hofsstadir	Iceland (North & West)
117 to 120	Gata, Kaldarholt, Efri-Reykir Biskupstungur, Ósabotnar	Iceland (South)
121, 122	Eskifjordur, Urridavatn	Iceland (East)
123, 124	Kamojang, Lahendong	Indonesia
125	NW Mt. Sabalan	Iran
126 to 128	Larderello, Piancastagnaio, Mt. Amiata, T. di Valdieri	Italy
129 to 132	Hatchobaru/Otake, Oguni, Kirishima, Yamagawa	Japan (Kyushu)
133 to 142	Kakkonda, Matsukawa, Sumikawa, Onikobe, Uenotai Okuaizu, Akinomiya, Hijiori, Ogachi, Mori	Japan (north)
143	Olkaria East (Olkaria 1)	Kenya
144 an 148	Cerro Prieto, Los Humeros, Los Azufres, Tres Virgenes, Cerritos Colorados	Mexico
149 to 151	Kawerau, Ngawha, Rotokawa	New Zealand
152	Momotombo	Nicaragua
153	Lihir (Ladolam)	Papua N.Guinea
154 to 156	Bacon-Manito, Palinpinon, Tongonan	Philippines
157, 158	S. Pedro do Sul, Ribeira Grande	Portugal
159	Chingshui	Taiwan
160 to 161	Pauzhetka (Pautzetsky), Mutnovsky (Dachny)	Russia
162	Qualibou caldera	St. Lucia
163	Pohang EGS	South Korea
164	El Vallés rift (Valles-Penedes)	Spain
165	Fjällbacka	Sweden
166 to 168	Basel 1 EGS, St. Gallen, Riehen	Switzerland
169 to 173	Kizildere, Germencik, Salavatlı-Sultanhisar, Balcova, Sorgun	Turkey
174	Rosemanowes Quarry	UK
175 to 179	Beowawe, Desert Peak, Dixie Valley, Steamboat, Bradys HS	USA (Nevada)
180 to 186	Coso, Heber, The Geysers, Susanville, Wendel HS, Long Valley Caldera, Glass Mtn.	USA (California)
187, 188	Raft River, Boise Front Fault	USA (Idaho)
189	Fenton Hill	USA (NM)
190, 191	Crystal Hot Springs, Roosevelt HS	USA (Utah)
192, 193	Klamath Falls, Neal Hot Springs	USA (Oregon)
194	Makushin	USA (Alaska)
195	Kilauea Volcano, East Rift Zone	USA (Hawaii)

CHAPTER 1

1 Introduction

1.1 Observations of fluid involvement in brittle fault zones

The permeability of rocks and sediments, and the structural features in the Earth's crust are central to solving problems of pore fluid flow both at present day and over geological time scales. The permeability contrasts in fault zones are important in coupled fluid-geomechanical models of faults (Chester and Logan 1986, Rice 1992, Sibson 2000, Yamashita and Tsutsumi 2018). According to review papers published over the past 100 years, the hydrogeological effects on fluid flow (e.g. barriers and conduits) have been observed at faults feeding thermal springs, in petroleum reservoirs, mines, tunnels, and dam foundations (Bryan 1919, Meinzer 1923, Louderback 1950, Snow 1965, Seeburger 1981). The evidence of enhanced permeability over geological time has been inferred from fractures and mineral veins (Newhouse 1942, Sibson 1981, Kerrich 1986), and similarities to the localization of active hydrothermal flow systems (Curewitz and Karson 1997, Rowland and Simmons 2012). My research follows the terminology for a fault zone's hydro-structural units that emerged from research in structural geology: fault core, damage zone, and the surrounding protolith or host rock (Chester and Logan 1986, Scholz and Anders 1994, Caine et al. 1996).

Brittle faults are structural discontinuities in the Earth's brittle crust, that offset the rocks and geology on either side of the fault. The shear displacement is locally concentrated along central deformation zones ("fault core" zone), along principal slip surfaces, and distributed heterogeneously in smaller faults and fractures in the wider "damage zone" (Chester and Logan 1986, Scholz and Anders 1994, Caine et al. 1996). The fault rocks within a fault core may include gouges and breccias (variably cemented) from cataclasis and brecciation, cataclasites from exhumed from larger depths, and ductile sheared mylonitic rocks (Engelder 1974, Sibson 1977, Woodcock and Mort 2008). In general, the damage zone ends and the protolith begins where the background frequency (spacing or distribution) of macroscopic fractures no longer decreases away from the fault core (Evans 1988, Savage and Brodsky 2011, Choi et al. 2016), and similarly for microfractures (Mitchell and Faulkner 2012), although blocks of protolith may exist in the damage zone. The protolith may also contains natural fractures from macroscopic to microscopic (Snow 1970, Seeburger and Zoback 1982). In this thesis, the bulk permeability data are derived from fault zones at the scale of meters to 100's of meters, and from macroscopic fractures that cut the porous rock matrix that contains discontinuities and pores microscopic scale.

A variety of fault geometries are seen in outcrops of crystalline metamorphic and plutonic rocks, and can be categorized by their inferred paleo-hydraulic behaviours (Scholz and Anders 1994, Caine et al. 1996). Mapping and outcrop testing of petrophysical properties, including permeability, and fracture distributions revealed different styles of heterogeneity and linkages to processes (Faulkner et al. 2010, Matonti et al. 2012, Johri et al. 2014). In large and heterogeneous fault zones, where multiple anastomosing faults (and their fault rocks) may exist, the permeability distribution is difficult to characterize, both in the rock matrix and in the bulk properties.

Some of the earliest *in situ* quantitative estimates of bulk fault permeability of fractures are from engineering projects (Snow 1965), but the most targeted hydraulic tests in fault zones have been done in fault-hosted geothermal reservoirs (Kassoy and Zebib 1978, Bodvarson and Benson 1982).

The role of faults in the flow system depends primarily on local geology. For example, in volcanic rocks with interlayered aquifer-aquitard units, the role of faults as conduits or barriers is uncertain and inferred from the combined geophysical, geochemical, and hydrogeological interpretations (Stimac et al. 2008, Pope et al. 2016). In higher porosity rocks in sedimentary basins, the problem of fault seals and compartmentalization of petroleum reservoirs (Jolley et al. 2010), resulted in studies of outcrops as analogues for fault permeability distributions at depth (Shipton et al. 2002, Flodin 2003, Michie and Haines 2016).

Despite the large amount of drilling and *in situ* hydraulic testing worldwide, there are no comprehensive summary statistics of fault permeability. Previous reviews included relatively few results at depths < 5km, with a discussion on the deepest scientific drilling projects or model-derived permeability estimates (Manning and Ingebritsen 1999, Townend and Zoback 2000, Stober and Bucher 2007, Ingebritsen and Manning 2010). Larger data compilations from bulk permeability tests in fractured metamorphic and plutonic rocks (upper 2km depth) presented useful trends but did not focus on fault zones or the permeability contrasts between faults and protoliths (Ranjram et al. 2015, Achtziger-Zupancic et al. 2017). In published global permeability maps for the upper 100 m of the continental crust (Gleeson et al. 2011), the effects of faults on aquifer properties is not accounted for. With a growing number of measurements, data compilation becomes difficult, while the geoscience specialization can lead to certain biases in data collection at different scales of measurement.

1.2 Research Objectives

The research project has three objectives, as described in Figure 1-1 and outlined here:
1) The first objective was to count and map the inferred simplified fault permeability structures at various locations and regions. This means counting where and how the fault permeability is measured and how it is represented and with what model. The permeability "structure" or conceptual models of permeability patterns across fault zones, had to be simplified to categories such as barrier, barrier-conduit, conduit.
2) The second objective is the comparison of permeability in fault zones from different test methods and scale of measurement. For example, the observations may include change in hydraulic head across a fault, fluid flow, gas seeps, aquifer tests, fracture mapping. Some observations are of natural conditions and some observations are of induced changes during testing or tunnel excavation. The scale of measurement describes the volume of rock tested hydraulically, or participating in the flow system.
3) The third objective was a quantitative, statistical description of the permeability distribution in fault zones world-wide in any available data (mostly in damage zones, and a relatively few measurements in fault core zones only). Integrated in this study is a discussion of processes that may control fault permeability at depth. The statistical approach allows to compare the fault zone permeability at different depths, and rock types, and fault types. I aimed to develop useful empirical relationships, from regression analysis, that could be used to predict the permeability of fault zones from the permeability of the protoliths and depth in the brittle crust.

The last part of the project was a relatively large field project to map the permeability of a fault zone the Wheeler River project (Paper 5 in the thesis). The scientific questions were to characterise the "components" of permeability that correspond to the main fault zone permeability and structural zones (fault damage zone, fault core, protolith). The studied fault is presently not considered to be active, due to lack of evidence for recent displacement or macro-seismic activity. The uranium deposit and the hydrothermal alteration, and fault rocks, have remarkably preserved permeability in the rock matrix and give evidence for the distribution of paleo-permeability. The permeability test results of this study are the compared with other well known active faults. A practical method was developed for testing drillcore samples directly at a mineral exploration site, over a wide range of matrix and small fracture (channelized) permeability, and to collect a large number of permeability measurements rapidly and at low cost.

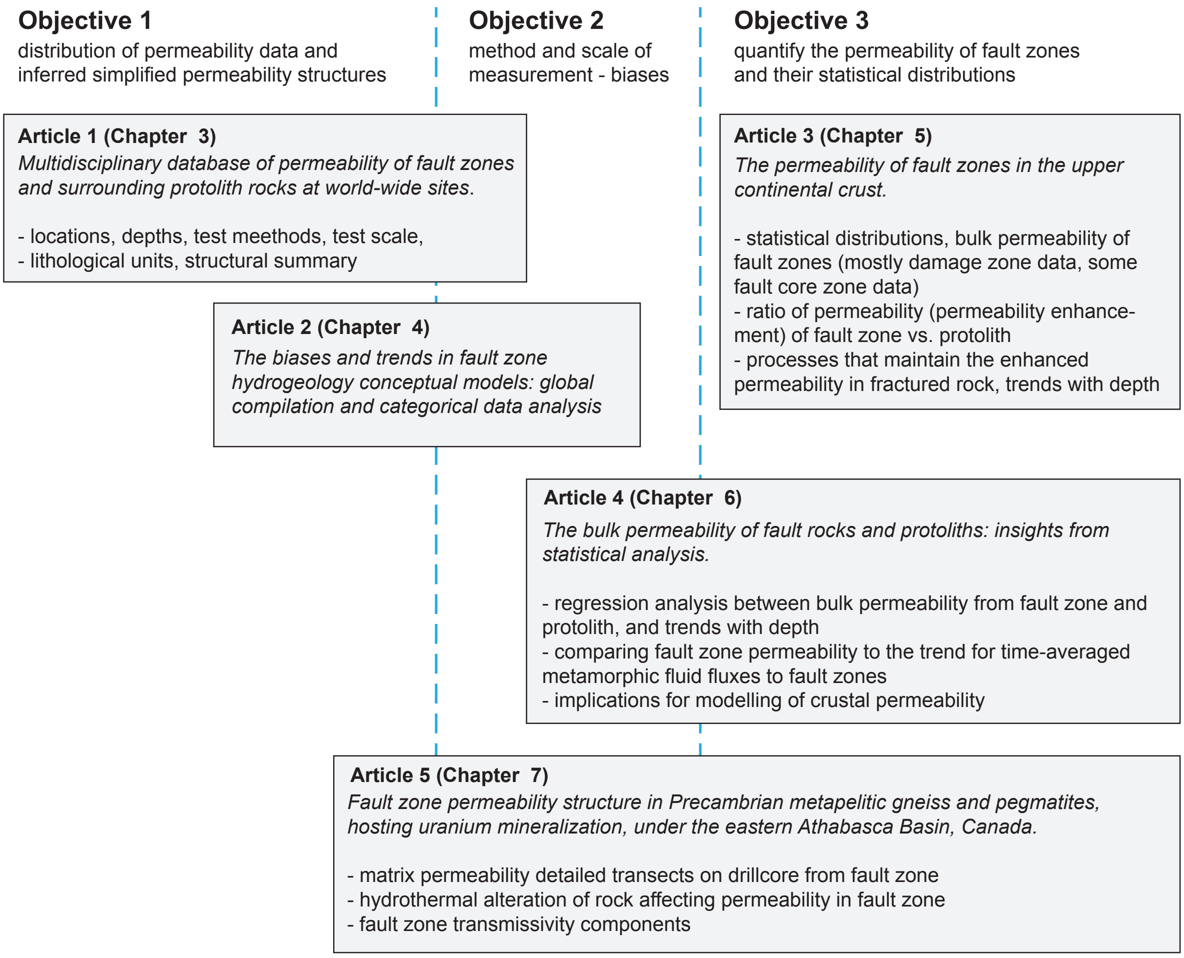

Figure 1-1 Three main objectives of the research and the five research articles in the thesis.

CHAPTER 2

2 Methodology

2.1 Thesis organization

This thesis is presented in the manuscript (article) style, where each article forms a chapter of this thesis. Each article contains an abstract, introduction with a comprehensive review of geoscientific literature (in support of that article), methods, results and discussion, conclusions, and references. The text of original articles was not edited, but the font was changed to match the thesis document style. The tables are also formatted to the common font and fitted to pages. The figure images are only sized to fit to thesis pages. There is a brief introductory text that has been added before ach article abstract, to link the article to the rest of the thesis.

- Chapter 2, provides an overview of the methods used in this research, to avoid repetition, because in each article (chapter) there are detailed descriptions of methods, with relevant references.
- Chapter 3, "Multidisciplinary database of permeability of fault zones and surrounding protolith rocks at world-wide sites", has the 1st article in the logical series, on the subject of the multi-disciplinary database.
- Chapter 4, "The biases and trends in fault zone hydrogeology conceptual models: global compilation and categorical data analysis", has the 2nd paper, is on the topic of biases in observations of fault zone hydrogeology, and presents statistical results (categorical data analysis).
- Chapter 5, "The permeability of fault zones in the upper continental crust", has the 3rd paper about the permeability trends with depth and processes controlling it. There is Appendix 1 with supplementary information (tables, descriptions of larger spreadsheeet tables).
- Chapter 6, "The bulk permeability of fault rocks and protoliths: Insights from statistical analysis", has the 4th paper that presents the results of regression analysis on permeability datasets from fault zones.

- Chapter 7, "Fault zone permeability structure in Precambrian metapelitic gneiss and pegmatites, hosting uranium mineralization, under the eastern Athabasca Basin, Canada", contains the 5th paper, about the permeability testing at my field site.
- Chapter 8 has the summary and conclusions.
- References after chapter 8 are for the introductory chapters 2 and 3 of the thesis.

2.2 Data sources for statistical analysis

In this study I used 429 datasets of permeability data from tests in fault zones at 364 locations world-wide (Figure 2-1). The scope of the work is global and multidisciplinary. There was no limit placed on data quantity or sources. In total, over 10000 publications were searched and more than 3000 used, as references for data (permeability, structure, geology) on fault zones that were then summarized or entered to the database. The various permeability data sources, often isolated from each other in the geoscientific literature, that contributed to this work (taken from Chapter 3).

2.3 The scale of hydraulic tests on fault rocks

An important aspect of the thesis is the careful separation of permeability data at two different test scales for most of the world-wide permeability tests. After a careful review, I applied the terms "matrix" permeability to refer to cohesive rock or incohesive fault gouge at outcrop or drillcore sample scale, that excludes macroscopic open fractures and joints, and "bulk" permeability for the total (or equivalent porous medium) permeability of some rock volume that contains the rock matrix blocks and the macroscopic fracture networks between the blocks. The main difference is that bulk permeability tests both the macroscopic fracture networks and the rock matrix, while the matrix permeability tests only the rock matrix and very small macroscopic fractures or parts of them, and microfractures. The terms are widely used in geothermal and hydrogeological research (e.g. Atomic Energy Control Board 1986, National Research Council 1996, Fisher 1998, Mitchell and Faulkner 2012). The matrix permeability of crystalline rocks is 2 to 4 orders of magnitude smaller than the bulk permeability of the same naturally fractured rocks (Brace 1980). At this scale of flow paths are pore networks in clastic rocks, and a range of small fractures of small length that do not cross the whole drillcore sample, and micro-fractures at mineral grain boundaries and intra-grain (Bossart and Mazurek 1991).

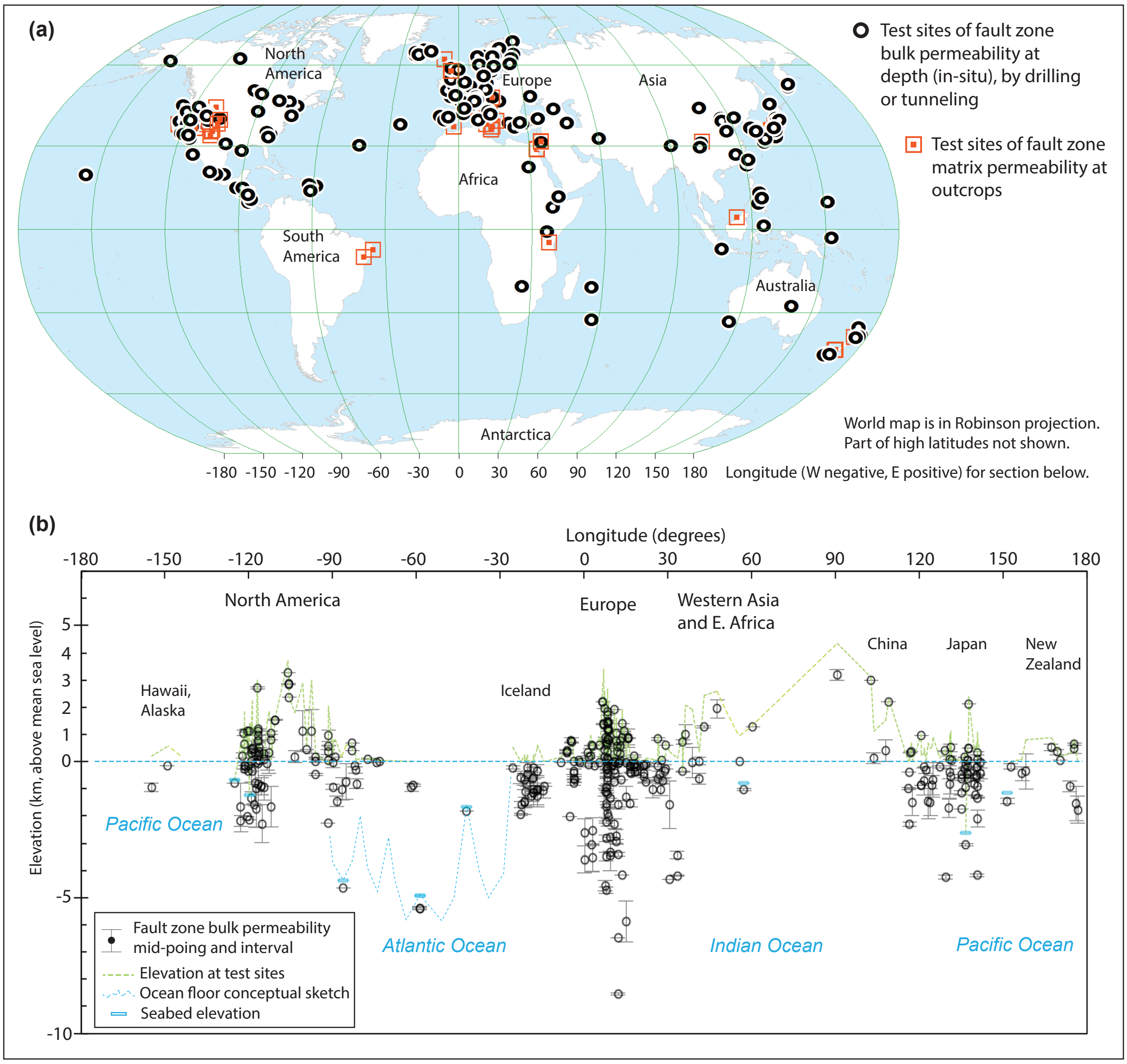

Figure 2-1 (a) World-wide locations of test sites of fault zone permeability shown with different symbols for bulk permeability at depth (in-situ by drilling or tunneling), and matrix permeability (at outcrops). In smaller maps in lower panels the test sites are separated by data source category. (b) Locations along geographic longitude and in-situ depth intervals permeability tests in fault zones. Elevation is relative to mean sea level of in-situ permeability test intervals in drillholes or tunnels. The topographic profile is plotted from elevations of the test sites, and is not a global average elevation. The sea floor elevation at oceanic sites is also indicated, with an added conceptual sketch of ocean floor (not actual transect).

The most prolific data were from in-situ permeability tests at bulk permeability scale, and these were used for most of the statistical analysis and results. The bulk permeability of fault is measured using a variety of methods (e.g. Becker et al 1994, Stober and Bucher 2007, Karasaki et al. 2014, Kitagawa and Kano 2016, Rutqvist 2017), including:

- water discharge tests from specific intervals in drillholes (e.g. "pump tests"),

- water injection tests or transient pressure perturbations in specific intervals of drillholes that were isolated by inflatable packers or other methods (e.g. "packer tests", drill-stem tests (DST), "slug tests", etc.),
- water flow logging from discrete zones in drillholes using flowmeter probes.

In underground tunnels, the groundwater discharge rates from fault zones and the protolith can be compared and the fault zone bulk permeability estimated (e.g. Masset and Loew 2010). Other large-scale measurements of heat flow, hydraulic head or pressure gradients across fault zones, and thermal water up-flow and discharge can be analysed and modelled to estimate the bulk permeability of conduits in fault zones (e.g. review in Bense et al. 2013). Other models of paleo-permeability evolution can be calibrated to geochemical data from rock samples or whole fault outcrops, giving a range of bulk permeabilities of the ancient flow system (e.g. Manning and Ingebritsen 1999, Howald et al. 2017). In this thesis, the emphasis in the statistical analysis is on *in-situ* tests in drillholes and tunnels, with minor contribution from calibrated or well-constrained fluid flow models using permeability at present time at exploited fault-hosted geothermal reservoirs (i.e. not paleo-permeability).

The matrix data are not used in the analysis of permeability with depth because of the small scale of measurements (not including larger fracture networks) and the uncertainty and poor constraints on the irreversible effects of compaction of porous samples at simulated effective depths. This issue is reviewed and discussed in more detail in Chapter 7. The number of datasets and study sites was also much smaller than for the *in-situ* (drilled) test sites.

The matrix permeabilities of fault rocks and in damage zones from the world-wide compilation of published data were summarized with descriptive statistics. The matrix permeability is measured at confining pressures in the laboratory on drillcore samples (Evans et al. 1997, Lockner et al. 2009), on samples taken from outcrops (Wibberley and Shimamoto 2003), or on cored from walls of underground excavations (Wenning et al. 2018). In relatively permeable rocks and sediments, the fault zones can be measured in ambient pressures directly on rock outcrops exposed at ground surface (Balsamo and Storti 2010, Okubo 2012). A few authors of previous publications have also attempted to measure matrix permeability at thin-section (microscopic) scale, and to upscale the results from microfractures to the outcrop (e.g. Gomila et al. 2016), although the microfracture connectivity is known to be weak at sample scale (Zoback and Byerlee 1975).

The matrix permeability along fault zone transects is useful in mapping the permeability patterns and to give some estimate of the bulk permeability and transmissivity of whole fault zone to fluid flow at present time. In this research project, at a field site described in the next section and in Chapter 7, the drillcore samples were tested using a N_2 gas permeameter probe in unconfined ambient air pressure conditions.

2.4 Description of field study site

The field site used in Chapter 7 is located at the Wheeler River project, and focusses on the Gryphon deposit (Figure 2-2). According to Denison Mines, the Wheeler River is the largest undeveloped uranium project in the infrastructure rich eastern portion of the Athabasca Basin region, in northern Saskatchewan (Denison Mines 2018). The Gryphon deposit and fault zone is a wide (>350m) fault zone, mainly with reverse slip since the Proterozoic, parallel to regional metasedimentary strata and structure of fold and thrust belt related to the Trans Hudson Orogeny around 1860 to 1775Ma (Bickford et al. 1990, Tran 2001). The steeply dipping and overturned folds in the orogen have been eroded and truncated to the unconformity surface (Annesley et al. 2005, Jeanneret et al. 2016). The protoliths are metapelites, pegmatite-rich metapelites, pegmatites, and pervasively silicified "metaquartzites". The fault zone is located below about 500m of Athabasca Group sandstones, but fault structures extend from the basement into the sedimentary strata, and possibly to the ground surface, but any outcrops are covered by glacial deposits. In the thesis, I also make references to protoliths and their permeabilities at the Olkiluoto research site in Finland, because of very similar geologic units and structures (Tuisku and Karki 2010).

Lastly, I compared the matrix permeability distribution of the inferred "preserved" permeability structure from >700 Ma age at the Gryphon fault zone with published data from two large active fault zones in Japan: the Median Tectonic Line (MTL), in Mie prefecture (Wibberley and Shimamoto 2003, Shigematsu et al. 2012), and Nojima fault, on Awaji Island, Hyogo prefecture (Ito et al. 2000, Mizoguchi et al. 2008). I selected the data from Japan because of my familiarity with that area, high quality of data, good data availability, and some similarities between the size and structure of the Gryphon fault zone and the MTL in cross-section.

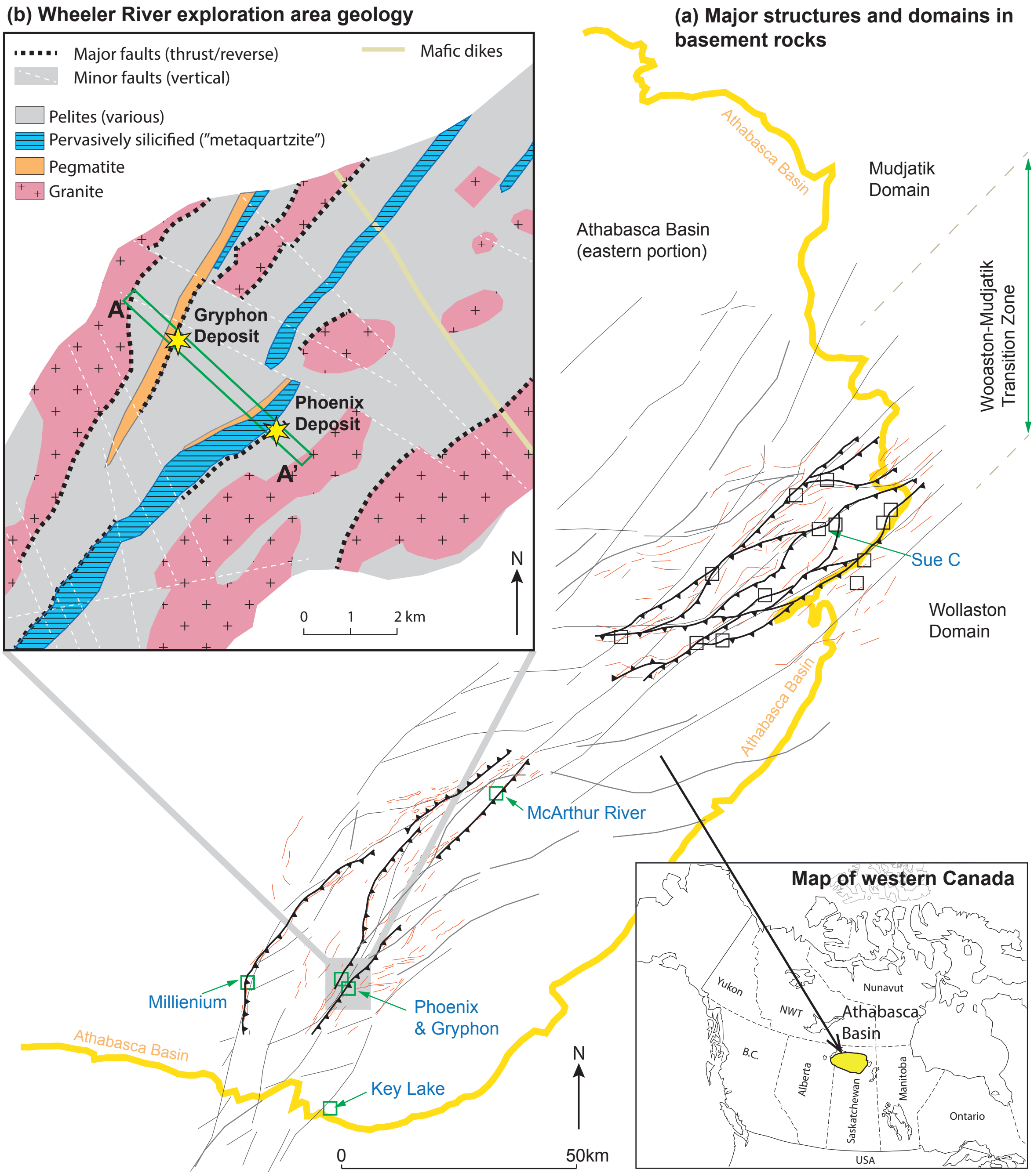

Figure 2-2 (a) The regional structure of the eastern portion of Athabasca Basin, Canada (inset map on lower right), uranium deposits along major faults near the unconformity surface (structure details after Thomas et al. 2014 of Cameco Corp.; regional geology simplified from Jeanneret et al. 2016), (b) geologic map of the Wheeler River exploration area (Denison Mines Ltd. 2018), with a cross-section A-A' indicated from Gryphon and Phoenix deposit.

CHAPTER 3

3 Multidisciplinary database of permeability of fault zones and surrounding protolith rocks at world-wide sites

In this article I describe the methods for a world-wide data review and the format and contents of the resulting database. These datasets are later used in statistical analysis and description in Chapters 3 to 6. The article was written in "Data Descriptor" format, as required by the journal *Scientific Data*. It does not contain any discussion or interpretations, or analyses, except brief literature review and listings of data sources. This article does not contain a conclusions section. The "Data Records" description is in **Appendix 1** of this thesis, although it appears inside the article in the publication format.

3.1 Abstract

The permeability properties of rocks and sediments, and the structural features in the Earth's crust are central to solving problems of pore fluid flow at present and over geological time scales. This data descriptor is for a world-wide database that contains summarized permeability estimates for 429 datasets, from tests in fault zones at 364 locations. The review covered over 9500 research items from multidisciplinary data sources. The main categories of data sources are studies of active faults and faulting processes, geothermal exploration, radioactive waste repository, groundwater resources, petroleum reservoirs, engineering projects). The objectives of this data compilation are to stimulate cross-disciplinary data sharing and communication on the topic of fault zone hydrogeology, to enable further statistical analysis and more informed inputs to models using crustal-permeability as parameters, and to compare the magnitudes of bulk and matrix permeability in different structural domains of fault zones.

3.2 Background and summary

The permeability property of rocks and sediments, and the structural features in the Earth's crust is central to solving problems of pore fluid flow at present and over geological time scales. The hydrogeological effects on fluid flow (e.g. barriers and conduits) have been observed at faults feeding thermal springs, in petroleum reservoirs, mines, tunnels, and dam foundations - according to the review papers published in the past 100 years (Bryan 1919, Meinzer 1923, Louderback 1950, Snow 1965, Seeburger 1981). The evidence of enhanced permeability over geological time has been inferred from fractures and mineral veins (Newhouse 1942, Sibson 1981, Kerrich 1986), and similarities to the localization of active hydrothermal flow systems (Curewitz and Karson 1997, Rowland and Simmons 2012). This article follows the terminology for fault zone's hydro-structural units that emerged from research in structural geology: fault core, damage zone, and the surrounding protolith or host rock (Chester and Logan 1986, Scholz and Anders 1994, Caine et al. 1996). Continued mapping and outcrop testing of petrophysical properties, including permeability, and fracture distributions revealed different styles of heterogeneity and linkages to processes (Faulkner et al. 2010, Matonti et al. 2012, Johri et al. 2014). Some of the earliest in-situ quantitative estimates of bulk fault permeability of fractures have been made at engineering projects (Snow 1965), but the most targeted hydraulic tests in fault zones have been done in fault-hosted geothermal reservoirs (Kassoy and Zebib 1978, Bodvarson and Benson 1982). At any location, the role of faults in the flow system depends on local geology. For example, in volcanic rocks with interlayered aquifer-aquitard units, the role of faults as conduits or barriers is uncertain and inferred from the combined geophysical, geochemical, and hydrogeological interpretations (Stimac et al. 2008, Pope et al. 2016). In higher porosity rocks in sedimentary basins, the problem of fault seals and compartmentalization of petroleum reservoirs (Jolley et al. 2010), resulted in studies of outcrops as analogues for fault permeability distributions at depth (Shipton et al. 2002, Flodin 2003, Michie and Haines 2016).

The data descriptor is for a compiled database of summarized permeability estimates for 429 datasets, from tests in fault zones, at 364 locations world-wide. The review spanned five years and 9500 research items such as journal papers, reports, conference proceedings. World-wide there are various permeability data sources, often isolated from each other in the geoscientific literature, that contributed to this data compilation:

- permeability of faults as parameter in geomechanical models of crustal-scale active faults (Rice 1992, Haneberg et al. 1999, Gratier et al. 2003, Yamashita and Tsutsumi 2018),
- permeability testing in outcrops exhumed from seismogenic depths (Evans et al. 1997, Wibberley and Shimamoto 2003, Lockner et al. 2009, Walker et al. 2010),
- fracture-aperture based estimates of fault paleo-permeability (Hashimoto et al. 2009, Gomila et al. 2016),
- permeability testing in outcrops of sediments poorly lithified rocks (Sigda et al. 1999, Okubo 2012, Balsamo and Storti 2013),
- in-situ hydraulic testing in recently active fault zones on continents (Ito et al. 2000, Doan et al. 2006, Karasaki et al. 2012, Xue et al. 2013, Matsumoto and Shigematsu 2018), and accretionary prisms near seduction zones (Saffer 2015),
- deep scientific drilling in metamorphic crust of recently low tectonic activity (Juhlin and Sandstedt 1989, NEDRA 1992, Huenges et al. 1997),
- permeability of fault zones inferred from the rate of migration of seismicity along faults (Nur and Booker 1972, Shapiro et al. 1999, Miller et al. 2004, Okada et al. 2015), and from other induced-seismicity cases (Talwani et al. 2007),
- permeability parameters in models of hydrothermal ore deposit formation (Ingebritsen and Appold 2012, Cox 2016), or fault zones in metamorphic complexes (Gottardi et al. 2013),
- geothermal exploration and production in naturally faulted reservoirs (Goko 2000, Sausse et al. 2006), and enhanced geothermal reservoirs in faulted rocks (Evans et al. 2005, Ladner and Häring 2009),
- thermal spring conduits along faults (Sorey and Lewis 1976, Lopez and Smith 1996, Gudmundsson et al. 2002, Muraoka et al. 2006),
- regional heat flow and permeability of the faulted crust (Manning and Ingebritsen 1999, Saar and Manga 2004, Saffer 2015),

- hydrogeological studies on radioactive waste storage repositories in faulted Precambrian shields (Bossart et al. 2001, Vaittinen et al. 2011), faulted mudrocks (Marschall et al. 2003, Ishii 2015), or faulted tuffs (Sweetkind and Drake 2007),
- hydrogeology of fault zones in long tunnels (Maréchal 1998, Ganerød et al. 2008, Masset and Loew 2010, Seebeck et al. 2014),
- assessment of groundwater resources in fractured and faulted crystalline basement rocks (Carlsson and Olsson 1977, Mäkelä 2012, Roques et al. 2014),
- petroleum reservoirs in sedimentary rocks, with fault barrier-conduit effects (Antonellini and Aydin 1994, Fisher and Knipe 2001),
- groundwater flow in faulted sedimentary basins (Person et al. 1996, Bense et al. 2013, Cilona et al. 2015).

The sampling and scale of permeability tests is important between the rock matrix permeability can be 2 to 4 orders of magnitude smaller than the bulk properties of the macroscopic fracture networks in low-porosity rocks (Brace 1980, Brace 1984, Clausser 1992, Schulze-Makuch et al. 1999). The relative effect of macroscopic fractures becoming more important in rocks of lower porosity and larger density (Lamur et al. 2017). In this compilation, the matrix permeability refers to tests on small (few cm size) rock samples or rock outcrop spots (Lockner et al. 2009, Mitchell and Faulkner 2012, Morrow et al. 2014), but does not include macroscopic fracture networks. The bulk permeability here refers to an estimate of permeability from in-situ hydraulic tests at length scales of meters to 100's meters that includes connected macroscopic fracture networks (e.g. Zoback and Hickman 1982, Caine and Tomusiak 2003).

Previous reviews included relatively few results at depths <5km, with a discussion on the deepest scientific drilling projects or model-derived permeability estimates (Manning and Ingebritsen 1999, Townend and Zoback 2000, Stober and Bucher 2007, Ingebritsen and Manning 2010). Larger data compilations from bulk permeability tests in fractured metamorphic and plutonic rocks (upper 2km depth) presented useful trends but did not focus on fault zones or the permeability contrasts between faults and protoliths (Ranjram et al. 2015, Achtziger-Zupancic et al. 2017). In the published world-wide average permeability maps of groundwater aquifers in the upper 100m of the continental crust (Gleeson et al. 2011), the effects of faults on aquifer properties were not yet taken into account.

The compilation and description of these permeability data has several objectives:

- First, this work aims to stimulate cross-disciplinary data sharing and communication. With a growing number of measurements, data compilation becomes difficult, while the geoscience specialization can lead to certain biases in data collection at different scales of measurement (Scibek et al. 2016). The multidisciplinary data search was important because most authors in particular geoscientific specialization do not reference works from outside of their field of study, thus creating rather limited reference links that tend to be re-used by subsequent authors.
- Second, this database - or the raw data in the reviewed reference works - can be used for statistical analysis of crustal-permeability trends with depth.
- The third objective is to compare the magnitudes of bulk and matrix permeability in fault damage zone, fault core, and the protolith, where the data are available. The matrix permeability, and its confining pressure-dependency on rock samples, has been reported and discussed extensively. This data compilation contains summaries of matrix permeability datasets, but most of the data are from in-situ test sites (drilled or tunnelled) and the corresponding bulk permeability estimates of fractured rocks.

3.3 Methods

3.3.1 Dataset review process

The concept of "systematic review" and meta-analysis is used many scientific fields (Moher et al. 2009), and here it was adapted to hydrogeological data that are both qualitative and quantitative. The search was comprehensive, using multiple databases, and then searching and reviewing all references listed in every publication found in the database, on the topic of fault zone permeability. The full search of reference lists in all publications was ultimately more systematic and complete, compared to the searches through academic journal or institutional report databases because the titles and keywords were moderately to poorly useful in locating the permeability datasets or supporting documents. The review process is described in Figure 3-1.

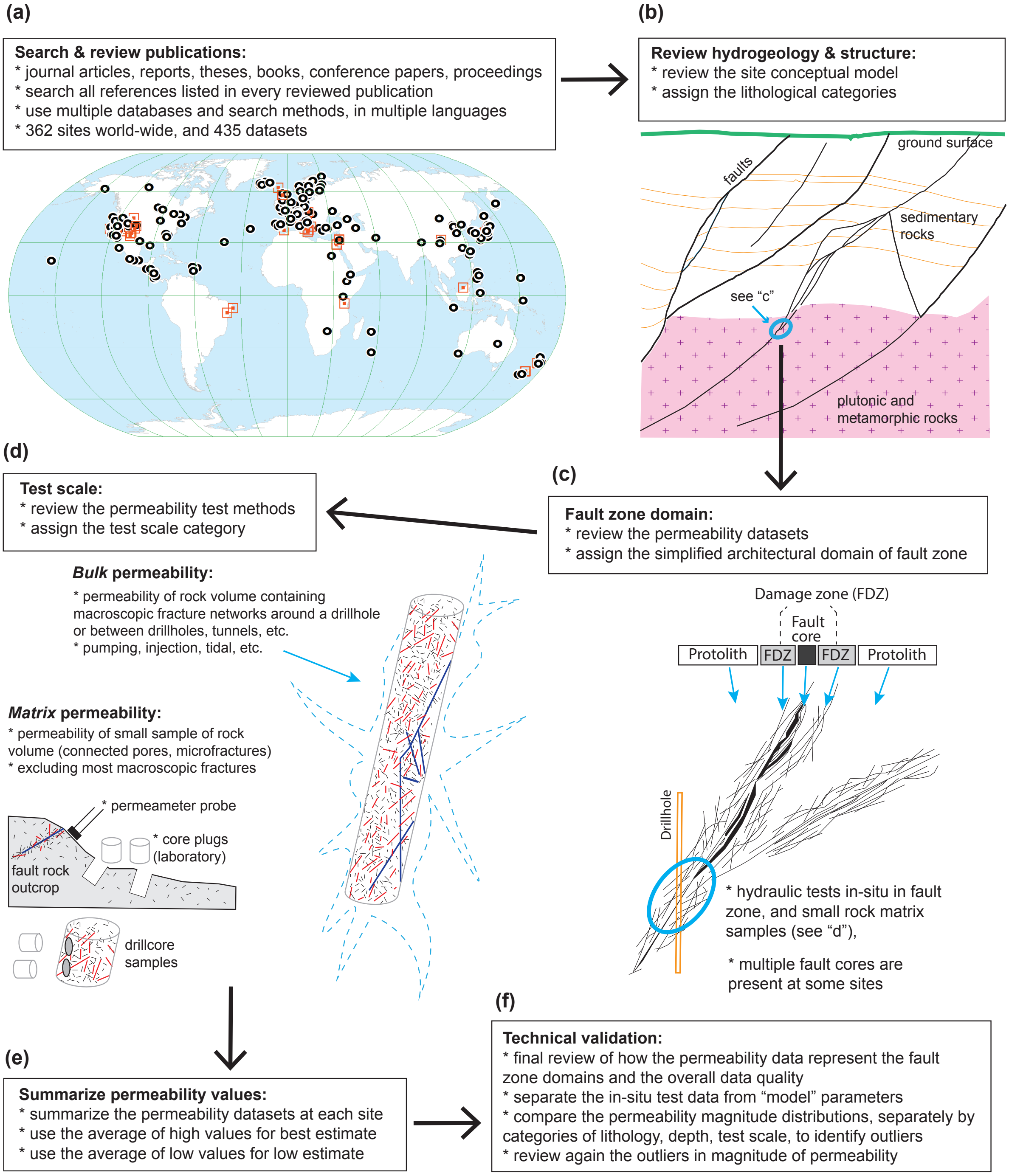

Figure 3-1 Schematic diagram of the permeability data compilation and review process: (a) search and review of publications (map of the world showing the locations of test sites in this study), (b) hydrogeology & structure at site scale (sketch based on Soultz-sous-Forêts geothermal site, modified after Vidal and Genter 2018), (c) fault zone structure and permeability domains (fault zone sketch modified after Vidal et al. 2015, and fault zone domains terminology after Caine et al. 1996), (d) permeability test scale (matrix, bulk (drillhole fracture model modified after Sausse et al. 2008), (e) summary of permeability values in database, (f) technical validation.

The first and still on-going step was a search for relevant publications. For each study location, the hydrogeological conceptual model was reviewed, geological structures summarized, the lithological category assigned, and the type of data available noted in the database. Next, the review focussed on the permeability data in relation to the fault structure. The datasets were separated according to the simplified fault zone domains. The permeability test scale was reviewed and assigned to either matrix or bulk category. The reviewed data were summarized for each dataset at each site. (see the following section about "Permeability summaries"). In the technical validation, each dataset was re-examined on the overall data quality and how it represented the fault zone domains. The magnitude of permeability distributions were compared in for all sites world-wide to identify outliers. This was done separately (in data subsets) by categories of lithology, depth, and test scale. The data outliers were reviewed again to confirm the values. The statistical work is in preparation for publication separately.

3.3.2 Data sources

The data sources are organized in six sections, defined loosely by the objectives and motivations of the studies, although many of the studies were multi-disciplinary (Table 3-1). The locations of in-situ and outcrop test sites are shown in Figure 3-2, and the depth and elevation distribution is plotted along longitude in Figure 3-3a.

Table 3-1 Data sources for inputs to the database, with dataset counts.

Database section	Reviewed datasets in database	# Datasets after review	Downhole in-situ bulk permeability	Outcrop only
Active faults and faulting processes	107	85	51	34
Geothermal reservoirs	164	136	136	0
Radioactive waste repositories	79	77	74	3
Water resources and contaminated sites	20	18	14	4
Petroleum reservoirs and faulting processes	61	41	12	29
Engineering projects	77	72	70	2
Totals	508	429	357	72

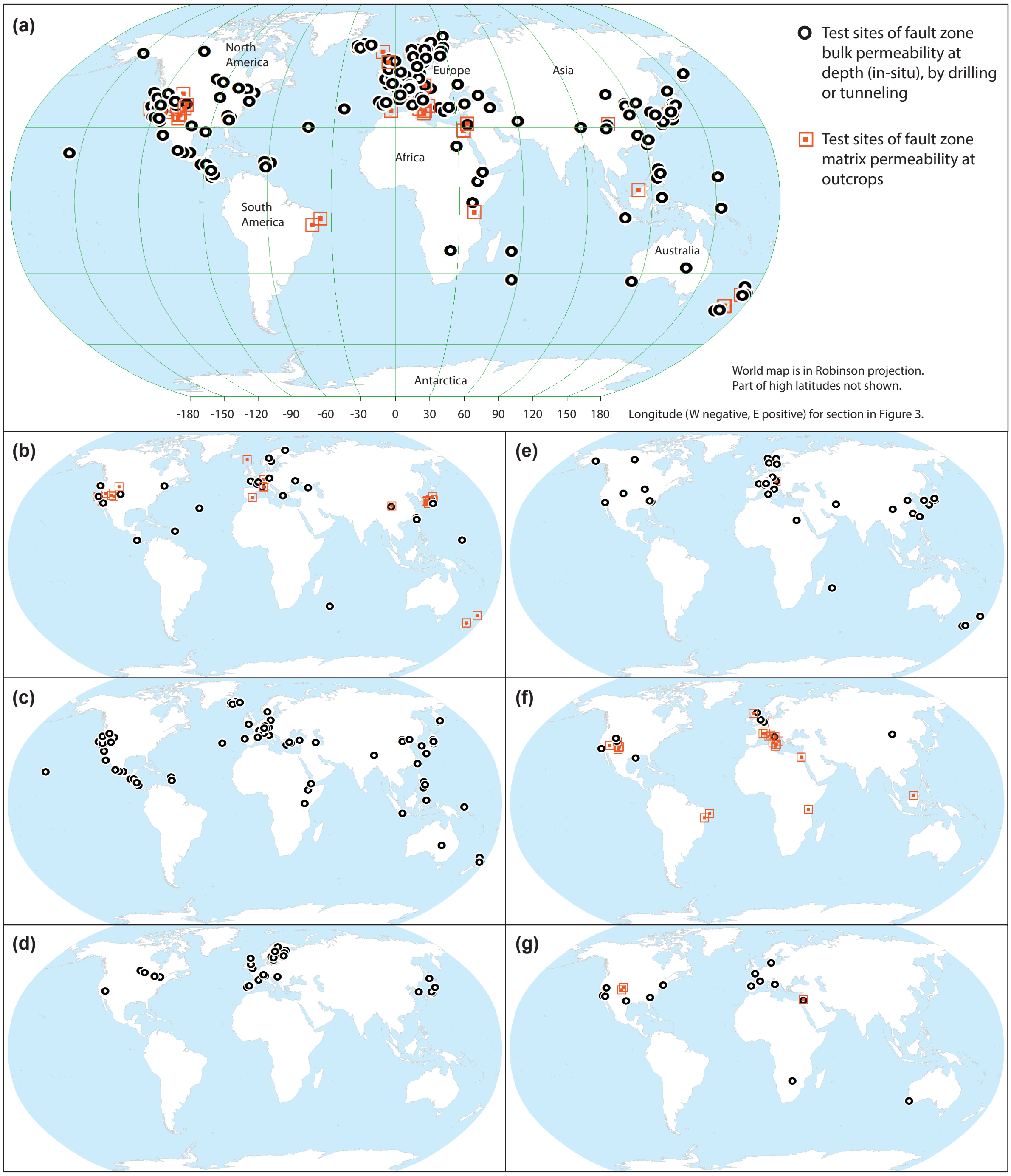

Figure 3-2 (a) World-wide locations of test sites of fault zone permeability shown with different symbols for bulk permeability at depth (in-situ by drilling or tunneling), and matrix permeability (at outcrops). In smaller maps in lower panels the test sites are separated by data source category: (b) active faults and faulting processes, (c) geothermal reservoirs, (d) radioactive waste repository studies, (e) groundwater resources and contaminated sites, (f) petroleum reservoirs and faults in sedimentary rocks, (g) engineering projects.

Active faults and faulting processes:

Approximately 2500 research items were reviewed at 110 locations, from structural and hydrogeological studies. Representative fault zone permeability values were entered for 85 datasets (Table 3-2). Excluded are permeability estimates for sites that could not be reviewed sufficiently or that could not be found. The database contains several estimates of paleo-permeability from fault outcrop mineralogy and geometry, but those were also clearly separated from the in-situ test results.

Geothermal reservoirs:

I reviewed the published data from 240 locations, and categorized 164 reservoirs as dominated by fracture permeability related to faults. We found bulk permeability estimates for 136 reservoirs (Table 3-3). Particularly useful sources of geothermal data were: UNU-GTP (United Nations Geothermal Training Programme) in Iceland, GRC (Geothermal Resources Council) database, and Stanford University Geothermal Workshops. The review and permeability summaries were also done for EGS (Enhanced Geothermal System) and HDR (Hot Dry Rock) sites. The enhanced permeability of faults after pressure injection ("fault stimulation") were stored separately from the values "before stimulation" (natural conditions). In many geothermal fields, the numerical models provide a good summary of site-wide bulk permeability, because the models are calibrated to in-situ hydraulic tests. In some cases were not able to review the original in-situ data, only the site-wide models. The notes in the database indicate the data source and in-situ test methods and/or models.

Radioactive waste repository studies:

The hydrogeological investigations motivated by test sites for nuclear waste disposal (Table 3-4), generally located in low-porosity fractured and faulted metamorphic, plutonic, and volcanic rocks, are a good data source (77 datasets). The reports containing the data are searchable through the INIS Repository database of the International Atomic Energy Agency (IAEA) and from national agencies such as Nagra (Switzerland), SKB (Sweden), Posiva Oy (Finland), and the USGS and U.S. Department of Energy, as well as national laboratories (United States), JAEA (Japan), AECL (Canada). Selected results have also been published previously in scientific journals.

Groundwater resources and contaminated sites:

Aquifer models average large volumes of material and in a few cases obtain estimates of fault zone conductance or hydraulic conductivity for groundwater flow across the fault, calibrating to observed hydraulic head distributions around the fault zone. Statistical studies on well yield correlations with fault zones were not useful because the well yield could not readily be converted to permeability, and because the datasets were regional and not site-specific. Of the hundreds of aquifer studies reviewed, only 18 datasets were used as representative of fault permeability structures (Table 3-5).

Petroleum reservoirs and faults in sedimentary rocks:

Many permeability measurements are done routinely by the petroleum industry, and the search results were from publically available articles and reports only. There are 61 published datasets on permeability of fault rocks in sedimentary basins and were able to use 41 of these. The data are largely from outcrop transects (29 sites). In 12 of the datasets, the matrix permeability values were reported from drilled cores from depth, and in a few cases permeability values were tested in-situ using hydraulic methods (Table 3-6).

Engineering projects:

This section relies upon reports and papers on hydraulic tests and observations in long tunnels, mines, and dams constructed in various lithologies and at depths up to 1.5 km. 72 datasets were used. Groundwater inflow to tunnels from fault zones can provide estimates of transmissivity and bulk permeability. The values can be compared to results of other in-situ hydraulic tests at the same sites (Table 3-7).

Table 3-2 List of sites for inputs to database section "Active faults and faulting processes".

Dataset #	Site Name	Country
1	Jorgillo fault	Chile
2, 3	Wenchuan, Yingxiu-Beichuan faults	China
4	Faroe Islands fault zones	Denmark
5, 6, 9	LSBB galeries lab, Ploemeur, Coaraze	France
7, 8, 12	fault outcrops in Rhine Graben, Bersezio faults	France
10, 11	Auriat, Sancerre-Couy drillholes	France
13, 14	Aigion and Pirgaki faults	Greece
15, 16	KTB	Germany
18, 19	Hanaore fault, Iida-Matsukawa fault	Japan
20 to 22	Median Tectonic Line sites, Matsusaka-Iitaka (ITA) obs.	Japan
23, 24	Nojima fault	Japan
25, 26	Shimanto accret. complex (Okitsu, Mugi outcrops)	Japan
27 to 31	Neodani (at Kinbara, Midori), Usukidani, Nishiyama, Tsugawa faults	Japan
32, 33	Atotsugawa fault, Tottori-ken Seibu EQ fault	Japan
34, 35	Taranaki Rift, Alpine fault drilling/outcrops	New Zealand
36, 37	Chelungpu, Pingshi faults	Taiwan (Rep. China)
38 to 40	SG-3 Kola, SG-8 Krovoy Rog, Tyrnauz	Russia & Ukraine
41	Carboneras fault	Spain
42, 43	Gravberg-1, COSC	Sweden
44 to 47	San Andreas (Cajon Pass, Cienaga Valley, SAFOD)	USA (California)
47 to 53	San Andreas fault system (Logan quarry, Big Pines, Golden Gate, Dry Lk, Hi Vista, Pinyon Flat obs.)	USA (California)
54, 55	Wildcat fault, Silver Creek fault	USA (California)
56	Elkhorn fault	USA (Colorado)
57	Stillwater fault (Dixie Valley)	USA (Nevada)
58 to 59	White Canyon, Spring and Sage Flat Hollow sites	USA (Utah)
60	Champlain Thrust	USA (Vermont)
61	East Fork thrust fault	USA (Wyoming)
Ocean drilling sites:		
62 to 66	Middle Valley, Barbados N. Ridge, Costa Rica Rift	(Atlantic Ocean)
67, 68, 69	Nankai Trough, Woodlark Basin	(Pacific Ocean)
70	SW Indian Ridge (Atlantis II FZ)	(Indian Ocean)
71, 72	Mid-Atlantic Ridge	(Atlantic Ocean)

Table 3-3 List of sites for inputs to database section "Geothermal reservoirs".

Dataset #	Site Name	Country
73	Habanero	Australia
74 to 79	Tianjin, Lishuiqiao, Xiongxian, Silapu, Zhangzhou, Yangbajing	China
80	Miravalles	Costa Rica
81, 82	Ahuachapan, Berlin	El Salvador
83, 84	Aluto-Langano, Dubti	Ethiopia
85, 86	Soultz-sous-Forêts, Rittershoffen	France
87	Bouillante (Guadeloupe Island)	France
88	Le Mayet de Montagne	France
89 to 93	Landau, Urach-3, Waldshut-T., Bad Teinach, Unterhaching,	Germany
94 to 96	Falkenberg, Groß Schönebeck, Bruchsal	Germany
97	Milos	Greece
98	Zunil	Guatemala
99	Platanares	Hoduras
100 to 102	Krafla, Namafjall (Bjarnaflag), Theistarekir	Iceland (North)
103 to 105	Nesjavellir, Hellisheidi, Ölfus-Bakki	Iceland (SW)
106 to 108	Svartsengi, Reykjanes, Ellidaar	Iceland (SW)
109 to 116	Botn, Glerardalur, Laugaland (Daelustod), Thelamork, Hjalteyri, Hamar, Laugerengi, Hofsstadir	Iceland (North & West)
117 to 120	Gata, Kaldarholt, Efri-Reykir Biskupstungur, Ósabotnar	Iceland (South)
121, 122	Eskifjordur, Urridavatn	Iceland (East)
123, 124	Kamojang, Lahendong	Indonesia
125	NW Mt. Sabalan	Iran
126 to 128	Larderello, Piancastagnaio, Mt. Amiata, T. di Valdieri	Italy
129 to 132	Hatchobaru/Otake, Oguni, Kirishima, Yamagawa	Japan (Kyushu)
133 to 142	Kakkonda, Matsukawa, Sumikawa, Onikobe, Uenotai Okuaizu, Akinomiya, Hijiori, Ogachi, Mori	Japan (north)
143	Olkaria East (Olkaria 1)	Kenya
144 an 148	Cerro Prieto, Los Humeros, Los Azufres, Tres Virgenes, Cerritos Colorados	Mexico
149 to 151	Kawerau, Ngawha, Rotokawa	New Zealand
152	Momotombo	Nicaragua
153	Lihir (Ladolam)	Papua N.Guinea
154 to 156	Bacon-Manito, Palinpinon, Tongonan	Philippines
157, 158	S. Pedro do Sul, Ribeira Grande	Portugal
159	Chingshui	Taiwan
160 to 161	Pauzhetka (Pautzetsky), Mutnovsky (Dachny)	Russia
162	Qualibou caldera	St. Lucia
163	Pohang EGS	South Korea
164	El Vallés rift (Valles-Penedes)	Spain
165	Fjällbacka	Sweden
166 to 168	Basel 1 EGS, St. Gallen, Riehen	Switzerland
169 to 173	Kizildere, Germencik, Salavatlı-Sultanhisar, Balcova, Sorgun	Turkey
174	Rosemanowes Quarry	UK
175 to 179	Beowawe, Desert Peak, Dixie Valley, Steamboat, Bradys HS	USA (Nevada)
180 to 186	Coso, Heber, The Geysers, Susanville, Wendel HS, Long Valley Caldera, Glass Mtn.	USA (California)
187, 188	Raft River, Boise Front Fault	USA (Idaho)
189	Fenton Hill	USA (NM)
190, 191	Crystal Hot Springs, Roosevelt HS	USA (Utah)
192, 193	Klamath Falls, Neal Hot Springs	USA (Oregon)
194	Makushin	USA (Alaska)
195	Kilauea Volcano, East Rift Zone	USA (Hawaii)

Table 3-4 List of sites for inputs to database section "Radioactive waste repositories".

Dataset #s	Site Names	Country
196 to 199	Whiteshell, Chalk River, Atikokan, E Bull Lake	Canada
200, 201	Down Ampney, Sellafield	England
202 to 205	Olkiluoto, Romuvaara, Leppävirta, Hästholmen	Finland
206	Tournemire	France
207	Bátaapáti (Üveghuta)	Hungary
208	Horonobe site (Hokkaido)	Japan
209 to 213	Mizunami URL, Tono Mine, Kamioka Mine, Kamaishi Mine	Japan
214, 215	Altnabreac St., Dounreay	Scotland
216	KAERI (KURT tunnel site)	South Korea
217 to 218	Los Ratones Mine, El Berrocal Mine	Spain
219 to 226	Äspö, Laxemar, Finnsjon, Stripa Mine, Forsmark, Fiskarfjärden, Lansjärv, Fjällveden, Gideå	Sweden
227	Grimsel	Switzerland
228 to 233	Leuggern, Boettstein, Kaisten, Schafisheim, Siblingen, Weiach	Switzerland
234, 235	Wellenberg, Mont Terri lab.	Switzerland
236	Yucca Mountain site (Nevada)	USA
237 to 238	Chalk Cove fault, Crucifix fault outcrops (California)	USA

Table 3-5 List of sites for inputs to database section "Groundwater resources and contamination".

Dataset #	Site Name	Country
239	Kojonup fault	Australia
240	Oukwe, graben bounding fault	Botswana
241	Carlsberg fault zone	Denmark
242	North Armorican Shear Zone (St-Brice en Cogles)	France
243	La Selvetat natural mineral water well-field	France
244 to 246	Yair, Ein Fashcha, and Kumeran faults	Israel
247	Matese massif	Italy
248	Cadalso de los Vidrios	Spain
249	Happy Valley fault	USA
250	Mission Cr. & Banning faults	USA
251	San Luis Valley	USA
252	Turkey Cr. watershed	USA
253	Handcart Gulch	USA
254	Savannah River Nuclear Power Plant site	USA
255	Project Shoal nuclear test site, Sand Springs Range	USA
256	Ramapo fault	USA
257	Pax Mountain fault	USA
258	Hickory Sandstone Aquifer	USA

Table 3-6 List of sites for inputs to database section "Petroleum reservoirs and faulting processes".

Dataset #	Site Name	Country
259	Margerethen quarry	Austria
260 to 263	Icapui, Tamaba, Coquerinho, Ablai outcrops, & Brejinho drill site	Brazil
263 to 264	Humur-B, Muweilih, Thal faults	Egypt
265	Penrith	England
266, 267	Quartier de l'Etang and Le Cross quarry outcrops, Restefond fault	France
268, 269	Boncavaï quarry outcrops, Casaperta fault	France
270, 271	Geleen and Peel Boundary faults (partly in Netherlands)	Germany
272, 273	Fucino Basin outcrops, Crotone Basin outcrops	Italy
274, 277	Scicli and Ispica faults, Favignana Island outcrops (Sicily)	Italy
275, 276	Pontrelli and Cantore & Madonna della Mazza quarries	Italy
278	Roccastrada fault	Italy
279	Ras ir Raheb and Madliena Tower sites	Malta
280	Miri Reservoir	Malaysia
281, 282	Rotliegendes and Northern North Sea basin reservoirs	(N. Sea)
283	Pisco Basin outcrops	Peru
284, 285	Lossiemouth fault outcrops, Clashach quarry outcrops	Scotland
286, 287	Newport-Inglewood fault, Santa Barbara Channel fault (California)	USA
288	Red fault system (Gulf of Mexico)	USA
289	Valley of Fire Park (Nevada)	USA
290 to 292	Sand Hill and Santa Ana faults, & Bosque, Canyon Trail (New Mexico)	USA
293, 294	Elmendorf site, & San Ysidro fault (New Mexico)	USA
295	Arbuckle Mountains (Oklahoma)	USA
296, 297	Arches National Park, Buckskin Gulch (Utah)	USA
298, 299	Big Hole and Moab faults (Utah)	USA
300, 301	San Rafael monocline, Little Grand Wash & Salt Wash faults (Utah)	USA
302	Trixie fault (Utah)	USA
303	South Owl Creek Mountain thrust fault (Wyoming)	USA
304	Leroy gas storage site (Wyoming)	USA

Table 3-7 List of sites for inputs to database section "Engineering projects".

Dataset #	Site Name	Country/Region
305	Klasgarten rockslide	Austria
306	SEMP fault zone	Austria
307 to 309	Vomp E. Tunnel, Brixlegg-E. Tunnel, Aica-Mules	Austria
310, 311	Semmering Base Tunnel, and Talhot segment	Austria
312 to 314	Con, Diavik, Giant mines (NWT)	Canada
315	mines in Canadian Shield region (Ontario, Quebec)	Canada
316, 317	Taining & Nibashan tunnels	China
318	Yanzhou coalfield	China
319 to 321	Mont Blanc, Modane, and Malgovert tunnels	France
322	Salazie-Amont tunel (Reunion Island)	France
323	Fanay-Augeres Mine	France
324	Poehla-Tellerhaeuser Ore Field	Germany
325	Lindau dam test site	Germany
326	Seyahoo Dam	Iran
327, 328	Gran Sasso Tunnel, Medau Zirimilis Dam	Italy
329, 330	tunnels in Japanese Alps, Enasan Tunnel	Japan
331, 332	Tomitaka Mine, Kanden tunnel to Kurobe Dam	Japan
333, 334	Manapouri Tunnel, TVZ water tunnels	New Zealand
335	Cromwell Gorge	New Zealand
336	Hvaler tunnel	Norway
337 to 339	Frøya, Oslofjord, and Romeriksporten tunnels	Norway
340	Venetia Mine	South Africa
341	Namtall Tunnel	Sweden
342 to 347	Gotthard Base Tunnels, Bedretto Tunnel	Switzerland
348 to 349	Unteralpreuss, and Sta. Maria-Nalp galleries	Switzerland
350	Furka Base Tunnel, Bedretto leg	Switzerland
351, 352	KW Oberhasli, and KW Goeschenen galleries	Switzerland
353	Lotschberg Base Tunnel	Switzerland
354	Cleuson-Dixence Gallery	Switzerland
355	Eklutna Tunnel (Alaska)	USA
356	San Jacinto Tunnel (California)	USA
357, 358	Straight Cr. Tunnel, Schwartzwalder Mine (Colorado)	USA
359	Edgar Mine (CSM) (Colorado)	USA
360	UPH-3 (Illinois)	USA
361	CAES/UPH facility at Triadelphia Res. (Maryland)	USA
362, 363	Monticello reservoir, Bad Cr. reservoir (S. Carolina)	USA
364	Hsuehshan Tunnel (Ping Lin Pilot Tunnel)	Taiwan

3.3.3 Permeability summaries

In the database, only summary values for datasets are reported, not all raw data from the original papers. This database's aim is to serve as a guide to the available datasets, and not a complete replication of those datasets. For each dataset, two representative permeability values were entered and assigned a simplified structural domain (fault core, fault damage zone, and the protolith) and permeability test scale (matrix and bulk). At most sites there is one dataset, but multiple datasets were defined at some study sites for different fault zones, lithological zones, or depth zones. At 18% of the study sites, there are multiple datasets. The notes about permeability test methods, data sources, and summary values are provided in the database records for each dataset.

The representative estimate of bulk permeability was taken as the most common value in the data cluster. Where only a few test values were taken, the maximum value was chosen. The low estimate of permeability was:

- For matrix permeability in the damage zone or the protolith, the median of low permeability data cluster in a dataset was taken. At a fault zone outcrop where matrix permeability transect showed permeability variation. In the wide damage zone it was most common low value to point out the background permeability.
- For drillcore samples of fault core, the low estimate of matrix permeability represents the least permeable samples.
- In case of in-situ well tests, the low estimate was for the approximate median of bulk permeability values.

The permeability values summarized were as logarithms of permeability (units of m^2), as is usually done in the geoscientific publications about crustal permeability. The data originally reported in the literature as transmissivity, hydraulic conductivity, or permeability thickness were converted m^2 units.

3.3.4 Geologic categories

Data subsets were assigned to very broad lithological categories such as: siliciclastic (coarse), mudrock, carbonate, volcaniclastic, volcanic igneous, plutonic, and metamorphic. There is large variability of mineralogical, petrophysical, hydrogeological properties within each of these categories, thus these are rather rough first-order groupings of permeability data. Where faults offset sedimentary strata against crystalline rocks, such as along range-front or graben-bounding faults, various configurations of basement topography and faults can occur (Reed 1983). The in-situ permeability test depth mid-points and intervals, by lithologic category, are shown in Figure 3-3b.

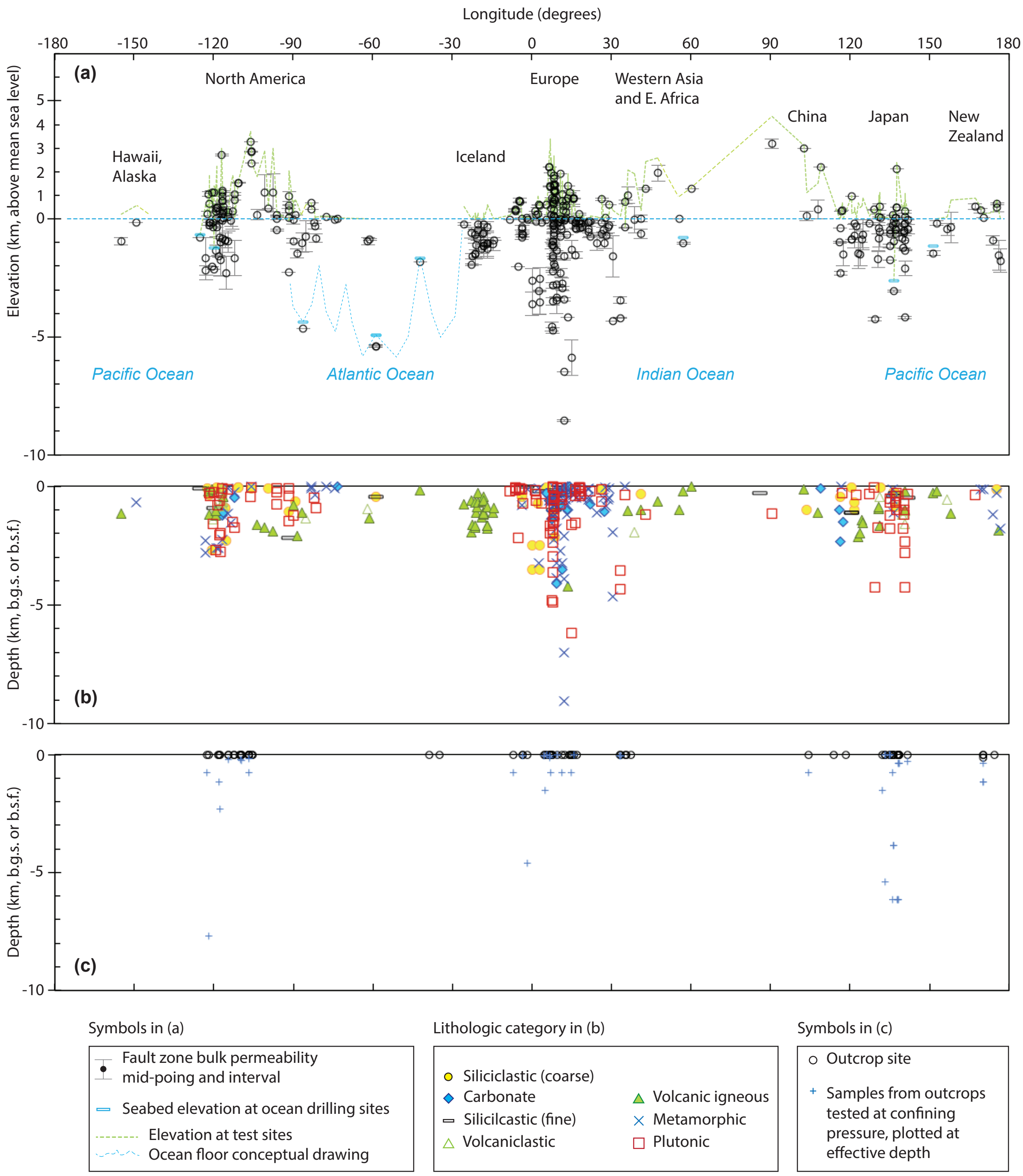

Figure 3-3 World-wide locations along geographic longitude and in-situ depth intervals permeability tests in fault zones. All sites are projected on one section and plotted along longitude. (a) Elevation relative to mean sea level of in-situ permeability test intervals in drillholes or tunnels. The topographic profile is plotted from elevations of the sites, and is not a global average elevation. The sea floor elevation at oceanic sites is also indicated, with an added conceptual sketch of ocean floor (not actual transect). (b) Depth of in-situ bulk permeability test intervals and lithologic category of protolith in tested fault zone. The depths are below ground surface for land sites and below sea floor for oceanic sites. (c) Outcrops of fault zones plotted at 0 depth, and the effective depths that correspond to the confining differential pressures of matrix permeability tests on some fault rock samples.

"Siliciclastic (coarse)" category included sandstone, interlayered sandstone with fine grained rocks; the most permeable flow pathways were attributed to fractured sandstone and conglomerate. Some detailed work on faulted sedimentary rocks at depths of hundreds of meters has been done in the context of nuclear repository and related hydrogeological programs (e.g. Gutmanis et al. 1998, Nohara et al. 2006). Also included are dataset summaries for deformation bands in sandstone and carbonate rocks, although these deformation features differ from faults and are also present away from fault zones (e.g. Ballas et al. 2015, Rotevatn et al. 2016). The database contains additional categories for the deformation bands and faulted unlithified siliciclastic sediments to aid searches for these data.

"Mudrock" category here means siliciclastic fine-grained rocks (Loucks et al. 2012, Rutter et al. 2017). This category thus includes clay, silt, claystone, mudstone, clay-rich siltstone, shale, and any argilliceous rocks. Fault zones were tested at several research sites (Williams et al. 1990, Ishii et al. 2011). Marl rock was placed in the mudrock category due to its geomechanical properties.

"Carbonate" category includes limestone, dolomite, and also brittle-faulted marble, due to their similar magnitude of strength and susceptibility to karst formation. Faulted outcrops have been tested with matrix permeability transects in a variety of carbonate rocks (e.g. Micarelli et al. 2006, Molli et al. 2010, Bauer et al. 2016). In-situ bulk permeabilities are mostly from geothermal reservoirs.

"Volcaniclastic" category has data mainly from tuff rocks and tuffaceous sediments. There is a large variability in hydraulic properties of tuffs because of their variable densities, porosities, and susceptibility to brittle deformation (Smyth and Sharp 2006). Most of the data are from tuffs at Yucca Mountain site (Sweetkind and Drake 2007) and at geothermal fields where tuffs and tuff breccias are interlayered andesites or basalts.

"Volcanic igneous" category is for intrusive and extrusive volcanic rocks, although these can be interlayered with volcaniclastics and other sediments. The permeable connected open fractures occur both along stratigraphic layers, dikes, and in steeply dipping fault zones (Axelsson and Bodvarsson 1987, Milicich et al. 2016). The zones of hydrothermal alteration causes large variability of both porosity and permeability (Siratovich et al. 2016).

"Plutonic" rock category here is for granitic and granodioritic rocks of continental shields, drillhole hydraulic test data were obtained from radioactive waste repository investigations in Sweden (10), Canada (6), Japan (2), Scotland (2), Spain (2). Deep geothermal exploration (Sausse et al. 2006), and geophysical research (Coyle and Zoback 1988, Xue et al. 2016) provided several outstanding datasets from fault zones in granitic rocks.

"Metamorphic" category is a large group with mixed lithology of various metamorphic rocks. As mentioned in the introduction, hydrogeological investigations for radioactive waste storage repositories have been done in metamorphic rocks in Sweden (4), Finland (7), Switzerland (3), Canada (1). A large amount of data is also available from engineering projects that are listed in the database. Faults in gneissic metasediments and granitic rocks were tested at the largest number of sites.

3.4 Technical validation

3.4.1 Matrix permeability uncertainty

The uncertainty of matrix permeability values depends on the method of testing (e.g. mini-permeameter on outcrop or drillcore spots, core plug tested in confined sleeve), type of fluid used and related effects of gas slippage, sample saturation, rock-water interactions. The uncertainty of single measurement varies and is difficult to review from the publications. Measurement error from factor of 2 to 10 is not unusual. However, a larger problem may be the representativeness of the data and the conceptual model of inferred in-situ conditions (e.g. estimated permeability at some depth at some confining pressure).

The pressure-dependency of matrix permeability depends on rock lithology and petrophysical properties (e.g. David et al. 1994, Morrow and Lockner 1994). Outside of fault zones in fresh rock samples of fine-grained siliciclastic rocks, the in-situ bulk permeabilities are of the same magnitude as the matrix permeabilities from outcrop samples (Uehara et al. 2012). However, permeable open fractures in fault zones cause larger differences and in-situ tests are preferable. For outcrops, the effective depth can be calculated from the confining effective pressure, although it is not the actual depth of the sample. In the case of unconfined tests that were done at ambient atmospheric pressure, on a drillcore sample or on rock outcrop, the depth was entered as 0m (ground surface). Since the pressure gradients vary in different geological environments and rock densities, these summary values are a rough approximation. The effective confining pressure (P_{eff}) is the difference between the confining pressure and the pore pressure. For the purposes of summary values in the database, the effective pressure is then the product of depth and effective pressure gradient, as shown in equation 1 (e.g. Zoback 2007):

$$\text{Effective Depth} = P_{eff} / ((\text{lithostatic P gradient - hydrostatic P gradient}) \quad [1]$$

where pressure is in MPa and pressure gradients are in MPa/km, here assuming an average lithostatic pressure gradient of 23 MPa/km and a hydrostatic gradient of 10 MPa/km, the effective pressure gradient is 13 MPa/km. The effective depths of matrix permeability for some outcrop samples are shown in Figure 3-3c.

3.4.2 Bulk permeability uncertainty

The main uncertainty is tied to sampling permeable structures of faults that are heterogeneous. Other technical difficulties during in-situ testing in drillholes and test interpretations are typically on the order of magnitude of bulk permeability value. The heterogeneity of hydraulic properties in fault zones, flow channelling in fractured rocks in general (Tsang and Neretnieks 1998), lead to practical difficulties of separating parts of fault zones for in-situ tests (Karasaki et al. 2012, Pasendorfer and Loew 2009). Fault strands or whole fault zones must be conceptualized as geometrically simplified permeable elements because the pumping/injection or smaller slug tests in drillholes have an averaging effect (e.g. Grasle et al. 2006), or where many drillholes and test intervals can be done the permeability fields can be mapped - also averaging large volumes of rock (e.g. Illman et al. 2009), but faults that are sealed and at not the dominant flow conduits are difficult to characterize through hydraulic tests (e.g. review in Scibek et al. 2016), thus the main focus of in-situ testing of faults is on fluid flow conduits, usually attributed to the permeable fractures within the fault damage zone, according to this review and references within, and more rarely in the fault core surrounded by low-permeability permeable damage zone (Leclère et al. 2015). In this review, where the in-situ test conditions were not specific to fault zone component, but were clearly in fractured rocks in the fault zone, the bulk permeability was associated to a fault damage zone in the database. The datasets and their attributes may be updated in further reviews.

During our review of the published datasets we compared conceptual models of fault's hydrology, the consistency of the results of hydraulic tests in fault zones, and parameters used in calibrated numerical flow models. In geothermal reservoirs, the exploited (pumped) hot fluid reservoirs occur in permeable fractured rocks with variable contribution of fault zones to the overall permeability distribution, and the conceptual models of some sites have changed over several decades of in-situ test work.

The qualitative data assessment consisted of:

- clarity and detail of reports,
- data quantity (e.g. number of drillholes and tests, types and scale of tests),
- additional supporting analyses for site-wide conceptual models, such as calibrated numerical flow models that include fault zones,
- structural mapping and analysis to support hydrogeological investigations,

The depth of data point or data cluster for "best estimate" and "low estimate" was entered to database (maximum, minimum, and mid-point depth). For sites with more than one in-situ test, the depths are approximate, depending on the scale and accuracy of the hydrogeological conceptual model that was presented. In single drillhole test intervals, the depth given is the approximate vertical depth below ground, and it may be accurate to 0.1 to 1m at most sites, but the hydraulic zone of influence at depth (the volume rock actually tested in-situ) might extend 100's of meters in any direction, thus the depth accuracy is not precisely known and we did not attempt to quantify it. In general, the depth accuracy is on the order of 10% of the value.

3.4.3 Permeability ratios

I calculated ratios of permeabilities for the different fault zone components and the protolith. A permeability ratio can be used to quantify the "conduit" magnitude or "barrier" magnitude of fault zone relative to the protolith. In 199 datasets, the bulk permeability ratio (fault damage zone / protolith) was calculated. There were fewer fault permeability datasets from sites (65) where the matrix permeability in both the fault damage zone and the protolith, and the permeability ratio could be calculated. Unfortunately in 40% of the datasets, the permeability ratio could not be calculated because the protolith was not tested sufficiently around the fault zone. The ratio of permeability requires that the data are from the same location and depth range to be comparable. A mismatch in test scale (e.g. matrix permeability of fault rock and bulk permeability of host rock) precludes the calculation of ratios at the same measurement scale.

3.5 References

References for tables are in the submitted database file, and due to large number of references (>1000), are not listed here. The list has been sorted alphabetically:

Achtziger-Zupancic, P., Loew, S. & Mariéthoz, G. (2017) A new global database to improve predictions of permeability distribution in crystalline rocks at site scale. *Journal of Geophysical Research, Solid Earth*, 122(5), 3513–3539

Antonellini, M. & Aydin, A. (1994) Effect of faulting on fluid flow in porous sandstones: petrophysical properties. *AAPG Bulletin*, 78(3), 355–377

Axelsson, G. & Bodvarsson, G. (1987) Analysis of production data from fractured liquid dominated geothermal reservoirs in Iceland. *GRC Transactions*, 11, 573–580

Ballas, G., Fossen, H. & Soliva, R. (2015) Factors controlling permeability of cataclastic deformation bands and faults in porous sandstone reservoirs. *Journal of Structural Geology,* 76, 1–21

Balsamo, F., Storti, F. (2010) Grain size and permeability evolution of soft-sediment extensional sub-seismic and seismic fault zones in high-porosity sediments from the Crotone basin, southern Apennines, Italy. *Marine and Petroleum Geology*, 27, 822–837

Bauer, H., Schröckenfuchs, T.C. & Decker, K. (2016) Hydrogeological properties of fault zones in a karstified carbonate aquifer (Northern Calcareous Alps, Austria). *Hydrogeology Journal,* 24(5), 1147–1170

Bense, V. F., Gleeson, T., Loveless, S. E., Bour, O. & Scibek, J. (2013) Fault zone hydrogeology. *Earth-Science Reviews*, 127, 171–192

Bodvarsson, M. G. & Benson, M. (1982) Well Test Data From Geothermal Reservoirs. Report LBL-13295, Lawrence Berkeley Laboratory, Berkeley, California

Bossart, P., Hermanson, J. & Mazurek, M. (2001) Äspö Hard Rock Laboratory Analysis Of Fracture Networks Based On The Integration Of Structural And Hydrogeological Observations On Different Scales. SKB Technical Report TR-01-21, Svensk Kärnbränslehantering AB, Stockholm, Sweden

Brace, W. F. (1980) Permeability of Crystalline and Argillaceous Rocks. *International Journal of Rock Mechanics and Mining Sciences & Geomechanics Abstracts*, 17(5), 241–251

Brace, W. F. (1984) Permeability of crystalline rocks: new in situ measurements. *Journal of Geophysical Research,* 89(B6), 4327–4330

Bryan, K. (1919) Classification of springs. *The Journal of Geology*, 27(7), 522–561

Caine, J. S. & Tomusiak, S. R. A. (2003) Brittle structures and their role in controlling porosity and permeability in a complex Precambrian crystalline-rock aquifer system in the Colorado Rocky Mountain Front Range. *GSA Bulletin*, 115(11), 1410–1424

Caine, J. S., Evans, J. P. & Foster, C. B. (1996) Fault zone architecture and permeability structure. *Geology*, 24, 1025–1028

Carlsson, A. & Olsson, T. (1977) Hydraulic properties of Swedish crystlaline rocks. *The Bulletin of the Geological Institutions of the University of Uppsala*, N.S. 7, 71–84

Chester, F. M. & Logan, J. M. (1986) Implications formechanical properties of brittle faults from observations of the Punchbowl fault zone, California. *Pure and Applied Geophysics*, 124, 80–106

Cilona, A., Aydin, A. & Johnson, N. M. (2015) Permeability of a fault zone crosscutting a sequence of sandstones and shales and its influence on hydraulic head distribution in the Chatsworth Formation, California, USA. *Hydrogeology Journal*, 23, 405–419

Clauser, C. (1992) Permeability of crystalline rocks. *EOS Transactions, American Geophysical Union,* 73, 233–237

Cox, S. F. (2016) Injection-driven swarm seismicity and permeability enhancement: implications for the dynamics of hydrothermal ore systems in high fluid-flux, overpressured faulting regimes. *Economic Geology*, 111(3), 559–587

Coyle, B.J. & Zoback, M.D. (1988) In situ permeability and fluid pressure measurements at ~2 km depth in the Cajon Pass research well. *Geophysical Research Letters*, 15(9), 1029–1032

Curewitz, D. & Karson, J. A. (1997) Structural settings of hydrothermal outflow: Fracture permeability maintained by fault propagation and interaction. *Journal of Volcanology and Geothermal Research*, 79, 149−168

David, C., Wong, T-f., Zhu, W. & Zhang, J. (1994) Laboratory measurement of compaction-induced permeability change in porous rock: implications for the generation and maintenance of pore pressure excess in the crust. *Pure and Applied Geophysics*, 143, 425–456

Doan, M. L., Brodsky, E. E., Kano, Y., & Ma, K. F. (2006) In situ measurement of the hydraulic diffusivity of the active Chelungpu Fault, Taiwan. *Geophysical Research Letters*, 33, L16317

Evans, J. P., Forster, C. B. & Goddard, J. V. (1997) Permeability of Fault related Rocks, and Implications for Hydaulic Structure of Fault Zones. *Journal of Structural Geology,* 19(11), 1393–1404

Evans, K., Genter, A. & Sausse, J. (2005) Permeability creation and damage due to massive fluid injections into granite at 3.5 km depth, at Soultz: 1. Borehole observations. *Journal of Geophysical Research,* 110, B04203

Faulkner et al. (2010) A review of recent developments concerning the structure, mechanics and fluid flow properties of fault zones. *Journal of Structural Geology,* 32, 1557–1575

Fisher, Q. J. & Knipe, R. J. (2001) The permeability of faults within siliciclastic petroleum reservoirs of the North Sea and Norwegian Continental Shelf. *Marine and Petroleum Geology*, 18(10), 1063–1081

Flodin, E.A. (2003) Structural Evolution, Petrophysics, And Large-Scale Permeability Of Faults In Sandstone, Valley Of Fire, Nevada. Ph.D. Thesis, Stanford University, California

Ganerød, G. V., Braathen, A. & Wilemoes-Wissing, B. (2008) Predictive permeability model of extensional faults in crystalline and metamorphic rocks; verification by pre-grouting in two sub-sea tunnels, Norway. *Journal of Structural Geology,* 30, 993–1004

Gleeson et al. (2011) Mapping permeability over the surface of the Earth. *Geophysical Research Letters*, 38, L02401

Goko, K. (2000) Structure and hydrology of the Ogiri field, West Kirishima geothermal area, Kyushu, Japan. *Geothermics*, 29, 127–149

Gomila, R., Arancibia, G., Mitchell, T. M., Cembrano, J. M., Faulkner, D. R. (2016) Palaeopermeability structure within fault-damage zones: A snap-shot from microfracture analyses in a strike-slip system. *Journal of Structural Geology,* 83, 103–120

Gottardi, R., Kao, P-H., Saar, P-H. & Teyssier, C. (2013) Effects of permeability fields on fluid, heat, and oxygen isotope transport in extensional detachment systems. *Geochemistry Geophysics Geosystems*, 14, 1493–1522

Grasle, W., Kessels, W., Kumpel, H-J. & Li, X. (2006) Hydraulic observations from a one year fluid production test in the 4000 m deep KTB pilot borehole. *Geofluids*, 6, 8–23

Gratier, J.-P., Favreau, P., & Renard, F. (2003) Modelling fluid transfer along California faults when integrating pressure solution crack sealing and compaction processes. *Journal of Geophysical Research,* 108(B2), 2104

Gudmundsson, A., Fjeldskaar, I. & Brenner S. L. (2002) Propagation pathways and fluid transport of hydrofractures in jointed and layered rocks in geothermal fields. *Journal of Volcanology and Geothermal Research*, 116, 257–278

Gutmanis, J.C., Lanyon, G.W., Wynn, T.J. & Watson, C.R. (1998) Fluid flow in faults: a study of fault hydrogeology in Triassic sandstone and Ordovician volcaniclastic rocks at Sellafield, north-west England. *Proceedings of Yorkshire Geological Society*, 52(2), 159–175

Haneberg, W. C., Mozley, P. S., Moore, J. C. & Goodwin, L. B. (Eds.) (1999) Faults and Subsurface Fluid Flow in the Shallow Crust. Geophysical Monograph 113, AGU

Hashimoto, Y., Nikaizo, A., & Kimura, G. (2009) A geochemical estimation of fluid flux and permeability for a fault zone in Mugi melange, the Cretaceous Shimanto Belt, SW Japan. *Journal of Structural Geology,* 31, 208–214

Huenges, E., Erzinger, J., Kuck, J., Engeser, B. & Kessels, W. (1997) The permeable crust: geohydraulic properties down to 9101m depth. *Journal of Geophysical Research,* 102(B8), 18255–18265

Illman, W.A., Liu, X., Takeuchi, S., Yeh, T-C. J., Ando, K. & Saegusa, H. (2009) Hydraulic tomography in fractured granite: Mizunami Underground Research site, Japan. *Water Resources Research*, 45, W01406

Ingebritsen, S. E. & Appold, M. S. (2012) The physical hydrogeology of ore deposits. *Economic Geology*, 107(4), 559–584

Ingebritsen, S. E. & Manning, C.E. (2010) Permeability of the continental crust: dynamic variations inferred from seismicity and metamorphism. *Geofluids*, 10, 193–205

Ishii, E. (2015) Predictions of the highest potential transmissivity of fractures in fault zones from rock rheology: Preliminary results. *Journal of Geophysical Research, Solid Earth*, 120, 2220–2241

Ishii, E., Sanada, H., Funaki, H., Sugita, Y. & Kurikami, H. (2011) The relationships among brittleness, deformation behavior, and transport properties in mudstones: An example from the Horonobe Underground Research Laboratory, Japan. *Journal of Geophysical Research,* 116, B09206

Ito, H., Kuwahara, Y., Kiguchi, T., Fujimoto, K., & Ohtani, T. (2000) Outline of the Nojima fault drilling by GSJ: Structure, physical properties and permeability structure from borehole measurements in GSJ borehole crossing the Nojima Fault, Japan. p.71-75 In: Ito et al. (Eds.) *Proceedings of the International Workshop on the Nojima Fault Core and Borehole Data Analysis*. Open File Report 00-129, U.S. Geological Survey

Johri, M., Zoback, M. D. & Hennings, P. (2014) A scaling law to characterize fault-damage zones at reservoir depths. *AAPG Bulletin*, 98(10), 2057–2079

Jolley, S. J., Fisher, Q. J., Ainsworth, R. B., Vrolijk, P. J. & Delisle, S. (Eds.) (2010) Reservoir Compartmentalization. Geological Society Special Publication 347

Juhlin, C., & Sandstedt, H. (1989) Storage of Nuclear Waste in Very Deep Boreholes: Feasibility Study and Assessment of Economic Potential. SKB Technical Report 89-39, Svensk Kärnbränslehantering AB, Stockholm, Sweden

Karasaki, K., Onishi, T. & Wu, Y-S. (2008) Development of Hydrologic Characterization Technology of Fault Zones. Lawrence Berkeley National Laboratory, California

Karasaki, K., Onishi, T., Doughty, C., Conrad, M., Gasperikova, E., Cook, P., & Ulrich, C. (2012) Development of a Hydrologic Characterization Technology for Fault Zones. Report LBNL-5862E, Lawrence Berkeley National Laboratory. Available on www since 2014 from University of California [http://escholarship.org/uc/item/3j52x603]

Kassoy, D. R. & Zebib, A. (1978) Convection fluid dynamics in a model of a fault zone in the earth's crust. *Journal of Fluid Mechanics*, 88(4), 789–792

Kerrich, R. (1986) Fluid infiltration into fault zones: chemical, isotopic, and mechanical effects. *PAGEOPH* 124(1/2), 225–268

Ladner, F. & Häring, M. O. (2009) Hydraulic characteristics of the Basel 1 Enhanced Geothermal System. *GRC Transactions*, 33, 199–203

Lamur et al. (2017) The permeability of fractured rocks in pressurised volcanic and geothermal systems. *Scientific Reports*, 7, 1–9

Leclère, H., Cappa, F., Faulkner, D., Fabbri, O., Armitage, P., Blake, O. (2015) Development and maintenance of fluid overpressures in crustal fault zones by elastic compaction and implications for earthquake swarms. *Journal of Geophysical Research Solid Earth*, 120, 4450–4473

Lockner, D., Tanaka, H., Ito, H., Ikeda, R., Omura, K. & Naka, H. (2009) Geometry of the Nojima Fault at Nojima-Hirabayashi, Japan – I. A Simple Damage Structure Inferred from Borehole Core Permeability. *Pure and Applied Geophysics,* 166, 1649–1667

Lopez, D. L., & Smith, L. (1996) Fluid flow in fault zones: Influence of hydraulic anisotropy and heterogeneity on the fluid flow and heat transfer regime. *Water Resources Research*, 32, 3227–3235

Loucks, R.G., Reed, R.M., Ruppel, S.C. & Hammes, U. (2012) Spectrum of pore types and networks in mudrocks and a descriptive classification for matrix-related mudrock pores. *AAPG Bulletin*, 96(6), 1071–1098

Louderback, G. D. (1950) Faults And Engineering Geology. In: *Application of Geology to Engineering Practice*, Vol. 1, 125–150, Geological Society of America, Berkeley

Mäkelä, J. (2012) Drilled well yield and hydraulic properties in the Precambrian crystalline bedrock of central Finland. Ph.D. Thesis, University of Turku, Finland

Manning, C. E. & Ingebritsen, S. E. Permeability of the continental crust: The implications of geothermal data and metamorphic systems. *Reviews Geoph.* 37, 127–150 (1999).

Maréchal, J.C. (1998) Les Circulations D'eau Dans Les Massifs Cristallins Alpins Et Leurs Relations Avec Les Ouvrages Souterrains. Thèse de doctorat N° 1769, École Polytechnique Fédérale De Lausanne, France

Marschall, P., Croisé, J., Schlickenrieder, L., Boisson, J-Y., Vogel, P., Yamamoto, S. (2003) Synthesis of Hydrogeological Investigations at The Mont Terri Site (Phases 1 To 5). Technical Report TR 2001-02, Mount Terri Project

Masset, O. & Loew, S. (2010) Hydraulic conductivity distribution in crystalline rocks, derived from inflows to tunnels and galleries in the central Alps, Switzerland. *Hydrogeology Journal*, 18, 863–891

Matonti, C., Lamarche, J., Guglielmi, Y., Marie, L. (2012) Structural and petrophysical characterization of mixed conduit/seal fault zones in carbonates: Example from the Castellas fault (SE France). *Journal of Structural Geology,* 39, 103–121

Matsumoto, N. & Shigematsu, N. (2018) In-situ permeability of fault zones estimated by hydraulic tests and continuous groundwater-pressure observations. *Earth, Planets and Space*, 70(13), 1–12

Meinzer, O.E. (1923) The Occurrence of Ground Water in the United States With a Discussion of Principles. Ph.D. Dissertation, reprinted from USGS Water Supply Paper 489. The University of Chicago Libraries, Illinois

Micarelli, L., Benedicto, A. & Wibberley, C.A.J. (2006) Structural evolution and permeability of normal fault zones in highly porous carbonate rocks. *Journal of Structural Geology,* 28, 1214–1227

Michie, E.A.H. & Haines, T.J. (2016) Variability and heterogeneity of the petrophysical properties of extensional carbonate fault rocks, Malta. *Petroleum Geoscience*, 22, 136–152

Milicich, S.D., Clark, J.P., Wong, C. & Askari, M. (2016) A review of the Kawerau Geothermal Field, New Zealand. *Geothermics*, 59, 252–265

Miller, S. A., Collettini, C., Chiaraluce, L., Cocco, M., Barchi, M. & Kaus, J. P. (2004) Aftershocks driven by a high‑pressure CO2 source at depth. *Nature*, 427, 724–727

Mitchell, T. M. & Faulkner D. R. (2012) Towards quantifying the matrix permeability of fault damage zones in low porosity rocks. *Earth and Planetary Science Letters*, 339–340, 24–31

Moher, D., Liberati, A., Tetzlaff, J. & Altman, D.G. (2009) The PRISMA Group Preferred reporting items for systematic reviews and meta-analyses: the PRISMA Statement. PLoS Med 6(7), e1000097

Molli, G., Cortecci, G., Vaselli, L., Ottria, G., Cortopassi, A., Dinelli, E., Mussi, M., Barbieri, M. (2010) Fault zone structure and fluid-rock interaction of a high angle normal fault in Carrara marble (NW Tuscany, Italy). *Journal of Structural Geology,* 32, 1334–1348

Morrow, C. A., Lockner, D. A., Moore, D. E. & Hickman, S. (2014) Deep permeability of the San Andreas Fault from San Andreas Fault Observatory at Depth (SAFOD) core samples. *Journal of Structural Geology,* 64, 99–114

Morrow, C.A. & Lockner, D.A. (1994) Permeability differences between surface-derived and deep drillhole core samples. *Geophysical Research Letters*, 21(19), 2151–2154

Muraoka, H., Sakaguchi, K., Nakao, S. & Kimbara, K. (2006) Discharge temperature–discharge rate correlation of Japanese hot springs driven by buoyancy and its application to permeability mapping. *Geophysical Research Letters*, 33, L10405

NEDRA (1992) *Characterization Of Crystalline Rocks In Deep Boreholes. The Kola, Krivoy Rog And Tyrnauz Boreholes*. SKB Technical Report 92-39, Svensk Kärnbränslehantering AB, Stockholm, Sweden

Newhouse, W. H. (1942) *Ore Deposits As Related To Structural Features*. Princeton University Press, Princeton, N. J.

Nohara, T., Tanaka, H., Watanabe, K., Furukawa, N. & Takami, A. (2006) In situ hydraulic tests in the active fault survey tunnel, Kamioka Mine, excavated through the active Mozumi-Sukenobu Fault Zone and their hydrogeological significance. *Island Arc*, 15, 537–545

Nur, A. & Booker, J. R. (1972) Aftershocks caused by pore-fluid flow? *Science*, 175, 885–887

Okada, T., Matsuzawa, T., Umino, N., Yoshida, K., Hasegawa, A., Takahashi, H., et al. (2015) Hypocenter migration and crustal seismic velocity distribution observed for the inland earthquake swarms induced by the 2011 Tohoku-Oki earthquake in NE Japan: implications for crustal fluid distribution and crustal permeability. *Geofluids*, 15, 293–309

Okubo, C. H. (2012) Spatial distribution of damage around faults in the Joe Lott Tuff Member of the Mount Belknap Volcanics, Utah: A mechanical analog for faulting in pyroclastic deposits on Mars. *Journal of Geophysical Research,* 117, E08003

Passendorfer, M., & Loew, S. (2010) Subsurface exploration and transient pressure testing from a deep tunnel in fractured and karstified limestones (Lotschberg Base Tunnel, Switzerland). *International Journal of Rock Mechanics and Mining Sciences*, 47, 121–137

Person, M., Raffensperger, J. P., Ge, S. & Garven, G. (1996) Basin-scale hydrogeologic modeling. *Reviews of Geophysics,* 34, 61–87

Pope, E.C., Bird, D.K., Arnorsson, S. & Giroud, N. (2016) Hydrogeology of the Krafla geothermal system, northeast Iceland. *Geofluids,* 16, 175–197

Ranjram, M., Gleeson, T. & Luijendijk, E. (2015) Is the permeability of crystalline rock in the shallow crust related to depth, lithology or tectonic setting? *Geofluids*, 15, 106–119

Reed, M.J. (1983) *Assessment Of Low-Temperature Geothermal Resources of the United States-1982*. Circular 892-73, U.S. Geological Survey

Rice, J. (1992) Fault stress states, pore pressure distributions, and the weakness of the San Andreas Fault. p.69–88, In: Evans, B. & Wong, T-f. (Eds.), *Fault Mechanics and Transport Properties of Rocks*. Academic Press, San Diego, California

Roques, C., Bour, O., Aquilina, L., Dewandel, B., Leray, S., Schroetter, J.M., Longuevergne, L., Le Borgne, T., Hochreutener, R., Labasque, T., Lavenant, N., Vergnaud-Ayraud, V., Mougin, B. (2014) Hydrological behavior of a deep sub-vertical fault in crystalline basement and relationships with surrounding reservoirs. *Journal of Hydrology,* 509, 42–54

Rotevatn, A., Fossmark, H.S., Bastesen, E., Thorsheim, E. & Torabi, A. (2016) Do deformation bands matter for flow? Insights from permeability measurements and flow simulations in porous carbonate rocks. *Petroleum Geoscience*, 23, 104–119

Rowland, J. V., & Simmons, S. F. (2012) Hydrologic, magmatic, and tectonic controls on hydrothermal flow, Taupo Volcanic Zone, New Zealand: implications for the formation of epithermal vein deposits. *Economic Geology*, 107, 427–457

Rutter, E., Mecklenburgh, J. & Taylor, K. (2017) Geomechanical and petrophysical properties f mudrocks: introduction. In: Rutter EH, Mecklenburgh J, Taylor KG (eds.), Geomechanical and Petrophysical Properties of Mudrocks. *Geological Society, London, Special Publications* 454, 1–13

Saar, M.O., Manga, M. (2004) Depth dependence of permeability in the Oregon Cascades inferred from hydrogeologic, thermal, seismic, and magmatic modeling constraints. *Journal of Geophysical Research,* 109, B04204

Saffer, D. M. (2015) The permeability of active subduction plate boundary faults. *Geofluids*, 15, 193–215

Sausse, J., Dezayes, C., Genter, A. & Bisset, A. (2008) Characterization of fracture connectivity and fluid flow pathways derived from geological interpretation and 3D modelling of the deep seated EGS reservoir of soultz (France). In: *Proceedings, Thirty-Third*

Workshop on Geothermal Reservoir Engineering Stanford University, Stanford, California, January 28-30, SGP-TR-185, Stanford University, California

Sausse, J., Fourar, M. & Genter, A. (2006) Permeability and alteration within the Soultz granite inferred from geophysical and flow log analysis. *Geothermics*, 35, 544–560

Scholz, C. H. & Anders, M. H. The permeability of faults. p.247-253, In: Hickman, S.H., Sibson, R., Bruhn, R. (Eds.), *The Mechanical Involvement of Fluids in Faulting*. USGS Open File Report 94-228 (U.S. Geological Survey, 1994).

Schulze-Makuch, D., Carlson, D. A., Cherkauer, D. S. & Malik, P. (1999) Scale dependency of hydraulic conductivity in heterogeneous media. *Ground Water*, 37(6), 904–919

Scibek, J., Gleeson, T. & McKenzie, J.M. (2016) The biases and trends in fault zone hydrogeology conceptual models: global compilation and categorical data analysis. *Geofluids*, 16, 782–779

Seebeck, H., Nicol, A., Walsh, J. J., Childs, C., Beetham, R. D. & Pettinga, J. (2014) Fluid flow in fault zones from an active rift. *Journal of Structural Geology,* 62, 52–64

Seeburger, D.A. (1981) Studies of Natural Fractures, Fault Zone Permeability, And A Pore Space-Permeability Model. Ph.D. Thesis, reprinted from Stanford Rock Physics Report #11, Stanford University, California

Shapiro, S. A., Audigane, P. & Royer, J-J. (1999) Large-scale in situ permeability tensor of rocks from induced microseismicity. *Geophysical Journal International*, 137, 207–213

Shipton, Z. K., Evans, J. P., Robeson, K. R., Forster, C. B., Snelgrove, S. (2002) Structural heterogeneity and permeability in faulted eolian sandstone—implications for subsurface modeling of faults. *AAPG Bulletin*, 86, 863–883

Sibson R. H. (1981) Fluid Flow Accompanying Faulitng: Field Evidence And Models. p.593–603, IN: AGU, Earthquake Prediction: An International Review, American Geophysical Union

Sigda, J.M., Goodwin, L.B., Mozley, P.S., Wilson, J.L. (1999) Permeability alteration in small-displacement faults in poorly lithified sediments: Rio Grande Rift, central New Mexico. In: Haneberg et al. (eds) *Faults and Subsurface Fluid Flow in the Shallow Crust*. Geophysical Monograph 113, American Geophysical Union

Siratovich, P.A., Heap, M.J., Villeneuve, M.C., Cole, J.W., Kennedy, B.M., Davidson, J., Reuschléb, T. (2016) Department Mechanical behaviour of the Rotokawa Andesites (New Zealand): Insight into permeability evolution and stress-induced behaviour in an actively utilised geothermal reservoir. *Geothermics*, 64, 163–179

Smyth, R.C. & Sharp Jr, J.M. (2006) The hydrology of tuffs. In: Heiken G (ed.) Tuffs - their properties, uses, hydrology, and resources. *GSA Special Paper*, 408, 91–111

Snow, D. T. (1965) A Parallel Plate Model of Fractured Permeable Media. Ph.D. Thesis, University of California, Berkeley

Sorey, M. L. & Lewis, R. E. (1976) Convective Heat Flow From Hot Springs in the Long Valley Caldera, Mono County, California. *Journal of Geophysical Research,* 81(5), 785–791

Stimac, J., Nordquist, G., Suminar, A., & Sirad-Azwar, L. (2008) An overview of the Awibengkok geothermal system, Indonesia. *Geothermics*, 37, 300–331

Stober, I. & Bucher, K. (2007) Hydraulic properties of the crystalline basement. *Hydrogeology Journal,* 15, 213–224

Sweetkind, D. S., Drake, R. M. II (2007) Characteristics of Fault Zones in Volcanic Rocks Near Yucca Flat, Nevada Test Site, Nevada. Open–File Report 2007–1293, U.S. Geological Survey

Talwani, P., Chen, L. & Gahalaut, K. (2007) Seismogenic permeability, k_s. *Journal of Geophysical Research,* 112, B07309

Townend, J. & Zoback, M. D. (2000) How faulting keeps the crust strong. *Geology*, 28, 399–402

Tsang, C-F. & Neretnieks, I. (1998) Flow channeling in heterogeneous fractured rocks. *Reviews of Geophysics*, 36(2), 275–298

Uehara, S., Shimamoto, T., Okazaki, K., Funaki, H., Kurikami, H., Niizato, T., & Ohnishi, Y. (2012) Can surface samples be used to infer underground permeability structure? A test case for a Neogene sedimentary basin in Horonobe, Japan. *International Journal of Rock Mechanics & Mining Sciences*, 56, 1–14

Vaittinen, T., Ahokas, H., Nummela, J., Paulamäki, S. (2011) Hydrogeological Structure Model Of The Olkiluoto Site – Update In 2010. Working Report 2011-65, Posiva Oy, Finland

Vidal, J. & Genter, A. (2018) Overview of naturally permeable fractured reservoirs in the central and southern Upper Rhine Graben: Insights from geothermal wells. *Geothermics*, 74, 57–73

Vidal, J., Genter, A. & Schmittbuhl, J. (2015) How do permeable fractures in the Triassic sediments of Northern Alsace characterize the top of hydrothermal convective cells? Evidence from Soultz geothermal boreholes (France). *Geothermal Energy*, 3(8)

Walker, R.J., Holdsworth, R.E., Imber, J., Faulkner, D.R., Armitage, P.J. (2013) Fault zone architecture and fluid flow in interlayered basaltic volcaniclastic-crystalline sequences. *Journal of Structural Geology,* 51, 92–104

Wibberley, C. A. J. & Shimamoto, T. (2003) Internal structure and permeability of major strike-slip fault zones: the Median Tectonic Line in Mie Prefecture, Southwest Japan. *Journal of Structural Geology*, 25, 59–78

Williams, G.M., Hooker, P.J. & Brightman, M.A. (1990) Field Studies About Radionuclide Migration, Natural Analogues And Faults In Clays. Nuclear Science And Technology. Final report EUR 13022 EN, Commission of the European Communities

Xue, L., Li, H.B., Brodsky, E.E., Xu, Z.Q., Kano, Y., Wang, H., Mori, J.J., Si, J.L., Pei, J.L., Zhang, W., Yang, G., Sun, Z.M., and Huang, Y. (2013) Continuous permeability measurements record healing inside the Wenchuan Earthquake Fault Zone. *Science*, 340(6140), 1555–1559

Xue, L., Brodsky, E.E., Erskine, J., Fulton, P.M. & Carter, R. (2016) A permeability and compliance contrast measured hydrogeologically on the San Andreas Fault. *Geochemistry, Geophysics, Geosysystems*, 17, 858–871

Yamashita, T. & Tsutsumi, A. (2018) Involvement of Fluids in Earthquake Ruptures, Field / Experimental Data and Modeling. Springer Japan KK

Zoback, M. D. & Hickman, S. (1982) In situ study of the physical mechanisms controlling induced seismicity at Monticello Reservoir, South Carolina. *Journal of Geophysical Research,* 87, 6959–6974

Zoback, M.D. (2007) Reservoir Geomechanics. Cambridge University Press

CHAPTER 4

4 The biases and trends in fault zone hydrogeology conceptual models: global compilation and categorical data analysis

This chapter is a research article written in 2015 and was published in 2016 in a special edition of *Geofluids* on the hydrogeology of fault zones. The initial statistical analysis was done on a smaller database of 700 publications, that was starting to take form at that time. Due to lack of numerical permeability data at that time, the categorical analysis was done that relies on counts within categories only. This method was ideal for exploring the biases and trends in observations in fault zones in various geoscience disciplines. This helped in the design of larger database that was done subsequently.

4.1 Abstract

To investigate the biases and trends in observations of the permeability structures of fault zones in various geoscience disciplines, we review and compile a database of published studies and reports containing more than 900 references. The global data are categorized, mapped, and described statistically. We use the chi-square test for the dependency of categorical variables to show that the simplified fault permeability structure (barrier, conduit, barrier–conduit) depends on the observation method, geoscience discipline, and lithology. In the crystalline rocks, the in situ test methods (boreholes or tunnels) favor the detection of permeable fault conduits, in contrast to the outcrop-based measurements that favor a combined barrier–conduit conceptual models. These differences also occur, to a lesser extent, in sedimentary rocks. We provide an estimate of the occurrence of fault conduits and barriers in the brittle crust. Faults behave as conduits at 70% of sites, regardless of their barrier behavior that may also occur. Faults behave as barriers in at least 50% of the sites, in addition to often being conduits. Our review of published data from long tunnels suggests that in crystalline rocks, 40–80% (median about 60%) of faults are highly permeable conduits, and 30–70% in sedimentary rocks. The trends with depth are not clear, but there are less fault conduits counted in tunnels at the shallowest depths. The barrier hydraulic behavior of faults is more uncertain and difficult to observe than the conduit.

4.2 Introduction

Globally, fault zones have been studied at many sites, and the permeabilty of rocks and their fracture networks have been estimated or tested in-situ at different sampling scales, described by different metrics in structural geology (Faulkner et al. 2010), hydrogeology (Bense et al. 2013), and other geoscience and engineering disciplines. Caine et al. (1996) proposed qualitative and quantitative metrics to describe the fault zone permeability styles (also called permeability structure or architecture), but despite having more than 1000 citations to the general concept of barrier-conduit, the proposed quantitative metrics have been only used at a small number (~10) of studies (e.g. Brogi 2008, Ganerød et al. 2008, Liotta et al. 2010). There is also ambiguity in the use of the qualitative metrics and conceptual models and the terminology (Shipton et al. 2013). It has been suggested by Bense et al. (2013) that multidisciplinary data integration is needed to help understand the fluid flow processes along fault zones.

In this study, a *simplified permeability structure* of a fault zone (following Caine et al. 1996) is used as a conceptual framework to classify the results from the compiled research sites. In order to compare a large number of sites and observations, a simple "end-member" type of conceptual model that can be applied at the majority of the sites is appropriate and this has been done by other authors. For example, at the Yucca Mountain nuclear repository site, Dickerson (2000) divided faults into simple barrier/conduit/conduit-barrier/none (offset only) categories. Similarly, Aydin (2000) used the categories of transmitting (conduit), sealing (barrier), vertically transmitting and laterally-sealing (conduit-barrier), and sealing or transmitting intermittently (transient conduit or barrier). A more fine categorization (e.g. weak or strong barrier, barrier/conduit permeability ratio, etc.), or, a quantitative mapping of permeability distributions and discrete fracture network models as proposed by Caine and Forster (1999), is not available at the majority of sites and this would results in too small counts of data to be useful for statistical analysis. Therefore, we use only three categories to count the permeability structures: 1) barrier, 2) conduit, and 3) barrier-conduit.

The definition of a conduit used here is where fault rock is more permeable than the protolith and the conduit geometry is usually conceptualized parallel to the fault plane and within the damage zone, in the majority of studies that we reviewed. The barrier is defined where the permeability zone somewhere in the fault structure affects the transverse flow of groundwater across the fault (the barrier permeability is less than the protolith). A barrier-conduit is where both the barrier and the conduit are present, as defined earlier. In this study we are not comparing parts of fault zones in this study (e.g. fault core vs. damage zone), or assess the magnitude permeability (e.g. how leaky is a barrier). For the purposes of counting of barrier and conduit frequencies at the global sites, these three categories (barrier, conduit, barrier-conduit) are exclusive. The barrier category means barrier only, where there was no observation of a conduit behavior of the fault. Similarly, the conduit category means conduit only (no observation of barrier effect). A fourth category was initially used for fault zones with "no observable hydrogeological impact", but the counts of such sites were too small to use in the statistical analysis together with the other data. It appears that the studies report a "positive result" where the fault has been characterized or tested successfully to some extent. Later in the paper we present proportions of conduit faults along 30 large tunnels. The faults that are not counted as conduits may be barriers or may have the same permeability as the protolith, although we could not assess these properties from inflow data in tunnels alone.

The objective of this research is to quantify the observational biases of fault zone hydrogeology and describe global occurrences and trends in the barrier, conduit, and barrier-conduit behavior. To do this, we analyse a large, new global dataset of published data and inferred conceptual models of fault zone hydraulic behavior. Statistical tests are used to detect biases of different test methods and of collections of methods across geoscience disciplines, and the results are used to discuss the knowns and unknowns of the fault zone permeability structures in Earth's the brittle crust.

4.3 Methods

4.3.1 Data sources

For our analysis, we reviewed published data and interpretations in multidisciplinary geoscientific and engineering literature, compiled from different geoscience fields, including hydrogeology, structural geology, reservoir and geotechnical engineering, and related industries. The data compilation is an example of secondary data analysis in order to answer new questions with older existing data (Glass 1976). This contrasts with primary data analysis, which is site-specific hydrogeological, structural, geothermal and other analysis of primary data (observations, tests, models, etc.). It is important to use a wide range of databases and search methods in meta-analysis of existing research data (Whiting et al. 2008). We used databases of academic journals, national geological surveys and organizations, atomic energy waste management and research organizations, and technical reports from industries. This study looked primarily publications in English, and less numerous papers and reports translated from Japanese, French, German, and Italian. We reviewed at least 1817 publications and found that about 914 had references to fault zone permeability (Table 4-1). Smaller subsets that satisfied various queries by selected categories were used for statistical analysis (698 for comparing results between geoscience disciplines). The following sections explain the data sources and methodology.

Table 4-1 (a) Counts of fault study sites reviewed and used in statistical analysis from five geoscience disciplines. (b) Counts of fault sites reviewed from geothermal and geophysical data sources but not used in statistical analysis.

	References	Used in analysis	Barrier only	Conduit only	Barrier & Conduit
(a) Geoscience discipline					
1) Structural Geology	231	186	59	42 *	37
2) Hydrogeology	490	308	87	164	57
3) Tunnels Engineering	175	110	10	70	30
4) Mine and Dam Engineering	40	42	10	24	8
5) Hydrocarbon Reservoirs	76	52	22	23	7
Subtotal (1 to 5)	1012	699	188	323	139
(b) Data reviewed but not used in statistical analysis due to lack of barrier					
6) Geothermal Reservoirs	700	143	3	140	0
7) Geophysics	105	73	0	66	0
Total (1 to 7, all sites)	1817	914			

*present-day permeability distribution (does not include paleo-conduits).

4.3.2 Data sources used in statistical analysis

Structural geology studies are typically at outcrops due to easier access, although scientific deep drilling is also an important component (e.g. reviews in Juhlin and Sandstedt 1989, Townend and Zoback 2000). In outcrop studies the data collection is usually focussed on small-scale probing and testing of rock matrix permeability on outcrop samples or shallow probe-holes (Okubo 2012, Walker et al. 2013). There are only a few studies of statistical analyses of hundreds of outcrop samples (Balsamo and Storti 2010). Permeability structures are also inferred from porosity and fracture distributions (Matonti et al. 2012, Mitchell and Faulkner 2012) and empirical laws or comparisons to permeability samples.

In this study, the "hydrogeology" category includes aquifer studies and research sites in fractured and faulted rocks of any lithology. The hydrogeology category had the largest sample size of fault zones, typically at depths less than 1000m. Permeability estimates and fault hydraulic behaviors are typically tested through borehole tests, observations of natural hydraulic and temperature gradients near faults, and through the geochemistry of waters (e.g. review by Bense et al. 2013). Hydrogeological tests (e.g. aquifer tests) are done in all other geoscience disciplines but we chose to separate the other geoscience disciplines to test statistically whether there are differences between them in how fault zones are viewed.

The tunnel engineering category includes long transportation and hydro-tunnels and is mostly in the domain of geotechnical and civil engineering, with a strong hydrogeology component. The permeability of fault zones is "detected" usually by observations, such as inflows of water during tunnel excavation, in pre-tunnelling drilling programs.

The category of "mines and dams" refers to large excavations that are not long transportation tunnels, although both dams and underground mines involve tunnels, although at smaller diameters usually than the transportation tunnels. Dam foundation works involve a large number of drillhole-based injection or pumping tests and fracture mapping. At open-pit mines the data quality varies greatly, but for fault zones it is usually limited to seepage observations or water table mapping.

The category of hydrocarbon reservoirs includes papers presenting conceptual models for fault hydraulics in sedimentary basins, although this category is very limited because data repositories are generally held privately by the petroleum industry. In sedimentary basins there has been a focus of studies on barrier faults and reservoir compartmentalization (e.g. Jolley et al. 2010). Reservoir outcrop analog studies (e.g. Antonellini and Aydin 1994, Solum et al. 2010) are included in the structural geology category. Fault conduits have been inferred from geomechanical analysis in studies of fractured hydrocarbon reservoirs (Gartrell et al. 2004, Hennings et al. 2012), in sedimentary and faulted crystalline rocks below sedimentary basins (Petford and McCaffrey 2003).

4.3.3 Data sources reviewed but not used in statistical analysis

Geothermal drilling is potentially a good source of data on fault conduits, for which we reviewed approximately 700 papers as part of an on-going study on this topic (Scibek et al. 2015). Descriptions of conceptual and numerical models of whole reservoirs are commonly published (Bjornsson and Bodvarsson 1990, O'Sullivan et al. 2001). Most of the permeability data collected by the industry is not published, while journal papers usually present only conceptual models (e.g. Serpen 2004) or results of numerical models (Magri et al. 2010). Fault conduits that discharge hydrothermal fluids are very common, and due to their large number and global distribution, warm- and hot-springs can provide useful insights into structural controls and the magnitude of permeability of conduits (Muraoka et al. 2006, Rowland et al. 2012, Faulds et al. 2015). We also reviewed published estimates of diffusivity estimates from cases of reservoir-induced seismicity along faults (Gupta 2002, Talwani et al. 2007), and naturally occurring migrating earthquake swarms (El Hariri et al. 2010, Chen et al. 2012, Okada et al. 2015). The conceptual models of fluid migration assume fault conduits and give no information about fault barriers. In both categories, the lack of representative fault barrier counts prevented us from using these data in the statistical analysis.

4.4 Data synthesis and fault zone attribute counting

4.4.1 Observation method categories

In this study we included sites where there inferred fault zone permeability structure was supported by permeability tests or hydraulic tests or other fluid flow phenomena along and across fault zones (e.g. natural tracers, geochemical properties), or a clearly presented conceptual model with supporting evidence. Numerical models of particular sites were only treated as supporting evidence and numerical models that were non-site-specific (hypothetical) or not robustly calibrated were not used. Papers describing fault zone morphology, lithology, and structure without any permeability tests were not used. The different data sources differ in their preferred methods of observations, their scales of measurement, depths of samples, and purpose of investigation of fault zones and non-faulted rocks. Consequently, each site was classified by observation type, depending on the type of test and the scale of test. In all the categories, the frequencies (counts) were tabulated for the occurrence of inferred simplified fault zone permeability structure conceptual models, forming the basis of our statistical analysis. The "raw data" counts were at first divided into more than 40 sub-categories of measurement methods, but after preliminary analysis we decided to aggregate the data into six categories of observation type. For example, the matrix permeametry measurements or estimates were grouped together, small-scale borehole interval hydraulic tests were grouped, large-scale hydraulic tests that measure a large volume of rock were also grouped, and so on.

The total number of data points for observation methods totalled 785, which is greater than the total number of data from different published references (698). The excess of "data points" in the counts of observation method data is because in 73 studies there were more than one observation method employed to probe the fault hydraulics, and another 50 references had unspecified observation method or method that did not fit in the main categories or the results were not conclusive. All study sites were treated equally, despite obvious variability, and potentially quality, of data available. We counted the data in conceptually exclusive categories, although in reality there are an unknown number of sites where fault zone permeability structure were mis-classified (e.g. barrier or conduit exists was not detected).

The categories of observation methods are as follows:

1) drill core and outcrop samples (rock matrix permeability tests, porosity-permeability conversions on matrix rock),
2) borehole hydraulic tests (including slug and packer tests on borehole intervals, drill stem tests),
3) borehole hydraulic tests at larger scale involving pumping tests and well production rates,
4) hydraulic head or pressure difference observations across fault zones,
5) water properties across fault zones (chemistry, temperature, or tracers),
6) tunnel inflow observations and drawdowns around tunnels with fault zone interactions.

4.4.2 Geoscience discipline categories

The data sources were categorized by geoscience or engineering discipline. The geoscience disciplines can be thought as grouped sets of methods and approaches to studies of fault zones and not exclusively a study discipline in the traditional sense. Initially all the reviewed sites were grouped into 7 categories for exploratory data analysis (Table 4-1), but the two categories *geothermal reservoirs* and *geophysics* contained only fault conduits, thus we excluded these two categories from statistical tests to avoid biasing the results with too many fault conduit spurious results where categories contain too few data counts (Cochran 1952). When counts are too low or zero, the Chi-squared test is less conservative and tends to produce a significant result. In the five remaining geoscience discipline categories there were 650 data sources describing the simplified fault zone permeability structures. The maps presented in Figure 4-1 are, to our knowledge, this is the first such maps published showing locations of fault zone test sites globally. The data is shown by categories of geoscience discipline and the simplified permeability structure.

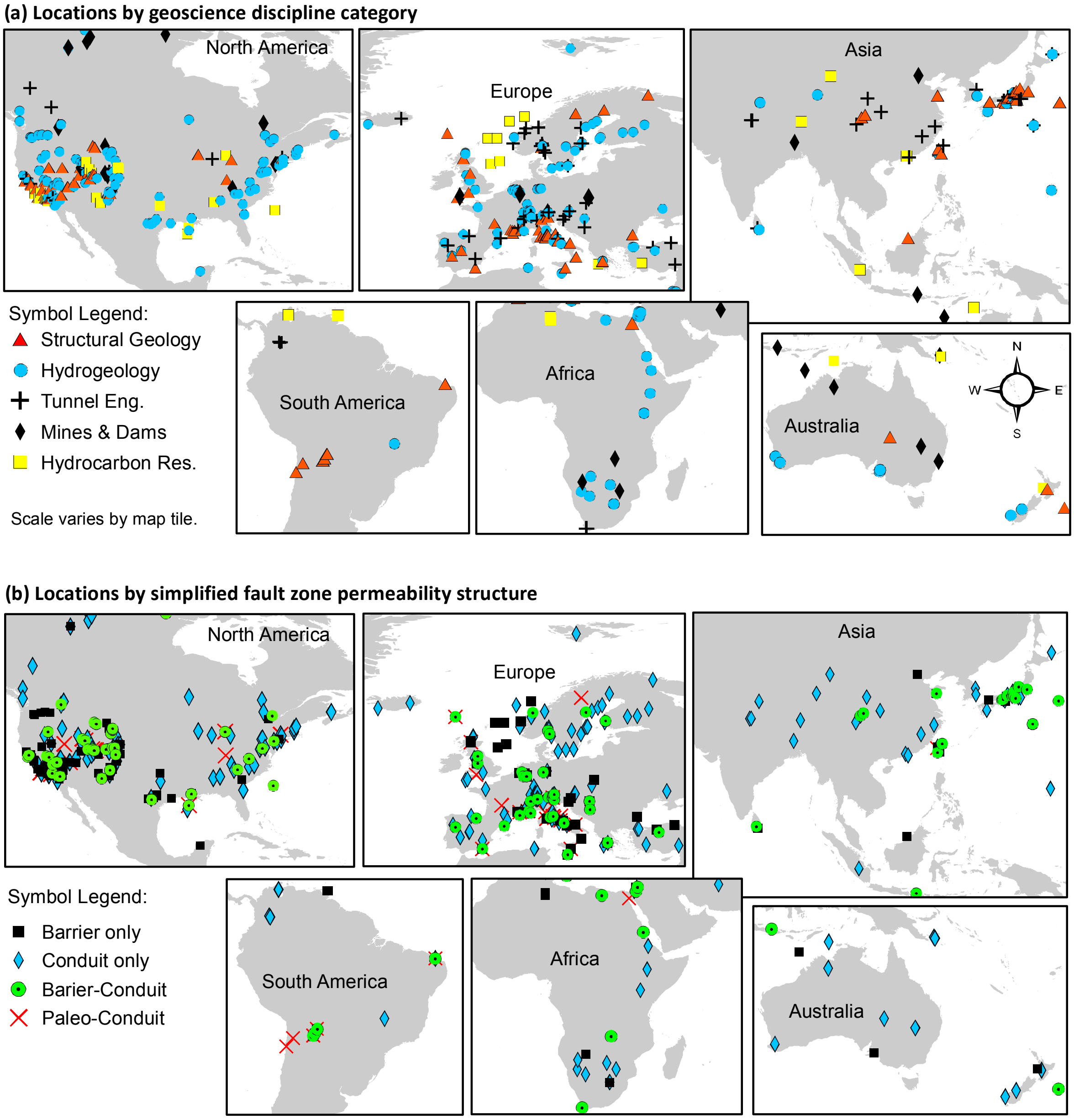

Figure 4-1 Locations of reviewed fault zone study sites categorized by (a) geoscience discipline of data source, (b) simplified conceptual model of fault zone permeability structure.

4.4.3 Lithology categories

The geological conditions were reviewed at the fault study sites to summarize the dominant lithological units in the database. These included: igneous intrusive rocks (mostly granitic at most sites), metamorphic rocks (usually it was gneiss), volcanic rocks (usually basalt or tuff, and we separate these into sub-categories), and sedimentary rocks (heterogeneous). In the results we present counts for these categories. For the statistical tests, described in the next section, only the most general lithological categories are used: 1) crystalline rocks and 2) sedimentary rocks. This is due to data limitations at the time of writing of this paper.

4.5 Categorical data analysis with Chi-Square test

4.5.1 Hypotheses tested

We frame the statistical analysis and hypothesis test in terms of the response variable *simplified fault zone permeability structure* and the explanatory variables: the observation method, geoscience discipline, and lithological categories. The null hypothesis is that there is no dependence of the response variable on the explanatory variable, and the alternate hypothesis is that there is a dependence. The underlying assumption is that the observations represent random samples from a very large global "population" of fault zones. Four hypotheses were tested for the dependence of simplified fault zone permeability structure on:

1) Observation method,
2) Geoscience discipline,
3) Lithological category (crystalline or sedimentary rocks),
4) Geoscience discipline (separately for crystalline and sedimentary rocks).

In hypothesis 4, we further explore the control of lithology on the test for dependence between the fault zone permeability structure and the geoscience discipline, but after filtering the data into two main lithological categories: crystalline rocks and sedimentary rocks.

4.5.2 Statistical methods

We use the Pearson Chi-Square test for independence of variables (Pearson 1900). The test determines whether there is a difference between two categorical variables in a sample which reflects real difference between these two variables in the global dataset (review by Voinov et al. 2013). This test has been used in medical, social and natural science fields to evaluate interactions between the categorical variables (Lewis and Burke 1949, Delucchi 1983). In hydrogeology, it has been used to compare fracture frequencies in lithological categories at a site in South Carolina containing a fault zone (La Pointe 2000). This test makes no assumptions about the shape of the population distribution, but it assumes random sampling from the population and a nominal or ordinal statistical scale of measurement. The simplified and applied methodology of hypothesis testing and Chi-square calculation is explained in many textbooks (e.g. Agresti 2002, Howell 2011). The underlying assumption is that the observations represent random samples from a very large global "population" of fault zones. The *contingency table* is used to show cross-classification of categorical variables of observed frequencies (counts), using notation after Agresti 2002:

$$\hat{\mu}_{ij} = \frac{n_{i+} \times n_{+j}}{n} \qquad [1]$$

where $\hat{\mu}_{ij}$ is the expected frequency at table cell with row i and column j, n_{i+} x n_{+j} is the product of marginal totals in the table (n_{+i} for rows totals and n_{+j} for column totals), and n is the total count of all data in the table. and the total of all counts in a table (n). The Chi-square statistic (χ^2) is calculated as the sum (across rows and columns) of normalized differences between observed and expected frequencies:

$$\chi^2 = \Sigma_i \ \Sigma_j \ \frac{\left(n_{ij} - \hat{\mu}_{ij}\right)^2}{\hat{\mu}_{ij}} \qquad [2]$$

The shape of the Chi-square sampling distribution depends on degrees of freedom, calculated from the product of (#rows - 1) by (#columns -1) in the contingency table. The strength of the association of these variables can be shown with a cell-by-cell comparison of the observed and expected frequencies using the standardized *Pearson Residual$_{ij}$*, where the sample marginal proportions are $\pi_{i+} = n_{i+}/n$ and $\pi_{j+} = n_{+j}/n$:

$$\text{Pearson Residual}_{ij} = \frac{n_{ij} - \hat{\mu}_{ij}}{\left[\hat{\mu}_{ij}(1-\pi_{i+})(1-\pi_{+j})\right]^{0.5}} \qquad [3]$$

The results of the Chi-square test are evaluated by calculating the left-tailed probability of having the computed χ^2 value, at a specified degrees of freedom, to the probability threshold of 0.001. If the calculated probability is less than 0.001 (usually for a large χ^2), then the difference between the observed distribution and the expected distribution is too large to be a result of random variation, and the null hypothesis will be rejected. For individual entries (table cells) in the contingency table, an absolute value of the Pearson Residual greater than 2 or 3 indicates a lack of fit of the null hypothesis (Agresti 2002).

4.6 Results

4.6.1 Hypothesis 1 test (simplified fault zone permeability structure vs. observation method)

The Chi-square statistic is 206 (Table 4-2) and the left-tailed probability of having this χ^2 at 10 degrees of freedom is $5x10^{-39}$, which is less than probability threshold of 0.001. Therefore, there is a strong evidence of association between the inferred permeability structures of fault zones and the observation method. This is apparent from the different shapes of the histograms of these categorical variables (Figure 4-2a). The Pearson residuals exceed the value of 3 in about half of the table cells, indicating significant deviations from expected frequencies (Figure 4-2b).

Table 4-2 Fault zone permeability structure model counts by categories of observation method: contingency table of observed, expected frequencies, and calculated Chi-square terms and standardized Pearson residuals. The categories of observation method table columns are: A - drill core and outcrop samples, B - borehole interval hydraulic tests (packer, slug), C - borehole interval large hydraulic tests (pump or injection), D - hydraulic head or pressure differences across fault, E - water chemistry, temperature, natural tracers, F - tunnel inflow or drawdown.

	A	B	C	D	E	F	Total	A	B	C	D	E	F
Observed frequencies								Expected frequencies					
Barrier	51	15	13	84	22	9	194	28	43	19	37	38	30
Conduit	32	120	47	19	97	85	400	59	89	38	75	78	61
Barrier-Conduit	32	39	15	45	34	26	191	28	42	18	36	37	29
Totals	115	174	75	148	153	120	785						
Chi-square terms and Chi-square result								Standardized Pearson residuals					
Barrier	17.9	18.2	1.7	61.5	6.6	14.4	120.3	5.3	-5.6	-1.6	10.0	-3.3	-4.7
Conduit	12.1	11.1	2.0	42.2	4.6	9.3	81.3	-5.4	5.4	2.1	-10.3	3.4	4.7
Barrier-Conduit	0.6	0.3	0.6	2.2	0.3	0.4	4.3	0.9	-0.7	-0.9	1.9	-0.7	-0.7
						$\chi 2$ =	206						

The following observations are made about the results:

a) Observations based on permeability from drill cores and outcrops favour the combined barrier-conduit permeability structures.

b) Borehole test results at small scale and large scale have suggest similar frequencies of fault conduits and barriers. Both favour the conduit permeability structure, and both provide fewer than expected barrier faults.

c) The methods relying on hydraulic head or pressure differences across fault zones result in more than expected barrier- fault models, less than expected conduit- fault models, and approximately the expected frequency of combined barrier-conduit fault models.

d) The observations of water chemistry and tracers across fault zones produce the expected results of the frequencies of conduit faults and barrier-conduit faults, except with less than expected barrier-only faults.

e) In tunnels, the observations relying on inflows result in more than expected conduit faults, but can be poor at detecting the barrier faults.

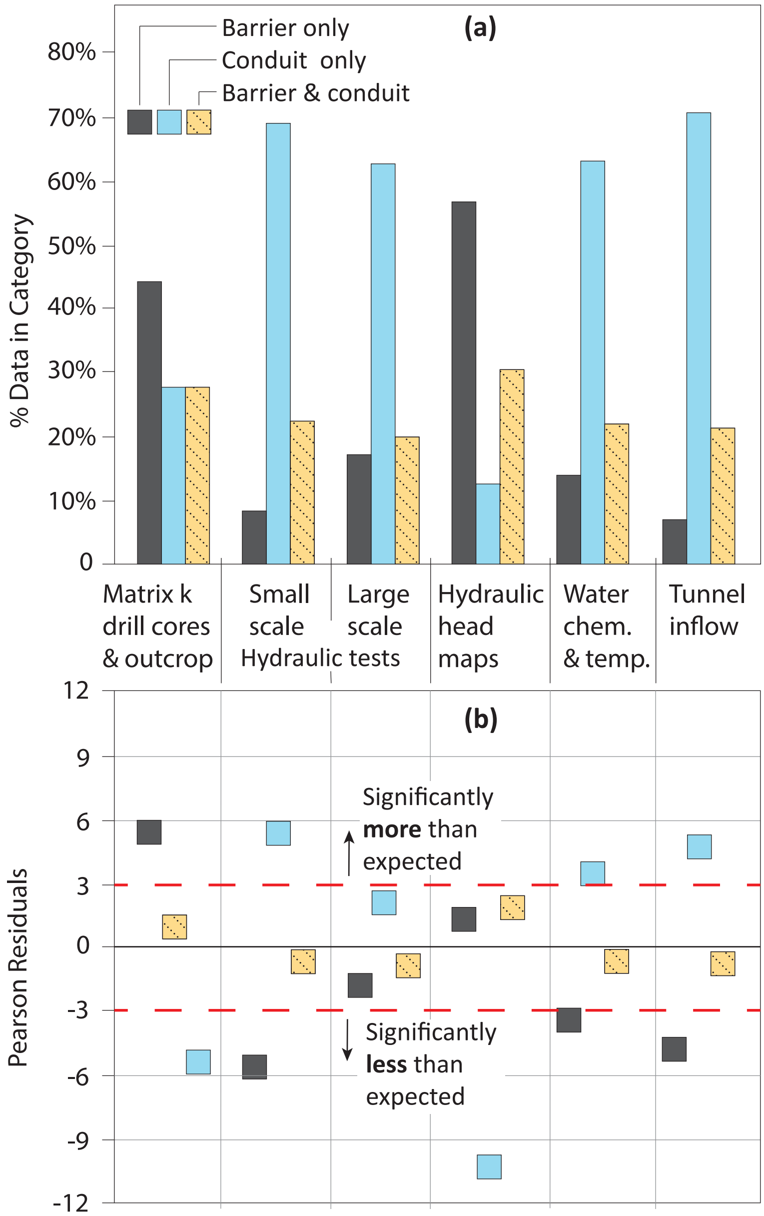

Figure 4-2 Summary histograms for the simplified fault zone permeability structures in observation method categories: (a) histograms relative frequencies by observation method, and (b) comparing the observed to expected frequencies of fault zone simplified permeability structures using the calculated Person Residuals from Chi-Square analysis of categorical data.

4.6.2 Hypothesis 2 test (simplified fault zone permeability structure vs. geoscience discipline)

The Pearson Chi-Square test results was $\chi^2 = 50$ ($p = 1.5\text{x}10^{-8}$), suggesting an association between the simplified fault zone permeability structure and the geoscience discipline (Table 4-3). The histograms in Figure 4-3a show graphically the differing counts, but the Pearson residuals (Figure 4-3b) only exceed the absolute value of 3 in two categories and are generally within the acceptable limits for other categories. Therefore, the dependence on the geoscience discipline is not as strong as for the observation method, perhaps because some observation methods are used in all geoscience disciplines. The analysis was done on five geoscience disciplines, as was mentioned earlier. This avoids distorting the expected frequencies for the whole table (i.e. the results tend to be more "significant" or extreme in Chi-square value when the seven categories are used with the very different frequencies or counts). The contingency table (Table 4-3) has 2 cells with frequencies less than 10 but greater than 5, that is deemed to be acceptable.

Table 4-3 Fault zone permeability structure model counts by categories of geoscience discipline: contingency table of observed, expected frequencies, and calculated Chi-square terms and standardized Pearson residuals. A - Structural geology, B - Hydrogeology, C - Tunnel Engineering, D - Mining and Dams, E - Hydrocarbon Reservoirs

	A	B	C	D	E	Total	A	B	C	D	E
Observed frequencies							Expected frequencies				
Barrier	59	87	10	10	22	188	40	89	32	12	15
Conduit	42	164	70	24	23	323	69	153	55	21	26
Barrier-Conduit	37	57	30	8	7	139	30	66	24	9	11
Totals	138	308	110	42	52	650					
Chi-square terms and Chi-square result							Standardized Pearson residuals				
Barrier	9.1	0.0	15.0	0.4	3.2	27.7	4.0	-0.4	-5.0	-0.8	2.2
Conduit	10.3	0.8	4.3	0.5	0.3	16.2	-5.1	1.7	3.2	1.0	-0.8
Barrier-Conduit	1.9	1.2	1.8	0.1	1.5	6.5	1.8	-1.7	1.7	-0.4	-1.5
						$\chi 2 =$ 50					

The following observations can be made:

1. In the structural geology category there are less conduit faults and more combined barrier-conduit faults than expected for the whole dataset.
2. In the categories of mine and dam engineering and hydrogeology, the occurrences of

fault permeability structures are approximately as expected.

3. The tunnelling engineering category has smaller than expected frequency of barrier faults and much more than expected conduit faults.

4. In the category of hydrocarbon reservoirs, the limited data highlights the well-known occurrence of barrier faults in sedimentary rocks.

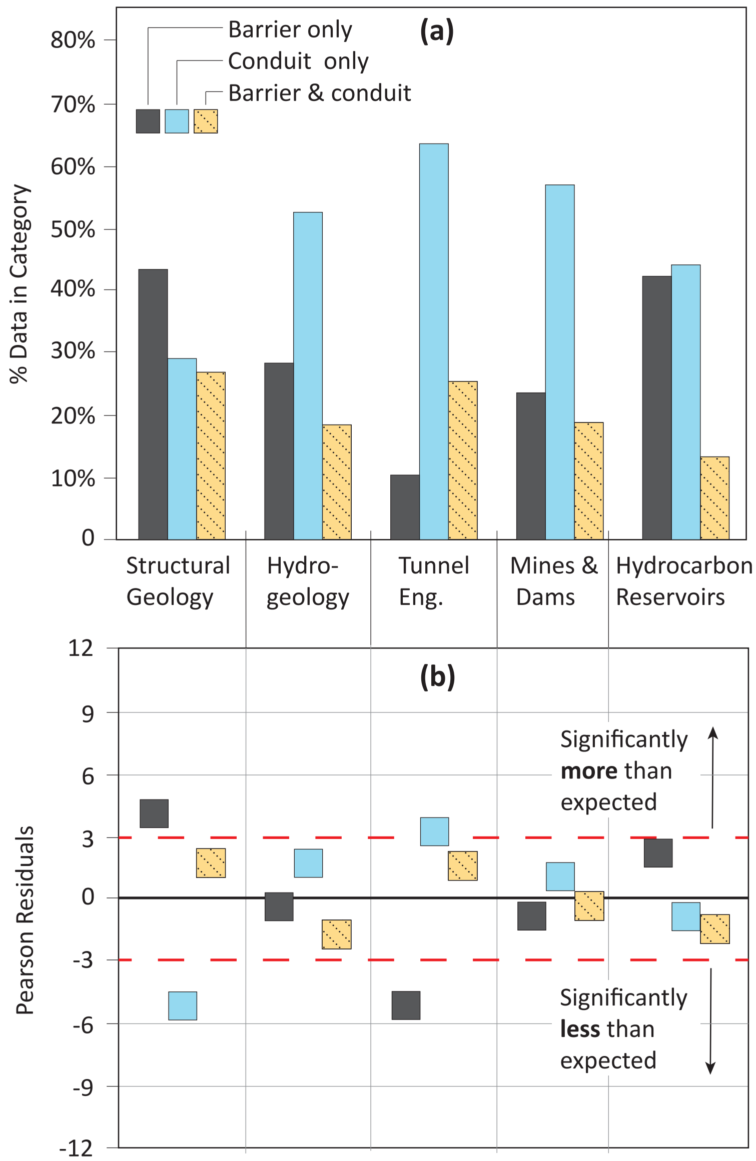

Figure 4-3 Summary histograms for the simplified fault zone permeability structures in geoscience discipline categories: (a) histograms of relative frequencies by geoscience discipline, and (b) comparing the observed to expected frequencies of fault zone simplified permeability structures using the calculated Person Residuals from Chi-Square analysis of categorical data.

4.6.3 Hypothesis 3 test (simplified fault zone permeability structure vs. lithology):

In order to investigate the effects of lithology on the previously determined results from hypotheses 1 and 2, we compared the frequencies of the simplified fault zone permeability structures between two main lithological categories: sedimentary rocks, and crystalline rocks. The latter refers here to the metamorphic and igneous "basement" rocks. We also summarized two other common sub-categories of lithology of interest: granitic rocks, and extrusive igneous rocks (basalts, andesites, etc.) (Table 4-4). The histograms are shown in Figure 4-4a. The geoscience disciplines that have the most fault zones in the crystalline rocks are tunnel engineering, mines and dams, and hydrogeology (between 40 and 50%), as shown in Figure 4-4b). Structural geology field sites are 68% in sedimentary rocks, and more than 90% of hydrocarbon reservoir studies compiled in this analysis are in sedimentary rocks. The Chi-square test returned a significant result ($p<0.001$) with a large χ^2 of 162, suggesting that the differences seen in the histograms between the sedimentary and crystalline rocks are significant.

Table 4-4 Comparing the frequencies of occurrence of data within lithological categories. The table shows the counts of fault zone simplified permeability structures, and the counts of fault zone sites within geoscience disciplines that have the specified lithology of protolith. A - Structural geology, B - Hydrogeology, C - Tunnel Engineering, D - Mining and Dams

	Simplified Permeability Structures					Geoscience Disciplines				
Lithology	Barrier	Conduit	Barrier-Conduit	Total	% Conduit	A	B	C	D	E
Sedimentary rocks	140	138	85	363		122	226	67	22	47
	39%	38%	23%		61%	68%	59%	47%	55%	92%
Crystalline rocks (metamorphic and igneous)	23	147	57	227		58	157	76	18	4
	10%	65%	25%		90%	32%	41%	53%	45%	8%
Other subcategories of lithology										
Granitic rocks	11	76	29	116		35	86	43	4	3
	9%	66%	25%		91%	19%	23%	31%	10%	6%
Basalt rocks	14	19	6	39		9	25	11	6	2
	36%	49%	15%		64%	5%	6%	7%	15%	4%

Other useful observations are:

1. In sedimentary rocks, barrier and conduit faults were equally common (~38%).
2. The occurrence of "any conduit", that is the sum of the two exclusive categories "conduit only" and "barrier and conduit", is 61% in the sedimentary rocks, and up to 90% in the

crystalline rocks.

3. The proportion of fault conduits in the sub-category of granitic rocks was about the same as in the main category of crystalline rocks. The fault conduit proportions in basaltic rocks were approximately the same as in sedimentary rocks.

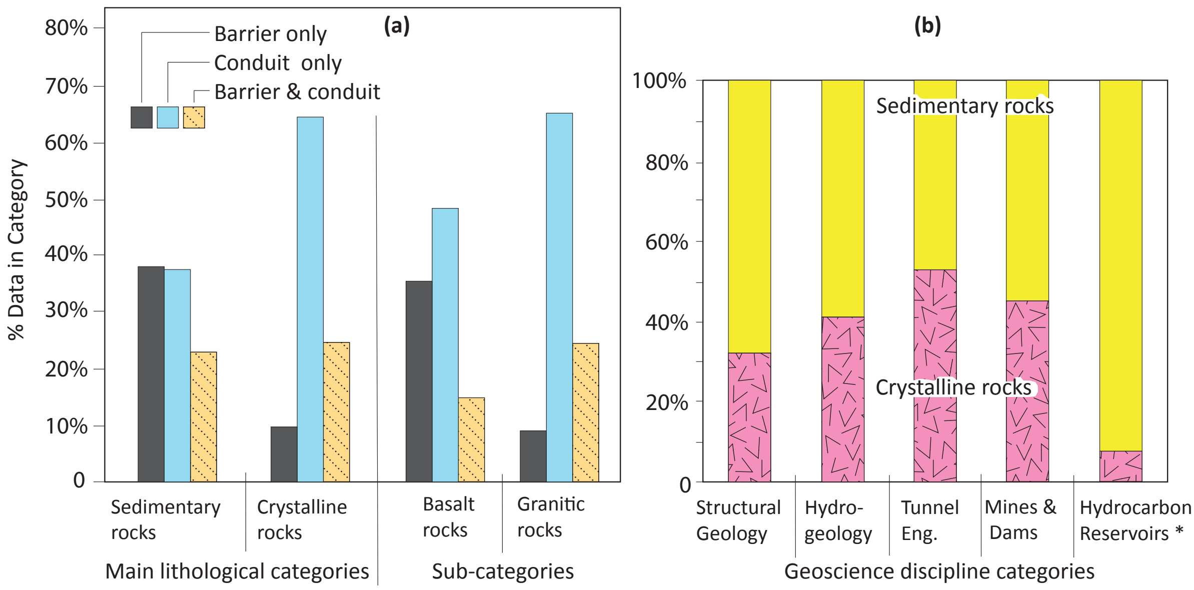

Figure 4-4 Comparing the (a) histograms of fault zone simplified permeability structures by lithology categories, and, (b) proportion of sample sites that have the dominant lithology in sedimentary or crystalline rocks in subsets of data by geoscience discipline.

4.6.4 Hypothesis 4 test (as in Hypothesis 2 but for sedimentary and crystalline rocks separately)

In the crystalline rocks (Figure 4-5a), there are significant differences between the geoscience disciplines ($\chi^2 = 37$, p = $9\text{x}10^{-8}$, see Table 4-5). There are 29% of barrier-only faults inferred in structural geology studies compared to only 5% to 6% in hydrogeology and tunnelling. Conduit-only faults dominate in hydrogeology (80%). The total count of any conduit fault is high in all geoscience disciplines (>70%) but is the highest in hydrogeology and tunnelling (95%). In the sedimentary rocks (Figure 4-5b), there are no significant differences between the counts of fault barriers and conduits in structural geology and hydrogeology ($\chi^2 = 1.6$, p = 0.18). There are about 30% and 37% for conduits and 47% to 40% for barriers.

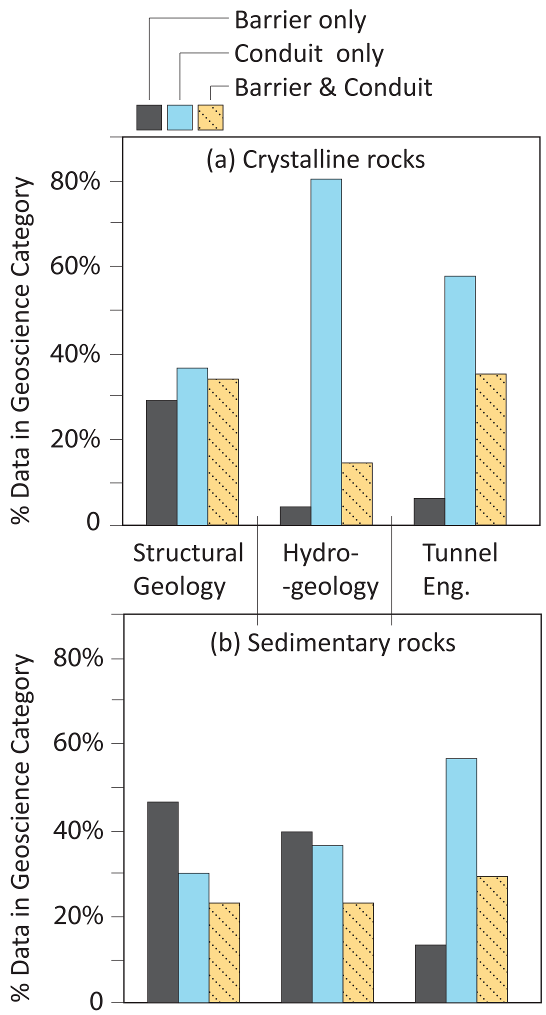

Figure 4-5 Comparing the proportions of barrier, conduit and barrier-conduit faults in the main lithological categories: (a) crystalline rocks, (b) sedimentary rocks.

Table 4-5 Comparing the frequencies of occurrence of permeability structures for three geoscience disciplines (Structural Geology, Hydrogeology, Tunnel Engineering) separately for the crystalline rocks (metamorphic and igneous), and for the sedimentary rocks.

(a) Crystalline rocks (metamorphic & igneous)						(b) Sedimentary rocks				
	Barrier	Conduit	Barrier & Conduit	Total	% Conduit	Barrier	Conduit	Barrier & Conduit	Total	% Conduit
Structural Geology										
	12	15	14	41		44	28	22	94	
	29%	37%	34%		71%	47%	30%	23%		53%
Hydrogeology										
	5	86	16	107		66	61	39	166	
	5%	80%	15%		95%	40%	37%	23%		60%
Tunneling										
	4	36	22	62		6	25	13	44	
	6%	58%	35%		94%	14%	57%	30%		86%

Tunnelling counts show the largest differences from expected frequencies, favoring more conduits (57%), but we have low counts (6 in barrier category) for tunnelling category in sedimentary rocks and this difference should be viewed with caution. We used a representative or "average" conceptual model for each site, including tunnels, thus the in-tunnel statistics of how many faults are crossed and how many caused water inflows are not included in the global statistics up to this point. Overall, the total percentage of fault conduits (any conduits) in sedimentary rocks is about 50 to 60% in the two most studied geoscience disciplines.

4.6.5 Estimating the proportion of fault conduits from long transportation tunnels

Faults have been known to be the dominant water inflow points in most tunnels (e.g. Goodman 1987) and numerous papers were published already about the statistics of fault properties in tunnels (Masset and Loew 2010, 2013). Faults crossed by tunnels can be complex structures with multiple fault cores (e.g. Lutzenkirchen 2002, Fasching and Vanek 2013). Here we use the published inflow summaries from 30 long transportation tunnels to provide another estimate of the relative occurrence of fault zone conduits (Table 4-6). The percentage of conduit faults was estimated relative to the total number of "major" fault zones (or groups of faults forming fault zones) crossed by the tunnel, taken from published tunnel-geologic cross-sections that also showed water inflow points. There was no information about fault barriers in most of these reports and we did not count them. We also note that a lack of reported inflow while crossing a fault zone does not imply that it is a barrier because the fault may be of the same bulk permeability as the host rock and may be heterogeneous. Up to this point we presented the global statistics of conduits and barriers that had no spatial component (no length or area) because all samples were reduced to simple counts within categories. However, in the tunnel data, there is a spatial-component because the inflow points occur along the length of the tunnel and at some depth. The data here is simplified to show the average depth of the tunnel.

Table 4-6 Summary of proportions (%) of fault conduits relative to the total number of major fault zones crossed in tunnels and drilled at research sites. Lithology listed in order of % occurrence in tunnel: G=granitic, GN=gneiss, S=sedimentary, S-L=limestone, M-S=metasedimentary, VS=volcanic sediments, tuffs, VB=basalt, andesite, VD=intrusive dikes.

Tunnels mainly in sedimentary and volcanic rocks

Tunnel name and location	Conduit (%)	Depth, m (avg., max)	Litho-logy	Method	References
Lotschberg, Switzerland	50%	600-1000	S(L)	brittle faults 50% inflows within the limestones	Pasendorfer and Loew 2010
Gran Sasso, Italy	40-50%	800 (1300)	S(L)	~4 of 9 faults along tunnel show inflows; major inflows from 2 fault zones (4 faults)	Boutitie and Lunardi 1975, Lunardi 1982, Celico *et al.* 2005
Hida, Japan	45%	750 (1000)	VS,VB,GN	3 of 7 major fault zones with inflows	Terada *et al.* 2008, Abe *et al.* 2002
la Línea, Colombia	40-55%	500 (800)	S, VS,VB,G	~ 13 of 23 faults are near inflow points	Suencun Casallas 2015
Syuehshan & Ping Lin, Taiwan	<85%	400 (700)	S	5 of 6 major normal faults were associated with poor tunneling conditions and water inflows	Chiu and Chia 2012, Tseng *et al.* 2001
Vaglia-Firenzuola-Raticosa, Italy	60-100%	300 (500)	S	tunnel inflows and isotope study (~13 of 22 fault clusters had inflows), impacts on springs & wells	Vincenzi *et al.* 2014, Ranfangni *et al.* 2015
Harold D.Roberts (W. part), USA	50%	150 (300)	S	~9 of 19 fault zones had inflows (counting groups of faults on cross-sections)	Wahlstrom and Hornback 1962
Lunner, and Skaugum, Norway	20-35%	100 (230)	S, VS, VD	Lunner: 2 of 6 fault zones had inflows; Skaugum: inflows mostly at lithological contacts, igneous dikes (1 of 5 "weakness zones" had large inflow)	Holmøy 2008, Holmøy and Nilsen 2013
Karahnjukar, Iceland	>40%	200	VB	2 of 5 faults with water inflow	Kroyer *et al.* 2007
Seikan, Japan	45%	100	S, VB, VS	4 of 9 major fault zones (>5 m^3/min inflow)	Hashimoto and Tanabe 1986
Tseung Kwan O Bay C, Hong Kong	70%	50	S	7 of 10 fault zones had water inflow contributions	GovHK 2007, McLearie *et al.* 2001
Tuzla, and Bolu, Turkey	25-45%	<100 (200)	S, G	Tuzla: 7 of 15 had "excessive water inflow", Bolu: 3 of ~12 had inflow (1 of 3 thrust structures)	Dalgic 2002, 2003

(Table 6) Tunnels mainly in gneiss and granite

Tunnel name and location	Conduit (%)	Depth, m (avg., max)	Lithology	Method	References
Gothard, Switzerland	70-76%	1200 (2000)	GN	# fault zones with hydraulic conductivity > mean ($6x10^{-9}$ m/s), suggesting a conduit	Masset and Loew 2013
23 tunnels, Switzerland	majority	800-1000	GN	statistical study: majority of inflow points from brittle overprint of existing brittle-ductile faults	Masset and Loew 2010, Lützenkirchen 2002
Mt.Blanc, France	>45%	1500 (2500)	G, S	> 9 of 20 fracture groups had inflows	Maréchal 1998
Ena (Enasan), Japan	35-85%	500 (1000)	G, V, GN	%86 inflows in 22 fault zones (37% > 1 m^3/min)	Yano *et al.* 1978
Aica-Mules, Austria	50-100%	800 (1200)	G, M	~100% faults with water inflow, ~50% large inflow	Perello *et al*. 2014
Manapouri, New Zealand	~80%	700 (1200)	G, M	~9 of 11 fault zone groups	Upton and Sutherland 2014
Višňové, Slovakia	65-75%	400 (600)	G, S	"significant" inflows were at 7 of 9 major faults (>25 smaller faults had 16 inflows)	Ondrášik *et al.* 2015
Cleuson-Dixence D, Switzerland	40%	250 (500)	GN, M-S,S	reports of grouting or inflow at 2 of 5 faults crossed; most were dry and clay-filled	Buergi 1999
Arrowhead E., USA	90-95%	200 (335)	G, GN	~18 of 19 fault zones crossed had inflows and required grouting; impacts on springs and wells	Bearmar 2012
H.D.Roberts (E part), USA	90%	210 (300)	GN	~12 fault zones with inflows, groups of faults	Wahlstrom and Hornback 1962
Rokko, and Hokuriku Japan	60-65%	150 (400)	G, VB	Rokko: inflow from 3 of 5 faults (post-earthquake); Hokuriku: 65% fault zones with inflow > 1 m^3/min	Asakura *et al.* 1998, Masuda and Oishi 2000, Takahashi 1965, Yoshikawa and Asakura 1981
Tseung Kwan O Bay E, Hong Kong	40-50%	120 (200)	G	~2 of 5 major fault zones with large inflows, ~8 of 17 individual faults	GovHK 2007
Taining, China	>70%	~150 (500)	G	> 5 of 7 fault and fracture zones had high inflows	Zhang *et al.* 2014
Romeriksporten, Norway	<60%	100 (200)	GN-G	8 of 10 leakages near faults in Lutvann (lake) area; whole tunnel 4-8 of 13 weakness zones with water	Holmøy 2008, Holmøy and Nilsen 2013
Frøya, Norway	50-65%	100 (120) sub-sea	GN-G	6 of 12 fault zones with inflows, 7 of 12 non-conducting faults in sub-sea section 4000-5600	Holmøy 2008, Holmøy and Nilsen 2013
Storsand, Norway	30%	125 (160)	GN-G	2 of 5 leakage zones in pre-drilling near faults	Holmøy 2008, Holmøy and Nilsen 2013
Hvaler, Norway	30-60%	75 (120) sub-sea	GN, G	~5 of 13 clusters of inflow points (16 pre-tunneling study found 16 fault zones	Banks *et al.* 1992, 1994
MWRA, USA	50-70%	70	M-S, G,VB	19 inflow zones correspond with 13 mapped lineament zones (68%), others do not	Mabee *et al.* 2002
Namtall, Sweden	50%	25 to 150	M-S, G	~5 of 10 fault zones with inflow, Lugeon tests	Stille and Gustafson 2010

(Table 6) Research sites in gneiss rocks

Tunnel name and location	Conduit (%)	Depth, m (avg., max)	Litho-logy	Method	References
Nagra 6 scientific drillholes, Switzerland	~45%	100-1600*	GN	faults are dominant permeable elements (43%); *depth below top of crystalline rock	Mazurek et al. 2000, Mazurek 1998, Thury *et al.* 1994
Gideå, and Fjällveden, Sweden	30-45%	200 (600)	GN	2 of 7 at Gidea, 4 of 9 at Fjällveden	Ahlbom *et al.* 1983, 1991
Äspö, Sweden	60%	400 (1000)	GN	# permeable major water conductive features	Bossart et al. 2001, Ahlbom and Smelie 1991
Forsmark site and tunnel, Sweden	75%	400 (900)	GN	65 flowing zones of 85 in boreholes (48 different deformation zones); in tunnel 4 of 4 with inflow	Carlsson and Christianson 2007, Follin and Stigsson 2014

4.7 Discussion

4.7.1 Biases in observing the fault zone permeability structure

The difference in observed frequencies of inferred fault permeability structures among the geoscience disciplines is partly explained by the choice of preferred test methods for each discipline. Alternatively, if the study sites are not randomly sampling fault properties in the Earth's upper brittle crust, the differences may be attributed to lithological, tectonic, and depth conditions. The differences between other geoscience disciplines occur partly because of geological conditions, and here we argue that it is also partly caused by biases in observation methods employed.

At outcrop studies of analogs of faulted hydrocarbon reservoirs, the matrix permeability tests and fracture mapping suggest a balanced barrier-conduit model because the fault core can be tested effectively at that scale ("Drill core & outcrop samples" category in Figure 4-2). The faults are heterogeneous and it is difficult to assign only one simple category of the permeability structure to describe the hydraulic behavior (Shipton et al. 2002). In-situ hydraulic tests are difficult in heterogeneous fault zones because of problems with separating the test intervals, difficulties of in-situ testing the narrow fault cores, and interpreting the results (Karasaki et al. 2008). In hydrogeological studies, at depths less than 1km below the top of the crystalline rock at research sites a large proportion of brittle faults are seen as conduits (e.g. Bossart et al. 2001, Geier et al. 2012, Stevenson et al. 1996, Stober and Bucher 2007), although some of the drillhole data may not be representative of the faults tested because of heterogeneity and channelling of fracture networks. Increasing the number of drillholes does help, such as at dam foundation investigations utilizing pre-grouting injection tests (Barani et al. 2004, Kawagoe and Osada 2005), except that at shallow depths the fault rocks and fractures related to damage zones exist in highly permeable and heterogeneous fractured media of the protolith. The conduit effects of faults may only appear after geostatistical analysis (Nakaya et al. 2002). In large underground mines counting the fault conduits over areas of a few square kilometers is also problematic. Recent statistical studies of large underground mines in Germany suggest a complex relationship of permeability of fault cores and damage zones at intersecting faults in three dimensional space (Achtziger-Zupancic et al. 2015 & Personal Communication) and is best shown statistically. In such cases it is not clear how to count the fault conduits and barriers. Is there an average permeability structure of a large site containing many faults and at what scale do the fault zones need to be tested and counted to provide useful representative hydraulic properties for site and regional models?

The proportion of barrier fault zones is more uncertain in this study than of the conduits because barriers are more difficult to detect with hydraulic tests. For large-scale characterization, observing the "barrier" nature of fault zones requires completely different methods than those for "conduits". In hydrogeological studies, groundwater aquifer compartmentalization is common in faulted sedimentary rocks (e.g. Mohamed and Worden 2006, Bense et al. 2013) and in crystalline rocks (e.g. Benedek et al. 2009, Takeuchi et al. 2013). While the presence of compartmentalization can be detected through cross-fault tests or observations of natural hydraulic or thermal gradients (Bense *et al*. 2013), typical hydraulic tests in boreholes rely heavily on interpretation of distant fault flow boundaries (e.g. Stober and Bucher 2007). The barrier effect is easily seen in some cases of large excavations around dams (Li and Han 2004) and open pit mines (McKelvey et al. 2002). It has been known for decades in tunnel engineering that during tunnel excavation, the barrier-conduit nature of faults may be recognized when a fault gouge “membrane” is penetrated when tunneling from the low-pressure side of a barrier, and sudden inflow to tunnel occurs (Henderson 1939, Brekke and Howard, 1972, Fujita 1978). In the large number of papers and reports reviewed, the majority of the cases described in geotechnical and engineering papers describe geotechnical instabilities of faults rather than water problems, although is some cases those occur at the same place. Therefore, we can qualitatively infer that there may exist a large proportion of barrier faults in the crust that are were not counted in this study as barriers.

4.7.2 Estimating the proportion of faults that are conduits

The proportion of fault zones that are permeable conduits to groundwater flow was estimated using two methods: counts of fault conduits at study sites (proportion is relative to total number of sites considered), and counts of fault conduits along long tunnels (the proportion is relative to the total number of major fault zones crossed in a tunnel).

From tunnelling data in the crystalline rocks the proportion of fault conduits varies from about 40% to more than 90%, with a median proportion of about 60% (Figure 4-6a). In tunnels excavated in sedimentary rocks there is a suggestion that the proportion of fault conduits is less than in the crystalline rocks (about 30% to 80%, and a median of about 50%). The large research sites where multiple faults were drilled and tested show proportion of conductive faults between 40% and 75%. A depth trend may exist in the crystalline rocks of increasing proportion of fault conduits, at least to about a 1km depth, but there is not enough data and too much uncertainty to test this quantitatively at this time, in our opinion, although it presents an interesting topic of research.

From the global counts of whole "sites" in the five geoscience disciplines we estimated that there were 70% fault conduits of any type. Figure 4-6b shows graphically that our simple categories may contain a range of different fault zone architectural styles as defined in Caine et al. (1996), and this study aggregates all types of conduits and all types of barriers, as long as that hydraulic behavior is observed. In tunnels water inflow will occur whether a fault is a "conduit only" or a "barrier-conduit", as long as it is a permeable conduit in the protolith, therefore the tunnel and global site data are comparable.

There are limitations and uncertainties in the tunnel data. Tunnels are grouted during construction to control in permeable zones to control the groundwater inflows, thus the inflow rates after completion may be much smaller than during construction. However, grout volumes have been shown to correlate with individual fault permeability structures (Ganerød et al. 2008) and reports of tunnels inflows and grouting are also correlated at most studies we reviewed. The weathering of fault zones may occur to depths greater than 100m and effectively seal the fault with clays. For example in northern Europe the faults are affected by paleo-weathering (Migoń & Lidmar-Bergström 2001) and this is thought to cause a reduction of fault permeability to such an extent that the fault conduit may not exist or may not be noticed during tunneling, for example in fjord-crossing sub-sea tunnels in Norway (Holmøy and Nilsen 2008, Nilsen 2012). Inflow rates are also controlled by boundary conditions and type of surficial materials (Cesano 2000), and the depth of tunnel below the water table. "Dry" faults may still be conduits but not be noticed during tunneling. Inflows may be erroneously attributed to fault zones in the crystalline rocks because about 50% of permeable conduits are reported by various authors to be outside of fault zones (Nilsen 2012, Masset and Loew 2010, 2013). These can include intrusive dikes and other permeable elements (Thury et al. 1997, Font-Capo et al. 2012, Mayer et al. 2014). Our guess is that the conduit proportions for each tunnel could be 10% higher or lower on the scale plotted in Figure 4-6a. Despite these limitations, these quantities provide useful insight into the hydrogeology of fault zones, although in a highly simplified presentation.

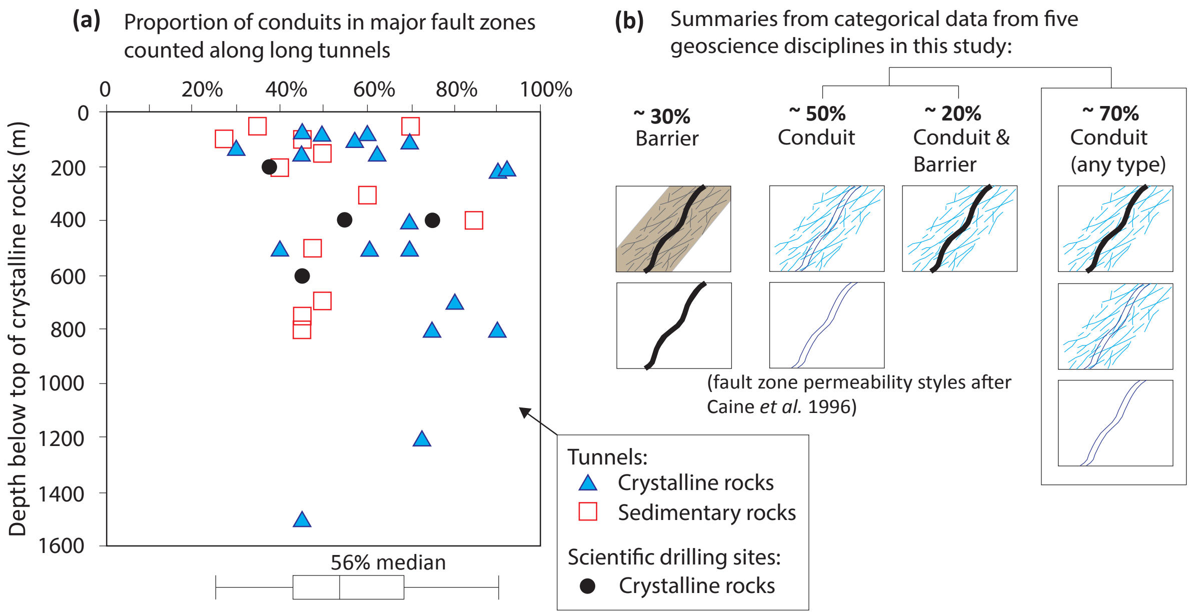

Figure 4-6 Global proportions and trends with depth of conduits in major fault zones (a) counted along long tunnels and representing several large research sites (Table 6 data summary), and, (b) estimates based on the global database of fault zone study sites from five geoscience disciplines (Table 1) and graphical description of fault zone permeability structural styles (Caine et al. 1996) included in our simplified categories.

4.8 References

The references for this paper are listed alphabetically.

Abe Y, Yasue K, Hara I (2002) Analysis of geological profile along the Hida Tunnel, Central Japan (1) — profiles for various formal fabric elements. Oyo technical report 22, 13–40

Achtziger-Zupancic P, Loew S, Hiller A, Mariéthoz G (2015) Fluid Flow and Fault Zone Damage in Crystalline Basement Rocks (Ore Mountains Saxony). AGU Fall Meeting, Abstract H12A-03, December 14-18, 2015, San Francisco

Agresti A (2002) Categorical data analysis, 2nd edition. John Wiley & Sons Inc. Published online 26 Mar 2003

Ahlbom K, L Carlsson, LE Carfsten, O Duran, N-Å Larsson, O Olsson (1983) Evaluation of the geological, geophysical and hydrogeological conditions at Fjällveden. SKBF/KBS.

Ahlbom K, Andersson J-E, Nordqvist R, Ljunggren C, Tiren S, Voss C (1991) Gidea study site. Scope of activities and main results. SKB Technical Report 91-51, Swedish Nuclear Fuel and Waste Management CO, Stockholm

Ahlbom K, Smelie J (1991) Overview of the Fracture Zone Project at Finnsjon, Sweden. *Journal of Hydrology*, 126, 1–15

Antonellini M, Aydin A (1994) Effect of faulting on fluid flow in porous sandstones: petrophysical properties. *AAPG Bulletin*, 78 (3), 355–377

Asakura T, Tsukada K, Matsunaga T, Matsuoka S, Yashiro K, Shiba Y, Oya T (1998) Damage to mountain tunnels by earthquake and its mechanism. Doboku Gakkai Ronbunshu, 20(659), 27-38 (in Japanese). English version accessed April 2016 at: https://www.pacific.co.jp/service/tech/thesis/risk/pdf/risk_12.pdf

Aydin A (2000) Fractures, faults, and hydrocarbon entrapment, migration and flow. *Marine and Petroleum Geology*, 17, 797–814

Balsamo F, Storti F (2010) Grain size and permeability evolution of soft-sediment extensional sub-seismic and seismic fault zones in high-porosity sediments from the Crotone basin, southern Apennines, Italy. *Marine and Petroleum Geology*, 27, 822–837

Banks D, Solbjorg ML, Rohr-Torp E (1992) Permeability of fracture zones in a Precambrian granite. *Quarterly Journal of Engineering Geology*, 25, 377–388

Banks D, Rohr-Torp E, Skarphagen H (1994) Groundwater resources in hard rock; experiences from the Hvaler study, southeastern Norway. *Applied Hydrogeology,* 94, 33–42

Barani HR, Lashkaripour G, Ghafoori M (2014) Predictive permeability model of faults in crystalline rocks; verification by joint hydraulic factor (JH) obtained from water pressure tests. *Journal of Earth System Science*, 123(6), 1325–1334

Bearmar M (2012) Arrowhead Tunnels project special uses permit geo-sciences specialist report geotechnical- geology-hydrogeology, September 2012. US Forest Service, San Bernardino, CA

Benedek K, Bőthi Z, Mező G, Molnár P (2009) Compartmented flow at the Bátaapáti site in Hungary. *Hydrogeology Journal*, 17, 1219–1232

Bense VF, Gleeson T, Loveless SE, Bour O, Scibek J (2013) Fault zone hydrogeology. *Earth-Science Reviews*, 127, 171–192

Bjornsson G, Bodvarsson G (1990) A survey of geothermal reservoir properties. *Geothermics*, 19(1), 17–27

Bossart P, Hermanson J, Mazurek M (2001) Äspö Hard Rock Laboratory Analysis of fracture networks based on the integration of structural and hydrogeological observations on different scales. SKB Technical Report TR-01-21, Swedish Nuclear Fuel and Waste Management Co, Stockholm, Sweden

Boutitie J, Lunardi P (1975) Tunnel autoroutier du Gran Sasso. Traversee de la faille de la Valle Freda. TRAVAUX. Revue Mensuelle No 482, Mai 1975

Brekke TL, Howard TR (1972) Functional classification of gouge materials from seams and faults in relation to stability problems in underground openings. Annual technical report 1971-1972, University of California, Berkeley, AD740807

Brogi A (2008) Fault zone architecture and permeability features in siliceous sedimentary rocks: Insights from the Rapolano geothermal area (Northern Apennines, Italy). *Journal of Structural Geology*, 30, 237–256

Buergi C (1999) Cataclastic fault rocks in underground excavations - a geological characterisation. PhD thesis No 1975, Ecole Polytechinique Federale de Lausanne, Switzerland

Caine JS, Evans JP, Foster CB (1996) Fault zone architecture and permeability structure.

Geology, 24, 1025–1028

Caine JS, Forster CB (1999) Fault zone architecture and fluid flow: insights from field data and numerical modeling. faults and subsurface fluid flow in the shallow crust, AGU Geophysical Monograph 113

Carlsson A, Christianson R (2007) Construction experiences from underground works at Forsmark, Compilation Report. SKB Report R-07-10, Swedish Nuclear Fuel and Waste Management Co., Stockholm

Celico P, Fabbrocino S, Petitta M, Tallini M (2005) Hydrogeological impact of the Gran Sasso motor-way tunnels (Central Italy). *Giornale di Geologia Applicata,* 1, 157–165

Cesano D, Olofsson B, Bagtzoglou AC (2000) Parameters regulating groundwater inflows into hard rock tunnels: a statistical study of the Bolmen Tunnel in Southern Sweden. *Tunneling and Underground Space Technology*, 15, 153–165

Chen X, Shearer PM, Abercrombie RE (2012) Spatial migration of earthquakes within seismic clusters in Southern California: Evidence for fluid diffusion. *Journal of Geophysical Research*, 117, B04301

Chiu Y-C, Chia Y (2012) The impact of groundwater discharge to the Hsueh-Shan tunnel on the water resources in northern Taiwan. *Hydrogeology Journal*, 20(8), 1599–1611

Cochran WG (1952) The $\chi 2$ test of goodness of fit. *Annals of Mathematical Statistics*, 25, 315–345

Dalgic S (2002) Tunneling in squeezing rock, the Bolu tunnel, Anatolian Motorway, Turkey. *Engineering Geology*, 67, 73–96

Dalgic S (2003) Tunneling in fault zones, Tuzla tunnel, Turkey. *Tunnelling and Underground Space Technology,* 18, 453–465

Delucchi KL (1983) The use and misuse of chi-square: Lewis and Burke revisited. *Psychological Bulletin*, 94 (1), 166–176

Dickerson RP (2000) Hydrologic characteristics of faults at Yucca Mountain, Nevada. Office of Scientific and Technical Information, Oak Ridge, TN, Technical Report, INIS-US--0629, OSTI ID: 860273

El Hariri M, Abercrombie RE, Rowe CA, do Nascimento AF (2010) The role of fluids in triggering earthquakes: observations from reservoir induced seismicity in Brazil.

Geophysical Journal International, 1-9

Fasching F, Vanek R (2013) Characterization and classification of fault zones. Austrian Society for Geomechanics Workshops "Characterization of Fault Zones", 9 Oct 2013, Salzburg, Austria

Faulds JE, Hinz NH (2015) Favorable tectonic and structural settings of geothermal systems in the Great Basin region, western USA: proxies for discovering blind geothermal systems. Proceedings World Geothermal Congress 2015, Melbourne, Australia

Faulkner DR, Jackson CAL, Lunn RJ, Schlische RW, Shipton ZK, Wibberley CAJ, Withjack MO (2010) A review of recent developments concerning the structure, mechanics and fluid flow properties of fault zones. *Journal of Structural Geology*, 32, 1557–1575

Follin S, Stigsson M (2014) A transmissivity model for deformation zones in fractured crystalline rock and its possible correlation to in situ stress at the proposed high-level nuclear waste repository site at Forsmark, Sweden. *Hydrogeology Journal*, 22, 299–311

Font-Capo J, Vazues-Sune E, Carrera J, Herms I (2012) Groundwater characterization of a heterogeneous granitic rock massif for shallow tunneling. *Geologica Acta*, 10(4), 395–408

Fujita K, Ueda K, Gomi M (1978) Excavation of tunnel through fractured zone with large quantity and high head of ground water. In: Tunneling Under Difficult Conditions. Kitamura (ed.) Proceedings of the International Tunnel Symposium, Tokyo. Pergamon Press

Ganerød GV, Braathen A, Wilemoes-Wissing B (2008) Predictive permeability model of extensional faults in crystalline and metamorphic rocks; verification by pre-grouting in two sub-sea tunnels, Norway. *Journal of Structural Geology*, 30, 993–1004

Gartrell A, Zhang Y, Lisk M, Dewhurst D (2004) Fault intersections as critical hydrocarbon leakage zones: integrated field study and numerical modelling of an example from the Timor Sea, Australia. *Marine and Petroleum Geology*, 21, 1165–1179

Geier J, Bath A, Stephansson O (2012) Comparison of site descriptive models for Olkiluoto, Finland and Forsmark, Sweden. Säteilyturvakeskus [Radiation and Nuclear Safety Authority], Helsinki, Finland. Report STUK-TR 14, 64 pp.

Glass GV (1976) Primary, secondary, and meta-analysis of research. *Educational Researcher*, 5(10), 3–8

GovHK (2007) Engineering Geological Practice in Hong Kong. GEO Publication No.

1/2007. 278p. Government of Hong Kong, Geotechnical Engineering Office. [Accessed Apr 2016: http://www.cedd.gov.hk/eng/publications/geo/geo_p107.html]

Gupta HK (2002) A review of recent studies of triggered earthquakes by artificial water reservoirs with special emphasis on earthquakes in Koyna, India. *Earth Science Reviews*, 58, 279–310

Hanano M, Kajiwara T (1999) Permeability associated with natural convection in the Kakkonda geothermal reservoir. *Geothermal Resources Council Transactions*, 23, 7–20

Hashlmoto K, Tanabe Y (1986) Construction of the Seikan Undersea Tunnel. Execution of the most difficult sections. *Tunnelling and Underground Space Technology*, 1(3/4), 373–379

Henderson LH (1939) Detailed Geological Mapping and Fault Studies of the San Jacinto Tunnel Line and Vicinity. The Journal of Geology, 47(3), 314–324. The University of Chicago Press

Hennings P, Allwardt P, Paul P, Zahm C, Reid Jr R, Alley H, Kirschner R, Lee B, Hough E (2012) Relationship between fractures, fault zones, stress, and reservoir productivity in the Suban gas field, Sumatra, Indonesia. *AAPG Bulletin*, 96(4), 753–772.

Holmøy KH , Nilsen B (2013) Significance of geological parameters for predicting water inflow in hard rock tunnels. *Rock Mechanics and Rock Engineering*, 47, 853–868

Holmøy KH (2008) Significance of geological parameters for predicting water leakage in hard rock tunnels. Doctoral Theses at NTNU, 2008:291, Norwegian University of Science and Technology

Howell D (2011) Chi-square test: analysis of contingency tables. In: Lovric M (ed.) International encyclopedia of statistical science. 1st ed. Springer, 250–252

Jolley SJ, Fisher QJ, Ainsworth RB, Vrolijk PJ, Delisle S (eds.) (2010) Reservoir compartmentalization. *Geological Society Special Publication,* 347, The Geological Society, London

Juhlin C, Sandstedt H (1989) Storage of nuclear waste in very deep boreholes: Feasibility study and assessment of economic potential. SKB Technical Report 89–39. Swedish Nuclear Fuel And Waste Management Co.

Karasaki K, Onishi T, Wu Y-S (2008) Development of hydrologic characterization technology of fault zones. Lawrence Berkeley National Laboratory, NUMO-LBNL

Collaborative research project report (in English and Japanese), 157p.

Kawagoe T, Osada M (2005) Characterization of hydrogeologic structure in a dam-site with developed fracture system (No.1). Koyama dam site. Study P.48. Japan Engineering Geology Society, October 2005, 137–140 (original in Japanese)

Kroyer J, Leist B, Evers H, Leech WD (2007) Kárahnjúkar Hydroelectric Project, Iceland. Extreme underground construction. In: Traylor and Townsend (eds.), Proceedings of 2007 Rapid Excavation and Tunneling Conference, SME

La Poite PR (2000) Predicting hydrology of fractured rock masses from geology. In: Dynamics of Fluids in Fractured Rock, Faybishenko B, Witherspoon PA, Benson SM (eds). AGU Geophysical Monograph 122, Washington D.C.

Lewis D, Burke CJ (1949) The use and misuse of the chi-square test. *Psychological Bulletin*, 46(6), 433–489

Li G, Han Z (2004) Principal engineering geological problems in the Shisanling pumped storage power station, China. *Engineering Geology*, 76, 165–176.

Liotta D, Ruggieri G, Brogi A, Fulignati P, Dini A, Nardini I (2010) Migration of geothermal fluids in extensional terrains: the ore deposits of the Boccheggiano-Montieri area (southern Tuscany, Italy. *International Journal of Earth Sciences (Geol Rundsch)*, 99, 623–644

Lunardi P (1982) The burst of a wall in a highway tunnel during construction. *Rock Mechanics, Suppl*., 12, 191–206

Lutzenkirchen VH (2002) Structural geology and hydrogeology of brittle fault zones in the central and eastern Gotthard Massif, Switzerland. PhD Thesis No. 14749, ETHZ, Zurich

Mabee SB, Curry PJ, Hardcastle KC (2002) Correlation of lineaments to ground water inflows in a bedrock tunnel. *Groundwater*, 40(1), 37–43

Magri F, Akar T, Gemici U, Pekdeger A (2010) Deep geothermal groundwater flow in the Seferihisar–Balcova area, Turkey: results from transient numerical simulations of coupled fluid flow and heat transport processes. *Geofluids*, 10, 388–405

Maréchal J-C (1998) Les criculations d'eau dans les massifs cristallins alpins et leurs relations avec les auvrages suterrains. These No 1769, École Polytechnique Fédérale de Lusanne, France

Masset O, Loew S (2010) Hydraulic conductivity distribution in crystalline rocks, derived from inflows to tunnels and galleries in the central Alps. *Switzerland Hydrogeology Journal*, 18(4), 863–891

Masset O, Loew S (2013) Quantitative hydraulic analysis of pre-drillings and inflows to the Gotthard Base Tunnel (Sedrun Lot, Switzerland). *Engineering Geology*, 164, 50–66

Masuda S, Oishi A (2000) Simulation of groundwater inflow into mountain tunnel. *Journal of the Japan Society of Engineering Geology,* 41(3), 126–134

Matonti C, Lamarche J, Guglielmi Y, Marie L (2012) Structural and petrophysical characterization of mixed conduit/seal fault zones in carbonates: Example from the Castellas fault (SE France). *Journal of Structural Geology*, 39, 103–121

Mayer JM, Allen DM, Gibson HD, Mackie DC (2014) Application of statistical approaches to analyze geological, geotechnical and hydrogeological data at a fractured-rock mine site in northern Canada. *Hydrogeology Journal*, 22, 1707–1723

Mazurek M, Gautschi A, Smith PA, Zuidema P (2000) The role of water conducting features in the swiss concept for the disposal of high-level radioactive waste. In Stober and Bucher (eds.), Hydrogeology of Crystalline Rocks, Water Science and Technology Library, Vol. 34, 105–125

Mazurek M (1998) Geology of the crystalline basement of northern Switzerland and derivation of geological input data for safety assessment models, Nagra Technical Report NTB 93-12. Nagra, Wettingen, Switzerland

McKelvey P, Beale G, Taylor A, Mansell S, Mira B, Valdivia C, Hitchcock W (2002) Depressurization of the north wall at the Escondida copper mine, Chile. In: Younger PL, Robins NS (eds.) Mine water hydrology and geochemistry. *Geological Society of London Special Publication* 198, 107–119

McLearie DD, Foreman W, Hansmire WH, Tong EKH (2001) Hong Kong strategic sewage disposal scheme stage I deep tunnels. Proceedings RETC conference, Chapter 40, 487–498

Migoń P, Lidmar-Bergström K (2001) Weathering mantles and their significance for geomorphological evolution of central and northen Europe since the Mesozoic. Earth Science Reviews, 56, 285–324

Mitchell TM, Faulkner DR (2012) Towards quantifying the matrix permeability of fault damage zones in low porosity rocks. *Earth and Planetary Science Letters*, 339-340, 24–31

Mohamed EA, Worden RH (2006) Groundwater compartmentalisation: a water table height and geochemical analysis of the structural controls on the subdivision of a major aquifer, the Sherwood Sandstone, Merseyside, UK. *Hydrology and Earth System Sciences*, 10, 49–64

Muraoka H, Sakaguchi K, Nakao S, Kimbara K (2006) Discharge temperature–discharge rate correlation of Japanese hot springs driven by buoyancy and its application to permeability mapping. *Geophysical Research Letters*, 33, L10405

Nakaya S, Taiyoh Yohmei T, Koike A, Hirayama T, Yoden T, Nishigaki M (2002) Determination of anisotropy of spatial correlation structure in a three-dimensional permeability field accompanied by shallow faults. *Water Resources Research*, 38(8), 1160

Nilsen B (2012) Characteristics of water Ingress in Norwegian subsea tunnels. *Rock Mechanics and Rock Engineering*, 47(3), 933–945

O'Sullivan MJ, Pruess K, Lippmann MJ (2001) State of the art of geothermal reservoir simulation. *Geothermics*, 30, 395–429

Okada T, Matsuzawa T, Umino N, Yoshida K, Hasegawa A, Takahashi H, Yamada T, Kosuga M, Takeda T, Kato A, Igarashi T, Obara K, Sakai S, Saiga A, Iidaka T, Iwasaki T, Hirata N, Tsumura N, Yamanaka Y, Terakawa T, Nakamichi H, Okuda T, Horikawa S, Katao H, Miura T, Kubo A, Matsushima T, Goto K, Miyamachi H (2015) Hypocenter migration and crustal seismic velocity distribution observed for the inland earthquake swarms induced by the 2011 Tohoku-Oki earthquake in NE Japan: implications for crustal fluid distribution and crustal permeability. *Geofluids*, 15, 293–309

Okubo, CH (2012) Spatial distribution of damage around faults in the Joe Lott Tuff Member of the Mount Belknap Volcanics, Utah: A mechanical analog for faulting in pyroclastic deposits on Mars. *Journal of Geophysical Research*, 117, E08003

Ondrášik R, Matejček A, Durmeková T (2015) experience from investigation of tectonically extremely deteriorated rock mass for the highway tunnel Višňové, Slovakia. In: G. Lollino et al. (eds.), Engineering Geology for Society and Territory – Volume 6, Applied Geology for Major Engineering Projects, Chapter 168, 927-930. Springer

Passendorfer M, Loew S (2010) Subsurface exploration and transient pressure testing from a deep tunnel in fractured and karstified limestones (Lotschberg Base Tunnel, Switzerland*)*. *International Journal of Rock Mechanics and Mining Sciences*, 47, 121–137

Pearson K (1900) On the criterion that a given system of deviations from the probable in the case of a correlated system of variables is such that it can be reasonably supposed to have arisen from random sampling. *Philos. Mag. Series* 5, 50, 157–172

Perello P, Baletto A, Burger U, Skut S (2014) Excavation of the Aica-Mules pilot tunnel for the Brenner base tunnel: information gained on water inflows in tunnels in granitic massifs. *Rock Mechanics and Rock Engineering*, 47, 1049–1071

Petford N, McCaffrey KJW (2003) Hydrocarbons in Crystalline Rocks. Geological Society Special Publication 214

Ranfagni L, Gherardi F, Rossi S (2015) Chemical and isotope composition of waters from Firenzuola railway tunnel, Italy. In: G. Lollino et al. (eds.), Engineering Geology for Society and Territory – Volume 6, 971–974

Rowland JV, Simmons SF (2012) Hydrologic, magmatic, and tectonic controls on hydrothermal flow, Taupo Volcanic Zone, New Zealand: implications for the formation of epithermal vein deposits. *Economic Geology*, 107, 427–457

Scibek J, McKenzie JM, Gleeson T, Lefebrve R (2015) Comparing permeability of fault zones of geothermal and non-geothermal regions, compiled in a global fault zone permeability database. AGU-GAC-MAC Conference, May 4-7, Montreal, Canada

Serpen U (2004) Hydrogeological investigations on Balcova geothermal system in Turkey. *Geothermics*, 33, 309–335

Shipton ZK, Evans JP, Robeson K, Forster CB, Snelgrove S (2002) Structural heterogeneity and permeability in faulted eolian sandstone—implications for subsurface modeling of faults. *AAPG Bulletin*, 86, 863–883

Shipton ZK, Caine JS, Lunn RJ (2013) The Terminology of Fault Zones in the Brittle Regime: Making Field Observations More Useful to the End User. American Geophysical Union, Fall Meeting 2013. Presentation Abstract #T53C-2595

Solum JG, Brandenburg JP, Naruk SJ, Kostenko OV, Wilkins SJ, Schultz RA (2010) Characterization of deformation bands associated with normal and reverse stress states in the Navajo Sandstone, Utah. *AAPG Bulletin*, 94(9), 1453–1475

Stevenson DR, Brown A, Davison CC, Gascoyne M, McGregor RG, Ophori DU, Scheier NW, Stanchell F, Thorne GA, Tomsons DK (1996) A revised conceptual hydrogeologic model of a crystalline rock environment, Whiteshell Research Area, SE Manitoba, Canada. Atomic Energy of Canada, Report AECL-11331,COG-95-271

Stille B, Gustafson G (2010) A review of the Namntall Tunnel project with regard to grouting performance. *Tunnelling and Underground Space Technology*, 25, 346–356

Stober I, Bucher K (2007) Hydraulic properties of the crystalline basement. *Hydrogeology Journal*, 15, 213–224

Suescun Casallas LC (2015) Evaluación del impacto de las aguas subterráneas durante la construcción del Túnel de la Línea en el macizo fracturado de la Cordillera Central de los Andes, Colombia. Univ. Nacional de Colombia, Bogota

Takahashi H (1965) Characters and some problems on the tunnel water. *Journal of the Japan Society of Engineering Geology*, 6(1), Released: June 04, 2010

Takeuchi S, Saegusa H, Amano K, Takeuchi R (2013) Hydrogeological characterization of deep subsurface structures at the Mizunami Underground Research Laboratory. *Journal of Geological Society of Japan*, 119(2), 75-90 (in Japanese)

Talwani P, Chen L, Gahalaut K (2007) Seismogenic permeability, k_s. *Journal of Geophysical Research*, 112, B07309

Terada M, Matsubara T, Moriyama M, Nakata M (2008) Excavation of the long evacuation tunnel in the underground with high pressure ground water by TBM of 4.5m in diameter. World Tunnel Congress 2008 - Underground Facilities for Better Environment and Safety - India

Thury M, Gautschi A, Mazurek M, Müller WM, Naef H, Pearson FJ, Vomvoris S, Wilson W (1994) Geology and hydrogeology of the crystalline basement of northern Switzerland. Nagra Technical Report NTB 93-01, Wettingen, Switzerland

Townend J, Zoback MD (2000) How faulting keeps the crust strong. *Geology*, 28, 399–402

Tseng D-J, Tsai B-R, Chang L-C (2001) A case study on ground treatment for a rock tunnel with high groundwater ingression in Taiwan. *Tunnelling and Underground Space Technology*, 16, 175–183

Upton P, Sutherland R (2014) High permeability and low temperature correlates with proximity to brittle failure within mountains at an active tectonic boundary, Manapouri Tunnel, Fiordland, New Zealand. *Earth and Planetary Science Letters*, 389, 176–187

Vincenzi V, Gargini A, Goldscheider N, Piccinini L (2014) Differential hydrogeological effects of draining tunnels through the Northern Apennines, Italy. *Rock Mechanics and Rock Engineering*, 47, 947–965

Voinov V, Nikulin M, Balakrishnan N (2013) Chi-squared goodness of fit tests with applications, 1st ed. Academic Press, Elsevier

Wahlstrom EE, Hornback VQ (1962) Geology of the Harold D.Roberts Tunnel, Colorado, West portal to station 468-49. *Geological Society of America Bulletin*, 73, 1477–1498

Walker RJ, Holdsworth RE, Imber J, Faulkner DR, Armitage PJ (2013) Fault zone architecture and fluid flow in interlayered basaltic volcaniclastic-crystalline sequences. *Journal of Structural Geology*, 51, 92–104

Whiting P, Westwood M, Burke M, Sterne J, Glanville J (2008) Systematic reviews of test accuracy should search a range of databases to identify primary studies. *Journal of Clinical Epidemiology*, 61, 357–364

Yano T, Yamada N, Suzuki I (1978) Construction of the Enasan Tunnel and the design of the second stage. In: Kitamura (ed.), Tunnelling under difficult conditions. Proceedings of the International Tunnel Symposium, Tokyo 1978. Pergamon Press

Yoshikawa K, Asakura T (1981) Problems of tunnelling in fractured zones. *Journal of the Japan Society of Engineering Geology*, 22-1, 145–159 (in Japanese)

Zhang G-H, Jiao Y-Y, Wang H (2014) Outstanding issues in excavation of deep and long rock tunnels: a case study. *Canadian Geotechnical Journal*, 51, 984–994

CHAPTER 5

5 The permeability of fault zones in the upper continental crust

This chapter describes the summary statistics of world-wide fault zone permeability, in fault damage zone, fault core, and protolith, the ratio of values between the fault zone and the protolith, to present the trends with depth, and to discuss the implications of these trends. No statistical tests were done. The discussion and presentation is descriptive and conceptual. The descriptive statistics are meant to serve as references and to simplify the data search for other geoscientists who study faults.

5.1 Abstract

Fault zones are a ubiquitous part of the of the Earth's brittle crust, influencing a wide range of processes including hydrothermal circulation and ore deposition, crustal strength, and seismicity. However, despite the large amount of drilling and *in situ* hydraulic testing worldwide, there are no comprehensive summary statistics and analyses of fault permeability. The results from a global compilation of 429 datasets (at 364 locations) show that the permeability decreases with depth, and the maximum values can be approximately bounded by a fitted curve. The permeability ratio of fault damage zone / protolith is typically +2 to +3 orders of magnitude. The maximum ratio value occurs at shallow depths of 0-3 km, mainly above the seismogenic layer, implying a damage-maintenance process that differs from the hypocentral distribution of earthquakes. We propose that effective permeability is maintained during exhumation by processes such as strain concentration in zones of weakness and groundwater-rock interaction.

5.2 Introduction

For fluid flow in the brittle crust, the barrier and conduit nature of fault zones depends on the permeability of the deformed rocks. Fault rock fabrics and styles of deformation seen in exhumed faults formed at different depths (Sibson 1977), but the seminal work by Caine et al. (1996) and others showed that the hydraulic and mechanical properties of major faults in crystalline ("basement") rocks tend to exhibit a narrow zone of deformation in the fault core (or multiple fault cores such as shown in Faulkner et al. (2010) surrounded by a damage zone of fractured rock. However, despite a large number of studies world-wide, the exact nature of controlling processes and the resulting permeability variation with depth is not clear.

In this work we provide an overview, depth-distribution, and discussion of fault permeability values that are summarized from 429 datasets at 364 different locations world-wide (Scibek 2019 submitted - a). Permeability values are compared at two scales: matrix and bulk, although much of the presentation here focuses on the more numerous bulk permeability values (83% of datasets) rather than the matrix permeability values (72 outcrop sites). *Matrix* permeability refers to the porous rock volume, includes microfractures and pore spaces, but excludes most of the macroscopic faults or fractures because of small sample volumes (Lockner et al. 2009, Mitchell & Faulkner 2012). Tests of matrix permeability are widely utilized in hydrogeology, petroleum geoscience, and structural geology. The total permeability at a larger test scale of meters to hundreds of meters is referred to here as *bulk* permeability (Lockner et al. 2009, Zoback & Hickman 1982). At the spatio-temporal scales of *in situ* hydraulic testing over length scales of meters to 100's of meters and time scales of hours to days, the bulk permeability may exceed the matrix value by ~2 to 4 orders of magnitude in low-porosity rocks that form most of the brittle crust (Brace 1980, Townend & Zoback 2000). The matrix and bulk permeabilities are measured with different techniques (Bense et al. 2013, Achtziger-Zupancic et al. 2017).

5.3 Methods

5.3.1 Permeability data sources

A world-wide fault permeability compilation from a variety of geoscience and engineering studies was recently submitted as a data descriptor and a database (see Chapter 3 of this thesis) including summaries of 429 datasets at 364 locations, and the references for sources. The reviewed publication sources were on various topics (number of datasets in brackets): active faults and faulting processes (85), geothermal reservoirs (136), radioactive waste repositories (77), water resources and contaminated sites (18), petroleum reservoirs and faulting processes (41), and engineering projects (72). For each site and dataset, a representative bulk permeability estimate was used, where available, for the simplified structural domains in fault zones: fault damage zone, fault core, and protolith. The next most basic categorization was by the dominant lithology of the protolith: siliciclastic (coarse), mudrock (siliciclastic fine), carbonate, volcaniclastic, volcanic igneous (often inter-layered with volcaniclastic layers), plutonic, metamorphic (gneiss was the most common).

The individual datasets include results of analyses and interpretations of one to several hydraulic tests, and at a few sites up to 100's of individual hydraulic tests, therefore the summary values had to be averaged. The averaging was done separately within the data clusters from fault damage zone, fault core (zone), and from protoliths (host rocks). The representative estimate was usually the most common value in the high permeability data cluster, but where only a few test values were taken, the maximum value was used to capture the fault conduit behavior that is usually difficult to sample *in situ*. A low estimate of permeability of fault damage zone, fault core (zone), and protolith is also summarized to clarify the range of values. In case of *in situ* well tests, the low estimate was for the approximate median of bulk permeability values. In fault core (zone), the low estimate of matrix permeability was for the least permeable samples, or for the low-permeability data cluster in case of more samples or transects across faults.

The hydraulic test results were originally reported in various units of transmissivity, hydraulic conductivity, or permeability-thickness, with reference to water as fluid at the *in situ* conditions tested, as reported in the original publications. The issues with scale effects, test representativeness, or relative permeabilities at geothermal reservoirs were addressed in the original publications. In some cases, the reported hydraulic conductivity or transmissivity values were converted to permeability in m^2 units by using appropriate water viscosity at the reported depth-temperature conditions. The error magnitude of individual points in our global sample is variably well known. Errors from hydraulic test interpretation and site-wide averaging or grouping of test data are typically 0.5 to 1 order of magnitude (log m^2) units, although smaller and greater errors may exist in some cases. The error in depth is likely <5% at depths >100s of meters. Collectively, the permeability values range over 10 orders of magnitude, and as statistical distributions are positively skewed (long-tailed) that are approximately log-normal. The permeability data were transformed by $\log_{10}$, and in this analysis and all figures and tables we refer to the logarithms of permeability of fault damage zone (k_{FDZ}) and protolith ($k_{Protolith}$).

5.3.2 Permeability-depth curves

The empirical "permeability-pressure sensitivity" functions of rock samples tested at effective confining pressure that partially compacts the pore spaces and micro-fractures (Brace 1978, David et al. 1994) depend upon the type of geologic material, granular or crystalline (Wong & Zhu 1999), and are usually expressed as an exponential function and its logarithm equivalent:

$$k = k_0 \exp(-\gamma\ (\sigma - \sigma_0)) \qquad [1]$$

$$\ln(k) = \ln(k_0) - \gamma(\sigma - \sigma_0)$$

where k is the permeability at effective pressure P_{eff}, k_0 is the initial rock volume permeability (m^2 units) at ambient pressure conditions or reference effective pressure P_0, and γ is the empirically derived pressure-sensitivity parameter.

For tests under hydrostatic conditions, effective pressure is simply $P_{eff.}$ It can be expressed as depth, adjusting the units of γ appropriately. Sample decompression, loading, handling, wetting and drying, test fluid type (gas, water, etc.) affect the pressure sensitivity and the measured matrix permeability (Morrow et al. 2014), while the open fractures are rarely tested in small samples.

A power-law curve in the form shown in Equation 2 is often used to fit trends of permeability with depth because the base-10 logarithms of values are convenient for showing the order of magnitude of values:

$$k = k_0\ (z)^{-\gamma} \qquad [2]$$

$$\log_{10}(k) = \log_{10}(k_0) - \gamma\ \log_{10}(z)$$

where the γ is the slope of the line on log-log plot, an empirically fitted parameter to the permeability-depth data and z is the depth below ground surface in km.

A *geothermal-metamorphic curve* (Equation 3) was defined by Ingebritsen and Manning (1999) as a best-fit curve to various permeability estimates including a) parameters in geothermal fluid flow models in several sedimentary basins, active mountain belts, volcanic areas at km or larger scale, and b) calculations of fluid fluxes during metamorphism, based on geochemical and petrological data from cm-sized outcrop specimens that had been exhumed from some depth. The question about what the upper bound of crustal permeability might be was explored by Ingebritsen and Manning (2010), using bulk permeability values taken from several deep drilling sites, or calculated from hydraulic diffusivity in several published cases of induced and natural seismicity migration. The curve fitted to these enhanced permeability phenomena in the crust is given in Equation 4:

$$\log_{10}(k) = -14 - 3.2 \log_{10}(z) \quad [3]$$

$$\log_{10}(k) = -9.8 - 5.5 \log_{10}(z) \quad [4]$$

One problem with such power-law curves is a divergence to infinity near 0 depth, therefore their use is limited to depths greater than 1km (Saar & Manga 2004). In this work, we modified the previously proposed curves (Equations 3 and 4) to have a realistic value and shape at shallow depths. This was accomplished by adding a curve shape parameter to change the inflection point of the curve, following the method used by Aizawa (2008) and Uehara et al. (2012), in a new form is:

$$\log_{10}(\mathrm{k}) = \log_{10}(\mathrm{k}_0) - \gamma \log_{10}(\mathrm{z} + \mathrm{z}_{\mathrm{inflection}}) \quad [5]$$

where z is depth in km below the ground surface or sea floor surface, $z_{\mathrm{inflection}}$ is a curve shape parameter, k_0 is the permeability (m^2 units) at depth $z + z_{\mathrm{inflection}} = 1$. Thus, the *modified geothermal-metamorphic curve* (Equation 6) and *damaged-crust curve* (Equation 7), respectively, are:

$$\log(\mathrm{k}) = -14 - 3.2 \log(z + 0.1) \quad [6]$$

$$\log(\mathrm{k}) = -9 - 6 \log(z + 1.2) \quad [7]$$

5.3.3 Permeability ratios

The permeability contrast between the fault rock and the protolith can be quantified by a ratio of the two paired permeability values, at the same location and depth, using either the bulk or the matrix permeability (that is, without mixing the two scales of measurement). Here we use the more abundant bulk permeability values from fault damage zones and protolith to define the ratio:

$$\mathrm{ratio}_{\mathrm{bulk}} = k_{FDZ} / k_{Protolith} \quad [8]$$

$$\log(\mathrm{ratio}_{\mathrm{bulk}}) = \log(k_{FDZ}) - \log(k_{Protolith})$$

where (k_{FDZ}) is the bulk permeability of fault damage zone, and $k_{Protolith}$ is the bulk permeability of protolith. When expressed as logarithms, the ratio becomes a difference, as can be seen on logarithmic graphs. As an estimate of the average global permeability ratio of the faulted crust to unfaulted crust, we explore using the ratio between the logarithms of the modified damaged crust curve (Equation 6) and the modified geothermal metamorphic curve (Equation 7) to obtain the ratio curve for a depth z (in km):

$$\log(\text{ratio}_{\text{global}}) = -5.4 \log(z + 1.5) + 3.2 \log(z + 0.15) + 4.2 \qquad [9]$$

5.3.4 Bulk permeability estimates for fault zones from tunnel inflows

There are numerous sites in the fault zone permeability database where inflow rates were used to estimate the transmissivity of tunnel sections, including fault zones from the seminal work by Maréchal (1999) and the highly detailed work in the Alpine tunnels by others (Masset & Loew 2010, Masset & Loew 2013). We found additional cases where tunnel inflow rates from fault zones were described, but not yet used for transmissivity calculations (see Supporting Information). The Goodman et al. (1964, 1965) formula can be used to estimate the transmissivity of fault zones from inflow rates in long tunnels (i.e. Massett & Loew 2010, 2011). The inflow rate per unit length of tunnel is related to hydraulic conductivity through the Goodman formula, solved for transmissivity, after Massett and Loew (2010):

$$T = Q_{total}\, 2.3 \log(2\, \Delta H/r) / (2\, \pi\, \Delta H) \qquad [10]$$

where T is transmissivity (m^2/s), ΔH is hydraulic gradient from water table to tunnel at fault zone location, Q_{total} (m^3/s) is the total inflow rate or a product of inflow rate per unit length of tunnel and the width of fault zone (L) along tunnel. Permeability is calculated from hydraulic conductivity (a product of transmissivity / zone length):

$$k = (\rho * g)/\mu * (T/L) \qquad [11]$$

where k is the average bulk permeability, μ is water dynamic viscosity (i.e. 10^{-3} Pa*s at a groundwater temperature of 10^{o}C), ρ is water density that is usually near 1000 kg/m^3, the gravitational constant g is 9.81 m/s^2, and L is length across fault zone.

5.3.5 Fault bulk permeability at EGS and HDR sites

We reviewed the permeability of faults under natural conditions and after injection stimulation at 21 research sites associated with Enhanced Geothermal System (EGS), Hot Dry Rock (HDR), or underground hard rock laboratories. These include several experiments at Soultz-sous-Forêts (Evans et al. 2005, Sausse et al. 2006), KTB (Huenges et al. 1997), Basel (Ladner & Haring 2009), LSBB (Guglielmi et al. 2015), Desert Peak (Benato et al. 2016), the Nojima fault observatory (Kitagawa & Kano 2016), and other sites. The ratio of fault permeability enhancement was calculated from fault zone permeability before/after the injection. The Supporting Information includes a more detailed review text and a summary of permeability values.

5.3.6 Regional seismicity-depth distributions

Seismicity-depth distributions were summarized from published seismological literature (without re-analysis) done in the same regions where most of the *in situ* fault zone permeability tests were done. In Europe, we used histograms from regions in France (i.e. Baroux et al. 2001, Bonjer 1997, Mazabraud et al. 2005), southern Iceland (Panzera et al. 2016), Sweden and Finland (Kaikkonen et al. 2000, SKB 2017), and Switzerland (Wiemer et al., 2016). We also included data from southern California (Tal & Hager 2015), Japan (Japan Meteorological Agency 2017), and the Taupo Volcanic Zone in New Zealand (Sherburn et al. 2003). The histograms of earthquake counts were plotted at mid-point of depth bins from the original tabulations. The values and references are listed in tables in the Supporting Information.

5.4 Results

5.4.1 Statistics of conduit behavior of fault damage zones

Permeability values show the conduit behavior of fault damage zones and the barrier effect of fault cores. Statistics were summarized for matrix permeability of fault rocks and protoliths (Figure 5-1a) and for bulk permeability of fault damage zones and protoliths (Figure 5-1b). The matrix permeability of fault cores can be quite variable. The median matrix permeability is $1x10^{-17}$ m^2 for fault gouge and cataclasite, and whereas many breccia samples were more permeable (median $1x10^{-14}$ m^2) than the gouges, the distribution is wide and some breccias are similarly permeable to some gouges. Bulk permeability behavior varies with lithology. In carbonate rocks (n=26 localities), highly permeable damage zones (10^{-12} m^2) are found adjacent to fault cores in many locations, although the permeability contrast to the protolith is only about one order of magnitude. In coarse siliciclastic rocks (n=26), the damage zone permeability (10^{-13} m^2) slightly exceeds that of the protolith ($7x10^{-13}$ m^2), and the fault core (10^{-14} m^2) may retard fluid flow. Siliciclastic mudrocks have low bulk permeability, even when fractured, but there is a high ratio between damage zone and protolith values (3 orders of magnitude, 10^{-15} m^2/ $8x10^{-19}$ m^2, n=13). Volcanic igneous rocks have been studied extensively (62 localities), and the permeability distribution is similar to that for volcaniclastic and coarse siliciclastic rocks. Finally, the largest sample size is from plutonic and metamorphic rocks (n=103 and 91, respectively), where the bulk permeability ratios (Figure 5-1c) are approximately 2 to 3 orders of magnitude between damage zones (4 to $7x10^{-14}$ m^2) and protolith ($2x10^{-16}$ m^2). The upper 10 km of the brittle crust is composed ~75% of metamorphic and plutonic rocks (Wilkinson et al. 2009).

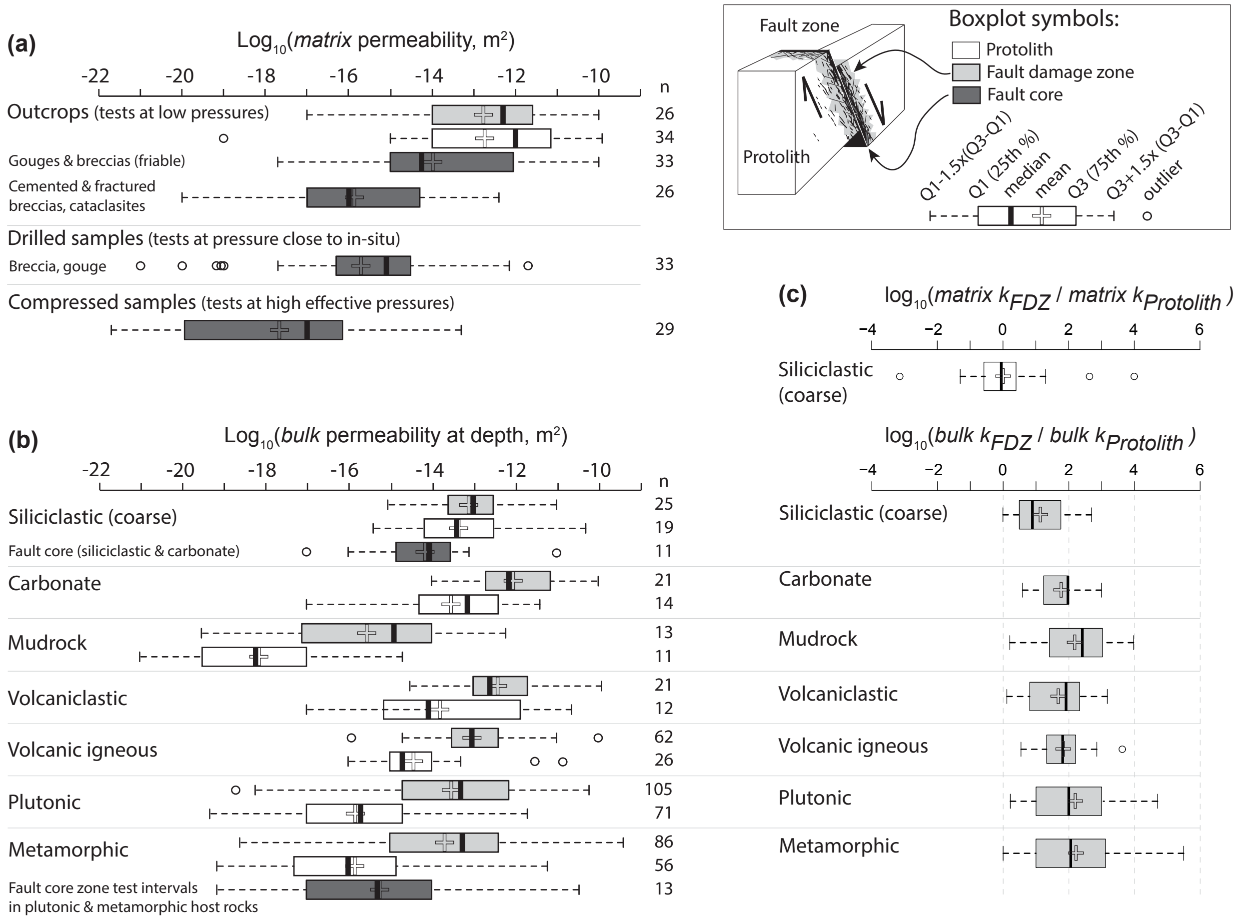

Figure 5-1 Fault zone permeability distributions (boxplots) for specific lithologies and fault zone structural domains. (a) Matrix permeability of fault damage zone, protolith, and fault core at outcrops (from low-pressure tests) and of fault core rocks at near in situ pressures. (b) Bulk permeability estimated from in situ tests in drillholes, comparing the fault damage zone, protolith, and fault core. The fault permeability architectural units (after Caine et al. 1996) are coloured to match the shading of boxplots in (a) and (b) for easier reference: fault core is dark grey, damage zone is light grey, and protolith is white. Fault core data are from coarse siliciclastic rocks and plutonic and metamorphic rocks only. Boxplot center lines show the medians and box limits the 25th and 75th percentiles; whiskers extend 1.5 times the interquartile range; outliers are represented by empty circles; crosses represent sample means. (c) Permeability ratio of fault damage zone to protolith, by lithological categories. The bulk permeability ratios can be compared to the corresponding data distributions for each lithologic category in part (b). Matrix permeability ratio shown only for siliciclastic coarse rocks (such as sandstones) at fault outcrop sites (upper portion of c).

5.4.2 Depth distribution of fault damage zone bulk permeability

The maximum value of damage-zone bulk permeability decreases with depth (Figure 5-2). Previously published global permeability-depth curves (Ingebritsen and Manning 1999, Ingebritsen and Manning 2010) have been modified to improve the fit to damage zone and protolith data at shallow depths (Saar and Manga 2004). The geothermal-metamorphic curve represents the maximum rock matrix permeability at large scale and over geological time-scales, whereas the damaged-crust curve represents the maximum bulk permeability of fault damage zones in the brittle crust (Figure 5-2a). Roughly 95% of the compiled fault damage zone data have bulk permeabilities exceeding 10^{-17} m^2. This result is consistent with the reported occurrence of hydrostatic conditions to about 9 km depth in the brittle crystalline crust (Townend and Zoback 2000), despite the potential of various geologic processes to generate overpressures (Neuzil 1995).

5.4.3 Bulk permeability ratio (contrast)

The conduit behavior of fault damage zones is represented by a bulk permeability ratio of fault damage zone to protolith (both fractured). The ratio values, already averaged for each site, are scattered widely and cluster near 1km depth where most of the *in situ* data have been collected. The ratio curve was calculated from the other two conceptual curves in Figure 2a, and not directly from the ratio data points, but it approximately follows a moving average along depth of the ratio point plot (it varies between 1.3 and 3.1, with a mean of 2.1). Assuming that that curve has some physical relevance in the way it was defined as the ratio of maximum permeability of fault damage zones to the protolith, at length scale of 100's meters that includes the effects of connectivity of fracture networks, the permeability ratio along this curve has a maximum value at near two kilometer depth (Figure 5-2b). The median and mean log ratio values are near 2 (two orders of magnitude permeability contrast) for all lithologies other than coarse siliciclastic rocks that show little contrast.

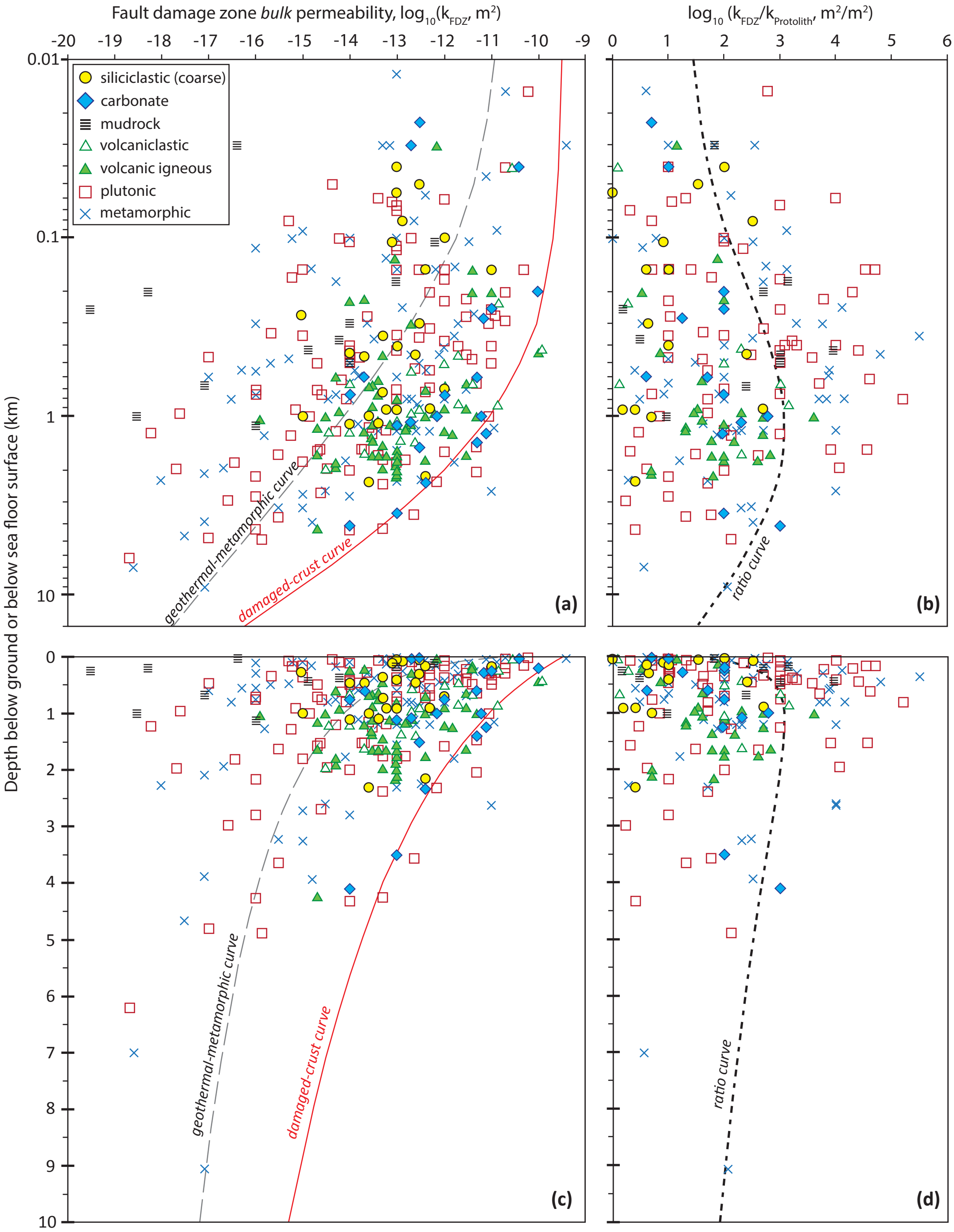

Figure 5-2 Logarithms of bulk permeability of fault damage zones, for different lithologic categories, plotted against depth below ground surface (or below sea floor surface) at a mid-point of tested *in situ* interval. The depth scale is logarithmic in the upper panels (a, b), and arithmetic in the lower panels (c, d). The lower plots are otherwise identical to the upper plots. In (a) or (c), the bulk permeability of fault damage zones is shown as representative points (one per dataset), the modified geothermal-metamorphic curve approximates the average permeability of the protolith, and the damaged-crust curve is an approximate upper bound of the bulk permeability of fault zones. In (b) or (d), the points represent the logarithms of ratio of bulk permeability (fault damage zone / protolith) for each dataset, and the ratio curve is the difference of log permeability values of the two curves in (a) and (c).

5.5 Discussion of processes

The largest measured ratios span the value required (~3 orders of magnitude) for dynamic changes in fault permeability to be triggered by pressure changes at seismogenic depths (Rice 1992). Such dynamic permeability changes during gas and fluid migration have been simulated for fluid-driven seismic sequences in metamorphic rocks at depths of 2 to 6 km (Miller et al. 2004) and along deeper shear zones that link to normal faults in hydrothermal flow systems (Gottardi et al. 2013). The fault permeability/protolith ratios reported here agree with such models. We also reviewed and plotted (Figure 5-3a) the ratios of fault permeability enhancement, relative to original fault permeability, from fault injection stimulation tests at sites of Enhanced Geothermal Systems (EGS) or Hot Dry Rock (HDR) (Smith 1983) that are summarized in the Supporting Information section). At all such sites, pre-existing faults of various sizes were either further sheared or dilated and sheared to increase the *in situ* bulk permeability of the fracture zone, typically by about 1 to 3 orders of magnitude increase. These permeability ratios also fall within the plotted ratio curve, thus not contradicting this simple conceptual model, although the depth-trend of such ratio remains uncertain due to the small number of deep test intervals in fault zones.

It appears that fault permeability is most different from protolith in the uppermost crust above seismogenic depths (Figure 5-3), which challenges the standard assumption that maintenance of fault permeability owes to co-seismic fault damage (Sibson 2000). The depth distribution of intra-plate seismicity is governed by rate and friction laws, such that in the upper 2 to 3 km of the brittle crust there is a stable and generally aseismic layer where fault cores contain unlithified gouge (Scholz 1998). We summarized the earthquake depth distributions from 18 regions world-wide (Figure 5-3b). Field evidence from fault outcrops shows that only a narrow (<1 m to cm scale) inner part of the gouge and breccia in fault core deforms co-seismically or aseismically during any one event (Yamashita & Tsutsumi 2018). Even during large intra-plate earthquakes, the seismicity and seismic moment (or potency) peaks between 5 to 10 km depth and is nearly absent in the aseismic layer (Fialko et al. 2005). The standard geological conceptual model is that the permeability structures of fault zones form at seismogenic depths, and experience recurring re-opening (reactivation), which competes with the permeability-reducing effects of cementation by mineral growth (Cox et al. 2015) and mineral dissolution and re-precipitation along fractures (Moore et al. 1994). Superimposed on these effects are perturbations by passing seismic waves from earthquakes located elsewhere, although these transient permeability enhancements have been shown to be temporary (< year) and generally affect permeability by < 0.5 order of magnitude (Elkhoury et al. 2006).

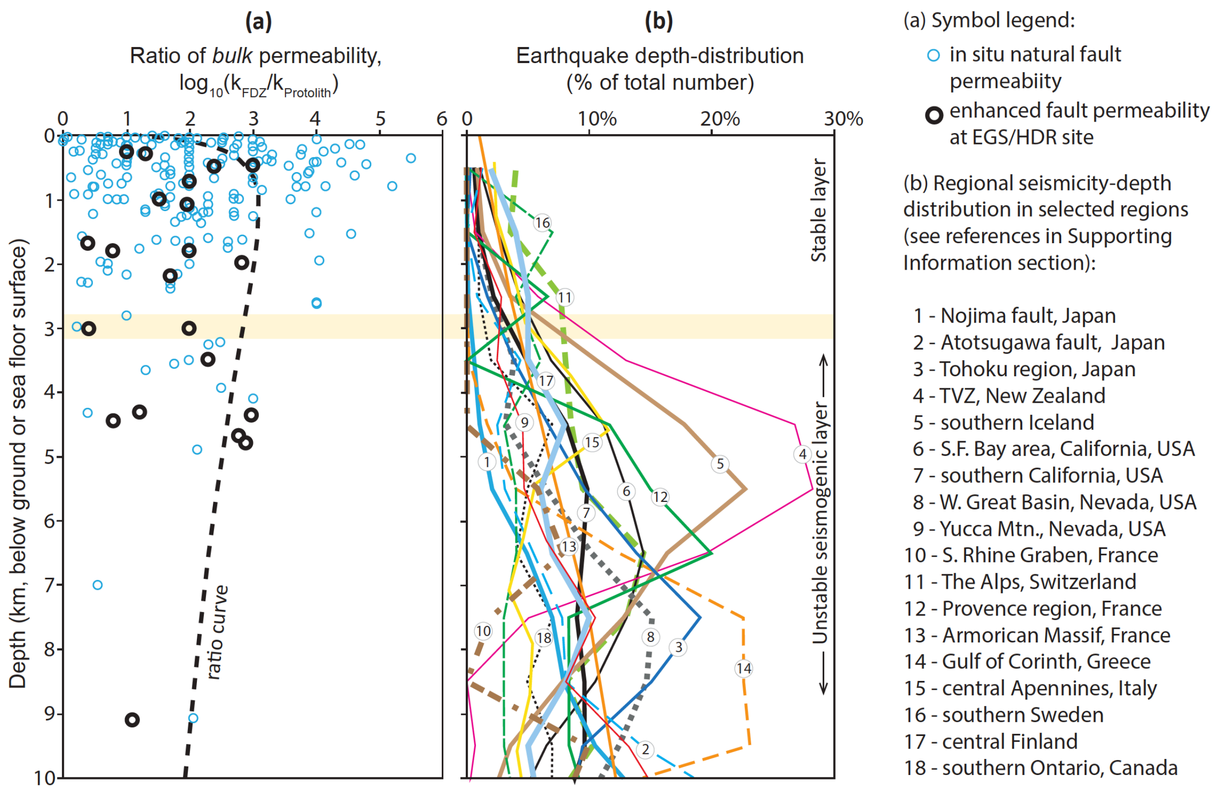

Figure 5-3 Comparison of the bulk permeability ratio (fault damage zone / protolith) to seismicity-depth distributions for 18 regions represented in the fault zone permeability data set, showing that fault permeability is most different from protolith in the uppermost crust above seismogenic depths. (a) Bulk permeability ratios at fault zone sites compared to the post- to pre-stimulation permeability ratios (magnitude of permeability enhancement) for 21 EGS/HDR projects; the permeability ratio curve from Figure 2b is plotted as a dashed line. (b) Seismicity-depth distribution from selected regions represented in the permeability data set.

The observed pattern in permeability contrast or ratio requires that either more damage is done or preserved at shallower depths, or that purely tectonic-geomechanical processes explain only part of the observed pattern and that other processes contribute significantly at shallow depths (i.e. above the seismogenic layer). In the upper 2 km of the crust, many damage zone / protolith permeability ratios of 3 to 6 orders of magnitude are observed in faults that are now exhumed to shallower depths, despite partial hydrothermal sealing and relatively few permeable fractures (Sausse and Ganter 2005). At small-scale, flow channels can be locally enhanced by circulating cool groundwaters (Mayo et al. 2014, Stober and

Bucher 2015). We speculate that the primary permeability-maintenance processes are water-rock interactions driven by circulating cool meteoric groundwaters and small-scale reactivation and elastic compliance of faults and fractures during exhumation.

5.6 Conclusions

The statistics for permeability from fault zones are consistent with conceptual models of conduit behavior of fault damage zones and the barrier effect of fault cores. The newly compiled world-wide data are compatible with modified versions of previously proposed permeability-trend curves. The proposed bounding curve for maximum fault zone bulk permeabilities in the brittle crust can be used to compare fault permeability data from different sites and eventually to test the trend lines against new and deeper *in situ* data.

The permeability ratio of fault damage zone / protolith is typically +2 to +3 orders of magnitude, and the maximum ratio value occurs at shallow depths of 0-3 km, mainly above the seismogenic layer.

The processes responsible for fault permeability maintenance during exhumation of rocks from larger depths may be tectonic and geomechanical or geochemical, including the interactions with meteoric groundwater with minerals filling previous fractures and pores.

More deep drilling and testing may eventually establish depth-trends to 10 km depth or deeper, and help to resolve outstanding questions about fluid and heat flow in active faults. In the interim, the bounding bulk permeability-depth curves and ratio values estimated here can serve as a reference for postulating fault permeability distributions at a global scale, provide context for comparison of study sites, and help to parameterize models for processes such as co-seismic flow along active faults (Miller 2004, Okada et al. 2015), or heat and fluid flow in major fault zones (Sutherland et al. 2017).

5.7 References

Achtziger-Zupancic, P., Loew, S., & Mariéthoz, G. (2017) A new global database to improve predictions of permeability distribution in crystalline rocks at site scale. *Journal of Geophysical Research Solid Earth*, 122, 3513–3539

Aizawa, Y. (2008) Permeability and porosity structures in Niigata Basin and Ursa Basin in the northern Gulf of Mexico, (Doctoral dissertation). Abstract retrieved Kyoto University (https://repository.kulib.kyoto-u.ac.jp/dspace/bitstream/2433/124364/1/yrigk03333.pdf). Kyoto, Japan: Kyoto University

Bense, V.F., Gleeson, T., Loveless, S.E., Bour, O., & Scibek, J. (2013) Fault zone hydrogeology. *Earth-Science Reviews*, 127, 171–192

Brace, W.F. (1978) Volume changes during fracture and frictional sliding: a review. *Pure and Applied Geophysics*, 116, 603–614

Brace, W.F. (1980) Permeability of crystalline and argillaceous rocks. *International Journal of Rock Mechanics and Mining Sciences & Geomechanics Abstracts*, 17(5), 241–251

Caine, J.S., & Tomusiak, S.R.A. (2003) Brittle structures and their role in controlling porosity and permeability in a complex Precambrian crystalline-rock aquifer system in the Colorado Rocky Mountain Front Range. *GSA Bulletin*, 115(11), 1410–1424

Caine, J.S., Evans, J.P., & Foster, C.B. (1996) Fault zone architecture and permeability structure. *Geology*, 24, 1025–1028

Cox, S.F. (2016) Injection-driven swarm seismicity and permeability enhancement: implications for the dynamics of hydrothermal ore systems in high fluid-flux, over-pressured faulting regimes. *Economic Geology*, 111(3), 559–587

David, C., Wong, T-f., Zhu, W., & Zhang, J. (1994) Laboratory measurement of compaction-induced permeability change in porous rock: implications for the generation and maintenance of pore pressure excess in the crust. *Pure and Applied Geophysics*, 143, 425–456

Elkhoury, J.E., Brodsky, E.E., & Agnew, D.C. (2006) Seismic waves increase permeability. *Nature*, 44, 1135–1137

Faulkner, D.R., Jackson, C.A.L., Lunn, R.J., Schlische, R.W., Shipton, Z.K., Wibberley, C.A.J., & Withjack, M.O. (2010) A review of recent developments concerning the structure, mechanics and fluid flow properties of fault zones. *Journal of Structural Geology*, 32, 1557–

1575

Fialko, Y., Sandwell, D., Simons, M., & Rosen, P. (2005) Three-dimensional deformation caused by the Bam, Iran, earthquake and the origin of shallow slip deficit. *Nature*, 435, 295–299

Goodman, R.E., Moye, D.G., van Schalkwyk, A., & Javandel, I. (1965) Ground water inflows during tunnel driving. *Bulletin of the International Association of Engineering Geologists*, 2(1), 39–56

Gottardi, R., Kao, P-H., Saar, P-H., & Teyssier, C. (2013) Effects of permeability fields on fluid, heat, and oxygen isotope transport in extensional detachment systems. *Geochemistry Geophysics Geosystems*, 14, 1493–1522

Guglielmi, Y., Cappa, F., Avouac, J-P., Henry, P., & Elsworth, D. (2015) Seismicity triggered by fluid injection–induced aseismic slip. *Science*, 348(6240), 1224–1226

Ingebritsen, S.E., & Manning, C.E. (1999) Geological implications of a permeability-depth curve for the continental crust. *Geology*, 27, 1107–1110

Ingebritsen, S.E., & Manning, C.E. (2010) Permeability of the continental crust: dynamic variations inferred from seismicity and metamorphism. *Geofluids*, 10, 193–205

Lockner, D., Tanaka, H., Ito, H., Ikeda, R., Omura, K., & Naka, H. (2009) Geometry of the Nojima Fault at Nojima-Hirabayashi, Japan – I. A simple damage structure inferred from borehole core permeability. *Pure and Applied Geophysics*, 166, 1649–1667

Manning, C.E., & Ingebritsen, S.E. (1999) Permeability of the continental crust: The implications of geothermal data and metamorphic systems. *Reviews of Geophysics*, 37, 127–150

Masset, O., & Loew, S. (2010) Hydraulic conductivity distribution in crystalline rocks, derived from inflows to tunnels and galleries in the central Alps, Switzerland. *Hydrogeology Journal*, 18, 863–891

Mayo, A.L., Himes, S.A., & Tingey, D.G. (2014) Self-organizing thermal fluid flow in fractured crystalline rock: a geochemical and theoretical approach to evaluating fluid flow in the southern Idaho batholith, USA. *Hydrogeology Journal*, 22, 25–45

Miller, S.A., Collettini, C., Chiaraluce, L., Cocco, M., Barchi, M., & Kaus, J.P. (2004) Aftershocks driven by a high-pressure CO2 source at depth. *Nature*, 427, 724–727

Mitchell, T.M., & Faulkner, D.R. (2012) Towards quantifying the matrix permeability of fault damage zones in low porosity rocks. *Earth and Planetary Science Letters*, 339–340, 24–31

Moore, D.E., Lockner, D.E., & Byerlee, J.D. (1994) Reduction of permeability in granite at elevated temperatures. *Science*, 265, 1558–1561

Morrow, C.A., Lockner, D.A., Moore, D.E., & Hickman, S. (2014) Deep permeability of the San Andreas Fault from San Andreas Fault Observatory at Depth (SAFOD) core samples. *Journal of Structural Geology*, 64, 99–114

Morrow, C.A., & Lockner, D.A. (1994) Permeability differences between surface-derived and deep drillhole core samples. *Geophysical Research Letters*, 21(19), 2151–2154

Neuzil, C.E. (1995) Abnormal pressures as hydrodynamic phenomena. *American Journal of Science*, 295, 742–786

Okada, T., Matsuzawa, T., Umino, N., Yoshida, K., Hasegawa, A. , Takahashi, H. et al. (2015) Hypocenter migration and crustal seismic velocity distribution observed for the inland earthquake swarms induced by the 2011 Tohoku-Oki earthquake in NE Japan: implications for crustal fluid distribution and crustal permeability. *Geofluids*, 15, 293–309

Rice, J. (1992) Fault stress states, pore pressure distributions, and the weakness of the San Andreas Fault. In B. Evans, T.-f. Wong (Eds.), Fault mechanics and transport properties of rocks (pp. 69-88). San Diego, CA: Academic Press

Saar, M.O., & Manga, M. (2004) Depth dependence of permeability in the Oregon Cascades inferred from hydrogeologic, thermal, seismic, and magmatic modeling constraints. *Journal of Geophysical Research*, 109, B04204

Scholz, C.H. (1998) Earthquake and friction laws. *Nature*, 391, 37–41

Sibson R.H. (1977) Fault rocks and fault mechanisms. *Journal of Geological Society of London*, 133(3), 191–213

Sibson, R.H. (2000) Fluid involvement in normal faulting. *Journal of Geodynamics*, 29, 469–499

Spitzer, M., Wildenhain, J., Appsilber, J., & Tyers, M. (2014) BoxPlotR: a web tool for generation of box plots. *Nature Methods*, 11, 121–122

Stober, I., & Bucher, K. (2015) Hydraulic conductivity of fractured upper crust: insights from hydraulic tests in boreholes and fluid-rock interaction in crystalline basement rocks. *Geofluids*, 15, 161–178

Sutherland, R., Townend, J., Toy, V., Upton, P., Coussens, J., Allen, M. et al. (2017) Extreme hydrothermal conditions at an active plate-bounding fault. *Nature*, 546, 137–140

Townend, J., & Zoback, M.D. (2000) How faulting keeps the crust strong. *Geology*, 28, 399–402

Uehara, S., Shimamoto, T., Okazaki, K., Funaki, H., Kurikami, H., Niizato, T., & Ohnishi, Y. (2012) Can surface samples be used to infer underground permeability structure? A test case for a Neogene sedimentary basin in Horonobe, Japan. *International Journal of Rock Mechanics & Mining Sciences*, 56, 1–14

Wilkinson, B.H., McElroy, B.J., Kesler, S.E., Peters, S.E., & Rothman, E.D. (2009) Global geologic maps are tectonic speedometers—Rates of rock cycling from area-age frequencies: *GSA Bulletin*, 121(5/6), 760–779

Wong, T-F., & Zhu, W. (1999) Brittle faulting and permeability evolution: hydromechanical measurement, microstructural observation, and network modeling. In W.C. Haneberg, P.S. Mozley, J.C. Moore, L.B. Goodwin (Eds.), Faults and subsurface fluid flow in the shallow crust. Geophysical Monograph Series (Vol. 113, pp. 83–99). Washington, DC: American Geophysical Union

Yamashita, T., & Tsutsumi, A. (2018) Involvement of Fluids in Earthquake Ruptures. Field/Experimental Data and Modeling. Springer Japan KK 2018. doi:10.1007/978-4-431-56562-8

Zoback, M.D., & Hickman, S. (1982) *In situ* study of the physical mechanisms controlling induced seismicity at Monticello Reservoir, South Carolina. *Journal of Geophysical Research*, 87, 6959–6974

References: Additional estimates of bulk permeability of fault zones from groundwater inflow rates to tunnels:

Goodman, R.E., Moye, D.G., van Schalwyk, A., & Javandel, I. (1964) Ground water inflows during tunnel driving. Paper presented at the 1964 Annual Meeting of the Association of Engineering Geologists at University of California. Berkeley, CA.

Jaeger, C. (1979) Rock mechanics and engineering. Second edition. Cambridge, England: Cambridge University Press

Haga, K. (1961) The fractured zone of the Kurobe transportation tunnel. *Geologie und Bauwesen [Geology and Civil Engineering]*, 26(2), 60–78

Logan, M.H. (1964) Effect of the Earthquake Of March 27, 1964, on The Eklutna Hydroelectric Project, Anchorage, Alaska. Professional Paper 545-A. Washington, DC: U.S. Geological Survey

Maréchal, J-C. (1999) Observation of alpine crystalline massifs from underground galleries [Observation des massifs cristallins alpins au travers des ouvrages souterrains]. 1. Hydraulic Conductivity at the "Massif" Scale [Caracterisation de la conductivite hydraulique a l'echelle du massif]. *Hydrogeologie*, 1, 21–32

Maréchal, J.C. (1998) Les circulations d'eau dans les massifs cristallins alpins et leurs relations avec les ouvrages souterrains, (Doctoral dissertation N° 1769). Lousanne, France: École Polytechnique Fédérale De Lausanne

Masset, O., & Loew, S. (2010) Hydraulic conductivity distribution in crystalline rocks, derived from inflows to tunnels and galleries in the central Alps, Switzerland. *Hydrogeology Journal*, 18, 863–891

Seebeck, H., Nicol, A., Walsh, J.J., Childs, C., Beetham, R.D., & Pettinga, J. (2014) Fluid flow in fault zones from an active rift. *Journal of Structural Geology*, 62, 52–64

Seebeck, H.C. (2013) Normal faulting, volcanism and fluid flow, Hikurangi subduction plate boundary, (Doctoral dissertation). Retrieved from UC Research Repository

(http://hdl.handle.net/10092/8884) Christchurch, New Zealand: University of Canterbury.
Strozzi, T., Delaloye, R., Poffet, D., Hansmann, J., & Loew, S. (2011). Surface subsidence and uplift above a headrace tunnel in metamorphic basement rocks of the Swiss Alps as detected by satellite SAR interferometry. *Remote Sensing of Environment*, 115(6), 1353–

1360

Yano, T., Yamada, N., & Suzuki, I. (1978) Construction of the Enasan Tunnel and the design of the second stage. In I. Kitamura (Ed.), Tunnelling Under Difficult Conditions, Proceedings of the International Tunnel Symposium (pp. 157–161). Tokyo, Japan: Pergamon Press

References: Seismicity-depth distributions in selected regions:

Baroux, E., Bethoux, N., & Bellier, O. (2001) Analyses of the stress field in south-eastern France from earthquakes focal mechanisms. *Geophysical Journal International*, 145, 336–348

Bonjer, K.P. (1997) Seismicity pattern and style of seismic faulting at the eastern border fault of the southern Rhine Graben. *Tectonophysics*, 275, 41–69

Chiaraluce, L., Valoroso, L., Anselmi, M., Bagh, S., & Chiarabba, C. (2009) A decade of passive seismic monitoring experiments with local networks in four Italian regions. *Tectonophysics*, 476, 85–98

Japan Meteorological Agency (2017) The Seismological Bulletin of Japan: Hypocenters. (hJp://www.data.jma.go.jp/svd/eqev/data/bulletin/hypoe.html)

Kaikkonen, P., Moisio, K., & Heeremans, M. (2000) Thermo mechanical lithospheric structure of the central Fennoscandian Shield. *Physics of the Earth and Planetary Interiors*, 119, 209–235

Ma, S., & Atkinson, G.M. (2006) Focal depth distribution for earthquakes with mN ≥2.8 in western Quebec, southern Ontario and northern New York. *Bulletin of Seismological Society of America*, 96, 609–623

Mazabraud, Y., Bethoux, N., & Deroussi, S. (2005) Characterisation of the seismological pattern in a slowly deforming intraplate region: Central and western France. *Tectonophysics*, 409, 175–192

Niwa, M., Kurosawa, H., & Ishimaru, T. (2011) Spatial distribution and characteristics of fracture zones near a long-lived active fault: A field-based study for understanding changes in underground environment caused by long-term fault activities. *Engineering Geology*, 119, 31–50

Panzera, F., Zechar, J.D., Vogfjord, K.S., & Eberhard, D.A.J. (2016) A revised earthquake catalogue for south Iceland. *Pure and Applied Geophysics*, 173, 97–116

Rigo, A., Lyon-Caen, H., Armijo, R., Deschamps, A, Hatfeld, D., Makropoulo, K., et al. (1996) A microseismic study in the western part of the Gulf of Corinth (Greece): Implications for large-scale normal faulting mechanisms. *Geophysical Journal International*, 126, 663–688

Ryall, A.S., & Vetter, U.R. (1982) Seismicity related to geothermal development in Dixie Valley, Nevada. Report to U.S. Department of Energy (Rep. DOE/NV/10054-3). Reno, NV: Seismological Laboratory, University of Nevada

Sherburn, S., Bannister, S., & Bibby, H. (2003) Seismic velocity structure of the central Taupo Volcanic Zone, New Zealand, from local earthquake tomography. *Journal of Volcanology and Geothermal Research*, 122, 69–88

SKB (2017) Quarterly reports on recorded EQs in Sweden, 2003 to 2011. Stockholm, Sweden: Svensk Kärnbränslehantering AB. (http://www.skb.com/publications)

Smith, K., Anderson, J.G., & Smiecinski, A.J. (2007) Seismicity in the vicinity of Yucca Mountain, Nevada, for the period October 1, 2004 to September 30, 2006. Report to U.S. Department of Energy (Rep. TR-07-002). Reno, NV: Seismological Laboratory, University of Nevada

Tal, Y., & Hager, B.H. (2015) An empirical study of the distribution of earthquakes with respect to rock type and depth. *Geophysical Research Letters*, 42, 7406–7413

Wiemer, S., Danciu, L., Edwards, B., Marti, M., Fäh, D., Hiemer S, et al. (2016) Seismic Hazard Model 2015 for Switzerland (SUIhaz2015). ETH, Zurich, Switzerland: Swiss Seismological Service

References: EGS and HDR sites:

Breede, K., Dzebisashvili, K., Liu, X., & Falcone, G. (2013) A systematic review of enhanced (or engineered) geothermal systems: past, present and future. *Geothermal Energy*, 1(4), 1–27

Entingh, D.J. (1999) A Review of geothermal well stimulation experiments in the United States. *Geothermal Resources Council Transactions*, 23, 175−180

Smith, M.C. (1983) A history of hot dry rock geothermal energy systems. In G. Heiken, F. Golf (Eds.), Geothermal energy from hot dry rock. *Journal of Volcanology and Geothermal Research*, 15, 1−20

Falkenberg HDR site

Baumgartner, J., Rummel, F., & Zhaotan, C. (1987) Wireline hydraulic fracturing stress measurements in the Falkenberg granite massif. *Geol. Jb.*, E 39, 83−99

Jung, R. (1989) Hydraulic *in situ* investigations of an artificial fracture in the Falkenberg granite. *International Journal of Rock Mechanics Mining Sciences & Geomechanics Abstracts*, 26(3-4), 301−308

Kappelmeyer, O., & Jung, R. (1987) HDR experiments in Bavaria. *Geothermics*, 16(4), 375−392

LSBB Galleries laboratory

Guglielmi, Y., Cappa, F., Avouac, J-P., Henry, P., Elsworth, D. (2015) Seismicity triggered by fluid injection–induced aseismic slip. *Science*, 348(6240), 1224−1226

Guglielmi, Y., Henry, P., Cappa, F., & Derode, B. (2013) Relationships between slow slip, seismicity and fluids leakage during a pressurized fault zone rupture *in situ* experiment: Importance for reservoir/caprock stimulation monitoring and efficiency assessment. Paper presented at 2013 Symposium of American Rock Mechanics Association

Jeanne, P., Guglielmi, Y., & Cappa, F. (2012) Multiscale seismic signature of a small fault zone in a carbonate reservoir: relationships between VP imaging, fault zone architecture and cohesion. Paper presented at AAPG Hedberg Conference on Fundamental Controls on Flow in Carbonates, July 8-13, 2012, Saint-Cyr Sur Mer, France

Jeanne, P., Guglielmi, Y., Lamarche, J., Cappa, F., & Marié, L. (2012) Architectural characteristics and petrophysical properties evolution of a strike-slip fault zone in a fractured porous carbonate reservoir. *Journal of Structural Geology*, 44, 93−109

Fjällbacka HDR site

Eliasson, T., Lindblom, U., Slunga, S., Sundqvist, U., & Wallroth, T. (1987) Some recent development in the Swedish Hot-Dry-Rock Project. Paper presented at Geothermal Resources Council Annual Meeting 1987

Jupe, A.J., Green, A.S.P., & Wallroth, T. (1992) Induced microseismicity and reservoir growth at the Fjallbacka Hot Dry Rocks Project, Sweden. *International Journal of Rock Mechanics Mining Sciences & Geomechanics Abstracts*, 29(4), 343−354

Sundquist, U., Wallroth, T., & Eliasson, T. (1988) The Fjallbacka HDR geothermal energy research project: Reservoir characterisation and injection well stimulation. Report Fj-9, Department of Geology, Chalmers University of Technology/University of Goteborg, Goteborg, Sweden

Wallroth, T., Eliasson, T., & Sundquist, U. (1999) Hot Dry Rock research expeiments at Fjällbacka, Sweden. *Geothermics*, 28, 617−625

Grimsel Rock Laboratory

Alexander, W.R., Frieg, B., Ota, K. (2009) Grimsel Test Site Investigation Phase IV. The Nagra-JAEA *in situ* study of safety relevant radionuclide retardation in fractured crystalline rock. Technical Report 00-07, Nagra, Wettingen, Switzerland

Amann, F., Gischig, V., Evans, K., Doetsch, J., Jalali, R., Valley, B., et al. (2018) The seismo-hydromechanical behavior during deep geothermal reservoir stimulations: open questions tackled in a decameter-scale *in situ* stimulation experiment. *Solid Earth,* 9, 115–137

Davey, A., Karasaki, K., Long, J.C.S., Landsfeld, M., Mensch, A., Martel, S.J. (1989) Analysis of the Hydraulic Data from the MI Fracture Zone at the Grimsel Rock Laboratory, Switzerland. NAGRA-DOE Cooperative Project (Rep. LBL-27864). Berkeley, CA: Lawrence Berkeley Laboratory

Jalali, M.R., Gischig, V., Doetsch, J., Krietsch, H., Amann, F., Klepikova, M. (2017) Mechanical, hydraulic and seismological behavior of crystalline rock as a response to hydraulic fracturing at the Grimsel Test Site. Paper presented at 51st American Rock Mechanics Association Symposium, San Francisco, CA.

Nojima-Ogura fault test site

Ito, H., Kuwahara, Y., Kiguchi, T., Fujimoto, K., & Ohtani, T. (2000) Outline of the Nojima fault drilling by GSJ: Sructure, physical properties and permeability structure from borehole measurements in GSJ borehole crossing the Nojima Fault, Japan. In H. Ito, K. Fujimoto, H. Tanaka, D. Lockner, D. (Eds.), Proceedings of the International Workshop on the Nojima Fault Core and Borehole Data Analysis, November 22-23, 1999, Tsukuba, Japan. Interim Report No EQ/00/1, Geological Survey of Japan. Open File Report 00-129, Washington, DC: U.S. Geological Survey

Kiguchi, T., Ito, H., Kuwahara, Y., & Miyazaki, T. (2001) Estimating the permeability of the

Nojima Fault Zone by a hydrophone vertical seismic profiling experiment. *The Island Arc*, 10, 348–356

Kitagawa, Y., & Kano, Y. (2016) Changes in permeability of the Nojima fault damage zone inferred from repeated water injection experiments. *Earth, Planets and Space*, 68, 185-194

Kitagawa, Y., Fujimori, K., & Koizumi, N. (2002) Temporal change in permeability of the rock estimated from repeated water injection experiments near the Nojima fault in Awaji Island, Japan. *Geophysical Research Letters*, 29(10), 1483

Lockner, D., Tanaka, H., Ito, H., Ikeda, R., Omura, K., & Naka, H. (2009) Geometry of the Nojima fault at Nojima-Hirabayashi, Japan – I. A simple damage structure inferred from borehole core permeability. *Pure and Applied Geophysics*, 166, 1649–1667

Mizoguchi, K., Hirose, T., Shimamoto, T., & Fukuyama, E. (2008) Internal structure and permeability of the Nojima fault, Southwest Japan. *Journal of Structural Geology*, 30, 513–524

Morrow, C.A. (2000) Permeability of deep drillhole core samples. In H. Ito, K. Fujimoto, H. Tanaka, D. Lockner, D. (Eds.), Proceedings of the International Workshop on the Nojima Fault Core and Borehole Data Analysis, November 22-23, 1999, Tsukuba, Japan. Interim Report No EQ/00/1, Geological Survey of Japan. Open File Report 00-129, Washington, DC: U.S. Geological Survey

Roeloffs, E.A., & Matsumoto, N. (2000) Hydrologic properties at the GSJ Hirabayashi borehole in the Nojima fault from analysis of pump test and time series data. In H. Ito, K. Fujimoto, H. Tanaka, D. Lockner, D. (Eds.), Proceedings of the International Workshop on the Nojima Fault Core and Borehole Data Analysis, November 22-23, 1999, Tsukuba, Japan. Interim Report No EQ/00/1, Geological Survey of Japan. Open File Report 00-129, Washington, DC: U.S. Geological Survey

Shimazaki, K., Ando, M., Nishigami, K., Oshiman, N. (1998) Water injection experiments at Ogura along the Nojima fault, Japan. *Earth Monthly-Extra,* 21, 33–37

Tadokoro, K., Ando, M., & Nishigami, K. (2000) Induced earthquakes accompanying the water injection experiment at the Nojima fault zone, Japan: Seismicity and its migration. *Journal of Geophysical Research*, 105, 6089–6104

Zhao, D., Kanamori, H., Negishi, H., & Wiens, D. (1996) Tomography of the Source Area of the 1995 Kobe Earthquake: Evidence for Fluids at the Hypocenter? *Science*, 274, 1891–1894

Ogachi HDR site

Audigane, P., Royer, J., & Kaieda, H. (2002) Permeability characterization of the HDR Soultz and Ogachi large-scale reservoir using induced micro-seismicity. *Geophysics*, 67, 204–211

Hori, Y., Kitano, K., Kaieda, H. (1994) Outline of Ogachi project for HDR geothermal power in Japan. *Geothermal Resources Council Transactions*, 18, 439–443

Ito, H. (2003) Inferred role of natural fractures, veins, and breccias in development of the artificial geothermal reservoir at the Ogachi Hot Dry Rock site, Japan. *Journal of Geophysical Research*, 108(B9), 2426

Kaieda, H., Sakunaga, S., Motojima, I., Kondo, H., Kiho, K. (1992) Ogachi project for HDR geothermal power in Japan, first hydraulic fracturing results. *Geothermal Resources Council Transactions*, 16, 493–496

Suenaga, H., Eguchi, Y., Yamamoto, T., Kitano, K. (2000) A fully three-dimensional thermo-hydraulic computation of the Ogachi HDR reservoir. Paper presented at World Geothermal Congress 2000, May 28 - June 10, 2000. Kyushu - Tohoku, Japan

Desert Peak EGS site

Benato, S., Hickman, S., Davatzes, N.C., Taron, J., Spielman, P., Elsworth, D., et al. (2016) Conceptual model and numerical analysis of the Desert Peak EGS project: Reservoir response to the shallow medium flow-rate hydraulic stimulation phase. *Geothermics*, 63, 139–156

Benato, S., Reeves, C.M., Parashar, R., Davatzes, N.C., Hickman, S., Elsworth, D., et al. (2013) Computational investigation of hydro-mechanical effects on transmissivity evolution during the initial injection phase at the Desert Peak EGS project, NV. Paper presented at 38th Workshop on Geothermal Reservoir Engineering at Stanford University (SGP-TR-198). Stanford, CA

Robertson-Tait, A., Lutz, S.J., Sheridan, J., & Morris, C.L. (2004) Selection of an interval for massive hydraulic stimulation in well DP 23-1, Desert Peak East EGS project, Nevada. Paper presented at 29th Workshop on Geothermal Reservoir Engineering at Stanford University (SGP-TR-175). Stanford, CA

Sanyal, S.K., Lovekin, J.W., Henneberger, R.C., Robertson-Tait, A., Brown, P.J., Morris, C., & Schochet, D. (2003) Injection testing for an enhanced geothermal systems project at Desert Peak, Nevada. *Geothermal Resources Council Transactions*, 27, 885–891

Stacey, R.W., Robertson-Tait, A., Drakos, P., & Zemach, E. (2010) EGS stimulation of well 27-15, Desert Peak geothermal field, Nevada. *Geothermal Resources Council Transactions*, 34, 451–456

Raft River EGS site

Ayling, B., & Moore, J. (2013) Fluid geochemistry at the Raft River geothermal field, Idaho, USA: New data and hydrogeological implications. Geothermics 47, 116–126

Bradford, J., McLennan, J., Moore, J., Glasby, D., Waters, D., Kruwell, R., et al. (2013) Recent developments at the Raft River geothermal field. Paper presented at 38th Workshop on Geothermal Reservoir Engineering at Stanford University (SGP-TR-198). Stanford, California

Bradford, J., McLennan, J., Moore, J., Podgorney, R., & Tiwari, S. (2015) Hydraulic and Thermal Stimulation Program at Raft River Idaho, a DOE EGS. *Geothermal Resources Council Transactions*, 39, 261–268

Bradford, J., McLennan, J., Moore, J., Podgorney, R., Plummer, M., & Nash, G. (2017) Analysis of the thermal and hydraulic stimulation program at Raft River, Idaho. *Rock Mechanics and Rock Engineering*, 50, 1279–1287

Covington, H.R. (1980) Subsurface geology of the Raft River geothermal field, Idaho. *Geothermal Resources Council Transactions*, 4, 113–115

Diek, A., White, L., Roegiers, J.C., Moore, J., & McLennan, J.D. (2012) Borehole preconditioning of geothermal wells for enhanced geothermal system reservoir development. Paper presented at 37th Workshop on Geothermal Reservoir Engineering at Stanford University (SGP-TR-194). Stanford, CA.

Plummer, M., Palmer, C., Podgorney, R., Bradford, J., & Moore, J. (2014) Hydraulic response to thermal stimulation efforts at Raft River based on stepped rate injection testing. Paper presented at 39th Workshop on Geothermal Reservoir Engineering at Stanford University (SGP-TR-202), Stanford, CA.

Hijiori HDR site

Kaieda, H. (2015) Multiple reservoir creation and evaluation in the Ogachi and Hijiori HDR projects, Japan. Paper presented at 2015 World Geothermal Congress. Melbourne, Australia

Kitani, S., & Tezuka, K. (1999) Geologic structure and fracture system of hot dry rock reservoir in Hijiori field Yamagata Prefecture, Japan. *Geothermal Resources Council Transactions*, 23, 281–287

Kobayashi, H., Kurigawa, M., & Sasaki, S. (1987) Hydraulic fracturing tests to make a geothermal reservoir for Hot Dry Rock development at Hijiori field, Japan. *Geothermal Resources Council Transactions*, 11, 553−558

Sasaki, S. (1998) Characteristics of microseismic events induced during hydraulic fracturing experiments at the Hijiori hot dry rock geothermal energy site, Yamagata, Japan. *Tectonophysics*, 289, 171–188

Sasaki, S., & Kaieda, H. (2002) Determination of stress tate from focal mechanisms of microseismic events induced during hydraulic injection at the Hijiori Hot Dry Rock site. *Pure and Applied Geophysics*, 159, 489–516

Takada, K., Arihara, N., & Osato, K. (1997) Simulation of circulation tests at the Hijiori hot dry rock wells. Paper presented at 21st Workshop on Geothermal Reservoir Engineering at Stanford University (GP-TR-155). Stanford, CA.

Tenma, N., Sato, Y., Matsuwagai, I., Kuriyagawai, M., Yamaguchii, T., Zyvoloski, G., & Miyairi, M. (1994) Model study of the reservoir character at Hijiori HDR test site. *Geothermal Resources Council Transactions*, 18, 475–478

Tenma, N., Yamaguchi, T., Matsunaga, I., Kuriyagawa, M., & Sato, Y. (1996) Interference of production between two wells during a one month circulation test at the Hijiori Hot Dry Rock test site. Paper presented at 21st Workshop on Geothemal Reservoir Engineering at Stanford University (SGP-TR-151). Stanford, CA.

Yamaguchi, T., Hiwaki, N., Abe, T., & Oikawa, Y. (1992) 90-day circulation test at Hijiori HDR test site. *Geothermal Resources Council Transactions*, 16, 417–422

Rosemanowes Quarry HDR site

Heath, M.J. (1985) Geological control of fracture permeability in Carnmenellis granite, Cornwall: implications for radionuclide migration. *Mineralogical Magazine*, 49, 233–244

Hirschberg, S., Wiemer, S., Burgherr, P. (2015) Energy from the Earth: Deep geothermal as a resource for the future? 2015 vdf Hochschulverlag AG an der ETH Zürich. doi:10.3218/3655-8

Pine, R., Ledingham, P., & Merrifield, C.M. (1983) In-situ stress measurements in the Carmenellis Granite-II. Hydrofracture tests at Rosemanowes Quarry to depths of 2000 m. *International Journal of Rock Mechanics Mining Sciences & Geomechanics Abstracts*, 20(2), 63–72

Pine, R.J. (1983) Pressure transient analysis for large scale hydraulic injections in the Carnmenellis granite, England. Paper presented at 9th Workshop Geothermal Reservoir Engineering at Stanford University (SGP-TR-74). Stanford, CA.

Pine, R.J., & Batchelor, A.S. (1984) Downward Migration of Shearing in Jointed Rock During Hydraulic Injections. *International Journal of Rock Mechanics Mining Sciences & Geomechanics Abstracts*, 21(5), 249–263

Richards, H.G., Parker, R.H., Green, A.S.P., Jones, R.H., Nicholls, J.D.M., Nicol, D.A.C., et al. (1994) The performance and characteristics of the experimental Hot Dry Rock geothermal reservoir at Rosemanowes, Cornwall (1985–1988). *Geothermics*, 23(2), 73–109

Watkins, D.C. (2003) Determining a representative hydraulic conductivity of the Carnmenellis Granite of Cornwall, UK, based on a range of sources of information. Paper presented at International Conference on Groundwater in Fractured Rocks, Prague, Chech Republic. In J. Krásný, Z. Hrkal, J. Bruthans (Eds.), IHP-VI, Series on Groundwater (No. 7), ISBN 92-9220-002-X

The NW Geysers EGS site

Garcia, J., Hartline, C., Walters, M., Wright, M., Rutqvist, J., Dobson, P.F., Jeanne, P. (2016) The Northwest Geysers EGS Demonstration Project, California, Part 1: Characterization and reservoir response to injection. *Geothermics*, 63, 97–119

Jeanne, P., Rutqvist, J., Rinaldi, A.P., Dobson, P.F., Walters, M., Hartline, C., & Garcia, J. (2015) Seismic and aseismic deformations and impact on reservoir permeability: the case of EGS stimulation at The Geysers, California, USA. *Journal of Geophysical Research Solid Earth*, 120, 7863–7882

Jeanne, P., Rutqvist, J., Vasco, D., Garcia, J., Dobson, P.F., Walters, M., et al. (2014) A 3D hydrogeological and geomechanical model of an Enhanced Geothermal System at The Geysers, California. *Geothermics*, 51, 240–252

Nielson, D.L., Walters, M.A., & Hulen, J.B. (1991) Fracturing in the Northwest Geysers, Sonoma County, California. *Geothermal Resources Council Transactions*, 15, 27–33

Persoff, P., & Hulen, J.B. (2001) Hydrologic characterization of reservoir metagreywacke from shallow and deep levels of The Geysers vapor-dominated geothermal system, California, USA. *Geothermics*, 30, 169–192

Sternfeld, J.N. (1989) Lithologic Influences on fracture permeability and the distribution of steam in the Northwest Geysers steam field, Sonoma County, California. *Geothermal Resources Council Transactions*, 13, 437–479

Fenton Hill HDR site

Birdsell. S.A., & Robinson, B.A. (1988) A three-dimensional hodel of fluid, heat, and tracer transport in the Fenton Hill hot dry rock reservoir. Paper presented at 13th Workshop on Geothermal Reservoir Engineering at Stanford Universily (SGP-TR-113). Stanford, CA

Brown, D., & DuTeux, R. (1997) Three principal results from recent Fenton Hill Flow testing. Paper presented at 21st Workshop on Geothermal Reservoir Engineering at Stanford University (SGP-TR-155). Stanford, CA

Dash, Z.V., Dreesen, D.S., Walter, F., & House, L. (1985) The massive hydraulic fracture of Fenton Hill HDR Well EE-3. *Geothermal Resources Council Transactions*, 9(2), 83–88

Dash, Z.V., Murphy, H.D., Aamodt, R.L., Aguilar, R.G., Brown, D.W., Counce DA, et al. (1983) Hot dry rock geothermal reservoir testing: 1978 to 1980. *Journal of Volcanology and Geothermal Research*, 15, 59–99

Duchane, D., & Brown, D. (2002) Hot Dry Rock (HDR) geothermal energy research and development at Fenton Hill, New Mexico. *GHC Bulletin*, 13–19

Fisher, H-N., & Tester, J.W. (1979) An analysis of the pressure transient testing of a man-made fractured geothermal reservoir. Paper presented at Geothermal Reservoir Engineering Workshop at Stanford University. Stanford, CA

Fisher, H.N., Tester, J.W. (1980) The pressure transient testing of a man-made fractured geothermal reservoir: An examination of fracture versus matrix dominated flow effect. (Rep. LA-8535-MS, 33 pp.). Los Alamos, NM: Los Alamos National Laboratory

Laughlin, A.W., Eddy, A.C., Laney, R., & Aldrich, M.J. Jr (1983) Geology of the Fenton Hill, New Mexico, hot dry rock site. *Journal of Volcanology and Geothermal Research*, 15, 21–41

Shapiro, S.A., Patzig, R., Rothert, E., & Rindschwentner, J. (2003) Triggering of seismicity by pore-pressure perturbations: permeability-related signatures of the phenomenon. *Pure and Applied Geophysics*, 160, 1051–1066

Yamamoto, T., Eguchi, Y., Kitano, K., Brown, D., Duchane, D., Fehler, M., & Ohnishi, H. (1998) Simulating Fenton Hill HDR test results using the GEOTH3D code. Paper presented at 23rd Workshop on Geothermal Reservoir Engineering at Stanford University (SGP-TR-158). Stanford, CA

Habanero EGS site

Baisch, S., Weidler, R., Voros, R., Wyborn, D., & de Graaf, L. (2006) Induced seismicity during the stimulation of a geothermal HFR reservoir in the Cooper Basin, Australia. *Bulletin of the Seismological Society of America*, 96(6), 2242–2256

Chen, D., & Wyborn, D. (2009) Habanero field tests in the Cooper Basin, Australia: a proof-of-concept for EGS. *Geothermal Resources Council Transactions*, 33, 159–164

Cox, S.F. (2016) Injection-driven swarm seismicity and permeability enhancement: implications for the dynamics of hydrothermal ore systems in high fluid-flux, overpressured faulting regimes—an invited paper. *Economic Geology*, 111(3), 559–587

Holl, H-G., & Barton, C. (2015) Habanero field - structure and state of stress. Paper presented at 2015 World Geothermal Congress. Melbourne, Australia

Llanos, E.M., Zarrouk, S.J., & Hogarth, R.A. (2015) Numerical model of the Habanero geothermal reservoir, Australia. *Geothermics*, 53, 308–319

Pohang EGS site

Kim, C-M., Raehee, H.R., Gi, Y.J., Jong, Ok. J.O., & Moon, S. (2016) Internal structure and materials of the Yangsan fault, Bogyeongsa area, Pohang, South Korea. *Geosciences Journal*, 20(6), 759–773

Lee, T.J., Song, Y., Park, D.W., Jeon, J., & Yoon, W.S. (2015) Three dimensional geological model of Pohang EGS pilot site, Korea. Paper presented at 2015 World Geothermal Congress. Melbourne, Australia

Park, S., Xie, L., Kim, K-I., Kwon, S., Min, K-B., Choi, J., Yoon, W-S., & Song, Y. (2017) First Hydraulic Stimulation in Fractured Geothermal Reservoir in Pohang PX-2 Well. Paper presented at 42nd Workshop on Geothermal Reservoir Engineering at Stanford University (SGP-TR-212). Stanford, CA

Song, Y., Lee, T.J., Jeon, J., & Yoon, W.S. (2015) Background and progress of the Korean EGS pilot project. Paper presented at 2015 World Geothermal Congress. Melbourne, Australia

Urach-3 HDR site

Genter, A. (1994) Structural analysis of core in the crystalline section of the borehole Urach 3 (Swabian Alb, Germany). Bureau de recherches géologiques et minières (BRGM), France

Heinemann, B., Troschke, B., & Tenzer, H. (1992) Hydraulic investigations and stress evaluation at the HDR test site Urach III, Germany. *Geothermal Rescources Council Transactions*, 16, 425–431

McClure, M.W. (2012) Modeling and characterization of hydraulic stimulation and induced seismicity in geothermal and shale gas reservoirs, (Doctoral dissertation). Retrieved from SearchWorks catalog. (http://purl.stanford.edu/dw028kp1342). Stanford University, CA.

McDermott, C.I., Randriamanjatosoa, A.L., Tenzer, H., Sauter, M., & Kolditz, O. (2005) Processes in crystalline HDR geothermal energy recovery: preliminary application to Spa Urach. *Geothermal Resources Council Transactions*, 29, 649–658

Stober, I. (2011) Depth- and pressure-dependent permeability in the upper continental crust: data from the Urach 3 geothermal borehole, southwest Germany. *Hydrogeology Journal*, 19(3), 685–699

Stober, I., & Bucher, K. (2000) Hydraulic properties of the upper continental crust: data from the Urach 3 geothermal well. Chapter 2 Hydraulic properties of crystalline rocks. In I. Stober, K. Bucher (Eds.), Hydrogeology of crystalline rocks. Water Science and Technology Library Series (Vol. 34), Dordrecht, The Netherlands: Springer. doi:10.1007 /978-94-017-1816-5

Stober, I., & Bucher, K. (2004) Fluid sinks within the earth's crust. *Geofluids*, 4, 143–151

Stober, I., & Bucher, K. (2007) Hydraulic properties of the crystalline basement. *Hydrogeology Journal*, 15, 213–224

Tenzer, H., Schanz, U., & Homeier, G. (2000) HDR Research programme and results of drill hole Urach 3 to depth of 4440 m – the key for realisation of a HDR programme in southern Germany and northern Switzerland. Paper presented at 2000 World Geothermal Congress. Kyushu - Tohoku, Japan

Basel EGS site

Deichmann, N., Krafta, T., & Evans, K.F. (2014) Identification of faults activated during the stimulation of the Basel geothermal project from cluster analysis and focal mechanisms of the larger magnitude events. *Geothermics*, 52, 84–97

Häring, M.O., Schanz, U., Ladner, F., & Dyer, B.C. (2008) Characterisation of the Basel 1 enhanced geothermal system. *Geothermics*, 37, 469–495

Kaeser, B., Kalt, A., & Borel, J. (2007) The crystalline basement drilled at the Basel-1 geothermal site, a preliminary petrological-geochemical study. Nuchatel, Switzerland: Institut de Géologie et d'Hydrogéologie, Université de Neuchâtel

Kraft, T., & Deichmann, N. (2014) High-precision relocation and focal mechanism of the injection-induced seismicity at the Basel EGS. *Geothermics*, 52, 59–73

Ladner, F., & Häring, M.O. (2009) Hydraulic characteristics of the Basel 1 Enhanced Geothermal System. *Geothermal Resources Council Transactions*, 33, 199–203

Miller, S.A. (2015) Modeling enhanced geothermal systems and the essential nature of large-scale changes in permeability at the onset of slip. *Geofluids*, 15, 338–349

Terakawa, T., Miller, S.A., & Deichmann, N. (2012) High fluid pressure and triggered earthquakes in the enhanced geothermal system in Basel, Switzerland. *Journal of Geophysical Research − Solid Earth*, 117, B07305

Soultz-sous-Forêts EGS site

Audigane, P., Royer, J., & Kaieda, H. (2002) Permeability characterization of the HDR Soultz and Ogachi large-scale reservoir using induced micro-seismicity. *Geophysics*, 67, 204–211

Baumgartner, J., Jung, R., Gerard, A., Baria, R., & Garnish, J. (1996) The European Hot Dry Rock Project at Soultz-sous-Forêts: Stimulation of the second deep well and the first circulation experiments. Paper presented at 21st Workshop on Geothermal Reservoir Engineering at Stanford University. Stanford, CA

Dezayes, C., Genter, A., & Valley, B. (2010) Overview of the fracture network at different scales within the granite reservoir of the EGS Soultz site (Alsace, France). Paper presented at 2010 World Geothermal Congress 2010. Bali, Indonesia

Dezayes, C., Genter, A., & Valley, B. (2010) Structure of the low permeable naturally fractured geothermal reservoir at Soultz. *Comptes Rendus Geoscience*, 342, 517–530

Evans, K., Genter, A., & Sausse, J. (2005) Permeability creation and damage due to massive fluid injections into granite at 3.5 k depth, at Soultz: 1. Borehole observations. *Journal of Geophysical Research*, 110, B04203

Evans, K., Moriya, H., Niitsuma, H., Jones, R., Phillips, W., Genter, A., et al. (2005) Microseismicity and permeability enhancment of hydrogeologic structures during massive fluid injections into granite at 3 km depth at the Soultz HDR site. *Geophysical Journal International*, 160, 388–412

Genter, A., & Traineau, H. (1992) Borehole EPS-1, Alsace, France: preliminary geological results from granite core analyses for Hot Dry Rock research. *Scientific Drilling*, 3, 205–214

Genter, A., & Traineau, H. (1996) Analysis of macroscopic fractures in granite in the HDR geothermal well EPS-l, Soultz-sous-Forêts, France. *Journal of Volcanology and Geothennal Research*, 72, 121–141

Genter, A., Castaing, C., Dezayes, C., Tenzer, H., Traineau, H., & Villemin, T. (1997) Comparative analysis of direct (core) and indirect (borehole imaging tools) collection of fracture data in the Hot Dry Rock Soultz reservoir (France). *Journal of Geophysical Research*, 102, 15419–15431

Genter, A., Vidal, J., Baujard, C., Dalmais, E., & Schmittbuhl, J. (2015) Permeability in deep-seated granitic rocks: lessons learnt from deep geothermal boreholes in the Upper Rhine Graben. Vingtièmes journées techniques du Comité Français d'Hydrogéologie de l'Association Internationale des Hydrogéologues. Aquifères de socle : le point sur les concepts et les applications opérationnelles. La Roche-sur-Yon

Gentier, S., Rachez, X., Ngoc, T.D.T., Peter-Borie, M., & Souque, C. (2010) 3D flow of the medium-term circulation test performed in the deep geothermal site of Soultz-sous-Forêts (France). Paper presented at 2010 World Geothermal Congress. Bali, Indonesia

Geraud, Y., Rosener, M., Surma, F., Place, J., Le Garzic, E., & Diraison, M. (2010) Physical properties of fault zones within a granite body: Example of the Soultz-sous-Forêts geothermal site. *CR Geoscience*, 342, 566–574

Jung, R. (1991) Hydraulic fracturing and hydraulic testing in the granitic section of borehole GPK1, Soultz-sous-Forêts. In J.C. Bresee (Ed.), European HDR Project at Soultz-sous-Forêts. *Geothermal Science & Technology*, 3(1-4), 149–197

Jung, R., Willis-Richards, J., Nicholls, J., Bertozzi, A., & Heinemann, B. (1995) Evaluation of hydraulic tests at Soultz-sous-Forêts, European HDR Site. Paper presented at 1995 World Geothermal Congress. Florence, Italy

Kosack, C., Vogt, C., Marquart, G., Clauser, C., & Rath, V. (2011) Stochastic permeability estimation for the Soultz-sous-Forêts EGS reservoir. Paper presented at 36th Workshop on Geothermal Reservoir Engineering at Stanford University (SGP-TR-191). Stanford, CA.

Ledésert, B., Hebert, R., Genter, A., Bartier, D., Clauer, N., & Grall, C. (2010) Fractures, hydrothermal alterations and permeability in the Soultz Enhanced Geothermal System. *Comptes Rendus Geoscience*, 342(7–8), 607–615

McClure, M.W., & Horne, R.N. (2011) Pressure transient analysis of fracture zone permeability at Soultz-sous-Forêts. *Geothermal Resources Council Transactions*, 35, 1487–1498

Michelet, S., & Toksoz, M.N. (2007) Fracture mapping in the Soultz-sous-Forêts geothermal field using microearthquake locations. *Journal of Geophysical Research*, 112, B07315

Sanjuan, B., Pinault, J., Rose, P., Gérard, A., Brach, M., Braibant, G., et al. (2006) Tracer testing of the geothermal heat exchanger at Soultz-sous-Forêts (France) between 2000 and 2005. *Geothermics*, 35, 622–653

Sausse, J., & Genter, A. (2005) Types of permeable fractures in granite. In P.K. Harvey, T.S. Brewer, P.A. Pezard, V.A. Petrov (Eds.), Petrophysical properties of crystalline rocks. *Special Publications* (Vol. 240, pp. 1–14). London, England: *Geological Society*

Sausse, J., Dezayes, C., Genter, A., & Bisset, A. (2008) Characterization of fracture connectivity and fluid flow pathways derived from geological interpretation and 3D modelling of the deep seated EGS reservoir of Soultz (France). Paper presented at 33rd Workshop on Geothermal Reservoir Engineering at Stanford University. Stanford, CA.

Sausse, J., Fourar, M., & Genter, A. (2006) Permeability and alteration within the Soultz granite inferred from geophysical and flow log analysis. *Geothermics*, 35, 544–560

Shapiro, S.A., Audigane, P., Royer, J-J. (1999) Large-scale *in situ* permeability tensor of rocks from induced microseismicity. *Geophysical Journal International*, 137, 207–213

Valley, B.C. (2007) The relation between natural fracturing and stress heterogeneities in deep-seated crystalline rocks at Soultz-sous-Forêts (France). (Doctoral dissertation No. 17385). Retrieved from ETHZ (doi:10.3929/ethz-a-005562794). Zurich, Switzerland: ETHZ.

Vogt, C., Marquart, G., Kosack, C., Wolf, A., & Clauser, C. (2012) Estimating the permeability distribution and its uncertainty at the EGS demonstration reservoir Soultz-sous-Forêts using the ensemble Kalman filter. *Water Resources Research*, 48, W08517

Weidler, R., Gerard, A., Baria, R., Baumgartner, J., & Jung, R. (2002) Hydraulic and micro-seismic results of a massive stimulation test at 5 km depth at the European Hot-Dry-Rock test site, Soultz, France. Paper presented at 27th Workshop on Geothermal Reservoir Engineering at Stanford University. Stanford, CA.

KTB (German Continental Deep Drilling Program) drill site

Baisch, S., Bohnhoff, M., Ceranna, L., Tu, Y., & Harjes, H-P. (2002) Probing the crust to 9 km depth: Fluid injection experiments and induced seismicity at the KTB superdeep drilling hole, Germany. *Bulletin Seismological Society of America*, 92, 2369–2380

Emmermann, R., & Lauterjung, J. (1997) The German Continental Deep Drilling Program KTB: Overview and major results. *Journal of Geophysical Research*, 102, 18179–18201

Grasle, W., Kessels, W., Kumpel, H-J., & Li, X. (2006) Hydraulic observations from a one year fluid production test in the 4000 m deep KTB pilot borehole. *Geofluids*, 6, 8–23

Hirschmann, G., Duyster, J., Harms, U., Kontny, A., Lapp, M., Wall, H.D., & Zulauf, G. (1997) The KTB superdeep borehole: petrography and structure of a 9-km-deep crustal section. *Geologische Rundschau*, 86(0), S3–S14

Huenges, E., Erzinger, J., Kuck, J., Engeser, B., & Kessels, W. (1997) The permeable crust: Geohydraulic properties down to 9101m depth. *Journal of Geophysical Research*, 102(B8), 18255–18265

Kessels, W., & Kuck, J. (1995) Hydraulic communication in the crystalline rock between the two boreholes of the continental deep drilling programme in Germany. *International Journal of Rock Mechanics and Mining Sciences & Geomechanics Abstracts*, 32, 37–47

Rothert, E., & Shapiro, S. (2003) Microseismic monitoring of borehole fluid injections: Data modeling and inversion for hydraulic properties of rocks. *Geophysics*, 68, 685–689

Shapiro, S.A., Audigane, P., & Royer, J-J. (1999) Large-scale *in situ* permeability tensor of rocks from induced microseismicity. *Geophysical Journal International*, 137, 207–213

Shapiro, S.A., Huenges, E., & Borm, G. (1997) Estimating the crust permeability from fluid-injection-induced seismic emission at the KTB site. *Geophysical Journal International*, 131, F15–F18

Shapiro, S.A., Kummerow, J., Dinske, C., Asch, G., Rothert, E., Erzinger, et al. (2006) Fluid induced seismicity guided by a continental fault: Injection experiment of 2004/2005 at the German Deep Drilling Site (KTB). *Geophysical Research Letters*, 33, L01309

Wagner, G.A., Coyle, D.A., Duyster, J., Henjes-Kunst, F., Peterek, A., Schröder, B., et al. (1997) Post-Variscan thermal and tectonic evolution of the KTB site and its surroundings. *Journal of Geophysical Research*, 102(B8), 18221–18232

Zimmermann, G., Burkhardt, H., & Engelhard, L. (2003) Scale dependence of hydraulic and structural parameters in the crystalline rock of the KTB. *Pure and Applied Geophysics*, 160, 1067–1085

Zimmermann, G., Korner, A., & Burkhardt, H. (2000) Hydraulic pathways in the crystalline rock of the KTB. *Geophysical Journal International*, 142, 4–14

Zoback, M.D., & Harjes, H-P. (1997) Injection-induced earthquakes and crustal stress at 9 km depth at the KTB deep drilling site, Germany. *Journal of Geophysical Research*, 102, 18477–18491

CHAPTER 6

6 The bulk permeability of fault rocks and protoliths: Insights from statistical analysis

Chapter 6 focuses on the regression of bulk permeability of fault zones and protoliths, where most of the test points within the fault zone are in the damage zone, including parts of fault core that could not be separated hydraulically in-situ. The chapter also provides a new conceptual discussion of the geothermal-metamorphic curve for permeability-depth relationship, linking the time-averaged fluid fluxes over geologic time to the fault zone permeability. The paper ends with new ideas and recommendations for about modeling the crustal permeability that includes the effects of fault conduits.

6.1 Abstract

In the Earth's brittle crust, the permeability contrast between deformed fault rocks and the surrounding host rocks largely determines how fault zones affect fluid flow. We compiled fault zone and protolith permeability data from numerous studies at individual sites to support a broad analysis of trends and correlations. Fault zones, here represented by data from fractured rocks within the fault damage zones, and in some cases including parts of the fault core that could not be separated from the damage zone in in-situ tests at depth. Thus defined, the bulk permeability of fault zones in metamorphic/plutonic rocks show a weak but significant trend of decreasing bulk permeability with depth. At depths of up to several km, these structures serve as fluid conduits (>10^{-17} m^2 threshold). The bulk permeability of fault zone and protolith are strongly correlated for rock types other than coarse-grained siliciclastic rocks. The permeability of fault zones in most rock types can be predicted empirically from the average permeability of the protolith, which explains >50% to 75% of variance. This result is not affected by the weaker trends of bulk permeability with depth. The regression trend between the fault and protolith bulk permeabilities remains unexplained, although we offer tentative hypotheses. Comparisons between fault damage-zone permeability values measured *in situ* and permeability values inferred indirectly from geologic evidence suggests that fault zones, rather than the undeformed protolith, control the

large-scale permeability of the Earth's crust.

6.2 Introduction

When modeling geomechanical behavior, fluid flow, and other coupled processes in the faulted brittle crust, the permeability contrast between a fault zone and protolith (host rock) is an essential consideration (e.g. Rice 1992, Scholz and Anders 1994, Townend and Zoback 2000). At the crustal scale, percolation of fluids over geologic time through faulted and not faulted crust are affected by the permeability evaluated at sufficiently large scales (e.g. Miller and Nur 2000, Zimmermann et al. 2003). In crustal rocks, "bulk permeability" typically refers to the results of *in situ* tests in naturally fractured rocks (or large fractured rock samples) and is normally higher than the "matrix permeability" of the cohesive solid rock that is micro-fractured and contains pore spaces between mineral grains (e.g. primary porosity in sedimentary rocks, pore spaces in pervasively altered feldspars, clay and other porous mineral fills in fractures, etc.) and inter-granular (Zoback and Byerlee 1975, Coyle and Zoback 1988). The depth-variation of both matrix and bulk permeability in the brittle crust is still poorly known due to scarcity of deep scientific drillholes, as shown in past reviews (e.g. Juhlin and Sandstedt 1989, Townend and Zoback 2000, Ingebritsen and Manning 2010, IEAGHG 2016) and regionally specific models and depth trends for permeability to a few kilometres depth (Thury et al. 1994, Huenges et al. 1997, Fisher 1998, Saar and Manga 2004, Stober and Bucher 2007, Vitovtova et al. 2014, Achtziger-Zupancic et al. 2017).

In this work we explore a global dataset from a recently developed database by Scibek (2019 submitted - a). The database summarizes best estimates of fault zone (damage zone, and in a some cases also the fault core as part of tested zone) and protolith permeability (429 datasets from 364 sites).

Locations in the database represent a very small sample of the Earth's faulted crust. One example is shown in Figure 6-1, comparing active fault maps of Japan and western USA states with hydraulic test site locations. Less than 0.1% of major Quaternary faults have been tested, based on the ratio of the number of test sites to the total fault length in km. This is an underestimate, because more than one drillhole or test site is needed to characterize bulk permeability of 1-km-long fault segments. Over large regions and many test sites, the depth distribution of hydraulic tests in fault zones can be compared (Figure 6-1
Figure 6-1**c**).

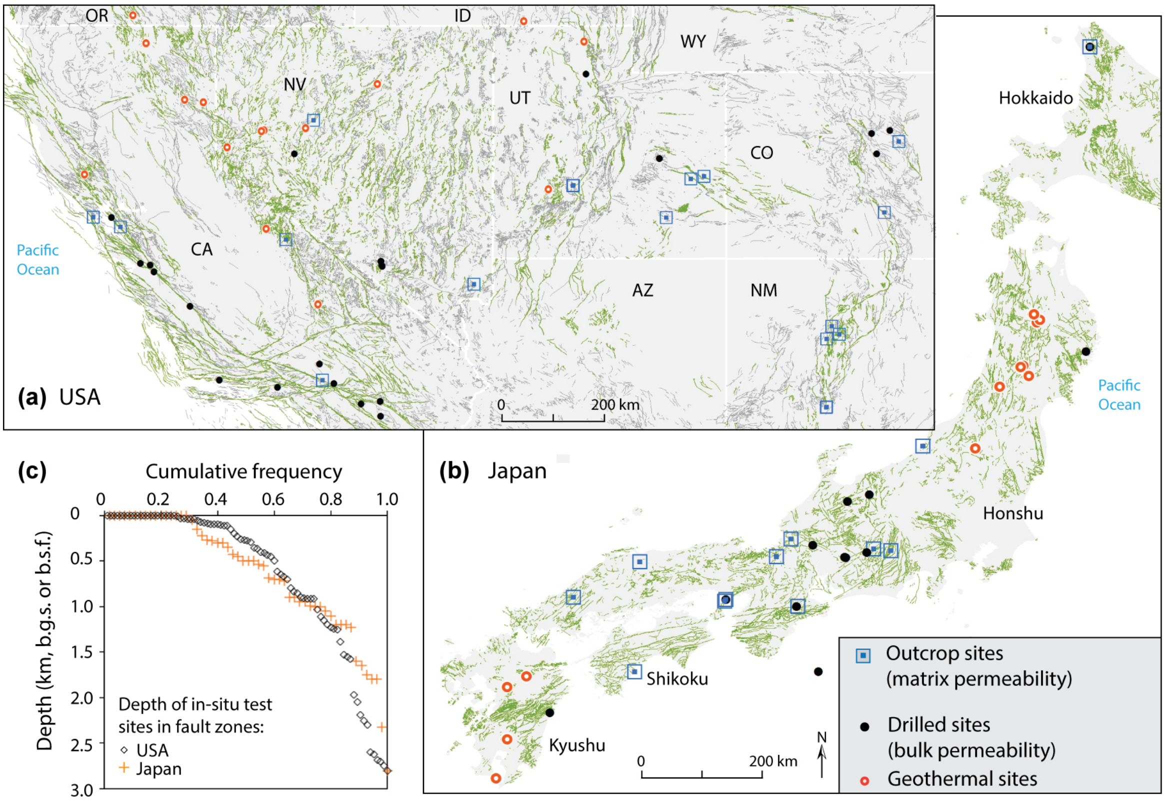

Figure 6-1 Locations of test sites in fault zones from the database of Scibek et al. (2019 submitted - a) and digital maps of major faults: (a) western USA - Quaternary faults in green shade (USGS 2006) and other faults in grey (USGS 2016), (b) Japan - active faults from (GSJ 2012), (c) cumulative frequency of in situ hydraulic tests with depth. Fault outcrop locations are at 0 depth.

A fault damage zone refers to more densely fractured rock than that of the sparsely fractured protolith. The damage zone may border or contain narrow fault core(s), including intensely deformed rocks along fault slip surfaces that may contain cataclastic rocks (Chester and Logan 1986, Caine et al. 1996). Most of the *in situ* hydraulic test data come from the damage zones of faults. At many geothermal fields, the tests are in faulted rocks but the fault core zone cannot be separated from the damage zone, thus the data represent fault zone in general. The fault core is a narrow zone of usually less-permeable fault rock than the fractured damage zone, and the narrow width limits the transmissivity component of fault core in the wider fault zone. Fault core rocks are difficult to isolate in-situ at depth in drillholes, are usually not transmissive enough to pump from, and injection tests may leak into adjacent fractures of the damage zone. In the database of permeability values and case studies, unless the fault core is proven to be isolated in the test from the damage zone, or the damage zone is proven to be less permeable and transmissive than the damage zone in the wider test interval, based on other test results, the overall bulk permeability is attributed to the damage zone. For example, at geothermal reservoirs, the fractured rocks in overlapping fault damage zones are the fluid sources, while fault cores are usually considered barriers to cross-fault flow and compartment boundaries. Evidence from inflow points in deep and long transportation tunnels, strongly suggests that the most permeable zones are usually associated with macroscopic fractures in the damage zone (e.g. Masset and Loew 2013, Holmoy 2008, Seebeck et al. 2014).

Drill core and outcrop samples from the fault core are usually tested in a laboratory permeameter apparatus to determine the matrix permeability. The matrix permeability is usually smaller in magnitude than the bulk permeabilities obtained from larger-scale tests in the damage zone (Brace 1980, 1984). Here we focus here on the bulk permeability of damage zones to characterize these conduits in the brittle crust.

6.3 Methods

6.3.1 Permeability datasets by lithologic category

Subsets of data were created by sorting according to simplified lithologic categories (Table 6-1). Regressions were done for each subset of these 9 lithological categories. These categories were: 1 - siliciclastic coarse, 2 - mudrocks, 3 - carbonate, 4 - volcaniclastic, 5 - volcanic igneous, 6 - all volcanic (volcaniclastic & volcanic igneous), 7 - plutonic (igneous intrusive), 8 - metamorphic, and 9 - plutonic & metamorphic (all basement rocks).

Each individual data point used in our study represents the best estimate of permeability from one dataset from a particular site. Scibek (2019 submitted - a) described the methods and here we summarize briefly. For each study site, permeability data were assigned to a simplified structural domain consisting of fault core, fault damage zone, and protolith, and to one of the two permeability test scales, matrix and bulk. At about 18% of the geographically distinct sites there were datasets for multiple fault zones, whereas for the remainder a single fault zone was tested. The mean or median values are reported as taken from original publications, and in a few cases the representative value was estimated as part of this review. The statistics refer to log permeability values (matrix and bulk permeability separately). This is discussed in methods and results. A representative permeability, was entered after a review of the available information, and in nearly all cases we relied on the conclusions and analyses of the original authors, in regards to the magnitude of fault zone permeability (or architectural components of fault zone where possible).

Table 6-1 Fault-zone permeability data by lithologic category.

Category	Lithologic sub-category	Fault Damage Zone (FDZ)	Protolith	Ratio (FDZ / Protolith)	Protolith *matrix*
Sedimentary					
siliciclastic	sandstone	19	13	11	3
	conglomerate	4	1	1	3
mudrock	siltstone	2	2	2	4
	argillite-claystone	2	2	2	2
	mudstone	5	3	3	3
	shale [a]	1	1	1	0
	marl	5	5	5	0
carbonate	limestone-dolomite	21	13	13	3
	marble [a]	1	1	1	0
Volcanic					
volcaniclastic	tuff	8	4	4	2
	tuff (welded)	5	4	4	0
	volcaniclastic conglomerates	4	2	2	2
volcanic	andesite-rhyolite	32	15	15	4
igneous	basalt	31	10	10	1
Plutonic					
	gabbro	4	3	3	1
	granite	80	63	62	10
	granodiorite	25	9	9	5
Metamorphic					
	metabasalt	1	1	1	1
	amphibolite	3	3	3	2
	chert	2	1	1	0
	gneiss	41	30	30	1
	granitic gneiss	4	2	3	1
	greywacke	8	4	4	1
	phyllite	3	1	1	0
	quartzite	5	3	3	0
	schist	12	7	7	1
	slate	1	1	1	1

[a] marble metamorphic rock was later lumped with carbonate category, was the shale rock with the more general mudstone category

Some sites had more data and details than others, for example:

- A single available value, a reported mean value from the original publication where raw data were not given,
- Where only a few test values were measured (e.g. drillholes), the maximum permeability value was used to represent the permeable flow pathway (fracture zone) among the other host rocks.
- Where the original authors of publications presented statistics on fault zone and host rock permeability, for example bulk permeability derived from transmissivity of

tunnel wall sections estimated from groundwater inflow rates (Masset and Loew 2010), bulk permeability from drillhole tests at geothermal sites (refs), or matrix permeability transects across fault outcrops (refs), the representative mean values were used for several notable or best described locations.

- At some sites, there was bulk permeability-depth distribution where the fault/fracture zones were anomalies (e.g. cluster of higher permeability values), and the median of such cluster was used.
- At many of the geothermal reservoir sites, the fault zone bulk permeabilities were provided as best-fit values from site-wide calibrated models.
- A low estimate was also entered for bulk permeability, usually a median, into the database for reference.

The text notes and summaries about the permeability values, their source, test methods, structural details, depths, and other information are accessible in the database (Excel and text format) file and it would be too large to include in this article. Our intention was not to overwhelm the global permeability database with site-specific fault zone data from only a few extensively studied areas, but to sample the representative data from those sites, and then compare hundreds of locations around the world for trends. At the most intensely drilled and tested locations there are publications that describe local permeability distributions and trends with depth and these are available from the original publications. The database lists those publication references and points to them. In this work, we compare many world-wide sites to each other and show world-wide trends, not local trends.

The averaging for each site reduced the variance in permeability that normally results from many individual hydraulic tests. Where both fault damage zone (k_{FDZ}) and the protolith ($k_{Protolith}$) bulk permeability was reported, we calculate the ratio of permeabilities. Errors from hydraulic test interpretation and site-wide averaging or grouping of test data are typically 0.5 to 1.0 orders of magnitude, although smaller and greater errors may exist in some cases.

The permeability values range over 10 orders of magnitude, with statistical distributions that are positively skewed (long-tailed) and approximately log-normal. Such distributions are typically seen in hydraulic property data (hydraulic conductivity, transmissivity, intrinsic permeability) from *in situ* tests in fractured rocks (Bedinger et al. 1986, Belcher et al. 2002, Sanchez-Vila et al. 2006). In this study, the permeability values were transformed to

$\log_{10}$(permeability) and the resulting distributions and compared to the normal distribution through the Shapiro-Wilk test (Shapiro and Wilk 1968) at a significance level of $\alpha = 0.05$. In most of the permeability subsets for various lithological categories the log(permeability) distributions were close to normal and passed this test.

The largest datasets are from plutonic and metamorphic rocks in the crystalline "basement", and particularly the Precambrian shields of Scandinavia and Canada, the metamorphic rocks in Alpine and Cordilleran orogens, and granitic rocks in Japan. The metamorphic rocks are varied, but gneissic rocks dominate this category (n=41). Two main categories of volcanic rocks were represented. The "volcaniclastic" category includes tuffs and ignimbrites. In the "volcanic-igneous" category, the largest datasets were from basaltic and andesitic rocks, tested in geothermal fields in Iceland and New Zealand. For coarse siliciclastic rocks, lithology was based on the most permeable unit (usually sandstone), according to the results of *in situ* tests and other published supporting information. Mudrocks were grouped together because of similarly low matrix and bulk permeability and rock strength, and most mudrock data were from <1 km, as were the shale and siltstone data. Some of the sedimentary rocks are weakly metamorphosed but have higher porosity and lower density than the older and denser metamorphic rocks that were placed in the metamorphic rock category. Some ambiguity exists here, and a few data points could be assigned to either group. All data from limestone and dolomite were combined, and some limestones are also variably metamorphosed (n=21).

6.4 Statistical analysis

The statistical analysis was carried on the world-wide compiled dataset of fault zone bulk permeability, and four regression models were fitted. These models are named A, B, C, and D here. The following regression models are fitted:

(A) log value of fault damage zone bulk permeability ($\log_{10} k_{FDZ}$) versus log value of average depth ($\log_{10}$ Depth)

(B) log value of protolith bulk permeability ($\log_{10} k_{Protolith}$) versus log value of average depth ($\log_{10}$ Depth)

(C) log value of fault damage zone bulk permeability ($\log_{10} k_{FDZ}$) versus log value of protolith bulk permeability ($\log_{10} k_{Protolith}$)

(D) residuals from regression model A of log value of fault damage zone bulk permeability (*residual* k_{FDZ}) versus residuals from regression model B of log value of protolith bulk permeability (*residual* $k_{Protolith}$).

The linear regression models $Y = \beta_0 + \beta_1 X$ were fitted by least squares estimation in the parametric ANOVA model for pairings of predictor variable (X) and response variable (Y). For example the regression model A was $\log_{10}(k_{FDZ}) = \beta_1 + \beta_1 (\log_{10}(\text{Depth}))$. The null hypothesis is that there is no effect and the alternate hypothesis that there was an effect, tested at a significance level of $\alpha = 0.05$. The P-values from an F-test indicate how compatible the data is with the fitted statistical model (Wasserstein and Lazar 2016), the r^2 (squared Pearson's correlation coefficient) estimates the proportion of variance of Y explained by regression of X, and the graphical presentation shows the variation. In the discussion of results we refer descriptively to "weak" ($r^2 \leq 0.1$), "moderate" ($0.1 < r^2 < 0.5$), and "strong" ($r^2 \geq 0.5$) correlation. The trends in error terms (residuals) were assessed for heteroscedasticity effects by using the Breusch-Pagan test at $\alpha = 0.05$ (Breusch-Pagan 1979). Matlab software is used for calculations (MathWorks Inc. 2016).

An underlying assumption is that the fault zone permeability (damage zone, fault core) values from the global data compilation represent a sample that is representative of the Earth's upper brittle crust. At later time, if more data become available, or some of the proprietary and unpublished data (e.g. from hydrocarbon and geothermal reservoirs and engineering projects) can be accessed and included in the statistical analysis, many more than the present 429 datasets could be used. In the upper 1km depth, a large proportion of the investigations of fault zones were done for the purpose of characterising the hydrogeology of potential radioactive waste repositories, in areas that were originally selected in sparsely populated and convenient locations (e.g. near existing nuclear power plants). Many of such facilities were originally selected in crystalline metamorphic or plutonic rocks. The fault zones were usually relatively small local structures at km to few km length, because these locations were biased against proximity to known active regional or continental scale faults. At 1 to a few km depth, explored geothermal fields often contain above average permeable fault zones where thermal fluids discharge upwards and cause thermal plumes, hot springs, fumaroles and other anomalies. Less active and mostly sealed fault zones are unlikely to have such vigorous geothermal flow systems. Thus, we note the likelihood of sampling bias in this instance: commercially viable geothermal fields require higher-than-normal permeability at depths generally in the range of 1 to 3km.

6.5 Results

6.5.1 Descriptive statistics and distributions

We first review basic descriptive statistics for the various rock types. In another publication (Scibek et al. 2019 submitted - b) the statistics of bulk permeability from fault damage zones and protoliths were presented as boxplots for seven different lithological categories, and the depth distribution for all individual test sites was shown. Here, Figure 2 illustrates the data aggregated into only three lithological categories: all plutonic & metamorphic ("crystalline basement") rocks, all volcanic rocks, and all sedimentary rocks. The depth distribution is simplified to five depth levels. The difference between fault damage zone and protolith bulk permeability is clearly seen in histograms plotted in a. Differences of 2 to 3 orders of magnitude occur in plutonic and metamorphic rocks, and slightly smaller-magnitude differences occur in volcanic rocks. However, in sedimentary rocks, the damage zone-protolith permeability difference is less than 1 order of magnitude.

The mean values of $\log(k_{FDZ})$ range from -12 to -13.7 (10^{-12} m^2 to $2x10^{-14}$ m^2). The median and mean values are of similar magnitude, owing to the approximately normal distributions. The observed range of damage-zone permeability is larger in denser, low-porosity rocks than in the more porous sedimentary rocks, because brittle-fractured crystalline rocks, regardless of low matrix permeable, can be highly permeable, but where the fractures are sealed, small and poorly connected, the bulk permeability approaches that of the matrix permeability. The matrix permeability values from fault damage zones also show some enhancement relative to matrix values from the protolith, but the results are less clear due to the smaller number of sites that yield such data.

Further insight regarding permeability contrasts is provided by paired data from sites where both damage zone and protolith bulk permeabilities were estimated (Figure 6-2 b). The ratio of $\log_{10}(k_{FDZ} / k_{Protolith})$ is equivalent to the difference of log permeabilities $\log_{10}(k_{FDZ}) - \log_{10}(k_{Protolith})$. For plutonic and metamorphic rocks, the ratio is thus 2 to 3. For sedimentary rocks, the paired data (excluding outcrop data) suggest that damage zones are relatively weak conduits through the protolith. The depth distribution of bulk permeability data is summarized as boxplots for discrete depth slices in Figure 6-2c. Data availability decreases with depth; in the upper 500 m there are 72 study sites, versus only 11 below 4 km depth. However, the data clearly show that the protolith is, on average, significantly less permeable than the damage zone at all depths.

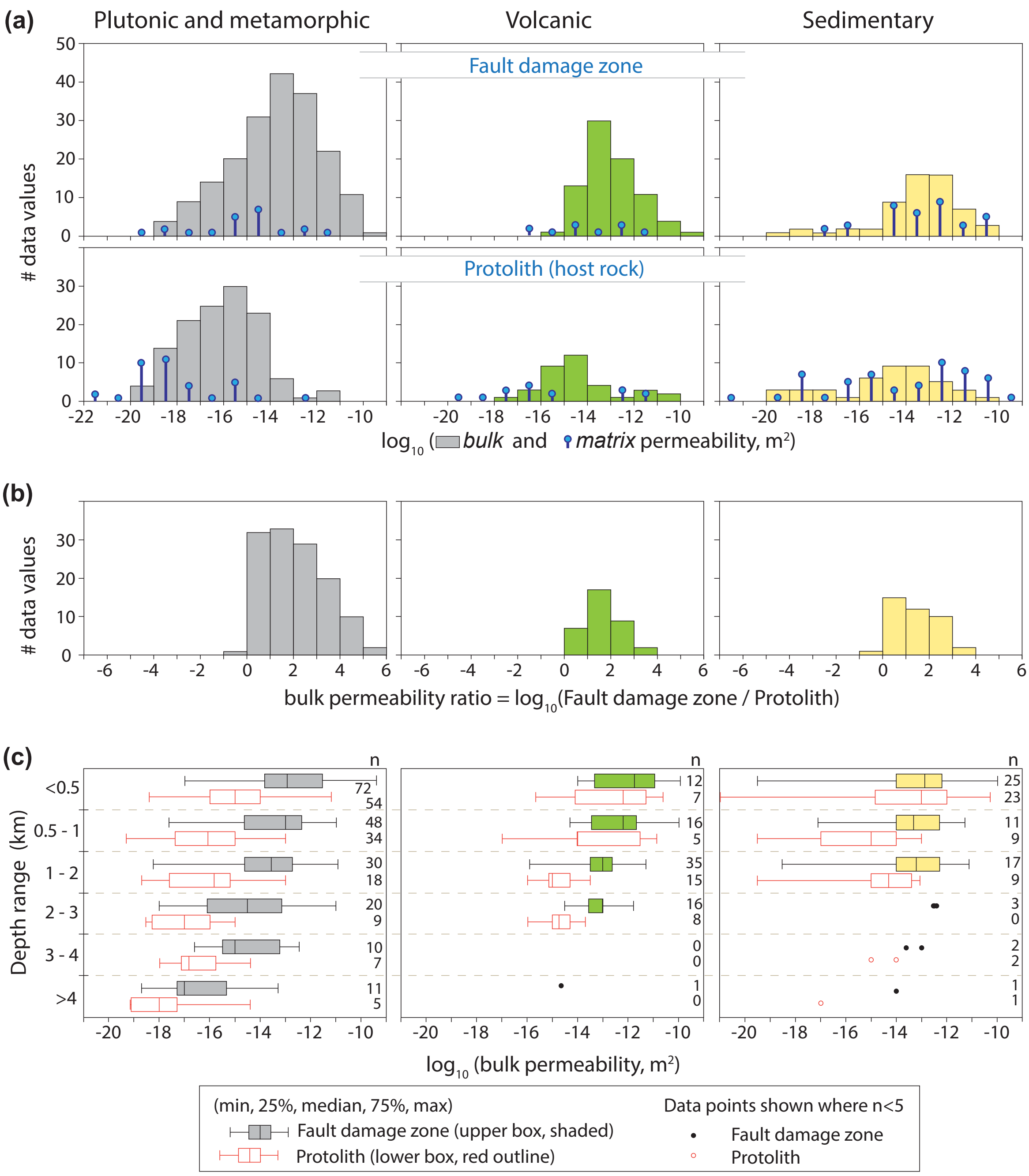

Figure 6-2 Summary of log values of bulk and matrix permeability of fault damage zone and protolith for datasets from plutonic & metamorphic rocks, volcanic rocks, and sedimentary rocks. (a) Histograms comparing bulk and matrix permeability in damage zone (upper panels) and protolith (lower panels). (b) Histograms of ratio of bulk permeabilities (fault damage zone/protolith). (c) Boxplots of bulk permeability distributions with depth: quartiles, median, minimum, and maximum, and individual data points where n<5.

Table 6-2 Descriptive statistics for bulk permeability of fault damage zones and protolith,) by lithologic category. [a]

Lithologic category	n [a]	Mean [b] (log m^2)	Median (log m^2)	Min (log m^2)	Max (log m^2)	Standard deviation
			Fault damage zone: $\log_{10}(k_{FDZ})$			
siliciclastic	25	-13.12	-13.00	-15.05	-11.00	0.87
mudrocks	13	-15.56	-14.90	-19.52	-12.22	2.28
carbonate	21	-12.04	-12.16	-14.00	-10.00	1.16
volcaniclastic	21	-12.42	-12.60	-14.52	-9.92	1.29
volcanic igneous	62	-13.04	-13.03	-15.92	-10.00	1.04
volcaniclastic & volcanic igneous	80	-12.87	-13.00	-15.92	-9.92	1.15
plutonic	105	-13.53	-13.30	-18.70	-10.22	1.87
metamorphic	86	-13.69	-13.26	-18.60	-9.40	1.90
plutonic & metamorphic	191	-13.60	-13.30	-18.70	-9.40	1.88
			Protolith: $\log_{10}(k_{Protolith})$			
siliciclastic	19	-13.35	-13.40	-15.40	-10.30	1.42
mudrocks	11	-18.15	-18.22	-21.00	-14.70	1.82
carbonate	14	-13.54	-13.14	-17.00	-11.40	1.48
volcaniclastic	12	-13.80	-14.08	-17.00	-10.64	2.02
volcanic igneous	26	-14.44	-14.70	-16.00	-10.85	1.20
volcaniclastic & volcanic igneous	35	-14.19	-14.52	-17.00	-10.64	1.56
plutonic	71	-15.83	-15.70	-19.32	-11.70	1.70
metamorphic	56	-15.85	-16.00	-19.16	-11.22	1.77
plutonic & metamorphic	127	-15.84	-16.00	-19.32	-11.22	1.73
			Ratio = $\log_{10}(k_{FDZ} / k_{Protolith}) = \log_{10}(k_{FDZ}) - \log_{10}(k_{Protolith})$ [c]			
siliciclastic	15	1.13	0.90	0.00	2.70	0.88
mudrocks	11	2.15	2.39	0.18	3.95	1.19
carbonate	14	1.76	1.98	0.60	3.00	0.71
volcaniclastic	12	1.65	1.89	0.09	3.15	1.05
volcanic igneous	26	1.80	1.79	0.52	3.60	0.73
volcaniclastic & volcanic igneous	35	1.77	1.89	0.09	3.60	0.86
plutonic	69	2.19	2.00	0.22	4.70	1.27
metamorphic	56	2.21	2.06	0.00	5.50	1.30
plutonic & metamorphic	125	2.20	2.00	0.00	5.50	1.27
siliciclastic matrix	22	0.00	-0.05	-3.14	4.00	1.41

a The individual values are best estimates for whole datasets from the database.

b All statistics are on $\log_{10}$ (permeability in m^2 units) from *n* datasets; mean = arithmetic mean of log permeability values.

c The ratio $\log_{10}(k_{FDZ} / k_{Protolith})$ is for paired values, each a best estimate.

6.5.2 Regression results for permeability-depth trends

Results from regression of bulk permeability versus depth show a weak but statistically significant trend of decreasing bulk permeability with depth for both damage zone and protolith and for most but not all rock types. Scatterplots and fitted regression models are presented in Figure 6-3 and statistics are listed in Table 6-3. Predictive values were generally low ($r^2 \sim 0.2$) and, for sedimentary rocks, were not significant at the $\alpha = 0.05$ level. The greatest predictive value was found in volcaniclastic rocks ($r^2 = 0.45$), but the number of study sites is small ($n = 25$). Damage zone data from volcanic igneous rocks is mainly from geothermal fields and shows a relatively narrow range of bulk permeability with a cluster near 1 km depth; the permeability-depth trend is poorly defined and very weak ($r^2 = 0.1$). Plutonic and metamorphic rocks, the largest category both in nature and in our data set, exhibit a weakly predictive permeability-depth trend similar to that found for most other lithologic categories ($r^2 \sim 0.2$). We also performed a parallel analysis in which regressions were calculated for the original depth units (not log-transformed), and similarly weak trends were found. The log-transformed data are more normally distributed.

6.5.3 Regression results for fault damage zone-protolith pairs for bulk permeability of macro-fractured rocks from in-situ tests

There are significant correlations between the bulk permeability of fault damage zones and protolith (Figure 6-4a) except for the single category of coarse siliciclastic rocks. The correlation is highest for mudrocks, carbonates, and volcaniclastics (0.70 ~ 0.77), rocks of weak to moderate compressive strength (Brandon 1974, Price 1983, Ishii et al. 2011, Kohno and Maeda 2012, Reyer and Philipp 2014). The correlation is lower, 0.56 ~ 0.63, in stronger rocks such as volcanic igneous, plutonic and metamorphic rocks (Hagiwara et al. 2004, Perras and Diederichs 2014, Lanaro and Matsui 2007, Glamheden et al. 2007, Kesonen 2015). All trend lines have a positive β_1 coefficients (slopes of fitted lines) of about 0.6 to 0.8, ranging up to nearly 1.0 for mudrocks. In our compilation, the mudrock category includes very weak claystones and moderately weak mudstones and marls (e.g. Ishii et al. 2011); there are no data from tight shales at larger depths.

Table 6-3 Results of linear regression on log values of bulk permeability from fault damage zone and protolith.

Datasets	Regression Statistics [a]					Normality (S-W) [b]		B-P Test [c]
	n	r^2	*p*	β1	β0	*p* for *Y*	*p* for *X*	*p*
Regression model A: $\log_{10}$(*bulk* kFDZ) = β0 + β1 $\log_{10}$(Depth)								
1. Siliciclastic (coarse)	25	0.064	0.22	-	-	0.37	0.14	0.83
2. Mudrock	13	0.030	0.57	-	-	0.49	0.076	0.30
3. Carbonate	21	0.18	0.06	-	-	0.48	**0.002**	0.85
4. Volcaniclastic	21	**0.45**	**8x10-4**	-2.40	-12.8	0.72	**8x10-4**	0.57
5. Volcanic igneous	62	**0.10**	**0.010**	-0.94	-13.1	0.27	**2x10-6**	0.29
6. Volcanic (4 & 5)	80	**0.19**	**5x10-5**	-1.37	-13.0	0.35	**2x10-7**	0.10
7. Plutonic	105	**0.21**	**7x10-7**	-1.43	-13.9	0.055	**3x10-4**	0.18
8. Metamorphic	86	**0.23**	**4x10-6**	-1.33	-14.1	0.075	**0.002**	0.08
9. Plut.& Met. (7 & 8)	191	**0.22**	**1x10-11**	-1.37	-14.0	**0.004**	**2x10-6**	**0.03**
Regression model B: $\log_{10}$(*bulk* kProtolith) = β0 + β1 $\log_{10}$(Depth)								
1. Siliciclastic (coarse)	19	0.17	0.08	**-**	**-**	0.35	0.06	0.34
2. Mudrock	11	6x10-4	0.93	-	-	0.94	0.15	0.81
3. Carbonate	14	**0.47**	**0.007**	-1.05	-14.1	0.51	**0.046**	0.77
4. Volcaniclastic	12	**0.55**	**0.006**	-3.41	-14.6	0.59	**0.013**	0.87
5. Volcanic igneous	26	0.11	0.1	-	-	**0.003**	**5x10-5**	0.10
6. Volcanic (4 & 5)	35	**0.25**	**0.002**	-1.73	-14.4	**0.007**	**4x10-5**	**0.012**
7. Plutonic	71	**0.21**	**7x10-5**	-1.42	-16.3	0.21	0.55	0.28
8. Metamorphic	56	**0.40**	**2x10-7**	-1.59	-16.4	0.28	**0.012**	0.89
9. Plut.& Met. (7 & 8)	127	**0.29**	**4x10-11**	-1.52	-16.4	0.091	**0.004**	0.33
Regression model C: $\log_{10}$(*bulk* kFDZ) = β0 + β1 $\log_{10}$(*bulk* kProtolith)								
1. Siliciclastic (coarse)	15	0.18	0.12	-	-	0.025	**0.60**	0.13
2. Mudrock	11	**0.70**	**0.001**	0.990	1.97	0.54	0.94	0.81
3. Carbonate	14	**0.77**	**4x10-5**	0.732	-1.86	0.39	0.51	0.72
4. Volcaniclastic	12	**0.76**	**2x10-4**	0.616	-3.65	0.35	0.59	0.61
5. Volcanic igneous	26	**0.63**	**1x10-6**	0.651	-3.23	0.47	**0.003**	0.27
6. Volcanic (4 & 5)	35	**0.70**	**3x10-10**	0.624	-3.56	0.32	**0.007**	0.98
7. Plutonic	69	**0.56**	**2x10-13**	0.797	-1.03	0.58	0.24	**0.037**
8. Metamorphic	56	**0.56**	**3x10-11**	0.794	-1.05	0.63	0.28	**0.003**
9. Plut.& Met. (7 & 8)	125	**0.56**	**1x10-23**	0.796	-1.04	0.29	0.28	**3x10-4**
Regression model D: (residuals from A) = β0 + β1 (residuals from B)								
1. Siliciclastic (coarse)	15	0.19	0.11	-	-	**0.012**	0.63	0.13
2. Mudrock	11	**0.68**	**0.002**	0.99	-0.44	0.34	0.94	0.87
3. Carbonate	14	**0.72**	**1x10-4**	0.92	-0.20	0.31	0.40	0.43
4. Volcaniclastic	12	**0.58**	**0.004**	0.56	-0.25	0.81	0.49	0.34
5. Volcanic igneous	26	**0.59**	**4x10-6**	0.74	-0.48	0.74	**0.043**	0.38
6. Volcanic (4 & 5)	35	**0.64**	**1x10-8**	0.66	-0.49	0.35	0.81	0.60
7. Plutonic	69	**0.44**	**5x10-10**	0.66	-0.25	0.20	0.21	**0.014**
8. Metamorphic	56	**0.41**	**1x10-7**	0.69	-0.03	0.53	**0.027**	**5x10-3**
9. Plut.& Met. (7 & 8)	125	**0.42**	**3x10-16**	0.67	-0.15	0.31	0.077	**5x10-4**

a All statistics are on $\log_{10}$ permeability (m^2 units) from n datasets; mean = arithmetic mean of log permeability values, r^2 is the proportion of variance explained, the *p*-value is for regression at significance level α=0.05 (significant values highlighted in bold font), and β_1 and β_0 are coefficients for the fitted line ($Y = \beta_0 + \beta_1 X$)

b Shapiro-Wilk (S-W) normality test one-tailed *p*-values are at significance level α=0.05

c Breusch-Pagan (B-P) test for heteroscedasticity of residuals one-tailed p-value at significance level α=0.05.

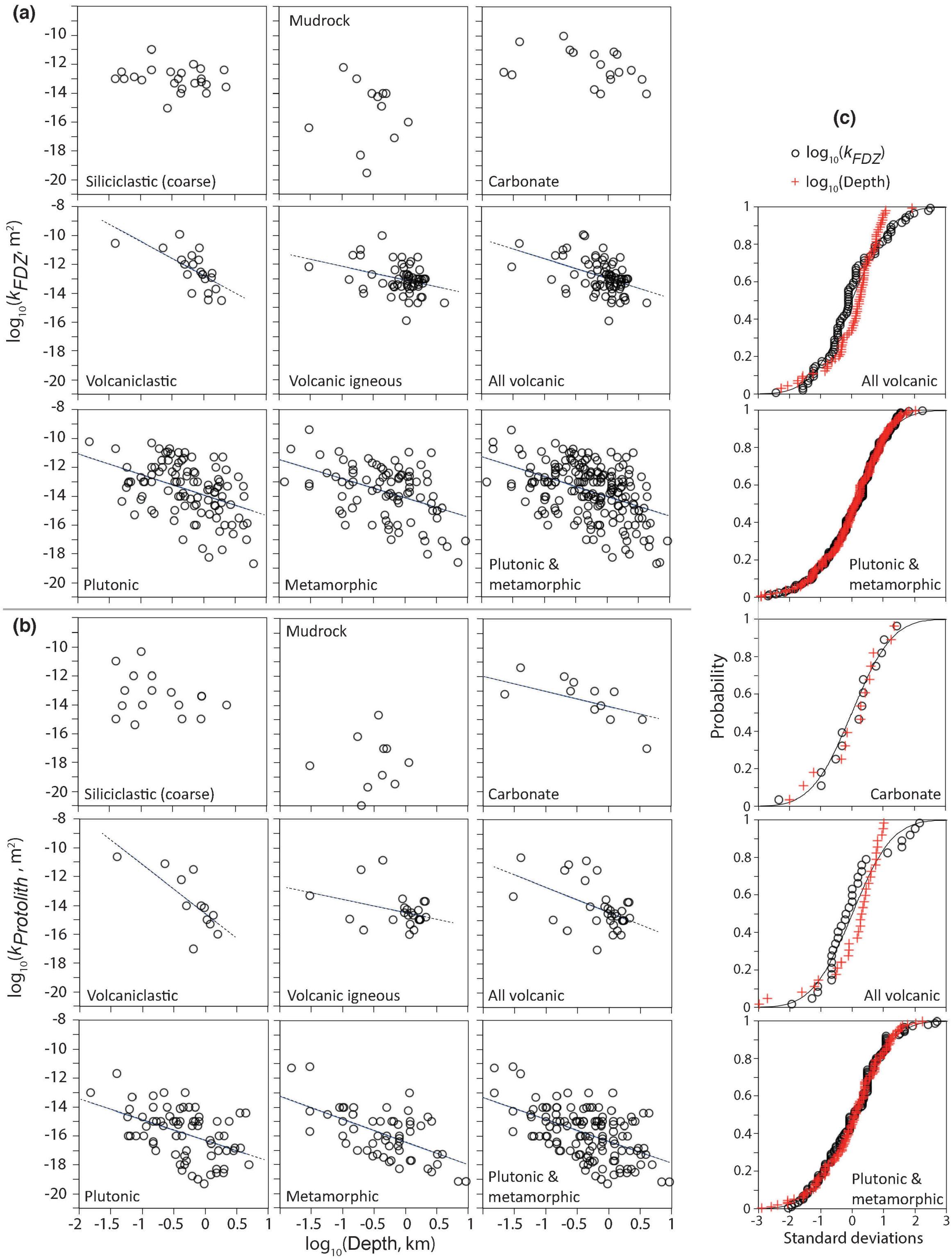

Figure 6-3 Regression lines and scatterplots of log bulk permeability values vs. depth by lithological categories. (a) Damage zone permeability vs. depth, (b) protolith permeability vs. depth, and (c) data distributions as probability-density functions compared to normal distributions.

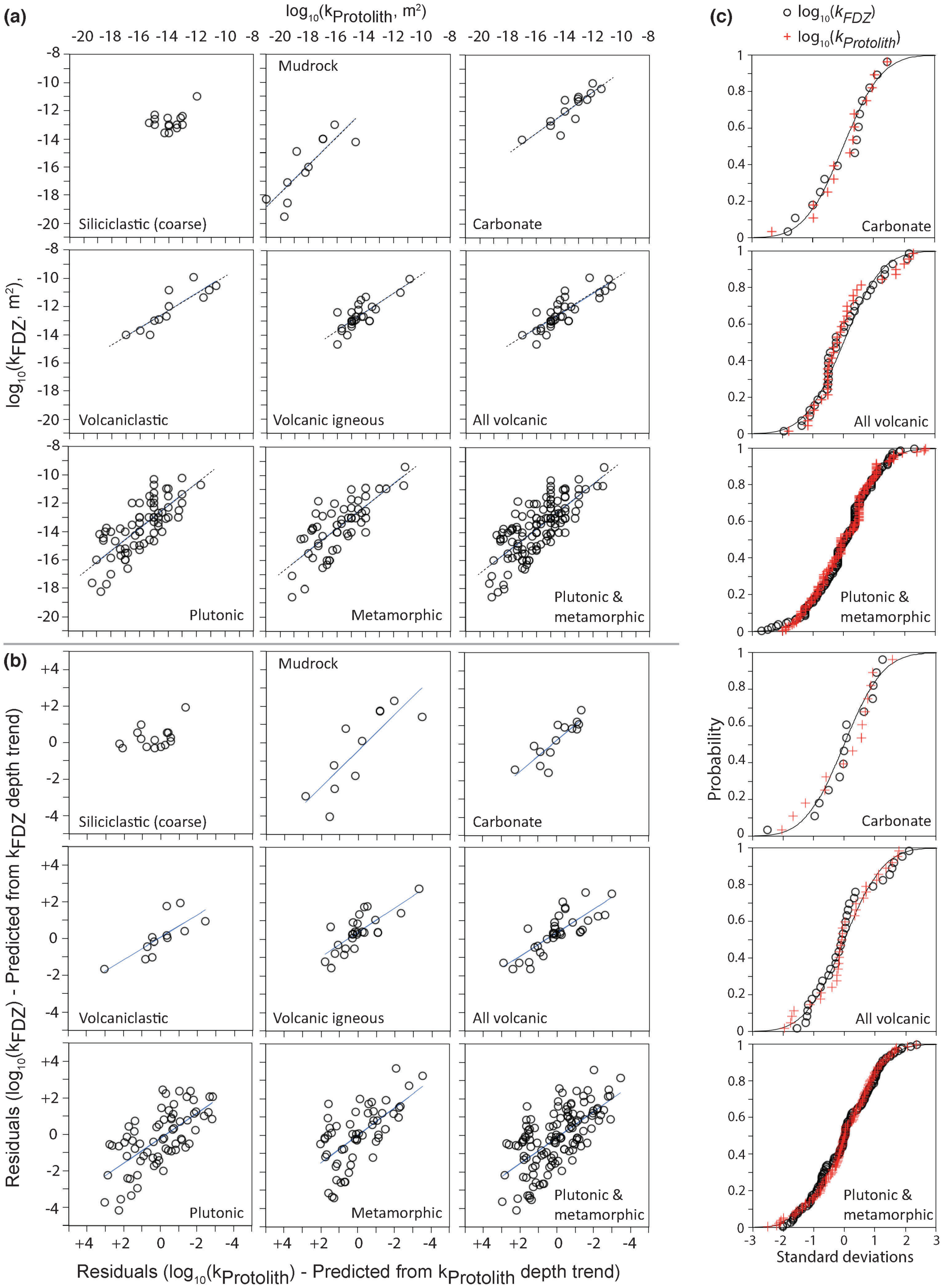

Figure 6-4 Regression lines and scatterplots of log bulk permeability values by lithological categories. (a) Regression of log10 (kFDZ) on log10 (kProtolith), (b) regression of residual kFDZ on residual kProtolith after removing depth trends, and (c) data distributions as probability-density functions compared to normal distributions.

In our final regression analysis, we investigate the potential effect of depth on the correlation between damage-zone and protolith permeabilities. This analysis was performed on the residuals from the permeability-depth regressions, so that the depth trend, if any, has been removed from the permeability data. The results are shown in Figure 6-4b and appear almost identical to the results for the non-transformed data, although the correlations are slightly lower (0.41 ~ 0.72). Although a small part of the variance accounted for in Figure 6-4a can be attributed to effects of depth (e.g. porosity decrease, stress increase), the results are essentially identical.

Residuals of the k_{FDZ} versus $k_{\mathrm{Protolith}}$ regression for plutonic and metamorphic rocks (the largest sample category) show a pattern of decreasing variance with the magnitude of $k_{\mathrm{Protolith}}$ (Figure 6-5a). This significant heteroscedasticity was detected by the Breusch-Pagan test (see Table 3-3 regression model C, p-values < 0.05). The graph of absolute residuals (Figure 6-5b) versus $k_{\mathrm{Protolith}}$ is similar to the graph of $k_{\mathrm{FDZ}}/k_{\mathrm{Protolith}}$ versus $k_{\mathrm{Protolith}}$ (Figure 6-5c). Mild forms of heteroscedasticity may be acceptable (Long and Ervin 2000), but indicate that the regression model does not explain all of the variance in the permeability data and the underlying processes that control them. The data show that where the protolith has low permeability, the $k_{\mathrm{FDZ}}/k_{\mathrm{Protolith}}$ ratio can be as large as 5 or 6. Where the protolith has high permeability, the ratios are smaller.

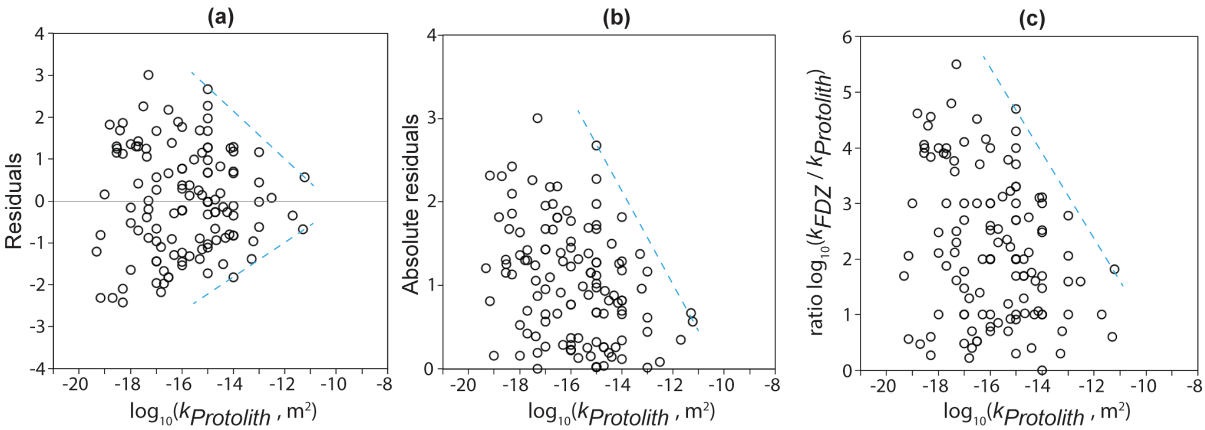

Figure 6-5 (a) Residuals from regression of k_{FDZ} on $k_{\mathrm{Protolith}}$ as a function of $k_{\mathrm{Protolith}}$, with lines drawn to indicate the trend of decreasing variance with increasing $k_{\mathrm{Protolith}}$, (b) squared residuals as a function of $k_{\mathrm{Protolith}}$ and the decreasing trend in variance that indicates heteroscedasticity, and (c) ratio of permeabilities $\log(k_{\mathrm{FDZ}}/k_{\mathrm{Protolith}})$ as a function of $k_{\mathrm{Protolith}}$.

6.6 Discussion

6.6.1 Possible reasons for correlation between damage-zone and protolith permeability

All lithologic categories, other than coarse siliciclastic rocks, exhibit moderate to strong correlation between the bulk permeability of the fault damage zone and that of the protolith. From a structural perspective, fault damage zones exhibit a large variety of geometries and fracture densities, depending on position along the fault and fault growth and interaction processes (Kim et al. 2004). The width of the damage zone usually scales with fault displacement but also depends on interaction with other fault segments (Childs et al. 2009). It is rather difficult to define fracture frequency in areas sampled by drilling only, but there is evidence that fault damage zone width does not tend to exceed 200 m (Savage and Brodsky 2011). From drilling alone, it is also difficult to estimate the background fracture frequency, and the damage zones from different structures can overlap (Johri et al. 2012). In this compilation of data we had no control over what parts of fault zone were tested in the original studies by other authors. The drillholes and tunnels and other test methods in-situ accesses different parts of fault damage zones and parts of fault cores together with damage zones. The boundaries of damage zones are not strictly mapped or defined by change in fracture density away from fault core, and the fault damage zones are often overlapping for various structures. The bulk permeability of the protolith is meant to represent the rock with "background" density of fracturing outside of fault damage zone. In reality, it was inferred by the more distal position of test zones and the lowest bulk permeability in test results. Thus, one possible explanatory hypothesis is that the fault damage zones are hydraulically wider and more connected to what has been inferred to be the protolith (i.e. the fault damage zones were wider). If that is the case, the protolith then may include a mix of the true protolith and the outer damage zone, if not of the main fault zone that was considered, than of another overlapping zone. In this review, it was not possible to definitely verify at all projects the damage zone extent.

The crystalline crust contains different generations or sets of fractures with heterogeneous hydraulic properties (Thury et al. 1994, Mazurek 2000). In deep drillholes (e.g. KTB, the deepest dataset used in our study), the geometry of connected fractures and resulting permeable zone(s) are uncertain (Zimmernann et al. 2000). The hydraulic test response is often modelled in terms of near-field and far-field permeability zones, with some preferential flow pathways (e.g. Evans et al. 2005). In regional fractured aquifers, test results over a wide range of transmissivity can exhibit heteroscedasticity (Painter et al. 2007). In relatively permeable protoliths with enough connected and permeable "background" fractures, the additional permeability contributed by fracture permeability in fault damage-zone may add one to several orders of magnitude permeability above that of the intact protolith. The same fault damage zone (permeability as in above example) cutting protoliths with relatively low permeability, can lead to greater contrast or ratio of permeability between the fault and protolith.

Our compilation includes diverse tectonic stress conditions and, as we have seen, the data exhibits only weak trends of bulk permeability with depth. The correlation that was established between the fault damage zone and protolith bulk permeabilities, where the damage zone to protolith ratio of permeability is greater by a magnitude that seem to depend partly on the rock type, can have a mechanical explanation. First, there is some evidence that stronger (compressive and tensile strength) rocks can maintain more permeable brittle fractures that lead to larger overall fault zone transmissivity (Ishii 2015). A second possible explanatory hypothesis is that both the damage zone and the protolith are affected by similar *in situ* processes over geologic time scales, that seal the fracture channels and other pores. In granitic rocks at geothermal sites, the location of permeable fractures is correlated with hydrothermal alteration (Sausse et al. 2005). In Chapter 7 of this thesis, I show that hydrothermal alteration in a fault zone leads to larger variation in permeability of rock matrix, both high an low values, and an overall increase in average permeability and transmissivity to fluid flow in the fault damage zone.

6.6.2 Comparing the permeability ratios and inferring the magnitude of fault conduit and barrier

Can the permeability ratios between the fault zone (e.g. damage zone fractures) and the protolith help us quantify, at least empirically from the data presented in this study, the effectiveness of fault-zone conduits in various rock types? For each lithologic category, the distribution of bulk permeability is delineated by polygons drawn on scatterplots in Figure 6-6a-d. A data envelope is delineated for matrix permeability data from fault damage zones in Figure 6-6e; such data are available mainly from sandstones, carbonates, and schists at outcrops (0 depth). A data envelope is delineated for matrix permeability data from fault cores in Figure 6-6f; these data are mainly from mudstones, carbonate rocks, and gneisses. A data envelope is also delineated for matrix permeability from coarse siliciclastic rocks in

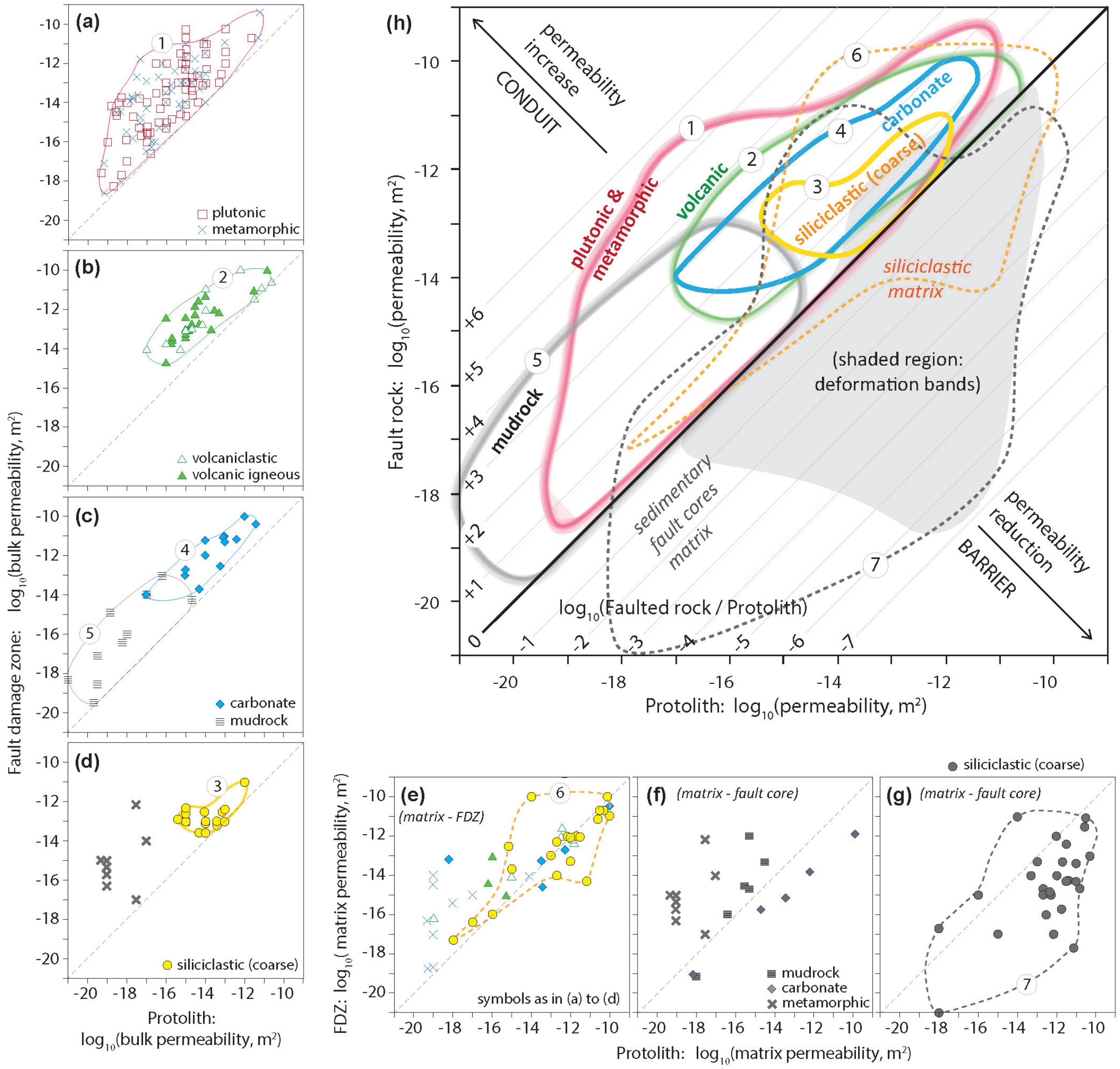

Figure 6-6 Bulk permeability of damage zone vs. protolith in (a) plutonic and metamorphic rocks, (b) volcanic rocks, (c) carbonates and mudrocks, (d) coarse siliciclastic rocks, and (e) damage zone matrix permeability for various rock types. Fault core matrix permeability for (f) mudrocks, carbonates, and metamorphic rocks and (g) coarse siliciclastic coarse rocks. (h) Comparing the magnitude of fault conduit and barrier behavior on plot of fault vs. protolith bulk permeability from this study, showing permeability data envelopes from (a) to (g). The permeability ratio labelled on the diagonal scale. The shaded region in (h) is for deformation bands (after Ballas et al. 2015) and a few fault cores from the database in this study.

Figure 6-6g; these data are mainly from outcrops that sample deformation bands in damage zones and in or near the fault core, and such data were reviewed recently by Ballas et al. (2015). Deformation bands are clearly not faults or fault rocks, but their barrier behaviour has been studied extensively are included here for comparison purposes only, as some do occur near faults. Finally, the data envelopes are compared together on one plot in Figure

6-6h. There, we infer that the positive log ratios of bulk permeability help to quantify the conduit effect of the fault zone, where as the negative log ratios indicate barrier effect for fluid flow in the protolith that is interrupted but such fault (or the example of non-fault deformation bands as well).

Although the fault barrier magnitude could be assessed in this method, this study was biased to the data that were available, from fault damage zones and protoliths. The permeability envelopes for the lithologic categories overlap considerably. The conduit behavior of fault damage zones is defined by bulk permeability ratios that attain up to +6 orders of magnitude in plutonic and metamorphic rocks, attain up to +3 orders of magnitude in all crystalline rock types, and average about +2 orders of magnitude for all lithologic categories other than coarse silicic rocks. There are essentially no negative permeability ratios, thus the potential barrier behavior of fault zones can only be inferred here from the matrix permeability data. The role of low-permeability fault cores as barriers to fluid flow has been studied by other authors for both plutonic and metamorphic rocks (Lockner et al. 2009) and sedimentary rocks (Aydin 2000, Bense and Person 2006).

6.6.3 On the importance of permeability-depth distribution

The bulk permeability data from *in situ* tests are compared to published permeability-depth curves in Figure 6-7. Manning and Ingebritsen (1999) defined a *geothermal-metamorphic curve* by fitting indirect permeability estimates from metamorphic fluid fluxes and thermal-fluid flow models of selected sedimentary basins, active mountain belts, and volcanic areas. Outcrop samples from metamorphic rocks were analysed geochemically to estimate time-integrated fluid fluxes, which can be converted to permeability values, and the assigned depth was the depth during peak metamorphism. The best-fit curve has a linear form for logarithms of permeability (k) at depth (z):

$$\log(\mathrm{k}) = -14 - 3.2 \log(z) \qquad [1]$$

where the coefficients $\beta_0 = -14$, $\beta_1 = -3.2$, k is in m^2, and z is in km. Below 0.8km depth, the same curve was used in a model by Saar and Manga (2004). A modified version of this geothermal-metamorphic curve was used by Scibek et al. (2019 submitted - a), described in Chapter 4, to fit permeability data at shallow depths (<1 km) and to converge to a real value at ground surface, and is also plotted in Figure 7.

In this study, we fit depth trends of bulk permeability to data from fault zones only, over a depth range 0 to 9km where the data points exist. However, trends to bulk permeability can be also fitted to the protoliths with some background fracturing density and a multitude of faults and other structures that lead to fracturing and permeability enhancement locally. One of the best recent works is by Achtziger-Zupancic et al. (2017), who fitted permeability trends to data set of 22000 values from in-situ tests over depth intervals (e.g. injection, pump, and other tests in drillholes and tunnels) in fractured rocks in the upper 2km of the crystalline crust (metamorphic or plutonic). The derived trend by those authors was:

$$\log(k) = -16.3 - 1.5 \log(z) \qquad [2]$$

This trend does not match the geothermal-metamorphic curve, and the data distribution differs from the fault zone data from our study. It is difficult to assess how permeability-depth trends at any point in the protolith relate to faults, or which of the thousands of in-situ tests are in fault zones and what part of fault zone. This study and the one by Achtziger-Zupancic et al. (2017) present two different approaches to looking at permeability in the upper part of brittle crust. We cannot extrapolate the permeability-depth trends from the regression analysis to depths greater than the data used to define those trends, and certainly not below the brittle-ductile transition zone, but we can compare the trends and the data distribution to the geothermal-metamorphic curve. The modified geothermal-metamorphic curve bisects the data cluster for damage zone bulk permeability (Figure 6-7a). In contrast, the geothermal-metamorphic curve exceeds the vast majority of the protolith bulk permeabilities at corresponding depths (Figure 6-7b). The broad trend of increasing permeability toward shallower depths in the crust appears consistent with both the modified geothermal-metamorphic curve and the present-day *in situ* data (Figure 6-7c shown on an arithmetic depth scale).

From the fault zone dataset in this study, we can infer that both the mean permeabilities obtained from regional fluid flow-geothermal models and time-averaged metamorphic fluid fluxes are consistent with the average bulk permeability of fault zones in the brittle crust, and not with the smaller permeabilities of the protolith. The upper 10 km of the Earth's crust consists mainly of metamorphic rocks (63%), plutonic rocks (11%), sedimentary rocks (23%), and volcanic rocks (4%), as calculated from data in Wilkinson et al. 2009 (see Supplementary Information). Thus the proportion of our *in situ* datasets from faulted metamorphic and plutonic rocks (about 75%) is reasonably representative of the upper crust.

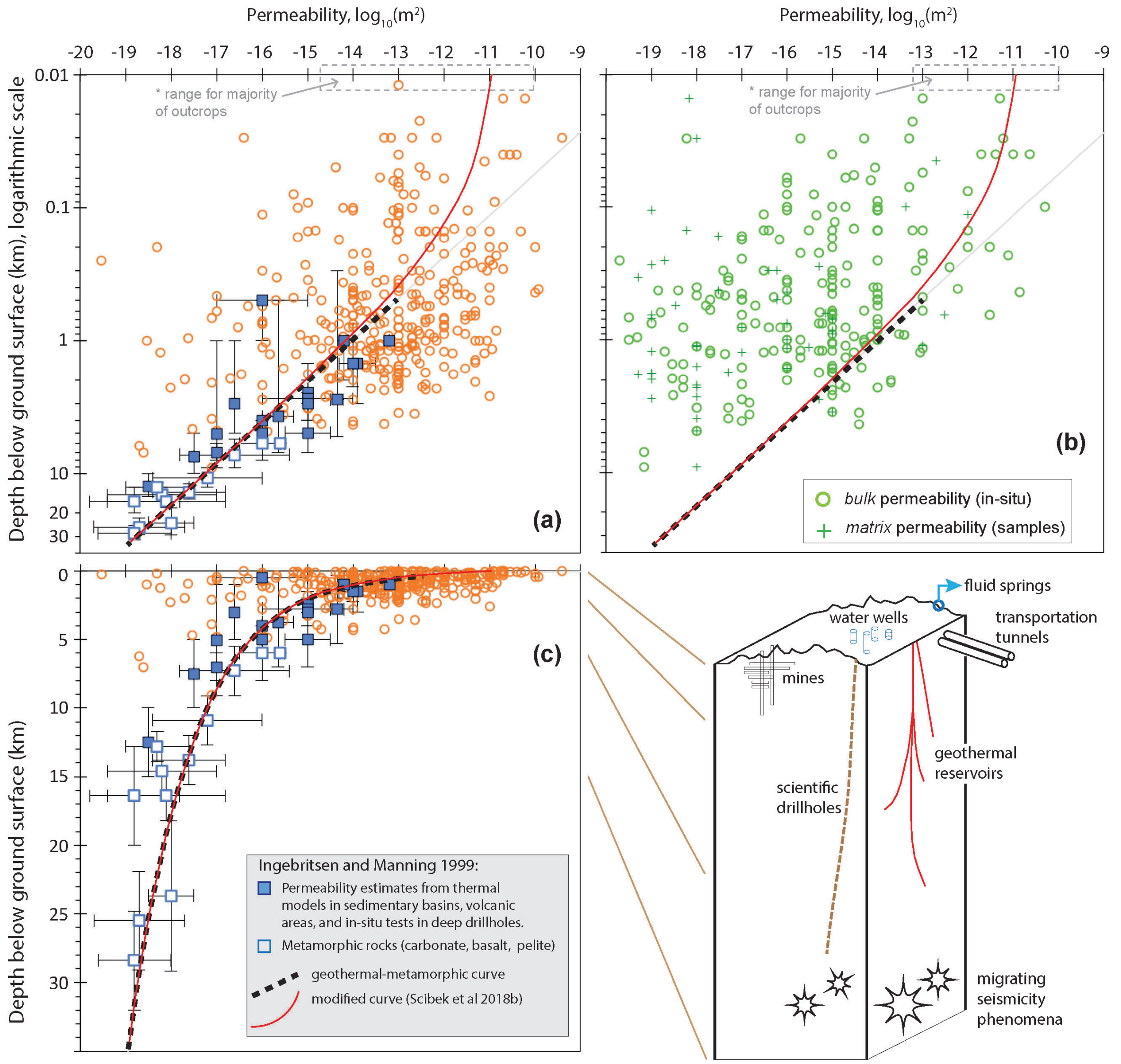

Figure 6-7 Comparison between *in situ* permeability data and the geothermal-metamorphic data used by Manning and Ingebritsen (1999). (a) Damage zone permeability, (b) protolith permeability at the same sites, and (c) the same as (a) but plotted on an arithmetic depth scale. The graphs in the two upper panels are plotted with logarithmic depth scales to clarify the data distribution at shallow depths. Curves are the geothermal-metamorphic curve (thick black dashed line) of Manning and Ingebritsen (1999) and the modified geothermal-metamorphic curve at depths <1 km (see Chapter 4).

Our results imply that the fluid fluxes related to deeper metamorphism are compatible with the bulk permeability of fault zones that cut the upper part of the brittle crust, such that over geologic time scales metamorphic fluids can easily be transferred towards shallower depths and ultimately the ground surface. These results are consistent with widespread hydrostatic conditions in crystalline rocks of the upper crust (Townend and Zoback 2000); significantly elevated fluid pressures occur mainly where crustal materials (e.g. argillaceous sedimentary rocks) have permeability lower than about 10^{-17} m^2 (Neuzil 1995, Manning and Ingebritsen 1999).

Table 6-4 Matrix permeability of protolith and bulk permeabilities of protolith and fault damage zones from various metamorphic and igneous rock types. Permeability values shown as $\log_{10}$(permeability in m^2) .

Rock type	*matrix* Protolith		*bulk* Protolith	*bulk* FDZ	n (Protolith, FDZ) [c]	References for matrix $k_{Protolith}$
	unconfined samples [a]	confined samples [b]	($k_{Protolith}$)	(k_{FDZ})		
Metamorphic						
schist, slate	-19 ... -15	-19.5	-15.2	-14.0	8, 16	1, 6, 24
greywacke	-19.3 ... -18		-15.1	-12.8	5, 9	1, 7
marl, phyllite	-20 ... -18		-16.7	-14.6	6, 8	12, 1
quartzite	-20 ... -17.7		-14.8	-12.6	3, 7	1, 31
limestone, marble	-18 ... -17		-13.9	-12.0	18, 27	1, 4, 6
gneiss (granitic)	-18.4 ... -17.2	-22.3 ... -20	-15.2	-13.8	2, 4	8, 1, 14, 20, 28
gneiss (various)	-20 ... -16		-16.3	-14.0	34, 46	1, 3, 4, 5, 14, 20, 28, 29
gneiss (amphibolite)	-21 ... -18.6		-18.5	-16.6	3, 4	3, 4, 20, 29
greenstone	-19.6					1
Volcanic igneous						
andesite, rhyolite	-15.3 ... -14		-14.4	-13.1	15, 33	26, 27
dense basalt, metabasalt	-21.4 ... -16	-22 ... -19	-14.3	-12.8	11, 34	10, 19, 20, 22, 25
Plutonic igneous						
gabbro	-18.7 ... -18	-22	-14.5	-13.9	3, 4	11, 18
granite (excluding damaged) [d]	-21 ... -16	-21.7 ... -16.7	-16.0	-13.7	68, 92	1, 2, 5, 9, 13, 15, 16, 20, 21, 29, 30
granodiorite, diorite	-20 ... 18	-21.5 ... -19	-15.8	-13.3	9, 30	1, 5, 14, 17, 23

a Unconfined drill core or outcrop samples tested at ambient air pressure or very low confining pressure.

b Samples tested at high confining pressure to simulate *in situ* conditions.

c Number of datasets averaged.

d Edges of cooling plutons can have more damaged matrix, e.g. Kakkonda granite (Sasaki 1998)

Table references for matrix permeability:

1 - Johnson (1983), 2 - Geraud et al. (2010), 3 - Huenges et al. (1997), 4 - Heikamp and Nover (2003), 5 - Maaranen et al. (2001), 6 - Zeigler (1976), 7 - Lockner et al. (1982), 8 - Wang et al. (2014), 9 - Brace et al. (1968), 10 - Gilbert and Bona (2016), 11 - Katayama et al. (2012), 12 - Enachescu et al. (1995), 13 - Schild et al. (2001), 14 - Morrow and Byerlee (1988), 15 - Fisher and Tester (1979), 16 - Pine and Batchelor (1984), 17 - Fujimoto et al. (2000), 18 - Hirose and Hayman (2008), 19 - Kopf (2001), 20 - Morrow et al. (1994), 21 - Morrow and Lockner (1997), 22 - Tsutsumi et al. (2004), 23 - Lockner et al. (2009), 24 - Wibberley and Shimamoto (2003), 25 - Walker et al. (2013), 26 - Lamur et al. (2017), 27 - Mielke et al. (2016), 28 - Hartikainen et al. (1997), 29 - Kuva et al. (2015), 30 - Havlova et al. (2012), 31 - Shabelansky et al. (2014).

6.7 Transient variations in fault-zone permeability

Large transient variations in permeability appear to occur in the continental crust (Ingebritsen and Manning 2010). A conceptual model of self-adjusting large-scale crustal permeability in response to tectonic and metamorphic-fluid forcing has been proposed (Rojstaczer et al. 2008), and various mechanisms have been proposed for rapid permeability adjustment by tectonic disturbances that affect fracture aperture and connectivity in some way (Elkhoury et al. 2006). We have seen that the data presented in this study are mainly from fault zones that currently constitute permeable pathways through the brittle crust. We cannot resolve time-variation in permeability from these data, but we can ask other related questions, such as: What proportion of brittle fault zones are permeable conduits in excess of the $>10^{-17}$ m^2 threshold? Do regions exist in the brittle crust where most of the fault zones appear sealed?

Geothermal areas exhibit some of the best evidence of transient permeability over geologic times ranging from millions of years (Dubois et al. 1996, Curewitz and Karson 1997) to years (Manga et al. 2012, Bonini 2013). About 30% of the total data in our analysis comes from geothermal energy production sites. In a world-wide recent survey of geothermal well outcomes at 57 geothermal fields (IFC 2013), at depths typically of 1 to 3 km, success rate ranged from about 50% in granitic/metamorphic rocks to 87% in volcanic areas, with a success rate of about 55% in sedimentary basins. Successful geothermal wells intercept fracture zones that are sufficiently permeable for high-volume fluid production or injection, and with adequate enthalpy (heat energy) in the case of production. Most of the failed wells reflect inadequate permeability, but some reflect drilling problems such as not reaching the reservoir or inadequate temperature despite adequate permeability (Sveinbjörnsson 2014). If we assume that in granitic and metamorphic rocks the dominant fluid-flow pathways are almost entirely in fault-related fracture zones, then the 50% success rate suggests widespread occurrence of permeable faults in active geothermal areas. However, geothermal projects are not in random locations in the brittle crust. They generally target natural heat- flow anomalies or hydrothermal discharges that reflect enhanced crustal permeability.

Another estimate of the proportion of permeable fault zones comes from a review by Scibek et al. (2016), who found that >50% of mapped fault zones have noticeable ability to focus and transmit groundwater flow, thus acting as conduits. This result was based mainly on hydrogeological observations in long transportation tunnels in active orogenic regions, which yield proportions of relatively permeable fault zones ranging from 30 to 90% (median about 55%) in metamorphic and folded sedimentary rocks. And at intensely drilled and tested hydrogeological research sites in Precambrian shields, practically all major structures contain permeable zones (relative to the protolith permeability) in the upper few hundred meters below the top of crystalline basement (Bossart et al. 2001, Posiva 2003, Follin and Stigsson 2014).

The apparent permeability of active fault zones also depends on the sampling effort and scale of hydraulic tests. This has been recently demonstrated for instance by observation drillholes and corresponding fault outcrop transects in southern Japan. At the Nojima fault observatory, the bulk permeability in fractured granite from *in situ* drillhole tests (~ 2x13 m^2) (Kitagawa and Kano 2016) is substantially larger than the matrix permeability previously sampled in outcrop (~10^{-14} to 10^{-16} m^2) (Mizoguchi et al. 2008) and in a few drillcore samples from >1 km depth (Lockner et al. 2009). The Nojima fault occurs in granitic protolith of low permeability (~10^{-20} m^2) adjacent to sedimentary rocks having more permeable matrix (10^{-15} to 10^{-17} m^2). The Median Tectonic Line fault zone has been drilled and tested at about 500 m depth, yielding bulk permeability of 5×10^{-17} to 5×10^{-16} m^2 (up to 10^{-15} m^2 in a shallower test hole), and is surrounded by sparsely fractured granitic protolith (~3×10^{-19} m^2) (Matsumoto and Shigematsu 2018). These values are similar to the most permeable fault rock matrix (~10^{-15} m^2) and undeformed protolith (~10^{-19} m^2) samples previously tested across an outcrop transect by Wibberley and Shimamoto (2003). Finally, recent hydraulic observations from a thrust zone about 900 m below the seafloor in the accretionary prism above the Nankai trough (Kinoshita and Saffer 2018) yield fault zone bulk permeability of about 10^{-12} m^2 at ~100s meters scale, much higher than the bulk permeability of the protolith (and possibly parts of the fault zone) previously obtained in smaller-scale *in situ* tests (10^{-15} to 10^{-16} m^2) or the matrix permeability of the sediments (10^{-18} to 10^{-16} m^2). The new *in situ* observations consistently returned higher bulk permeability values compared to drillcores or smaller-scale *in situ* tests. These results are compatible with our world-wide summaries and also fit the global depth-distribution near the modified geothermal-metamorphic curve presented in this study and in Scibek et al. (2019 submitted - b).

Therefore, it appears that the majority of "adequately" sampled major fault zones constitute significant fluid conduits at the present time (bulk permeability >10^{-17} m^2 threshold). Large crustal blocks with complete sealing of existing fault zones in crystalline rocks have not yet been found. Over time, as more data have been collected, the brittle crust has begun to appear more permeable.

6.8 Estimating the global crustal permeability distribution

Figure 6-8 presents a potential method to estimate the global distribution of crustal permeability, including the relationships found and discussed herein. Base maps of geological units and structures are combined with drillhole and geophysical data to construct a simplified geo-cellular model (e.g. Peters et al. 2018), with an example from the EarthCube (2018) project shown here. A model of the digital crust (Fan et al. 2015) contains three-dimensional blocks with geological properties, such as lithology, porosity, density, and permeability, either locally tested or assigned by rock type from regional averages. Since individual fault zones cannot be modelled within the cells, an empirical approach might be used to modify the hydraulic properties of cells that host fault zones. A first step might be to estimate the favorability of fault zone segments or fault systems with respect to regional stress fields (e.g. Townend and Zoback 2000). Locations of unmapped faults are not known, or the distributions of faults in unmapped regions. The suggestion here is to use the same statistics for particular lithological categories from regions where faults had been tested and attempt to assign the mean value (e.g. mean of permeability ratio of fault /protolith) to other unmapped regions, until better local data are obtained. Information on recent tectonic activity, current thermal anomalies, and discharge of thermal waters might also be used in the model (e.g. Muraoka et al. 2006, Faulds et al. 2011). The global occurrence of permeable conduits in different rock types (Figure 6-8 a) could be incorporated. The contribution of this study is to enable estimation of damage zone permeabilities in different rock types by using regional data for protolith bulk or matrix permeability (Figure 6-8 b). Time-dependent processes might be empirically parameterized using numerical models and calibrated locally. Generalized permeability-depth trends and bounds on reasonable values at various crustal depths could provide additional constraints (Figure 6-8 c).

For realistic fluid flow calculations in hydrothermally active regions, or over geologic time scales, fault zone permeabilities are needed. Empirical models based on observational data constraints can provide initial estimates of the effectiveness of fault zone conduits in the brittle crust in different rock types. Such models can be adopted where site-specific permeability data are lacking. Previous models have adopted various models for decreasing fault permeability with depth (e.g. Cappa 2009, Lupi et al. 2011), but were not calibrated or constrained to global statistics. From this study, only about 50% of the variance can be explained in fault zone bulk permeability, by knowing the protolith bulk permeability, and the variation of values is large. It can be argued that such prediction is better than 0% or a complete lack of prediction, thus a good starting point for some models that require hydraulic properties of fault zones and where none have been tested.

At shallow crustal depths (<~1 km), rocks tend to be more fractured and conductive to groundwater in what has been termed the hydro-geomechanically active and decompressed zone (Maréchal 1999), where the bulk permeability of fractured protolith can be enhanced by several orders of magnitude by stress-unloading cycles of glaciation (Grämiger et al. 2017) and surficial weathering (Dewandel et al. 2006). Textbook permeability values for fractured aquifers are typically from this shallow layer (e.g. Gleeson et al. 2011). Even at shallow depths, fault zones are known to enhance vertical fluid flow in low-permeability crystalline rocks and reduce sub-horizontal groundwater flow due to compartmentalization. However, the permeability distributions in surficial aquifers (Gleeson et al. 2014) that are used in continental-scale groundwater flow models (de Graaf et al. 2015) generally do not yet take major structures into account.

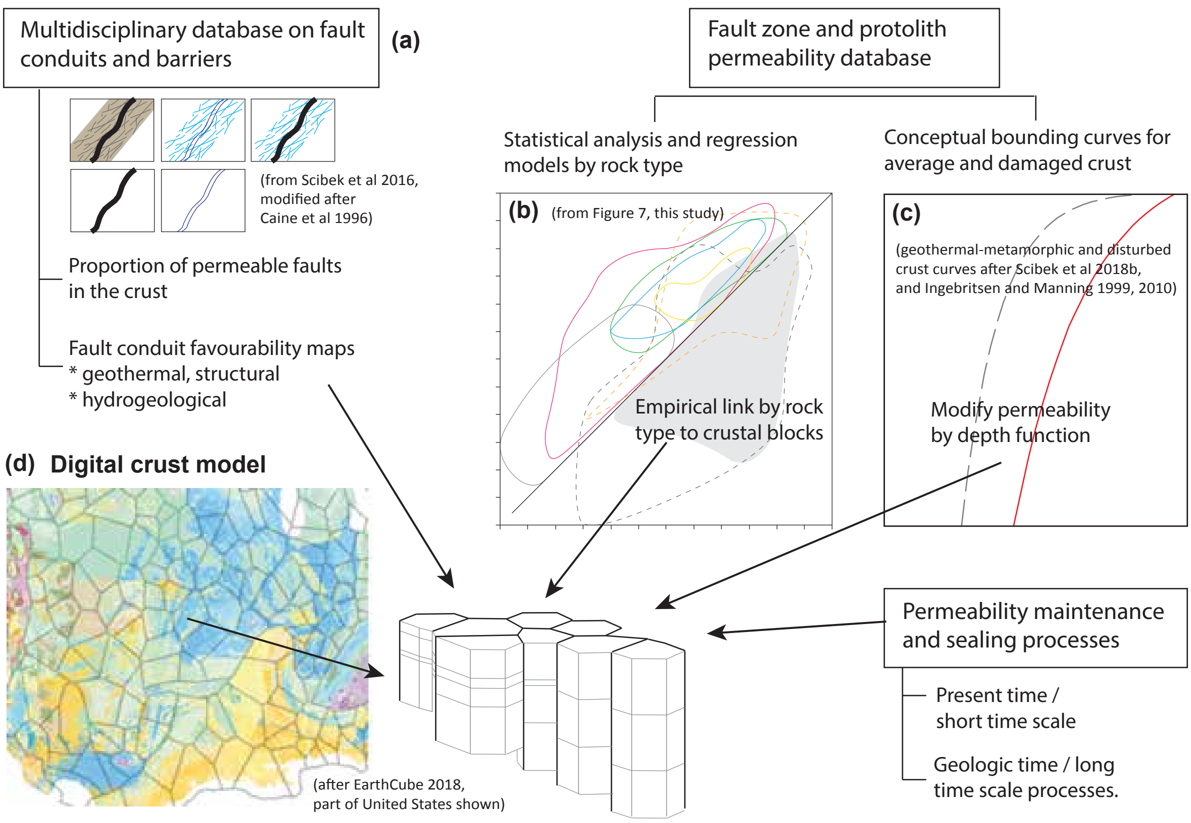

Figure 6-8 Schematic workflow for incorporating statistical results from this study into a digital crust model. (a) Simplified classification of fault zone hydraulic models, (b) fault damage zone vs. protolith scaling ratios by rock type, (c) permeability vs. depth trends and bounds, (d) digital crust implementation in EarthCube.

6.9 Conclusions

There is a weak but statistically significant trend of decreasing bulk permeability with depth, for both fault damage zone and protolith, in plutonic, metamorphic, and volcanic (but not sedimentary) rocks. However, global *in situ* permeability data are unevenly distributed with depth, and the number of tested sites decreases with depth.

The majority of tested fault zones in the upper few kilometres of the brittle crust are significant fluid conduits at the present time (bulk permeability $>10^{-17}$ m^2 threshold). The protolith is on average significantly less permeable than the damage zone at all depths. Time-averaged crustal fluid fluxes related to rock metamorphism are consistent with the average bulk permeability of fault zones in the brittle crust, rather than protolith permeabilities.

There is a significant correlation between the bulk permeability of the fault damage zone and that of the protolith, except in the case of coarse siliciclastic rocks. The ratio of fault/protolith permeability is greatest in the low-porosity metamorphic and plutonic rocks that constitute both our largest sample and the bulk of Earth's brittle crust, with a much smaller difference in sedimentary rocks. Much of the variation in damage zone bulk permeability can be explained by the scaling with protolith permeability in mudrocks, carbonates, and volcaniclastic rocks (>70%); volcanic igneous rocks (60%); and plutonic and metamorphic rocks (55%).

The nature of this scaling is not clear yet, and we hypothesize that:

- The damage zones are hydraulically wider and more connected to the distant fractured protolith than would appear to be the case from purely structural mapping.
- Over geologic time scales, both the damage zone and the protolith are affected by similar *in situ* processes that affect permeability.
- Scaling effects in hydraulic testing influence the mapping of transmissive elements.

6.10 References

Aben, F. M., Doan, M.-L., Mitchell, T.M., Toussaint, R., Reuschlé, T., & Fondriest, et al. (2016) Dynamic fracturing by successive coseismic loadings leads to pulverization in active fault zones. *Journal of Geophysical Research Solid Earth*, 121, 1–23

Achtziger-Zupancic, P., Loew, S., & Mariéthoz, G. (2017) A new global database to improve predictions of permeability distribution in crystalline rocks at site scale. *Journal of Geophysical Research Solid Earth*, 122, 3513–3539

Aydin, A. (2000) Fractures, faults, and hydrocarbon entrapment, migration and flow. *Marine and Petroleum Geology*, 17, 797–814

Barthélémy, J-F. (2009) Effective permeability of media with a dense network of long and micro fractures. *Transport in Porous Media*, 76, 153–178

Barton, C.A., Zoback, M.D., & Moos, D. (1995) Fluid flow along potentially active faults in crystalline rock. *Geology*, 23(8), 683–686

Bedinger, M.S., Langer, W.H., & Reed, J.E. (1987) Synthesis of hydraulic properties of rocks with reference to the Basin and Range Province, southwestern United States. *Water Supply Paper* 2310, Denver, Colorado: U.S. Geological Survey

Belcher, W.R., Sweetkind, D.S., & Elliott, P.E. (2002) Probability distributions of hydraulic conductivity for the hydrogeologic units of the Death Valley regional ground-water flow system, Nevada and California. *Water Resources Investigations Report* 02-4212. Carson City, Nevada: U.S. Geological Survey

Bense, V.F., Gleeson, T., Loveless, S.E., Bour, O., & Scibek, J. (2013) Fault zone hydrogeology. *Earth-Science Reviews*, 127, 171–192

Bonini, M. (2013) Fluid seepage variability across the external Northern Apennines (Italy): Structural controls with seismotectonic and geodynamic implications. *Tectonophysics*, 590, 151–174

Bossart, P., Hermanson, J., & Mazurek, M. (2001) Äspö Hard Rock Laboratory analysis of fracture networks based on the integration of structural and hydrogeological observations on different scales. Svensk Kärnbränslehantering AB (SKB), Technical Report TR-01-21, Stockholm, Sweden

Brace, W.F. (1980) Permeability of crystalline and argillaceous rocks. *International Journal* *of Rock Mechanics and Mining Sciences & Geomechanics Abstracts*, 17(5), 241–251

Brace, W.F. (1984) Permeability of crystalline rocks: new in situ measurements. *Journal of Geophysical Research*, 89(B6), 4327–4330

Brandon, J.R. (1974) Rock mechanics properties of typical foundation rock types. Summarizing physical and mechanical tests of rock samples from several types of foundation sites. Report REC-ERC-74-10, 99 pages. U.S. Bureau Of Reclamation, Denver, Colorado

Breusch, T.S., & Pagan, A.R. (1979) Simple test for heteroscedasticity and random coefficient variation. *Econometrica*, 47 (5), 1287–1294

Caine, J.S., Evans, J.P., & Foster, C.B. (1996) Fault zone architecture and permeability structure. *Geology*, 24, 1025–1028

Cappa, F., J. Rutqvist, & Yamamoto, K. (2009) Modeling crustal deformation and rupture processes related to upwelling of deep CO2-rich fluids during the 1965–1967 Matsushiro earthquake swarm in Japan. *Journal of Geophysical Research*, 114, B10304

Chester, F.M., & Logan, J.M. (1986) Implications for mechanical properties of brittle faults from observations of the Punchbowl Fault Zone, California. *PAGEOPH*, 124(1/2), 79–106

Childs, C., Manzocchi, T., Walsh, J.J., Bonson, C.G., Nicol, A., & Schopfer, M.P.J. (2009) A geometric model of fault zone and fault rock thickness variations. *Journal of Structural Geology*, 31, 117–127

Cox, S.F. (2016) Injection-driven swarm seismicity and permeability enhancement: implications for the dynamics of hydrothermal ore systems in high fluid-flux, over-pressured faulting regimes. *Economic Geology*, 111(3), 559–587

Coyle, B.J., & Zoback, M.D. (1988) In situ permeability and fluid pressure measurements at ~2 km depth in the Cajon Pass research well. *Geophysical Research Letters*, 15(9), 1029–1032

Curewitz, D., & Karson, J.A. (1997) Structural settings of hydrothermal outflow: Fracture permeability maintained by fault propagation and interaction. *Journal of Volcanology and Geothermal Research*, 79, 149–168

de Graaf, I.E.M., Sutanudjaja, E.H., van Beek, L.P.H., & Bierkens, M.F.P. (2015) A high-resolution global-scale groundwater model. *Hydrological Earth System Sciences*, 19, 823–837

Dewandel, B., Lachassagne, P., Wyns, R., Maréchal, J.C., & Krishnamurthy, N.S. (2006) A generalized 3-D geological and hydrogeological conceptual model of granite aquifers controlled by single or multiphase weathering. *Journal of Hydrology*, 330, 260–284

Dezayes, C., Genter, A., & Valley, B. (2010) Structure of the low permeable naturally fractured geothermal reservoir at soultz. *Comptes Rendus Geosciences*, 343, 7-8, 517–530

Dubois, M., Ougougdal, M.A., Meere, P., Royer, J-J., Boiron, M-C., & Cathelineau, M. (1996) Temperature of paleo- to modern self-sealing within a continental rift basin : The fluid inclusion data (Soultz-sous-Forêts, Rhine graben, France). *European Journal of Mineralogy*, 8, 1065–1080

EarthCube (2018) Project by Division of Advanced Cyberinfrastructure (ACI) and the Geosciences Directorate (GEO) of the US National Science Foundation (NSF). (available at https://www.earthcube.org/digitalCrustDemonstration)

Ehrenberg, S.N., & Nadeau, P.H. (2005) Sandstone vs. carbonate petroleum reservoirs: A global perspective on porosity-depth and porosity-permeability relationships. *AAPG Bulletin*, 89(4), 435–445

Enachescu, C., Lavanchy J-M, Ostrowski L, Senger R, Wozniewicz J (1995) Hydrological investigations at Wellenberg: hydraulic packer testing in boreholes SB4a/v and SB4a/s, methods and field results. NAGRA, Technical Report 95-02, Wettingen, Switzerland

Evans, K., Moriya, H., Niitsuma, H., Jones, R., Phillips, W., Genter, A., Sausse, J., Jung, R., & Baria, R. (2005) Microseismicity and permeability enhancment of hydrogeologic structures during massive fluid injections into granite at 3 km depth at the Soultz HDR site. *Geophysical Journal International*, 160, 388–412

Fan, Y. Richard, S., Bristol, R.S., Peters, S.E., Ingebritsen, S.E., Moosdorf, N., et al. (2014) DigitalCrust – a 4D data system of material properties for transforming research on crustal fluid flow. *Geofluids*, 15, 372–379

Faulds, J.E., Hinz, N.H., Coolbaugh, M.F., Cashman, P.H., Kratt, C. Dering, G. et al. (2011) Assessment of Favorable Structural Settings of Geothermal Systems in the Great Basin, Western USA. *GRC Transactions*, 35, 777–783

Faulkner, D.R., Jackson, C.A.L., Lunn, R.J., Schlische, R.W., Shipton, Z.K., Wibberley, C.A.J., & Withjack, M.O. (2010) A review of recent developments concerning the structure, mechanics and fluid flow properties of fault zones. *Journal of Structural Geology*, 32, 1557–1575

Fisher, A.T. (1998) Permeability within basaltic oceanic crust. *Reviews of Geophysics*, 36(2), 143–182

Fisher, H-N., & Tester, J.W. (1979) An analysis of the pressure transient testing of a man-made fractured geothermal reservoir. Workshop on Geothermal Reservoir Engineering, Stanford University, Stanford, California, December 12, 1979

Fisher, Q., Kets, F., & Crook, A. (2013) Self-sealing of faults and fractures in argillaceous formations: Evidence. Technical report NAB 13-06, Nagra. Wettingen, Switzerland

Follin, S., & Stigsson, M. (2014) A transmissivity model for deformation zones in fractured crystalline rock and its possible correlation to in situ stress at the proposed high-level nuclear waste repository site at Forsmark, Sweden. *Hydrogeology Journal*, 22, 299–311

Fujimoto, K., Takahashi, M., Doi, N., & Kato, O. (2000) High permeability of Quaternary granites in the Kakkonda geothermal area, northeast Japan. Proceedings of the World Geothermal Congress 2000, 1139–1344

Geier, J., Bath, A., & Spephansson, O. (2012) Comparison of site descriptive models for Olkiluoto, Finland and Forsmark, Sweden. Report STUK-TR 14. Radiation and Nuclear Safety Authority, Helsinki, Finland

Geraud, Y., Rosener, M., Surma, F., Place, J., Le Garzic, E., & Diraison, M. (2010) Physical properties of fault zones within a granite body: Example of the Soultz-sous-Forêts geothermal site. *Comptes Rendus Geoscience*, 342, 566–574

Gilbert, L.A., & Bona, M.L. (2016) Permeability of oceanic crustal rock samples from IODP Hole 1256D. *Geochemistry, Geophysics, Geosystems*, 17, 3825–3832

Glamheden, R., Fredriksson, A., Röshoff, K., Karlsson J., Hakami, H., Christiansson, R. (2007) Rock Mechanics Forsmark Site descriptive modelling Forsmark stage 2.2. Report R-07-31. Swedish Nuclear Fuel and Waste Management Co., SKB. Stockholm, Sweden

Gleeson, T., Moosdorf, N., Hartmann, J., & van Beek, L.P.H. (2014) A glimpse beneath earth's surface: GLobal HYdrogeology MaPS (GLHYMPS) of permeability and porosity. *Geophysical Research Letters*, 41, 3891–3898

Gleeson, T., Smith, L., Moosdorf, N., Hartmann, J., Durr, H.H., Manning, A.H., van Beek, L.P.H., & Jellinek, A.M. (2011) Mapping permeability over the surface of the Earth. *Geophysical Research Letters*, 38, L02401

Grämiger, L. M., Moore, J.R., Gischig, V.S., Ivy-Ochs, S., & Loew, S. (2017) Beyond debuttressing: Mechanics of paraglacial rock slope damage during repeat glacial cycles. *Journal of Geophysical Research Earth Surface*, 122, 1004–1036

Gratier, J.-P., Favreau, P., & Renard, F. (2003) Modeling fluid transfer along California faults when integrating pressure solution crack sealing and compaction processes. *Journal of Geophysical Research*, 108(B2), 2104

GSJ (2012) Seamless digital geological map of Japan 1: 200,000. Jul 3, 2012 version. Research Information Database DB084, Geological Survey of Japan, National Institute of Advanced Industrial Science and Technology (AIST), Tokyo, Japan

Hagiwara, S., Sakamoto, Y., Takebe, S., & Nakayama, S. (2004) Data on mechanical properties of rocks in Japan for subsurface disposal of radioactive waste (JAERI-Data/Code--2004-004). Japan Atomic Energy Research Institute Tokai-mura, Ibaraki, Japan

Hartikainen, K., & Hartikainen, J. (1998) Posiva's site investigations in Olkiluoto, Kivetty, Romuvaara and Hästholmen by He-gas methods in 1997. Working Report 98–17e, Posiva Oy, Helsinki, Finland

Hartikainen, K., Hartikainen, J., & Timonen, J. (1997) Through-Diffusion, Permeability, Channel-Flow and In Situ Results for Porosity and Migration Properties of Rock Samples by He-Gas Methods. Working report POSIVA-97-13. Posiva Oy, Helsinki, Finland

Havlová, V., Vecerník, P., Najser, J., Sosna, K., & Breiter, K. (2012) Radionuclide diffusion into undisturbed and altered crystalline rocks. *Mineralogical Magazine*, 76(8), 3191–3201

Heikamp, S., & Nover, G. (2003) An Integrated Study on Physical Properties of a KTB Gneiss Sample and Marble from Portugal: Pressure Dependence of the Permeability and Frequency Dependence of the Complex Electrical Impedance. *Pure and Applied geophysics*, 160, 929–936

Hirose, T., & Hayman, N.W. (2008) Structure, permeability, and strength of a fault zone in the footwall of an oceanic core complex, the Central Dome of the Atlantis Massif, Mid-Atlantic Ridge, 30 N. *Journal of Structural Geology*, 30, 1060–1071

Huenges, E., Erzinger, J., Kuck, J., Engeser, B., & Kessels, W. (1997) The permeable crust:

Geohydraulic properties down to 9101m depth. *Journal of Geophysical Research*, 102(B8), 18255–18265

IEAGHG (2016) Fault permeability. Report produced by GNS Science Consultancy, New Zealand, for the International Energy Agency Environmental Projects Ltd. (IEAGHG), Report: 2016/13, October 2016. Cheltenham, UK

IFC (2013) Success of geothermal wells: A global study. Report by GeothermEx Inc. for International Finance Corporation (IFC), World Bank Group, Washington, D.C.

Ingebritsen, S.E., & Manning, C.E. (1999) Geological implications of a permeability-depth curve for the continental crust. *Geology*, 27, 1107–1110

Ingebritsen, S.E., & Manning, C.E. (2010) Permeability of the continental crust: dynamic variations inferred from seismicity and metamorphism. *Geofluids*, 10, 193–205

Ishii, E., Sanada, H., Funaki, H., Sugita, Y., & Kurikami, H. (2011) The relationships among brittleness, deformation behavior, and transport properties in mudstones: An example from the Horonobe Underground Research Laboratory, Japan. *Journal of Geophysical Research*, 116, B09206

Ishii, E. (2015) Predictions of the highest potential transmissivity of fractures in fault zones from rock rheology: Preliminary results. *Journal of Geophysical Research Solid Earth*, 120, 2220–2241

Johnson, G.R. (1983) Rock property measurements and analysis of selected igneous, sedimentary, and metamorphic rocks from world-wide localities. Open-File report 83-736, U.S. Geological Survey

Johri, M. (2012) Fault damage zones – observations, dynamic modeling, and implications on fluid flow. Phd Dissertation, [https://srb.stanford.edu/fault-damage-zones-observations-dynamic-modeling-and-implications-fluid-flow]. Stanford University, California

Juhlin, C., & Sandstedt, H. (1989) Storage of nuclear waste in very deep boreholes: Feasibility study and assessment of economic potential. Svensk Kärnbränslehantering AB (SKB), Technical Report 89–39, Stockholm, Sweden

Katayama, I., Terada, T., Okazaki, K., & Tanikawa, W. (2012) Episodic tremor and slow slip potentially linked to permeability contrasts at the Moho. *Nature Geoscience*, 5, 731–734

Kesonen, A. (2015) Mechanical properties of Finnish rocks based on uniaxial compressive strength and tensile strength tests. MSc thesis, Aalto University

Kim, Y-S., Peacock, D.C.P., and Sanderson, D.J. (2004) Fault damage zones. *Journal of Structural Geology*, 26, 503–517

Kinoshita, C., & Saffer, D. M. (2018) In situ permeability and scale dependence of an active accretionary prism determined from cross-borehole experiments. *Geophysical Research Letters*, 45, 6935–6943

Kitagawa, Y., & Kano, Y. (2016) Changes in permeability of the Nojima fault damage zone inferred from repeated water injection experiments. *Earth, Planets and Space*, 68, 185

Kohno, M., & Maeda, H. (2012). Relationship between point load strength index and uniaxial compressive strength of hydrothermally altered soft rocks. *International Journal of Rock Mechanics & Mining Sciences*, 50, 147–157

Kopf, A. (2001) Permeability variation across an active low-angle detachment fault, western Woodlark Basin (ODP Leg 180), and its implication for fault activation. Geological Society, London, *Special Publications*, 186, 23–41

Kuva, J., Voutilainen, M., Kekäläinen, P., Siitari-Kauppi, M., Timonen, J., & Koskinen, L. (2015) Gas phase measurements of porosity, diffusion coefficient and permeability in rock samples from Olkiluoto bedrock, Finland. *Transport in Porous Media*, 107(1), 187–204

Lamur, A., Kendrick, J.E., Eggertsson, G.H., Wall, R.J., Ashworth, J.D. & Lavallée, Y. (2017) The permeability of fractured rocks in pressurised volcanic and geothermal systems. *Scientific Reports*, 7, 6173

Lanaro, F., & Matsui, H. (2007) BEM-DDM Modelling of Rock Damage and Its Implications on Rock Laboratory Strength and In-situ Stress. Report: JAEA-Research 2007-093. Mizunami, Gifu, Japan: Japan Atomic Energy Agency

Lockner, D., Tanaka, H., Ito, H., Ikeda, R., Omura, K., & Naka, H. (2009) Geometry of the Nojima Fault at Nojima-Hirabayashi, Japan – I. A simple damage structure inferred from borehole core permeability. *Pure and Applied Geophysics*, 166, 1649–1667

Lockner, D.A., & Beeler, N.M. (2002) Rock failure and earthquakes. In: Lee, H.K., Kanamori, H., Jennings, P.C., Kisslinger, C. (Eds.), International Handbook of Earthquake & Engineering Seismology, Part A, Volume 81A, 1st Edition. p.505–537. Academic Press

Lockner, D.A., Summers, R., Moore, D., & Byerlee, J.D. (1982) Laboratory Measurements of Reservoir Rock from the Geysers Geothermal Field, California. *International Journal of Rock Mechanics and Mine Sciences & Geomechanics Abstracts*, 19, 65–80

Long, J.S., & Ervin, L.H. (2000) Using heteroscedasticity consistent standard errors in the linear regression model. *The American Statistician*, 54(3), 217–224

Lupi, M., Geiger, S., & Graham, C.M. (2011) Numerical simulations of seismicity‐induced fluid flow in the Tjörnes Fracture Zone, Iceland. *Journal of Geophysical Research*, 116, B07101

Maaranen, J., Lehtioksa, J., & Timonen, J. (2001) Determination of porosity, permeability and diffusivity of rock samples from Äspö HRL using the helium gas method. Äspö Hard Rock Laboratory, International Progress Report IPR-02-17, Svensk Kärnbränslehantering AB, Stockholm, Sweden

Manga, M., Beresnev, I., Brodsky, E.E., Elkhoury, J.E., Elsworth, D., Ingebritsen, S.E., Mays, D.C., & Wang, C-Y. (2012) Changes in permeability caused by transient stresses: Field observations, experiments, and mechanisms. *Reviews of Geophysics*, 50, RG2004

Manning, C.E., & Ingebritsen, S.E. (1999) Permeability of the continental crust: The implications of geothermal data and metamorphic systems. *Reviews of Geophysics*, 37, 127–150

Maréchal, J. C. (1999) Observation des massifs cristallins alpins au travers des ouvrages souterrains: 2. Definition du role hydrogeologique de la zone decomprimee. *Hydrogeologie*, 2, 33–42

Masset, O., & Loew, S. (2013) Quantitative hydraulic analysis of pre-drillings and inflows to the Gotthard Base Tunnel (Sedrun Lot, Switzerland). *Engineering Geology*, 164, 50–66

Matsumoto, N., & Shigematsu, N. (2018) In-situ permeability of fault zones estimated by hydraulic tests and continuous groundwater-pressure observations. *Earth, Planets and Space*, 70(13), 1–12

MathWorks Inc. (2016) Matlab, R2016b

Mielke, P., Weinert, S., Bignall, G., & Sass, I. (2016) Thermo-physical rock properties of greywacke basement rock and intrusive lavas from the Taupo Volcanic Zone, New Zealand. *Journal of Volcanology and Geothermal Research*, 324, 179–189

Miller, S.A., & Nur, A. (2000) Permeability as a toggle switch in fluid-controlled crustal processes. *Earth and Planetary Science Letters*, 183, 133–146

Miller, S.A., Collettini, C., Chiaraluce, L., Cocco, M., Barchi, M., & Kaus, J.P. (2004) Aftershocks driven by a high-pressure CO2 source at depth. *Nature*, 427, 724–727

Mitchell, T.M., & Faulkner, D.R. (2012) Towards quantifying the matrix permeability of fault damage zones in low porosity rocks. *Earth and Planetary Science Letters*, 339–340, 24–31

Mizoguchi, K., Hirose, T., Shimamoto, T., & Fukuyama, E. (2008) Internal structure and permeability of the Nojima fault, Southwest Japan. *Journal of Structural Geology*, 30, 513–524

Moore, D.E., Lockner, D.E., & Byerlee, J.D. (1994) Reduction of permeability in granite at elevated temperatures. *Science*, 265, 1558–1561

Morrow, C., & Byerlee, J. (1988) Permeability of rock samples from Cajon Pass, California. *Geophysical Research Letters*, 15, 1033–1036

Morrow, C., Lockner, D., Hickman, S., Rusanov, M., & Rockel, T. (1994) Effects of lithology and depth on the permeability of core samples from the Kola and KTB drill holes. *Journal of Geophysical Research*, 99(B4), 7263–7274

Morrow, C.A., & Lockner, D.A. (1994) Permeability differences between surface-derived and deep drillhole core samples. *Geophysical Research Letters*, 21(19), 2151–2154

Morrow, C.A., & Lockner, D.A. (1997) Permeability and porosity of the Illinois UPH 3 drillhole granite and a comparison with other deep drillhole rocks. *Journal of Geophysical Research*, 102(B2), 3067–3075

Muraoka, H., Sakaguchi, K., Nakao, S., & Kimbara, K. (2006) Discharge temperature–discharge rate correlation of Japanese hot springs driven by buoyancy and its application to permeability mapping. *Geophysical Research Letters*, 33, L10405

Neuzil, C.E. (1995) Abnormal pressures as hydrodynamic phenomena. *American Journal of Science*, 295, 742–786

Nuzzo, R. (2014) Statistical errors. P values, the 'gold standard' of statistical validity, are not as reliable as many scientists assume. *Nature*, 506, 150–152

Perras, M.A., & Diederichs, M.S. (2014) A review of the tensile strength of rock: Concepts and testing. *Geotechnical and Geological Engineering*, 32, 525–546

Peters, S.E., Husson, J.M., & Czaplewski, J. (2018) Macrostrat: a platform for geological data integration and deep-time earth crust research. *Geochemistry, Geophysics, Geosystems*, 19, 1393–1409

Pine, R.J., & Batchelor, A.S. (1984) Downward migration of shearing in jointed rock during hydraulic injections. *International Journal of Rock Mechanics Mining Sciences & Geomechanics Abstracts*, 21(5), 249–263

Posiva (2003) Baseline conditions at Olkiluoto. Report Posiva 2003-02, Posiva Oy, Helsinki, Finland

Price, R.H. (1983) Analysis of rock mechanics properties of volcanic tuff units from Yucca Mountain, Nevada Test Site. Sandia report SAND82-1315, Aug 1983. Sandia National Laboratories, Albuquerque, New Mexico

Reyer, D., & Philipp, S.L. (2014) Empirical relations of rock properties of outcrop and core samples from the Northwest German Basin for geothermal drilling. *Geothermal Energy Science*, 2, 21–37

Rice, J. (1992) Fault stress states, pore pressure distributions, and the weakness of the San Andreas Fault. In B. Evans, T.-f. Wong (Eds.), Fault mechanics and transport properties of rocks (pp. 69-88). San Diego, CA: Academic Press

Saar, M.O., & Manga, M. (2004) Depth dependence of permeability in the Oregon Cascades inferred from hydrogeologic, thermal, seismic, and magmatic modeling constraints. *Journal of Geophysical Research*, 109, B04204

Saffer, D.M. (2015) The permeability of active subduction plate boundary faults. *Geofluids*, 15, 193–215

Sanchez-Vila, X., Guadagnini, A., & Carrera, J. (2006) Representative hydraulic conductivities in saturated groundwater flow. *Reviews of Geophysics*, 44, RG3002, 1–46

Sanyal, S.K., & Morrow, J.W. (2011) An investigation of drilling success in geothermal exploration, development and operation. *GRC Transactions*, 35, 233–237

Sasaki, S. (1998) Characteristics of microseismic events induced during hydraulic fracturing experiments at the Hijiori hot dry rock geothermal energy site, Yamagata, Japan. *Tectonophysics*, 289, 171–188

Sausse, J., & Genter, A. (2005) Types of permeable fractures in granite. In P.K. Harvey, T.S. Brewer, P.A. Pezard, V.A. Petrov (Eds.), Petrophysical properties of crystalline rocks. *Special Publications* (Vol. 240, pp. 1–14). London, England: *Geological Society*

Savage, H.M, & Brodsky, E.E. (2011) Collateral Damage: Evolution with displacement of fracture distribution and secondary fault strands in fault damage zones. *Journal of Geophysical Research*, 116, 14

Schild, M., Siegesmund, S., Vollbrecht, A., & Mazurek, M. (2001) Characterization of granite matrix porosity and pore-space geometry by in situ and laboratory methods. *Geophysical Journal*, 146(1), 111–125

Scholz, C.H. & Anders, M.H. (1994) The permeability of faults. p.247-253, In: Hickman, S.H., Sibson, R., Bruhn, R. (Eds.), *The Mechanical Involvement Of Fluids In Faulting*. Open File Report 94-228, U.S. Geological Survey

Scibek, J. (2019 submitted - a) Multidisciplinary database of permeability of fault zones and surrounding protolith rocks at world-wide sites. Submitted to Scientific Data journal

Scibek, J., Gleeson, T., & McKenzie, J.M. (2016) The biases and trends in fault zone hydrogeology conceptual models: global compilation and categorical data analysis. Geofluids, 16,782–798

Scibek, J., Gleeson, T., Ingebritsen, S., & McKenzie, J. (2019 submitted - b) The Permeability of Fault Zones in the Upper 1 Continental Crust. Submitted to Geophysical Research Letters, AGU

Seebeck, H., Nicol, A., Walsh, J.J., Childs, C., Beetham, R.D., & Pettinga, J. (2014) Fluid flow in fault zones from an active rift. *Journal of Structural Geology*, 62, 52–64

Shapiro, S.S., & Wilk, M.B. (1965) An analysis of variance test for normality (complete samples). *Biometrika*, 52(3 and 4), 591–611

Shabelansky, A.H., Bernabe, Y., Mok, U., & Evans, J.B. (2014) Temperature influence on permeability of Sioux quartzite containing mixtures of water and carbon dioxide. *International Journal of Rock Mechanics & Mining Sciences*, 70, 546–551

Stober, I., & Bucher, K. (2007) Hydraulic properties of the crystalline basement. *Hydrogeology Journal* 15, 213–224

Sveinbjörnsson, B.M. (2014) Success of High Temperature Geothermal Wells in Iceland.

Report ÍSOR-2014/053, Iceland GeoSurvey, Reykjavík, Iceland. 42 pp.

Thury, M., Gautschi, A., Mazurek, M., Müller, W.M., Naef, H., & Pearson et al. (1994) Geology and hydrogeology of the crystalline basement of northern Switzerland. Nagra Technical Report NTB 93-01, Wettingen, Switzerland

Townend, J., & Zoback, M.D. (2000) How faulting keeps the crust strong. *Geology*, 28, 399–402

Tsutsumi, A., Nishio, S., Mizoguchi, K., Hirose, T., Uehara, S., Sato, K., Tanikawa, W., & Shimamoto, T. (2004) Principal fault zone width and permeability of the active Neodani fault, Nobi fault system, Southwest Japan. *Tectonophysics* 379, 93–108

U.S. Geological Survey (2006) Quaternary fault and fold database for the United States. List of cooperators: Alaska - Alaska Department of Natural Resources, Arizona - Arizona Geological Survey, California - California Geological Survey, Colorado - Colorado Geological Survey, Idaho - Idaho Geological Survey, Illinois - Illinois State Geological Survey, Louisiana - Louisiana Geological Survey, Montana - Montana Bureau of Mines and Geology, Nevada - Nevada Bureau of Mines and Geology, New Mexico - New Mexico Bureau of Mines and Mineral Resources, Texas - Texas Bureau of Economic Geology, Utah - Utah Geological Survey. Accessed Mar 16 2016, http//earthquakes.usgs.gov/regional/qfaults/

U.S. Geological Survey (2016). Digital fault maps for US States. Accessed Mar 16 2016, http//earthquakes.usgs.gov/regional/qfaults/

Uehara, S., Shimamoto, T., Okazaki, K., Funaki, H., Kurikami, H., Niizato, T., & Ohnishi, Y. (2012) Can surface samples be used to infer underground permeability structure? A test case for a Neogene sedimentary basin in Horonobe, Japan. *International Journal of Rock Mechanics & Mining Sciences*, 56, 1–14

Valley, B.C. (2007) The relation between natural fracturing and stress heterogeneities in deep-seated crystalline rocks at Soultz-sous-Forêts (France). Doctoral thesis, ETH Zurich, Switzerland. [Downloaded from https://doi.org/10.3929/ethz-a-005562794]

Vitovtova, V.M., Shmonov, V.M., & Zharikov, A.V. (2014) The porosity trend and pore sizes of the rocks in the continental crust of the Earth: evidence from experimental data on permeability. *Izvestiya, Physics of the Solid Earth*, 50(5), 593–602

Walker, R.J., Holdsworth, R.E., Imber, J., Faulkner, D.R., & Armitage, P.J. (2013) Fault zone architecture and fluid flow in interlayered basaltic volcaniclastic-crystalline sequences. *Journal of Structural Geology*, 51, 92–104

Wang, H., Xu, W., Shao, J., & Skoczylas, F. (2014) The gas permeability properties of low-permeability rock in the process of triaxial compression test. *Materials Letters*, 116, 386–388

Wasserstein, R.L., & Lazar, N.A. (2016) The ASA's Statement on p-Values: Context, Process, and Purpose. *The American Statistician*, 70(2), 129–133

Wibberley, C.A.J., & Shimamoto, T. (2003) Internal structure and permeability of major strike-slip fault zones: the Median Tectonic Line in Mie Prefecture, Southwest Japan. *Journal of Structural Geology*, 25, 59–78

Wilkinson, B.H., McElroy, B.J., Kesler, S.E., Peters, S.E., & Rothman, E.D. (2009) Global geologic maps are tectonic speedometers—Rates of rock cycling from area-age frequencies. *GSA Bulletin*, 121(5/6), 760–779

Wyering, L.D., Villeneuve, M.C., Wallis, I.C., Siratovich, P.A., Kennedy, B.M., Gravley, D.M., & Cant, J.L. (2014) Mechanical and physical properties of hydrothermally altered rocks, Taupo Volcanic Zone, New Zealand. *Journal of Volcanology and Geothermal Research*, 288, 76–93

Yamashita, T., & Tsutsumi, A. (2018) Involvement of fluids in earthquake ruptures. Field/experimental data and modeling. Japan: Springer. doi:10.1007/978-4-431-56562-8

Zeigler, T.W. (1976) Determination of rock mass permeability. Technical Report S-76-2, U.S. Army Engineer Waterways Experiment Station, Vicksbury, Miss. Prapared for U.S. Army, Washington, D.C.

Zhang, L. (2017) Engineering properties of rocks. 2nd edition. Cambridge, MA: Elsevier. ISBN: 978-0-12-802833-9

Zharikov, A.V., Vitovtova, V.M., Shmonov, V.M., & Grafchikov, A.A. (2003) Permeability of the rocks from the Kola superdeep borehole at high temperature and pressure: implication to fluid dynamics in the continental crust. *Tectonophysics*, 370, 177–191

Zimmermann, G., Korner, A., & Burkhardt, H. (2000) Hydraulic pathways in the crystalline rock of the KTB. *Geophysical Journal International*, 142, 4–14

Zoback, M.D., & Byerlee, J.D. (1975) The effect of microcrack dilatancy on the permeability of Westerly granite. *Journal of Geophysical Research*, 80(5), 752–755

CHAPTER 7

7 Fault zone permeability structure in Precambrian metapelitic gneiss and pegmatite, hosting uranium mineralization under the eastern Athabasca Basin, Canada

This last chapter describes my field-based research on the hydrogeology of a large fault zone where the permeability structure is complex but also well-preserved and accessible by mineral exploration drilling.

7.1 Introduction

The number of in-situ tests in faulted metamorphic rocks is large, particularly at geothermal fields, engineering projects and also intensively tested as several planned radioactive waste repositories (e.g. review in Chapter 3). Detailed transects at discrete intervals are scarce and difficult to separate the different deformation zones in heterogeneous multi-stranded faults (Karasaki et al. 2012). Transects have been done in active fault zones that have relatively clearly defined geometries, tested directly on packer-separated intervals (Matsumoto and Shigematsu 2018), or indirectly by observing tidal responses (Xue et al. 2013). However, the test scale and level of detail varies between study locations, while the types of observations and tests may support one or more types of conceptual model of fluid flow in a fault at present time or paleo-flow at other geologic time (Scibek et al. 2016).

From matrix permeability and porosity data, of particular interest are permeability contrasts between the fault rocks and the variably deformed or damaged host rocks, because of the conduit and barrier effects on fluid flow. The matrix permeability has been tested on many fault outcrops and in drillcore transects across major active faults (Evans et al. 1997, Wibberley and Shimamoto 2003, Lockner et al. 2009, Morrow et al. 2014). In most cases, the conceptual models of fluid flow in faults can be inferred, but the details inside the fault zone and the porosity and permeability is poorly known because of low resolution of in-situ hydraulic and rock permeability data in fault zones. Another important aspect of this problem is the evolution of porosity and permeability over geologic time. A detailed study of in-situ rock properties in fault zones can help to map the alteration geochemistry, sequence of alteration events, and cross-cutting relationships of various structures or zones, as is routinely done at many mineral exploration projects, but the porosity and permeability of those rocks and zones of rocks is rarely collected at all, or where tested, not in sufficient spatial distribution and detail to allow progress on the questions of permeability and porosity evolution.

In this work, we estimate the matrix permeability distribution in a major reverse fault zone the Gryphon uranium deposit located on the Wheeler River project in northern Saskatchewan, Canada. The Gryphon deposit is hosted within the metasedimentary basement rocks below the regional sub-Athabasca unconformity. Here, the fluid flow through fault zones and mixing with saline basinal fluids is important for understanding the formation of uranium deposits. One of the unanswered questions is of "percolation conditions", or porosity and permeability within fault zones (Mercadier et al. 2014). In this work I develop a practical medium-accuracy drillcore testing methods that allows low-cost and rapid testing of rock samples at between 1 to 0.1m intervals over 800m long drillholes, and allow a detailed permeability transects across the fault zone over multiple inclined and parallel drillholes that sample the strands of faults and fault rocks over a zone. Statistic analysis is used to compare the permeability magnitude in different rock types, different fault rocks, and hydrothermal alteration zones in the fault zone.

7.2 Regional geology and structure

The study site is in the eastern Athabasca Basin (late Paleoproterozoic age), in Precambrian (approximately 2450 to 1850Ma) felsic metasedimentary and igneous rocks that belong to the Wollaston domain fold belt (Moon 1968), over Archean granitic basement (Lewry and Sibbald 1977, Annesley et al. 2005). The Wollaston, Mudjatik and other regional domains were defined by their metamorphic and tectonic origin (Lewry and Sibbald 1977). The Wollaston and Mudjatik domains are separated by a wide tectonically disturbed (sheared, faulted) zone called the Wollaston-Mudjatik Transition Zone that forms the metamorphic grade boundary (Annesley and Madore 1994, Annesley et al. 2005) (Figure 2-2 in Chapter 1). The rocks now exhumed at Wheeler River site have metamorphic grade of upper amphibolite to granulite facies (Denison Mines unpublished geological data), similar to other metamorphic rocks in the region (Ray and Wanless 1980). The metasediments of Wollaston

Group are locally migmatitic (contain partially melted metasediment during high-grade metamorphism), locally larger cross-cutting pegmatites, as well as widespread larger leucogranitic intrusions (Annesley et al. 2005, Jeanneret et al. 2016). The larger granitic intrusions have been dated to 1760 to 1770Ma (Bickford et al. 1992), and 1795Ma at Wheeler River (Annesley et al. 2005), thus are pre-Athabasca. The fold belt and ductile shear zones, and later brittle fault zones formed during the Trans-Hudson orogeny at 1860 to 1775Ma (Bickford et al. 1990, Tran 2001). The tectonic stresses resulted in transpressional deformation, producing shear zones and later strike-slip and reverse faults (Annesley et al. 2005, Jeanneret et al. 2016). The steeply dipping and overturned folds in the orogen have been eroded and truncated to the unconformity surface, leaving a pattern of steeply dipping metasedimentary strata (Annesley et al. 2005, Jeanneret et al. 2016).

The pre-Athabasca faulting history was mainly ductile shear zones, followed by brittle faulting along the same deformation zones. The whole Wollaston-Mudjatik Transition Zone may be affected by mylonitization in a major crustal-scale transcurrent shear–fault zone (Annesley et al. 1994, 2005). Syn-deposition of basin, as described from stratigraphic relationships in the basal sediments of Read Formation, followed by post-Athabasca brittle reactivations, and a minor reactivation stage syn- or post-uranium mineral deposit formation (Annesley et al. 2005, Thomas et al. 2014). In the earliest deformation zones, the rheological contrasts of folded, altered, and intruded rocks during ductile-brittle transition conditions likely led to localization of shear zones along those boundaries, and most of subsequent brittle faulting as reverse or thrust faults. The major faulting events and most of the brittle deformation imprint on the region was accomplished by 1720Ma (Annesley et al. 2005), thus only slightly overlapping with the formation of the Athabasca Basin, in agreement with the small fault offsets in the sedimentary strata and the unconformity.

The Athabasca Basin began filling around 1810 to 1750Ma and the deposition lasted until about 1650Ma (Rainbird et al. 2007, Alexandre et al. 2007), with maximum stratigraphically-defined thickness of 3800m, as proposed by Ramaekers et al. (2007), some 1500 to 1700m of it still remaining in the centre of the basin. The maximum burial depth in the centre was estimated from fluid inclusion data as 4 to 5km (Ramaekers 2004 review and references within). The uranium mineralization events and hydrothermal fluid flow in fault zones were related to a combination of tectonic and magmatic events between 1640 and 900Ma, and mainly between 1380 and 1330Ma when most of the major deposits formed (Hoeve and Quirt 1987, Kotzer and Kyser 1995). Later uranium migration and ore re-deposition (1280 to 225Ma) (Cumming and Krstic 1992).

In the Wheeler River project, the crystalline basement of the Wollaston domain is covered by ~300 to 550m of Athabasca Group sediments (fluvial sandstone of Manitou Falls formation and the basal conglomeratic Read formation), thus the basement geology is interpreted from exploration drilling and geophysical interpretations by Denison Mines, focused on two deposit areas Phoenix and Gryphon (Figure 2-2b). The major trust faults exploit in most cases the major lithological boundaries between granitic (and pegmatitic as at Gryphon) intrusions and metapelitic domains, or between pervasively silicified "metaquartzite" domains and pelitic rocks (as at Phoenix). NE-SW regional structural trends and lineaments, corresponding to a mapped ridge along the unconformity that connects locally higher topographic highs related to reverse faults (Bethune et al. 2013). The discontinuous or stepped pattern of the major faults is partly due to lateral offsets by sub-vertical SE-NW trending faults that do not follow the regional fabric, as is clear from the basement geologic map.

7.3 Protoliths

7.3.1 Metapelites

Metapelites such as gneisses and schists form during intermediate pressure metamorphism of shales, and are found in many orogenic belts - fold belts and mountain belts (Bucher and Frey 2002). At the Wheeler River project area, as in most of the Wollaston domain, the metapelites, or pelitic gneisses, have gneissic banding and deformation, contain garnets and leucosomes (small quartz and feldspar rich neosome or melt), are locally pegmatitic. Pelites usually originate from metaorphism of mudrocks/shales, siltstones and wackes. In drillcore logged by Denison Mines, pelite is defined as having over 40% aluminous minerals: including typical pelitic minerals such as biotite, garnet, cordierite, and sillimanite. Semipelites and psammopelite (less aluminous minerals, and notably less biotite) are also common in the study area (Annesley et al. 2005). The peak metamorphism likely occurred at depths up to 35 km in these rocks (Jeanneret et al. 2016).

Graphitic pelitic gneisses occur as discrete strata, interlayered in other pelitic gneiss units, and are common in this region. The graphite content in the pelitic protolith depends on the carbonaceous content in the protolith mudrock during metamorphism (Pattison 2006), and this was likely the graphitisation in the Wollaston group rocks (Card 2012). The faults that follow the lithologic and rheologic contact between graphitic pelite and metaquartzite or pegmatite-rich blocks are usually the locations of hydrothermal (from fault zones) and basinal fluid mixing and uranium precipitation often leading to the development of large high-grade uranium deposits characteristic of this region. In major fault zones, there is also hydrothermal graphite (sourced from gases in thermal waters) that can form graphite veins and localize fault strain (Craw and Upton 2014). Vein-shaped graphitic gneiss zones are present at some deposits in the eastern Athabasca that parallels the regional fabric, and some fault segments follow the rheological contrast that the weaker graphitic units present (e.g. Millenium deposit - Guffey 2017).

7.3.2 Metaquartzites

Metaquartzites are locally important stratigraphic units in the Wollaston domain, because they form fault wall blocks of reverse or thrust faults, and topographic ridges along the unconformity at many of the uranium deposits (Harvey and Bethune 2000). Metaquartzites may derive from arkose sandstones (meta-arkose) or from other quartz-rich rocks, but the origin of metaquartzites in the fold belt from McArthur River, through Wheeler River exploration area are not yet fully explained. Card (2012) noted that the metaquartzite often grades into pelitic gneissic or pegmatite rocks, from the massive quartz rock that contains remnant planar fabrics. The lack of sharp boundaries, lack of sedimentary fabrics, and remnant gneissic fabrics also point to metamorphism leading to a silicified version of the host metasedimentary or pegmatitic rock (Card 2012, 2014). In that case, the rocks are pervasively silicified metamorphosed metasediments, and not true quartzites. Quartzites (meta-arkose) of sedimentary origin are rather rare in the Wollaston domain that is dominated by pelites and granitic rocks. Outcrops are found on the northern shores of Lake Athabasca (Chandler 1978, Harper 1983), and near Hidden Bay near Wollaston Lake (Wallis 1971), and can be recognized by granular and brecciated texture, and are interlayered with dolomites or metapelites. Some coarse grained quartzites form by recrystallisation of siliceous rock (granulites) that appear similar to massive quartz veins (Johnstone and Mykura 1989). Volkert and Drake (1999) gave examples from New Jersey, where the metaquartzite probably was formed from quartzose sandstone, where as near graphitic pelite the metaquartzite may also contain substantial graphite (up to 40%) at some graphite mines. The quartzite was described as massive (up to 8m wide units), containing quartz and feldspar medium sized grains, but also foliated and layered similar to gneiss fabrics (Volkert et al. 2000).

7.3.3 Pegmatitic melts and intrusions in metasediments

Pegmatites are intrusive rocks that originated from the same melts of the host rocks, but elsewhere, and migrated beyond the original strata as veins or dikes (Johnstone and Mykura 1989). The thickest neosomes (or melts) might have mobilized to form larger zones, and in places the host rock is mostly melted and converted to pegmatite texture, with only a few streaks or zones left of the original rock. Pelitic and semipelitic gneisses and migmatitic leucosome are often interlayered and parallel to prevailing foliation, and the remaining paleosome (unmelted host rock) is enriched in aluminous minerals making it more pelitic (Johnstone and Mykura, 1989).

Anatectic granite (diatexite or anatectite) is a homogeneous rock formed from in-situ partial melts of the metapelites. It occurs in patches in the host rock and in pegmatitic layers, with gradational contacts (Bucher and Grapes 2011), or rather, gradational increase or decrease in granitic or metapelitic patches and zones. These partial melts occur widely in metapelites (e.g. Mark et al. 1998, Spear et al. 1999, Milord et al. 2001). In the Eastern Alps, Habler and Thöni (2001) interpreted the previously mapped pegmatites as mobilizates of pelites, where the larger mobilizate bodies formed layers with other strata, meters to >100m in width. Volkert et al. (2000) reported fewer melts in graphitic zones of pelitic gneiss. At the uranium mines in the eastern Athabasca region anatectites are sometimes called pegmatites locally, although these are anatectic melts, given the patchy gradational textures and lack of sharp intrusive contacts and often disconnected irregularly shaped "pegmatite" bodies found by drilling (Parslow et al. 1985, Bruneton 1993, Thomas et al. 2014). On outcrops of migmatitic pelites near Wollaston Lake, there are irregular bulbous bodies <1m wide, or as ductile deformed thin interlayers within pelite (Wallis et al. 1971). The pegmatites and anatectites tend to contain elevated uraninite content (higher background radiation detected in drillcore) and are locally weakly mineralized (Annesley et al. 2000, McKeough et al. 2013). Jeanneret et la 2016 suggested that the uranium-enriched pegmatites formed from uranium-enriched magma intruding the already partially melted protolith metasediment. From the above summary it appears that the gradational and highly irregular distribution of pegmatitic melts within pelitic gneisses at Wheeler River, as seen in the drillcore, fits such model, while the deposit geological model (blocks, wireframes) defined distinct pegmatite units where the pegmatite dominates the lithology. For porosity and permeability distributions of pegmatitic bodies, the distinction is important for large-scale continuity of intrusions vs. discontinuous/enclosed bodies.

In this paper we also compare the rock properties between the Gryphon fault zone and a research site in Finland, at Olkiluoto, because of very similar geology, lithology (pelitic migmatites, metapelites and other gneisses), metamorphism, structure, porosity and permeability of rocks. At Olkiluoto, the bedrock is composed of pelitic migmatites, biotite gneisses (metapelites), and hornblende gneisses, and granite gneisses (Tuisku and Karki 2010). At Olkiluoto, Finland, the metapelites underwent partial dehydration melting through decomposition of biotite, sillimanite, plagioclase and quartz during the peak of regional metamorphism, producing the migmatites during temperature estimated at 660 to 700°C and relatively low pressure of about 3.5 to 4kbar (Tuisku and Karki 2010), at around 1860Ma, a similar metamorphic history to the Wollaston Group under the eastern Athabasca Basin.

7.4 Gryphon fault zone and deposit

At the Gryphon deposit, a major reverse fault zone, dipping 50° to the south-east, hosts a uranium deposit that has been explored extensively by Denison Mines Corp. ("Denison")using more than 200 drillholes. The fault zone is approximately 500m wide, contains multiple groups of faults and fault strands in each, as is collectively referred to here as the Gryphon fault zone (Figure 7-1). There are two central and interacting fault strands (names taken from on-site geological model) that are separated by about 200m, but that have overlapping damage zones: "Offset" faults, "G" fault, "Linkage" faults in central block, and the "Basal" fault (Denison Mines geological model).

The Offset faults that cut the pelitic and graphitic pelitic gneisses and form a series of steps along the unconformity with 10 to 20m offsets and collectively about 60m. These fault slip planes appear to diverge near the unconformity from a much narrower fault zone a few hundred meters deeper along the dip. The faults generally follow the regional fabric and lithological boundaries of pelitic protoliths. In the hanging wall of the G fault is graphitic pelitic gneiss , and the footwall contains the "Quartz-Pegmatite assemblage"(quartzite or quartz-rich rock plus pegmatite with minor pelitic gneiss layers). The hanging wall graphitic pelite (2% to 15% graphite) is about 150 m thick. Below the fault are several thin zones of pervasively silicified rocks of pelitic and pegmatitic lithology. The two major faults are linked by smaller and shallow-dipping (10 to 30 degrees) plays ("Linkage" faults) that might be Riedel shears that cut pegmatitic rock units known as "Basal Pegmatite" in the block model of the deposit. Uranium mineralization occurs as irregular lens-shaped bodies along the main fault planes (dipping 30 to 50 degrees). The smaller splay (linkage) faults have higher grade uranium at fault intersections with the larger structures and main slip planes. The middle of the fault zone cuts mostly pegmatite and narrow layers of pelite. The Basal fault offsets pegmatite rocks and minor layers of pelitic gneiss.

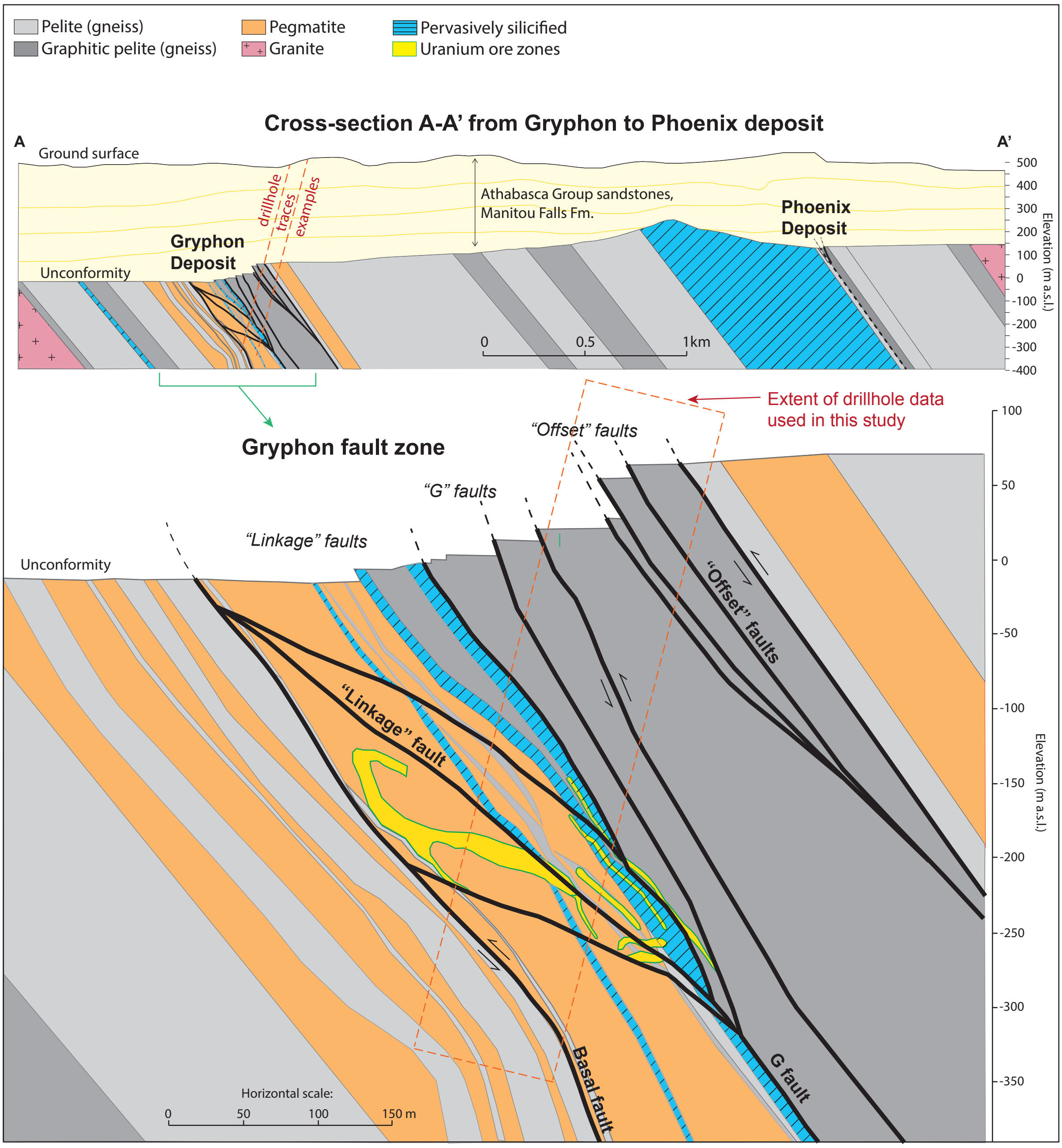

Figure 7-1 The geology and structure from Gryphon to Phoenix deposit at Wheeler River site, (a) cross-section of the Athabasca Basin and the upper portion of basement rock, and (b) structure of the Gryphon fault zone.

The footwall protolith below the Basal fault is a large block named ("Basal Pelite"), although it is an alteration of pegmatite (anatectite)-pelite sequence that has been modelled as discrete layers parallel to regional foliation. We can compare this lithology and structure to another site in pelitic gneisses in western Finland, at Olkiluoto underground research site for radioactive waste repository. There, the pelitic gneisses and veined gneisses host "pegmatite" layers and elongated bodies, parallel to regional foliation, with diffuse boundaries (Front and Paananen 2006). The Gryphon fault zone and deposit site at Wheeler River fits closely with the model from Olkiluoto research site (Finland). The geologic model of Gryphon, described in the next section, has discrete layers of "pegmatite", interlayered with metapelite, but the drillcore does not contain sharp intrusive boundaries between these rocks, except where offset by faults and only locally. The actual distribution of these anetectites is highly irregular, from cm-scale patch-shaped bodies, to clusters of patches, to mostly granitic zones a few meters wide, but containing small patches of undeformed metapelite that hasn't melted yet. Rather, the boundaries of the model layers are based on granitic content in 3m drillcore sections and are averaged among many drillhole intercepts.

The fault zone at Gryphon deposit has an obvious offset at the unconformity at some fault strands, from a few meters to 30m. This preserved fault blocks were post-depositional with the Manitou Falls formation in the Athabasca Basin but may only represent a fraction of the total displacement of these faults that led to the accumulation fine-grained fault rocks in the central deformation zones. As there is no further obvious offset between the Athabasca group sediments, these offsets likely represent the last phase of tectonic activity and the formation of the most recent and weakest fault rocks (e.g. gouges) and not the lithified (cataclastic) fault rocks. At other locations in the basin, half-graben normal faults have 50m to maximum 100m vertical displacements (Ramaekers 2004), but in the eastern Athabasca basin the vertical throws at unconformity are typically 5m to 50m (Li et al. 2015). However, prior to basin infill, the fault kinematics may have been different. Major strike-slip faults in the eastern part of Athabasca Basin, such as the Tabebarnor fault (length >600km) has minimum displacement of about 2km (Elliott 1994; Davies 1998).

7.4.1 Fault core zone and fault rocks

In the metapelite block between the Offset faults and the G fault, there are multiple fault cores and several fault strands, each with 10 to 50cm of fault gouge. The fine-grained gouge matrix contains breccia clasts (Figure 7-2a) and is categorized as gouge by texture if there are

<30% clasts (Sibson 1977, Woodcock and Mort 2008). The gouge is black to grey, but the matrix grain size is poorly sorted, has some clay, but silt to sand sized grains form the fine matrix. The larger clasts are composed of quartzite or metapelite. Relatively fine breccias are also present locally (Figure 7-2b) and contain metapelite fragments. In the clay alteration halo, the fault gouge and breccia are altered to white clay (Figure 7-2d). Cataclasites are present in variable degree of recrystalisation and alteration. Cataclasites and the host rocks are affected by clay alteration locally (Figure 7-2e) or completely bleached, silicified, desilicified, and converted to unrecognizable mass. Between fault core zones are present locally mixed zones of highly fractured rock and breccias of quartzite and metapelite (see also Figure 7-2g), sometimes with fractured older cemented sheared rock or cataclasite (Figure 7-2f). In the zones of uranium mineralization within the Gryphon fault zone, along some parts of the Linkage Faults, the cataclasites and cemented fault breccias are altered by clays (white to grey), locally altered by redox fronts of reddish-brown colour (Mercadier et al. 2011), while the uraninite grew in previously altered porous breccia clasts that now appear black with pitchblende mineral. In the metaquartzite and silicified rocks, coarse fault breccias are common and are cemented by quartz, some with drusy quartz growths in open vugs and veins. The sequences of alteration are complex, with strong evidence of silicification, followed by desilicification, sericite and various clay alteration in place of the quartz. The gouges and breccias along the Basal fault were difficult to recognize because of clay alteration.

Clay gouges are usually composed of various rock fragments of host rocks (e.g. quartz, K-feldspar, plagioclase), fragments of re-fractured fault rocks, and a finer matrix of phyllosilicates (kaolinite, dravite, chlorite, muscovite, illite and smectite mix) (Wu et al. 1979, Numelin et al. 2007, Haines et al. 2009). Clay-poor coarse gouges are the most permeable (Morrow et al. 1984). Illite and smectite may be authigenic clays (from within the gouge matrix), while chlorite is present in the rock fragments, and kaolinite is related to weathering or other shallow-depth hydrothermal processes, and any diagenetic reactions during fault rock exhumation to shallow depths (Haines et al. 2012). Some fault outcrops contain significant amounts of low-temperature clays (smectites, kaolinites, and also zeolite minerals), some likely formed by chemical weathering (Solum et al. 2003, Niwa et al. 2016). At depths 200 to 1000m depths, illite is usually the dominant clay (Isaacs et al. 2007). The porosity structure in fault gouges is heterogeneous. An example is the SAFOD drillhole in San Andreas fault (Janssen et al. 2011), where the total porosity of 2.8 to 6.7% could be attributed to 30% fracture porosity, 32% inter-clay layer porosity, 17% intergranular porosity, and the rest smaller scale porosity. Porosities of unconfined natural gouges at outcrops from major tectonic faults with wide gouges zones are 12-27% (Carboneras fault - Faulkner and Rutter 2000).

The cataclasites can form at mid-crustal depths to a few km above the brittle-ductile transition zone (Sibson 1983), but relative to the fault gouges and breccias, these are should represent the older faulting episodes along this fault zone. The most friable fault gouges and breccias are likely the most recent faulting events are show little cementation or alteration. The widths of fault rocks, such as cataclasites, are correlated with fault displacement in fault zones that developed in metamorphic rocks, but only for order of magnitude (logarithmic) values (Hull 1988). The scaling ratio is on average displacement/thickness of fault rock is about 100, but the variation is large and for a fault rock width of 1m, the displacement can range by one order of magnitude about the trend (from 10 to 1000m).

7.4.2 Fault damage zone

The fault damage zone contains the distributed brittle deformation in the form of smaller splay faults, fractures with small slip offsets, dilational fractures without offsets, microfractures, and other mineralogical alterations (Chester and Logan 1986, Caine et al. 1996). In general, different patterns of damage can be recognized near the fault tip, along the fault, or in linkage zones between faults (Kim et al. 2004). However, the mapped width of damage zone along the fault trace in plan view and in cross-section, at outcrop and in the upper 1km depth is highly variable, a long-known fact (e.g. Hobbs et al. 1965), and fault core and damage zone width varies along the fault segment (e.g. Chigira et al. 2016), and is complicated by overlapping damage zones of other faults (e.g. Peacock et al. 2017). The change in fracture frequency (or cumulative distribution) along a transect can identify the end of damage zone (Choi et al. 2016), and this also applies to microfractures around the fault core (Mitchell and Faulkner 2012). The earliest shear deformation is preserved from ductile shear and microscopic penetrative strains at mineral grain scale, that are not modified at shallower crustal depths (e.g. Takagi et al. 2012).

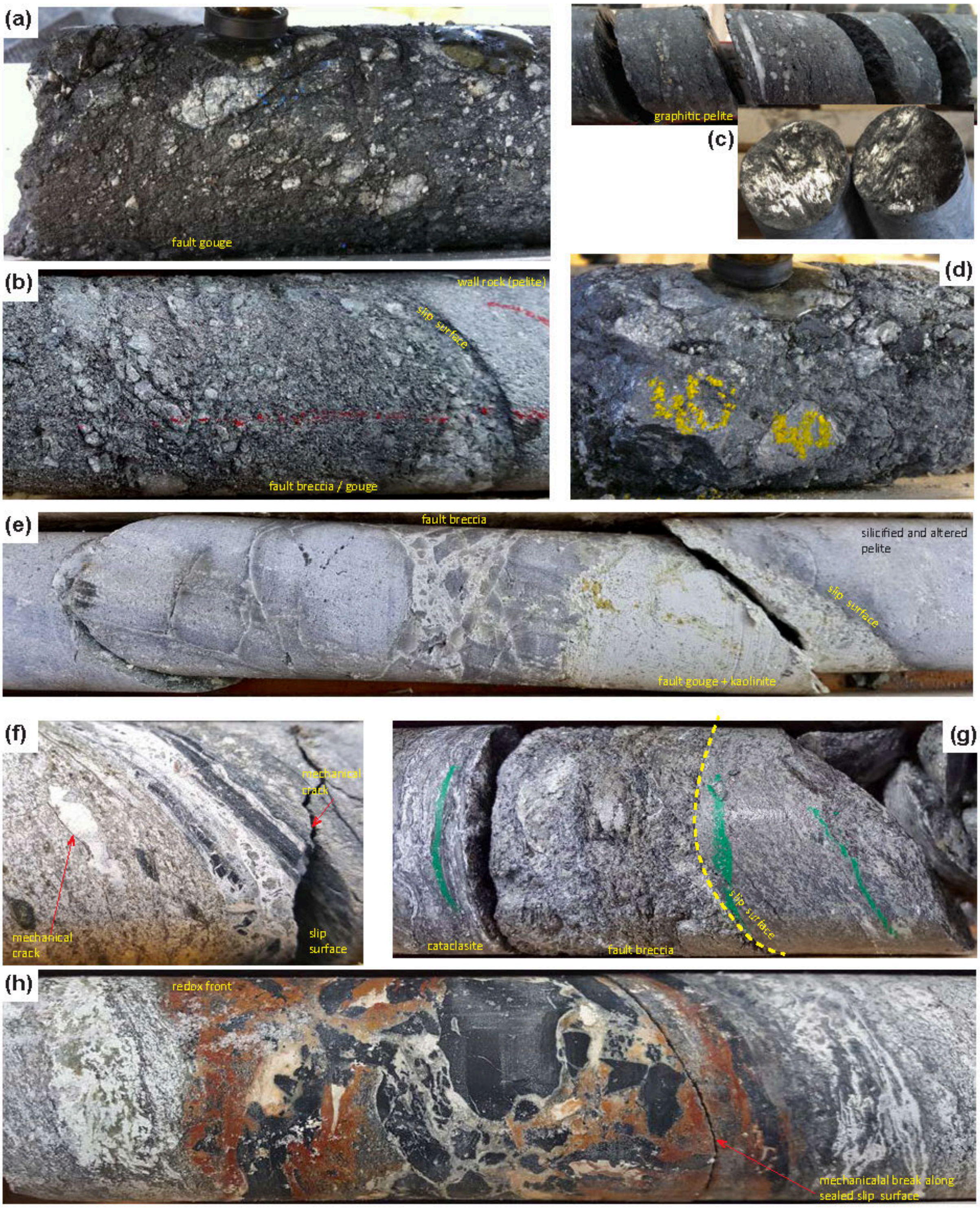

Figure 7-2 (a) Fault gouge with breccia in Offset Faults (WR-668D2, ≈ 620m), (b) strand of Offset Fault core with fine breccia (WR-687, 558m), (c) damage zone in graphitic metapelite with slickensides of cm-scale displacement shears, (d) fault breccia in G-Fault, (e) dravite+kaolinite+illite altered fault breccia and gouge in weakly altered metapelite (WR-690), (f) clay-altered cemented breccia and cataclasite (WR-688D1, ≈ 306.5m), (g) fault breccia from older cataclasite in clay-altered metapelite in G fault, (h) cemented fault breccia in linkage faults, redox fronts (reddish) and clay alteration (white-grey), hosting uranium mineralization (black).

Along the shallow dipping linkage faults inside the fault zone, the densely fractured zones are 2 to 20m wide. The fractured zones that form the damage zone of the larger faults are 100's metres wide and overlapping. Fracture density is asymmetric near the fault core zones of each fault and highly variable along the fault strands. Most if not all fractures are partly or completely sealed by mineral fills, and some of the weakly bonded fractures opened during the drilling process, thus the geotechnical fracture logs only give a partial picture of the damage zone shape and size. The layered lithology and variable rock alteration by hydrothermal fluids created a complex and heterogeneous distribution of fractures, fault rocks, porosity, and permeability that is the subject of this study.

The smaller fractures in the damage zone are either filled or have tightly fitting slickensides (from incipient rough and stepped slickensides to smooth and polished), and generally do not show any evidence meteoric water interaction (i.e. no hematite staining, no alteration of rock walls). Slickensides form easily on graphitic surfaces in fault damage zones, and fault strands will exploit the weaker parts of host rocks (often graphitic) (Craw and Upton 2014). In drillcore here, the curvature of these surfaces and dense spacing along drillcore suggests that the slip displacement cannot be more than 10cm, and that graphitic metapelite readily smears the graphite flakes (Figure 7-2**c**).

The fracture coating on shear surfaces is usually graphite (in graphitic metapelite), chlorite (very common), and other hydrothermal minerals such as limonite. The slickenside coating appears thin (<1mm). In the published work from other locations, Lee (1991) showed that slickenside surfaces have a zonation of mineralogy that can consist of quartz material (0.2 to 1mm thick), a thin (<1mm) zone of deformed host rock, and shear bands in host rock. Small mineral filled (calcite, quartz) veins also show mm to cm slip displacement on some drillcore samples. Slickenside surface covered by chlorite has very low porosity ≈ 0.1% (Siitari-Kauppi et al. 2010). Shales show similar mechanical behaviour to graphitic metapelites and similar small-displacement slickensided slip surfaces (Ogata et al. 2014), citing an example from 700m deep drillhole in Norway and outcrops. The densely fractured zones (≈ 80 fractures/meter) appear in outcrop as conjugate low-angle slip surfaces around a central crushed zone (fault core with gouges and breccias) (Ogata et al. 2014). The offsets on such shear fractures are small, cm or 10's cm at most.

The whole Gryphon fault zone is also cut by younger sub-vertical W to NW striking normal faults, thus cross-cutting the G fault at oblique or normal angle, in map view spaced at 100 to 150m apart (SRK Consulting Inc. & RPA Inc. 2018). Some uranium ore migration and re-deposition has taken place along these smaller structures near intersections with larger faults in the fault zone. These sub-vertical faults shown little or no offset in most places, but some have lateral slip (slickenlines perpendicular to the sub-vertical dip of shear plane in drillcore). The fracture aperture is nearly always cemented closed (≈ 1 to a few mm), but occasional open channels remain in zones of groundwater circulation at present time. In silicified rocks, such vertical faults were found to be permeable, correlated with drilling fluid losses at the nearby Phoenix deposit, and contained 0.5 to 1cm wide dissolution channels within the silica cement of the fracture.

7.5 Rock alteration zones

The Gryphon deposit is thought to be an example of basinal fluid "ingress" model and mixing with up-flowing hydrothermal fluids (Jefferson et al. 2007). The nearby Phoenix deposit at Wheeler River is an example of "egress" type deposit, where the hydrothermal fluids existed the basement rock and reacted with rocks and fluids at the unconformity. In the eastern Athabasca Basin, the uranium deposits formed after the basin deposition by mixing of reducing and oxidizing fluids sourced from basinal brines and from the hydrothermal up-flowing fluids along parts of permeable fault zones and at the unconformity, the set up of long-duration redox fronts, and extensive fluid-rock interactions (Sopuck et al. 1983, Sibbald 1985, Hoeve and Quirt 1987, Fayek and Kyser 1997, Renac et al. 2002). The Gryphon deposit is no exception with distinctive alteration zones and "halos" occurring around the deposit and above it in the overlying Athabasca Group sandstones.
Figure 7-3 describes the known alteration zones at the Gryphon deposit that have been mapped by Denison Mines (SRK Consulting 2015b, SRK Consulting Inc. & RPA Inc. 2018) on drillcore samples in every 3m interval, using short-wave infrared spectrometer (Arcoptix FT-NIR spectrometer), a method widely for exploration in the Athabasca Basin (Zhang et al. 2001). The alteration zones pervasively affect the rock matrix, but there is much more local porosity enhancement or sealing (by silica or clays) than is shown on this map.

7.5.1 Paleo-weathering and regolith

Surficial weathering (bio-geo-chemical and mechanical) has affected the exhumed and exposed metamorphic and plutonic basement rocks, in the post-Hudsonian orogeny in the case of the Wollaston Domain in the eastern Athabasca Basin area. The paleo-regolith, which is preserved below the sub-Athabasca unconformity, comprises various alteration zones (MacDonald 1985): upper clay altered (bleached) zone (0.01 - 1m), hematite zone (2 - 10m), white clay zone (feldspars replaced by clay) (2 - 6m), green/red zone (3 - 22m). The total depth of regolith or paleo-alteration zone depends partly on lithology, from the sampling done by MacDonald 1985, where the average thickness over depth was 21m in meta-arkose or meta-quartzite, 42m in semipelitic gneiss, 34m in pelitic gneiss. The deepest zone was 223m in a suspected fault zone. The regolith profile in metapelites at Wheeler River and in the eastern Athabasca area is similar to other sites world-wide in the same lithologies. At Olkiluoto, Finland, the weathered zone is characterized by alteration of biotite and feldspar alteration, and visible redox fronts (goethite, hematite and iron oxyhydroxides), and other remnant hydrothermal alteration products in fractures in fault zone (Lindberg 2009). The highly weathered regolith occurs in topographic depressions to a thickness of a few meters (Aaltonen et al. 2010), the weathering alteration is pervasive and extends down for 100 to 200m. At outcrops in other regions, 50m deep weathering profiles show irregularly shaped alteration zones of various intensity (less altered with highly altered patchy zones inter-fingering), interrupted by sharp contacts of fault gouges and pegmatitic dikes (Borrelli et al. 2014).

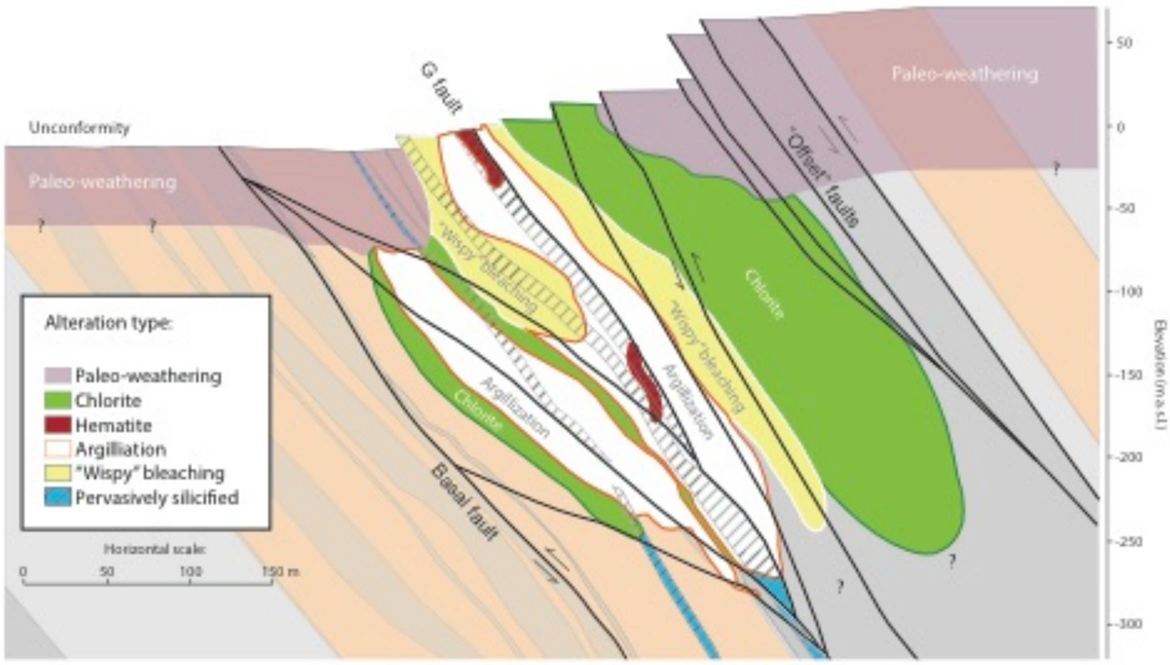

Figure 7-3 Mapped alteration zones at the Gryphon fault zone and uranium deposit, from regular 3m interval sampling of drillcore and short-wave infrared spectrometry (SRK Consulting 2015b, SRK Consulting Inc. & RPA Inc. 2018).

At the Gryphon site, the intense paleo-weathering both seals the fractures and creates open porosity in the coarse grained pegmatites that appear to suffer most of the permeability enhancement, in small patches <10cm wide, embedded in the metapelite.

7.5.2 Alteration assemblages by temperature and fluid type

The regionally pervasive alteration is from retrograde metamorphism (cooling and depressurizing path, during uplift related to orogeny). Regionally, outside of the hydrothermal zones, the main alteration is sericitization and chloritization of most of the minerals in rocks (Bruneton 1993).

In magmatic hydrothermal systems, the alteration assemblages (e.g. Shanks 2012) can be grouped into zones from higher to lower temperature, although there is much overlap as minerals at successively lower temperatures replace some of those formed at higher temperatures and change the visible rock texture and color:

- propylitic alteration by Na-rich fluids at high temperature
    - at temperatures corresponding to the greenshist facies metamorphism, or in hot hydrothermal system, or in distal zone to a porphyry system (a magmatic intrusion),
    - biotite or amphibole minerals are altered to mineral assemblage of chlorite, epidote, calcite, illite, pyrite.
- phyllic alteration by hot acidic fluids (H+ metasomatism)
    - produces a mineral assemblage quartz, sericite, pyrite, but often preserves original texture (grain shapes, sizes), so that it might be apparent if the original rock was a pegmatite or a gneiss,
    - sericitic (fine texture) alteration of mica phyllosilicate is formed through alteration of plagioclase,
- argillic alteration by acidic fluids at lower temperature
    - clays at replace plagioclase (kaolinite, dickite, smectite, halloysite, pyrophyllite, paragonite),
    - many clays form during low-temperature mixing of hydrothermal fluids with seawater or basinal saline fluids (Galan and Ferrell 2013).

7.5.3 Chlorite, illite, tourmaline

The protoliths have been chloritised and the pegmatites albitised that caused color changes in plagioclase and minor porosity changes. Nano-scale porosity in feldspar crystals is created through albitisation process that helps to promote later alterations (Putnis and Austrheim 2010), and important over geologic time scales, but not measurable at drillcore sample scale or permeability tests. Some of the pelitic gneisses experienced metasomatic reactions (without fluids) that grew biotite, garnets, sillimanite minerals Card and Noll (2016), and more mineral heterogeneity creates more altered patches later that locally increases porosity.

Illite clay is very common and forms in acidic or oxidizing conditions at higher temperature than Kaolinite, although there is some overlap of temperature ranges. It is a common alteration mineral in metasediments and granitic rocks. In drillcore it appears as soapy to transparent, grey to green waxy or powdery coverings of mineral grains, and sometimes fills fractures. However, at the Gryphon deposit, illite occurs with kaolinite, or rather, has been over-printed by kaolinite and is difficult to separate visually. At other sites, such as Olkiluoto, illite is strongly correlated with fracture zones away from the main pervasive alteration volume, where it affects an irregular and large volumes 10's to a few 100's meters wide (Aaltonnen et al. 2008).

Hydrothermal tourmalines, or Mg-alteration, are represented by dravite at the Gryphon deposit. Dravite is a common alteration mineral that is present within the alteration halos near the deposit and in some fault gouges inside the fault zone. It is difficult to recognize because of other more prominent other alteration, but where seen it appears "white-green" or bluish, and in thin section as fibrous aggregates Mercadier et al. 2012), or as coatings in vugs from earlier desilicification, as seen at the Phoenix deposit (Wang 2017). Some porosity may be preserved between long fibers (Rabiei et al. 2015). At other deposits in this region, tourmaline crystals were found with pink dravite (Tremblay 1982).

7.5.4 Sericite texture of mica alteration (phengite, paragonite)

In pegmatites, the sericitization appears as whitish fine texture. Sericite fine mica alteration texture and the mica minerals found at the Gryphon deposit that are responsible are phengite (formed in oxidizing conditions) and paragonite (formed in reducing conditions) (SRK Consulting Inc. & RPA Inc. 2018). The phengite sericite alteration appears to extend down into the Gryphon fault zone along the G faults, to a depth of about 100m below the unconformity, and along the Basal fault near the unconformity. However, the mineral changes to paragonite in the reduced zone where the uranium deposit formed. The color can vary from white to pale yellow, grey-white, etc., and appears as pearly fine-grained mass.

7.5.5 Argillic alteration (e.g. kaolinite)

Kaolinite clay zone extends down to the top of the uranium deposit, although fractures filled with kaolinite can be seen cutting across the redox fronts that are related to uranium mineralisation (Mercadier et al. 2011). The alteration can be pervasive or spotty, and in fractures it tends to form the fills. Kaolinite and other clays, such as illite, may occur together. Kaolinite white clay is one of alteration products from feldspars. It is also often found in zones of mixing of acidic or oxidising meteoric waters in hydrothermal plumes in fault zones, and in overburden sediments above fault zones that discharge thermal waters from hot geothermal reservoirs below (Chambefort et al. 2016). Kaolinite alteration "wedges" are commonly found where fault zones allow meteoric fluids to penetrate deeper and mix with other hydrothermal fluids in the fault zone. At Olkiluoto, Finland, the pervasively kaolinitised rocks contain 5 to 30% kaolinite by volume and have been drilled and excavated in a tunnel. The wedge-shaped alteration zone extends down into the fault zone some 100 to 200 m on average, maximum 250 m below bedrock surface, while smaller kaolinite zones extend deeper along fracture zones (Aaltonen et al. 2008). In gneisses weakly altered by kaolinite clay, but preserving most of the original rock appearance, the total porosity was higher, 4 to 6%, and permeability 2 to 5 x10^{-16} m^2 (Aaltonen et al. 2009).

Kaolinite is a coarse-grained clay with about 30% porosity of pure kaolinite at 5MPa effective pressure (or about 500 m depth), and not compacted kaolinite can reach porosity 60 to 70% porosity (Mondol et al. 2007). Kaolinite is the most permeable clay in most of the sedimentary rocks and also at this fault zone. Illite is another very common clay in fault gouges and in hydrothermal alteration zones that may appear similar to kaolinite. For example, sandstones partially filled by kaolinite lining pores have matrix permeability 10^{-13} to 10^{-12} m^2, compared to sandstones with pores filled partially with fibrous illite permeability 10^{-16} m^2 (North 1985). A less permeable, more porous, and finer grained clay is smectite. In partially filled pores of altered crystalline rock and in sedimentary rock, the distribution of clay aggregates that constrict the pores determines the permeability (Howard 1992).

7.6 Permeability testing methods

In past reviews on the subject of permeability sampling from drillcores, Jensen et al. (1994) suggested that the choice of measurement method should be dictated by scales of geological variation present and intended application of data, and locally with smaller volumes of investigation but at a higher sampling density than typical core plug method. Corbett et al. (2001) suggested a sampling strategy to test all hydrogeologic units, anomalous zones, and to avoid rigidly measuring samples at fixed volume scale and intervals. Here the test spots were at least every 3m in the protoliths, fault rocks were intensely sampled (every drillcore piece of fault gouge or breccia), and multiple test spots were done on some fault rock pieces and some altered rocks. Several drillholes provided the drillcore for tests. The longest transect was done on WR-665, from the top of Athabasca sandstone, through the Gryphon fault zone in metasediments and into the Basal Pegmatite wall rock. The fault cores of Offset fault and G fault strands were tested in several drill holes. Since the transect across the deposit was done in WR-665, but the uranium-mineralized fault core zone part was not available at the time (already broken down for sampling), the missing segment was tested in adjacent and parallel new drillhole that became available later.

7.6.1 Probe tip seal on rock

The gas probe permeameters can be used on smooth surfaces of rocks of high enough permeability to be detectable with the device, given the uncertainties of probe tip seal (and gas leaks) and other effects. The permeameter probe test results are usually compared with a laboratory test results on a few selected drillcore pieces and smaller core plugs or slices extracted (Halvorsen and Hurst 1990), although the smaller samples may miss the most permeable features in drillcore (vuggy channels, small fractures, channels in larger fractures, altered weak rock). Core slabs offer a sooth surface for testing with probes and can be done routinely (e.g. Rogiers et al. 2014a). In friable rocks and sediments in outcrops and samples, lower pressures must be used to avoid disturbing the sample (e.g. Davis et al. 1994). It is difficult to measure the gas leaks, and it may vary with roughness of rock surface and the method of use of device (Sharp et al. 1994). The surface roughness of drillcore piece side, the seal quality affects the results of probe permeameters and any leak causes an overestimate of permeability (Filomena et al. 2014). Although the leak rate can be reduced by application of larger load on the probe tip (Tidwell and Wilson 1997), there are practical limits to the load before the sample fractures or is indented (in friable samples). Various methods of sealing of permeameter probe tip have been proposed and tried, one being epoxy rings on small core plug discs (Sharp et al. 1994), using expandable seal rings in small drilled holes into the outcrop (Dinwiddie et al. 2003), but the proportion of the leak to total gas flow is larger for rocks of low permeability. With the rubber tip seal alone, in rocks below certain permeability the leak rate is greater than the gas flow into the rock sample, making the tests impractical and incorrect.

Several different rubber seals were tested for the gas permeameter probe and N_2 leaks occurred on most of the drillcore surfaces. The N_2 gas leaks between the probe tip and the rock surface were detected by spray of soapy water mist on the probe tip/rock contact, to generate bubbles. The leak rate did depend on the load applied on the probe tip, but did not stop completely. A load of >50lb (~ 400psi at the probe tip surface area) was required to minimize the leak, but such loads were not possible on weak clay-altered or friable drillcore samples. The smallest leak rate was on naturally smooth glassy surfaces (e.g. metaquartzites, silicified rocks, unaltered migmatitic rocks, graphitic pelite or fresh cordierite pelitic gneiss). On most of the drillcore rock surfaces that appeared smooth without magnification, the gas leaks were significant and often dominant, greatly increasing the apparent permeability. On altered rocks, the apparent permeability due to gas leak was several orders of magnitude larger than the actual rock permeability, when compared to the completely sealed probe tip against rock at the same spot. The N_2 gas exit pattern during leaky tests (rubber tip only) was mostly around the rubber tip and not in the drillcore piece sides. The same spots were sealed with epoxy ring, leaving an opening for gas injection. Without the gas leak at the probe tip, the gas exit pattern was three-dimensional and from most of the sides of the sample, often over the whole sample diameter. The non-leaky result had effective permeability much lower (orders of magnitude) than the leaky result. The apparatus itself had no measurable leaks when tested against a metal surface.

To solve the leak problem, a permanent epoxy resin seal ring was applied and bound to the mineral rock surface (Figure 7-4). The epoxy o-ring size is slightly larger than the probe tip, and we use the diameter of the epoxy o-ring in the calculation of the probe tip diameter. With the smooth epoxy ring, the load required to seal the rubber tip was only 4.5 to 6.8 kg (10 to 15 lb) on the probe tip (≈ 70 to 100psi pressure on surface are of probe seal tip). Most of the weak rocks could be tested without apparent damage or deformation.

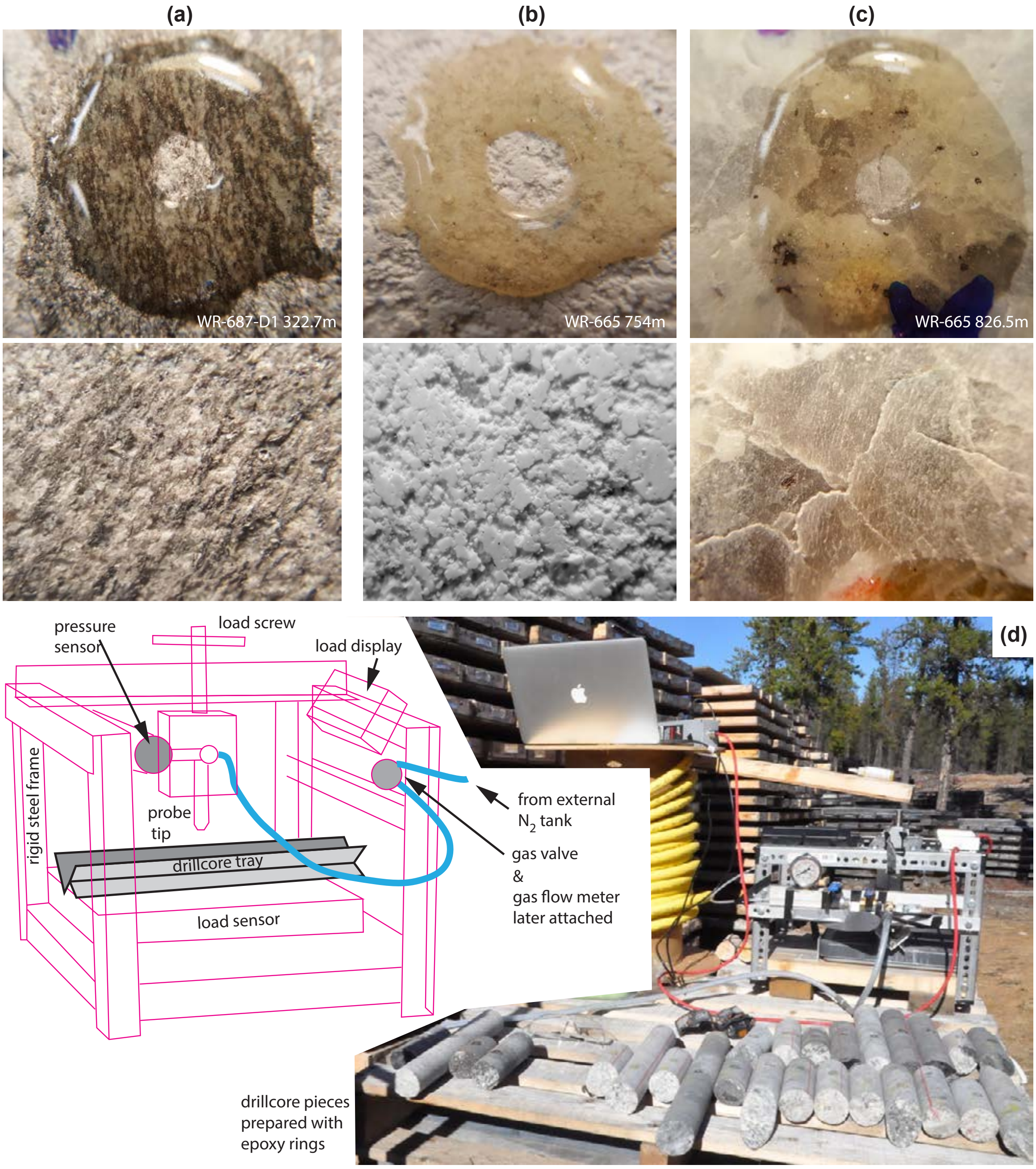

Figure 7-4 Epoxy resin seal ring at test spots on dry drillcore surfaces and surface roughness under about 10x magnification: (a) pelitic gneiss, (b) desilicified and clay altered gneiss, (c) silicified pegmatitic rock with <0.1mm wide fractures and microfractures, (d) apparatus schematic and example of field site setup with prepared pelite pieces in drillhole WR-665.

7.6.2 Potential effects of drilling damage on sample surface

The surface of the drillcore pieces has rough mineral surface that has been damaged to some extent by the drilling process. In strong rocks such as pelitic gneisses, the drilling process disrupts locally the original rock texture and creates more pore space and connections within a thin outer zone of the drillcore piece, that can be observed in thin section and dye studies on samples (Waber et al. 2009). The action of drill cutter from rotary drill method on gneiss rock was investigated at a research tunnel at Olkiluoto, Finland. The rock in on the walls of drilled hole had an average porosity in greater than undisturbed host rock by a factor 2.25 (Autio 1996). The effect on matrix permeability was an increase from 7×10^{-20} to 4.5×10^{-19} m^2, by the same factor. Such excavation damage zone (also applied to tunnel walls) increased the rock permeability up to 10^{-18} m^2 from original 10^{-19} to 10^{-20} m^2, depending on rock type (Autio et al. 2003).

At Forsmark, Sweden, drillcore samples (diamond drilling method) in granodiorite at 560m depth were analysed using autoradiographic methods after impregnation (Waber et al. 2011). There was a modification of porosity in a 6mm wide zone around the circumference, in rock with original porosity of 0.55 to 0.86%. Similar studies were done at Olkiluoto, Finland, on gneiss drillcores from 600m depth (Meier et al. 2015). The expected stress release was estimated from rock strength properties and depressurization of sample that caused expansion or pore space by 0.003 to 0.005%, or 1/100 of the average gneiss porosity (0.64 to 0.37%). However, observations showed that the affected porous rim was about 5mm deep around the sample and that most of the drillcore samples were undisturbed. For the present study, the gas from probe may enter slightly faster through the outer rim of the sample but the flow through sample is still limited by the bulk property of the sample and not only the outer rim. An outer rim damage may be detected by observing gas bubbles that only exit around the probe tip and not elsewhere in the sample.

Overall, we can expect some damage to the drillcore sample of gneiss or granite, but the effect can range from insignificant to an order of magnitude in highly damaged rock. At Wheeler River site, most of the tested drillcore was not visibly weathered, and some drillcore was drilled only a few days or weeks before the tests. Visibly damaged rock in some older drillcore was avoided. The damage included showing discing, pressure-relief cracking along foliation that did not appear as part of natural in-situ fractures, or cracking and desintegration due to clay mineral swelling on repeatedly dried and wetted (e.g. in green zones of regolith).

7.6.3 Constant flow rate test

In a constant discharge rate or flow test, there is a constant pressure difference across the sample once the flow condition stabilizes. For a compressive ideal gas, Darcy's law and one-dimensional glas flow equaiton gives Equation 1 (Bear 1972, Ho and Webb 2006):

$$\frac{\mathrm{Q}}{A} = \frac{k_{(to\ gas)}}{L\ \mu_{gas}} \frac{\left((\mathrm{p}_1)^2 - (\mathrm{p}_0)^2\right)}{2\ \mathrm{p}_1} \qquad [1]$$

where k is permeability of rock matrix, L is sample length, Q is the volumetric flow rate through cross-sectional area A (also, Q/A is the Darcy velocity), μ_{gas} is the dynamic viscosity of gas (here N_2), P_1 is the gas pressure upstream of gas from of sample, and P_0 is the pressure "downstream" of the sample. The effective permeability represents a rather complex flow process through interconnected pores and fractures (Renard and Allard 2013, Hunt and Sahimi 2017). For the case of the downstream pressure being the atmospheric pressure, $P_0 = P_{atm}$ is the atmospheric pressure for unconfined samples. Gases are obviously useful for permeability measurements in low-porosity rocks because of lower gas viscosity and easier flow through small pores.

The probe permeameter is sealed against the drillcore rock surface (Figure 7-5a), the pressure is charged in the apparatus behind a valve, and after opening the valve the pressure inside the apparatus acts on the rock sample and sets up a gas pressure gradient toward the boundary condition with the atmospheric pressure. This is shown in Figure 7-5b (flow net from Tartakovsky et al. 2000) for homogeneous permeability distribution and a with flat surface at the top. The flow net will adjust and be constrained to the circular surface of drillcore piece but the high gradient and flow rates will remain near the probe tip. In this case the seal is the epoxy seal that is attached to the rock surface, while the rubber seal presses against the epoxy from above. The apparatus was designed for working in rough field conditions at an exploration site, to be able to test 20 to 40 cm long drillcore pieces (Figure 7-5d), manually adjusted load (with digital sensor) on probe tip against rubber seal and epoxy ring typically at 20 lb load (pressing at about 150 psi on probe tip seal surface area), with a stiff light weight metal frame, and basic valves, pressure and temperature sensors (vibrating-wire sensor from RST Instruments Inc.), gas flow meter from Alicat Inc., and N_2 gas flow lines to 30 kg external tank.

For permeameter probe tip injection to a flat surface of a disc-shaped drillcore piece, as shown in Figure 7-5b, Goggin et al. (1988) derived an analytical solution in this form:

$$k_{(to\ gas)} = \frac{\mathrm{Q}\,\mu_{gas}\ 2\,\mathrm{p}_1}{r_{inner}\ G_0\left((\mathrm{p}_1)^2 - (\mathrm{p}_0)^2\right)} \qquad [2]$$

where q is the volumetric flow rate at probe tip, μ is the gas viscosity, P_1 is the pressure at probe tip (inlet into the sample), P_0 is the atmospheric pressure, $2\pi r_i$ is the cross-sectional area of samples exposed to the probe tip, G_0 is dimensionless factor for gas flow geometry in the rock sample. The subscript in $k_{(to\ gas)}$ signifies that the result is not yet corrected for gas slip effects (discussed later in this section).

The geometric factor G_0 depends on the ratio of tip-seal thickness (outer radius / inner radius) and the sample radius or depth. In our apparatus, the inner tip seal radius is 2.4 mm, the outer sea radius is 10 mm, the ratio of radii here is 4.2 and the drillcore radius is 23.8 mm (NQ size diameter 47.6 mm). The solution is approximately equal to the half-space theoretical solution where the sample radius is at least 4x the probe tip radius (Goggin et al. 1988). For large drillcore plug diameters (more than 4x greater than probe tip seal radius), and the value of G_0 is between 4 and 4.5. Furthermore, the highest pressure gradient and flow rate is in the rock volume just below the probe tip and around it to a depth of a few cm, and much less contribution from the bottom and more distant sides of the sample (Tartakovsky et al. 2000, Molz et al. 2003). The permeameter can effectively sample the small-scale heterogeneity in highly porous rocks (Tidwell et al. 1999), but the apparent permeability is approximate because of the various geometric complexities that deviate from the half-space rectangular cross-section solution.

The N_2 gas indeed does flow through the whole sample and discharges from a three-dimensional, sometimes anisotropic, pore network (e.g. Figure 7-5c). The detection of gas bubbles from the tested sample is an important diagnostic observation that can help determine the heterogeneity of samples and the type of porosity involved in conducting the gas flow (Goggin 1993). In this study, a fine mist of soap water onto the sample surface during the test. The N_2 gas bubbles show the locations of dominant pore channels or channels in small fractures or vugs, and the size and speed of bubble formation gives a qualitative measure of gas flow rate at each spot. For each test on drillcore, photo and video records were used to map the gas bubble patterns. The fine mist only wets the outside of the rock sample and does not seem to affect the test result, as shown by repeated tests on the same sample (without removing the probe seal), with and without the mist spray.

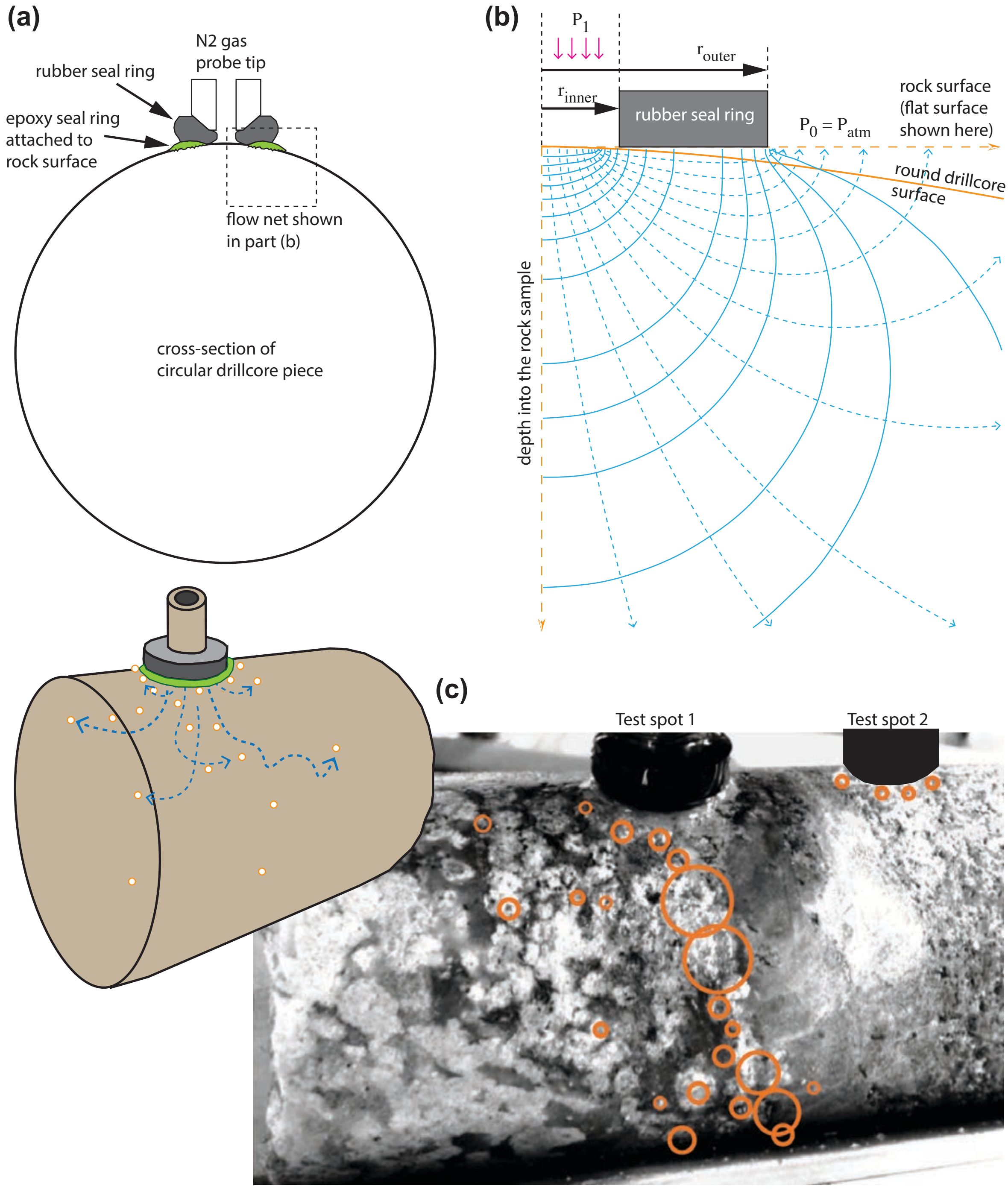

Figure 7-5 (a) Section through drillcore sample showing probe tip seal geometry, (b) flow lines and pressure equipotential lines with probe tip outer to inner seal radius ratio of 4 (after Tartakovsky et al. 2000), (c) example of gas exit pattern on altered gneiss sample in two different spots (spot 1 has more connected pores than spot 2).

7.6.4 Unsteady gas flow test (pressure-decay test)

In unsteady gas flow permeameters, a pressure gradient is applied to the confined sample and the pressure decrease (pressure "decay") rate is monitored and analysed (Brace et al. 1968, Jones 1972). The typical pressure time series is shown graphically in Figure 7-6a (after Persoff and Hulen 2001). In this study, the gas pressure gradient at initial time (the magnitude of the pressure pulse at time 0) was chosen at about 50 psi (0.345 MPa). This pressure gradient produced good results on the unsaturated samples of rocks in the time period of tests that were practical per test at one spot (< 20 min). In the most permeable rock samples ($k > 10^{-15}$ m^2), the initial pressure dropped so rapidly that the pressure transducer datalogger only captures the next second of data, and in those cases the initial pressure is lower. In comparison, the commercial laboratory-grade permeameters test specially machined and polished core plugs held in Hassler cell holders, and apply pressure across the sample, and analyse the instantaneous rate of pressure decrease across the sample (Ruth and Kenny 1989, Jones 1992), or use a higher pressure (≈ 20 MPa) (Jones 1997). The instantaneous flow rate is estimated from the logarithm ratio of pressure measurements, which is the same as the difference of logarithms of pressure measurements.

The solution was originally derived by Brace et al. 1968 for a two-reservoir flow system, with the sample in between. For the case where the gas slip flow is insignificant (see later Klinkenberg effect) the solution has the following form (after Liang et al. 2001 and clarified with longer subscripts:

[3]

$$\frac{p1_{later} - p2_{later}}{p1_{later} + p2_{later}} = \frac{p1_{initial} - p2_{initial}}{p1_{initial} + p2_{initial}} exp\left(-\frac{p2_{initial}}{\mathrm{V1}} + \frac{p1_{initial}}{\mathrm{V2}}\right)\frac{\mathrm{A}\ k_{(to\ gas)}}{\mathrm{L}\ \mu_{gas}}(t_{later} - t_{initial})$$

and rearranged to solve for permeability:

[4]

$$k_{(to\ gas)} = \frac{\mathrm{L}\ \mu_{gas}}{\mathrm{A}\ (t_{later} - t_{initial})}\left(-\frac{p2_{initial}}{\mathrm{V1}} + \frac{p1_{initial}}{\mathrm{V2}}\right)^{-1} \ln\left[\left(\frac{p1_{later} - p2_{later}}{p1_{later} + p2_{later}}\right) / \left(\frac{p1_{initial} - p2_{initial}}{p1_{initial} + p2_{initial}}\right)\right]$$

where:

t is the time, $t_{initial}$ and t_{later} are two different times of pressure measurements on pressure decay curve (e.g. at time 0 or at some other initial time for a data segment),

V_1 and V_2 are the small N_2 gas reservoir volumes in the apparatus upstream (1) and downstream (2) of the sample (m^3),

p1 and p2 are the pressures in gas reservoir (1) upstream and (2) downstream of the sample (Pa), and with subscripts initial and later for the different times at start and end of data segment,

L is the length of cylindrical sample being tested against the flat cut surface (m),

A is the cross-sectional area for gas flow through cylindrical sample being tested (m^2).

In an unconfined rock sample, the downstream reservoir is the atmosphere that is approximately infinitely large compared to the upstream reservoir, thus $p1_{initial}/V_2 = 0$, and the p2 = patm or atmospheric pressure. Assuming that the atmospheric pressure does not change singificantly during the test, $p2_{initial} = p2_{later} = p_{atm}$, and one of the terms in Equation 5 simplifies. In a probe-tip permeameter, the depth into the sample and the cross-sectional area are for gas flow under the probe tip and the seal ring, the flow net and pressure gradient adjusts to the circular shape of the drillcore piece. For hemispherical flow and flow geometry as in (Goggin et al. 1988) and Equation 2, the solution becomes: (e.g. see Lechler 2002), and using the same notation as above:

[5]

$$k_{(to\ gas)} = \frac{\mathrm{V1}\ \mu_{gas}}{p_{atm}\ \mathrm{r}_i\ G_0} \ln\left[\left(\frac{p1_{later} - p_{atm}}{p1_{later} + p_{atm}}\right) / \left(\frac{p1_{initial} - p_{atm}}{p1_{initial} + p_{atm}}\right)\right] / (t_{later} - t_{initial})$$

where r_i is the tip seal inner radius at the probe tip, G_0 is the geometric flow coefficient.

Any segment of the pressure-decay curve (e.g. Figure 7-6c) can be used for this analysis to obtain the same permeability value , and this was confirmed by trying various time periods for pressure values. The permeability can be determined graphically by plotting the transformed pressure vs. change in time:

[6]

$$k_{(to\ gas)} = \frac{\mathrm{V1}\ \mu_{gas}}{p_{atm}\ \mathrm{r}_i\ G_0} \left(\frac{transformed\ pressure}{(t_{later} - t_{initial})}\right)$$

[7]

$$transformed\ pressure = \ln\left[\left(\frac{p1_{later} - p_{atm}}{p1_{later} + p_{atm}}\right) / \left(\frac{p1_{initial} - p_{atm}}{p1_{initial} + p_{atm}}\right)\right]$$

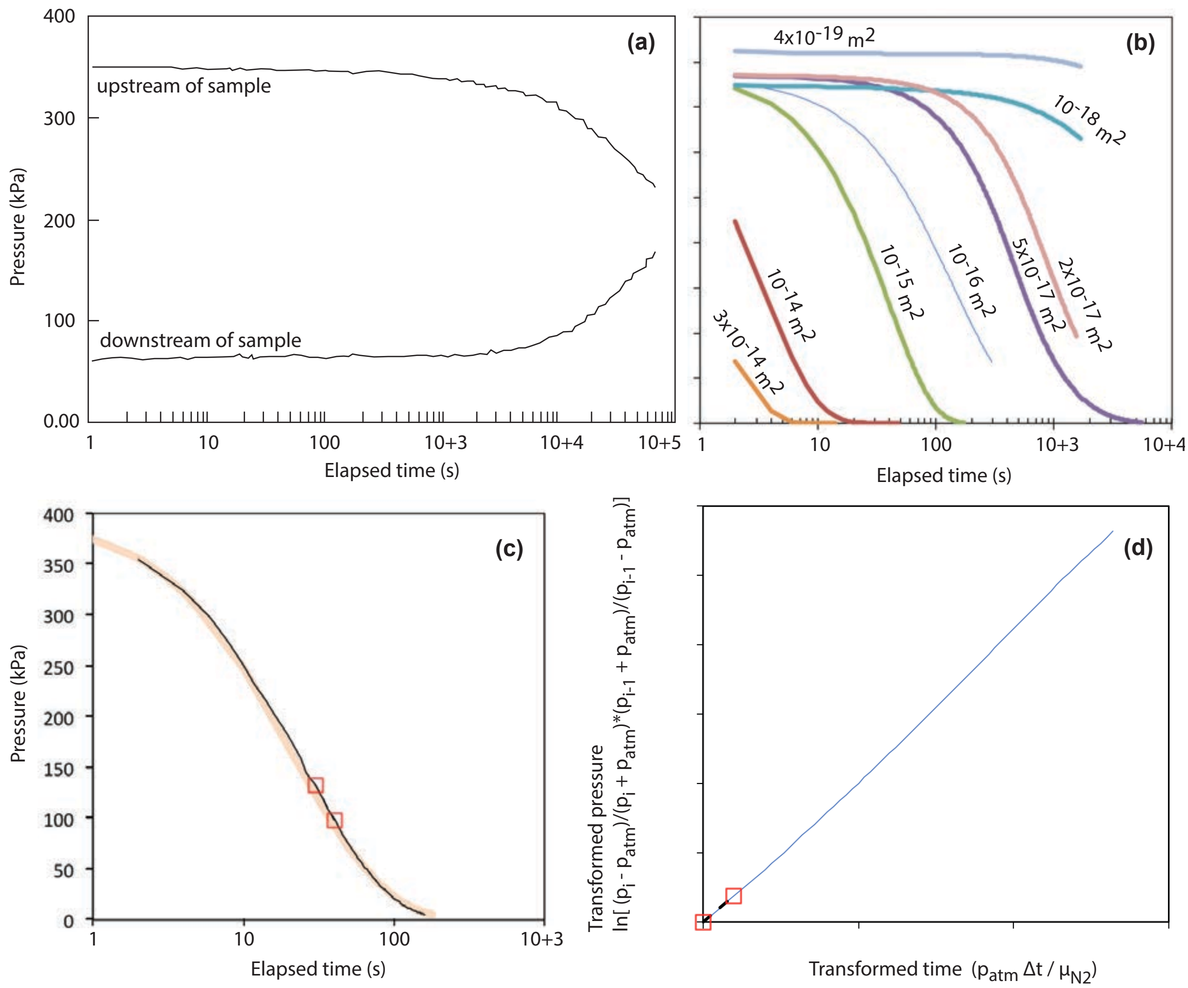

Figure 7-6 (a) Example of pressure-decay permeameter time-series for a test in rock of low permeability at initial pressure about 350 kPa above the sample (after Persofff and Hulen 2001), (b) unconfined sample probe pressure-decay curves from several tests in this study for rocks of different permeabilities, (c) pressure-decay curve selected segment (between square points), and compared to analytical solution in thick orange line for one reservoir permeameter test (Kaczmarek 2008), (d) plot of transformed pressure vs. transformed time for a small segment of pressure-decay curve.

The least squares method is used to find the linear trend for (transformed pressure) vs. (change in time), passing through the 0,0 origin (Figure 7-6d). With that line slope coefficient and the other constants (assumed) in Equation 6, the permeability value is calculated. The plot is also diagnostic of how well the mathematical mode fits the actual gas flow through the sample. The data segments were used where the transformed pressure vs. change in time was linear. In some tests, at early time, sometimes the flow behaviour is different than at later time, because the sample saturation changes as the N_2 gas flows through the sample, essentially forcing any water out or aside and establishing dominant flow paths.

In more permeable rocks ($k > 10^{-17}$ m^2), the gas flow rates displayed more scatter and perhaps some non-Darcian turbulent flow effects, or channelled flow (highly anisotropic in some samples).

The gas flow in porous media follows Darcy's Law but it also has a slip effect due to molecular motions of gas, described experimentally by Klinkenberg (1941):

$$k0 \ = \ k_{water}\left(1+\frac{b}{(p_2+p_1)/2}\right) \qquad [8]$$

where b is the Klinkenberg constant (Pa), k is the apparent matrix permeability measured with gas or water (m^2), $(p_2+p_1)/2$ is the mean pressure difference across the sample, for inlet (p_2) and outlet (p_1) pressures in Pa units. Each rock type may have different response to gas slippage, depending on internal pore space geometry and porosity.

The analytical solution for Klinkenberg corrected permeability from the one-reservoir pressure-decay test, with the Klinkenberg coefficient b in the equation, was derived by Kaczmarek 2008:

$$p2 \ = \frac{(2b+p_{atm})\left(\dfrac{p2_{initial}-p_{atm}}{p2_{initial}+2b+p_{atm}}\right)+p_{atm}exp\left[\dfrac{A\,k_0}{\mathrm{L\,V_2}\,\mu_{gas}}(b+p_{atm})t\right]}{exp\left[\dfrac{A\,k_0}{\mathrm{L\,V_2}\,\mu_{gas}}(b+p_{atm})t\right]-\left(\dfrac{p2_{initial}-p_{atm}}{p2_{initial}+2b+p_{atm}}\right)} \qquad [9]$$

where all the terms were defined in previous equations and use the same notation. The pressure function from Equation 9 is compared in Figure 7-6**c** to pressure-decay data from one of the tests, for sample with permeability $2\text{x}10^{-15}$ m^2 .

For many samples over a wide range of permeability, a trend curve is usually fitted:

$$b = Bk_0{}^{-C} \qquad [10]$$

where k_0 is uncorrected permeability in some selected units, and B and C are curve fitting parameters. For sandstones, over a permeability range 10^{-14} to 10^{-20} m^2, $C \approx 0.36$ and $B = 1.5\text{x}10^{-7}$ (for k_0 in m^2 and b in MPa) (Jones 1972, Tanikawa and Shimamoto 2006).

For partly saturated samples tested with N_2, Sampath and Keighin (1982) fitted a curve from tests on partly saturated samples using N_2 gas, and Kaczmarek 2008 provided it in metric units in this form:

$$b = 9550(10^{+15}\, k_0/\phi)^{-0.53} \qquad [11]$$

where b is in Pa, k_0 is in m^2, and ϕ is effective porosity. In Table 7-1, the calculated b are compared for typical permeability and porosity values, and average pressure 0.4 MPa across unconfined sample in ambient atmospheric pressure, thus average pressure difference $(0.5+0.101)/2 \approx 0.3$ MPa. Equation 10 produces larger Klinkenberg b values than Equation 11, and permeability to gas is greater than that for water because of this gas slip effect, by a factor 3 to 8 for rocks of low permeability below 10^{-18} m^2.

Table 7-1 Typical b values calculated with Equation 10 and 11.

		from Equation 10		from Equation 9	
k_0 (m^2)	porosity	b (MPa)	$(1 + b/P_{avg})$	b (MPa)	$(1 + b/P_{avg})$
$5x10^{-20}$	0.5%	0.11	1.36	2.1	7.91
10^{-18}	1%	0.032	1.11	0.69	3.28
10^{-17}	1%	0.010	1.03	0.29	1.97
10^{-15}	5%	0.002	1.01	0.053	1.18

The limit of the apparatus at low-permeability end of range, the ambient pressure and temperature started to noticeably add noise to the pressure data by affecting the pressure inside the apparatus. In rocks with permeability 1 to 5 $x10^{-20}$ m^2, the thermal and pressure noise effects strongly affected some tests, depending on the conditions, and the permeability could not be accurately estimated. The practical lower limit for this apparatus is approximately $5x10^{-20}$ m^2, although with thermal insulation and more controlled ambient pressure conditions, the sensors could test to permeability 10^{-20} m^2. The uncertainty in the result at this low range is about half order of magnitude due to data noise alone, and the Kilinkenberg gas slip also adds another half order of magnitude change to the permeability value. Where the results were ambiguous between apparent permeability 10^{-19} to 10^{-20} m^2, the tests were repeated or extended in time, or recorded as <detection limit ($\sim 5x10^{-20}$ m^2).

7.7 Evaluation of consistency of results for samples

7.7.1 Water saturation of drillcore samples

Water trapped in pores interfere with the gas flow and reduce the apparent permeability because of two-phase flow. Although the complete drying of drillcore pieces is desirable, it requires additional time and cost, and some rocks must be assayed for mineral content and are not available, unless tested for permeability soon after drilling. At the drilling site, these samples had varying saturation, most were visibly dry after sitting in storage for months, but some were partly saturated. The pelitic gneiss rock takes about 60 days at 105°C temperature to completely dry, and then the re-saturation takes about one week (Hakala and Haikkila 1997). At the Wheeler River site, the drilling fluid used in exploration diamond drills was fresh water with polymer powder, producing a liquid of higher viscosity than water, but of almost identical density. The drillcore was also washed on site during geological logging by water sprays. Then, most of the drillcore was dried in the core logging shacks or outside under covered stacks. In the summer season, the humidity is about 30% to 50%. For saturation up to 40% or 50%, the effect is rather small (about factor of two decrease), and it takes about 80% saturation to reduce the air permeability of homogeneous medium by one order of magnitude (Lenhard and Parker 1987). Rock moisture content is unavoidable on natural rock outcrops, and moisture in drillcore adds to error and variability in measured apparent permeability. For example, the Sutherland et al. 1993, and Davis et al. 1994 reported that in highly permeable sandstones (>10^{-12} m^2), a change by factor 1.5 from dry to 25% saturation was typical, and worse in less permeable sandstones (10^{-15} to 10^{-14} m^2). In clays, physicochemical interactions between clays and water occur. Kaolinite clay has the largest pores and permeability (10^{-17} to 10^{-15} m^2), compared to illite (10^{-19} to $5x10^{-17}$ m^2), and smectite (10^{-21} to $5x10^{-17}$ m^2) (Mesri and Olson 1971). In clay-rich fault gouges, Faulkner and Rutter (2000), found a one order of magnitude reduction of matrix permeability from argon gas compared to tests with water, on samples compacted to 200 MPa.

The results of steady-state gas flow method were compared for 14 of the attempted 23 samples of gneiss and sandstone from Wheeler River, re-tested after drying at the same epoxy spots on those samples. These tests were done after drying of samples for several months at room temperature, and using the same apparatus that was used at the drilling site and exploration camp. The other samples had too rapid gas flow to measure with the gas flow meter attached to, thus the range of matrix permeability compared here is only from 10^{-19} to

10^{-16} m^2, values typical of most of the rocks at the Gryphon fault zone. The main uncertainty is with the ability to measure steady gas flow at low flow rates in the portable apparatus. Figure 7-7**a** shows that the steady-state permeability was for most of the tested samples within one order of magnitude of the pressure-decay method. This confirms the validity of the assumptions that are specific to the pressure-decay curve method (e.g. volume of gas in the apparatus, flow geometry through the sample, pressure sensing and analysis method. A further 30 samples were re-tested after drying completely at about 100^{o}C in an oven at the field site. The results are compared in Figure 7-7**b** for different rock types. Considering the sample handling, transport, and possible cracking during desication, and the repeatability of the same test (probe seal, injection pressure), the effect of drying was relatively small (within factor of 2 to 5 of permeability) for the most porous rocks such as fault gouges, desilicified pegmatites (vuggy episyenites), and altered porous pelite and pegmatite. About half of the less permeable ($\approx 10^{-17}$ m^2) rocks were also not affected much by drying, but a few samples of both weakly and strongly clay-altered gneiss were much more permeable (2 to 3 orders of magnitude) after drying than before. The less permeable drillcore samples are more difficult to dry in ambient storage conditions after drilling. Those samples were likely saturated with water during the initial testing and the gas was merely mobilising the water flow in the pore space, thus the inconsistent result is due to the incorrect choice of fluid viscosity. The viscosity of nitrogen gas (1.7×10^{-5} Pa*s) is about two order of magnitude greater than that of water (10^{-3} Pa*s) at 20^{o}C temperature and atmospheric pressure. The viscosity and gas slip differences due to sample moisture can collectively account for the observed results.

We can expect that the field test results for the most porous permeable rock samples ($>10^{-16}$ m^2) should be little affected by partial saturation, and about 30% of less permeable samples might be underestimated as to their permeability (e.g. some of the very low permeability outliers, $k \approx 10^{-20}$ m^2, are likely closer to the mean value about 10^{-17} m^2). It appears that most of the results will be correct and broadly useful despite lack of complete drying of all samples, although more calibration tests for dry and moist samples are desirable in this type of project.

7.7.2 Heterogeneity of sample spots

Another potential problem is sample heterogeneity of porosity and permeability at cm to 10 cm length scale. The choice of sample spots for probe seal might not give access to the permeable pore network to induce gas flow in the whole sample, as theorized. In up to 30 drillcore samples, of various lithology and alteration grade, 4 to 6 test spots were prepared and all tested sequentially using the pressure-decay method and compared in Figure 7-7**c**. The results are plotted sorted by the mean permeability value, and the individual test results about the mean (in vertical columns above the sample described by the geologic symbols). The least permeable samples were pervasively silicified and weakly clay-altered pegmatite or gneiss, clay altered paleo-weathered pegmatite with hematite alteration, and some well-cemented sandstones. The test results for permeability lower than 10^{-20} m^2 were indicated at the detection limit of 10^{-20} m^2 shown here. The data noise increases greatly near $5x10^{-21}$ m^2 and the results are difficult to quantify with this apparatus below this value, but the pressure decay that results in permeability of 10^{-20} m^2 is clearly observable and above the pressure data noise. The most permeable samples were from sandstone, intensely weathered pegmatite, and desilicified vuggy "episyenite" rock of uncertain protolith. The results show that heterogeneity of porous media led to about 1 to 2 orders of magnitude range of matrix permeability, and typically about 1 order of magnitude. Testing any of the sample points would capture broadly the magnitude of permeability (roughly the same ranking order as the mean values). No systematic bias appears in the results either by magnitude of permeability or by rock type, and the heterogeneity within the samples appears to cause more or less random variation in permeability values.

Lastly, the results of about 1200 pressure-decay tests on as many samples from the Gryphon fault zone site are compared as a magnitude of matrix permeability vs. the logarithm of slope of pressure-decay curve segment in Figure 7-7**d**. This simplistic presentation shows that the slope of the pressure decay curve (in the log-log plot) does indeed have high correlation with the log of permeability value. Above 10^{-16} m^2, there is more scatter in the results, presumably due to variation in gas slip factor, turbulent flow of gas, and variability of gas flow geometries among the samples (deviating from homogeneous porous medium of the analytical solution). This likely also includes the effects of strong anisotropy and fracture channel flow that were noted in some tests. However, the variation of this type is still within about one order of magnitude of permeability value and most of the results appear to cluster tightly along the overall trend. This observation confirms that the slope of segments of pressure-decay curves are good predictors of matrix permeability in this simple test method. The more permeable the sample, the faster the gas flow and faster the pressure decrease from the initial pressure pulse.

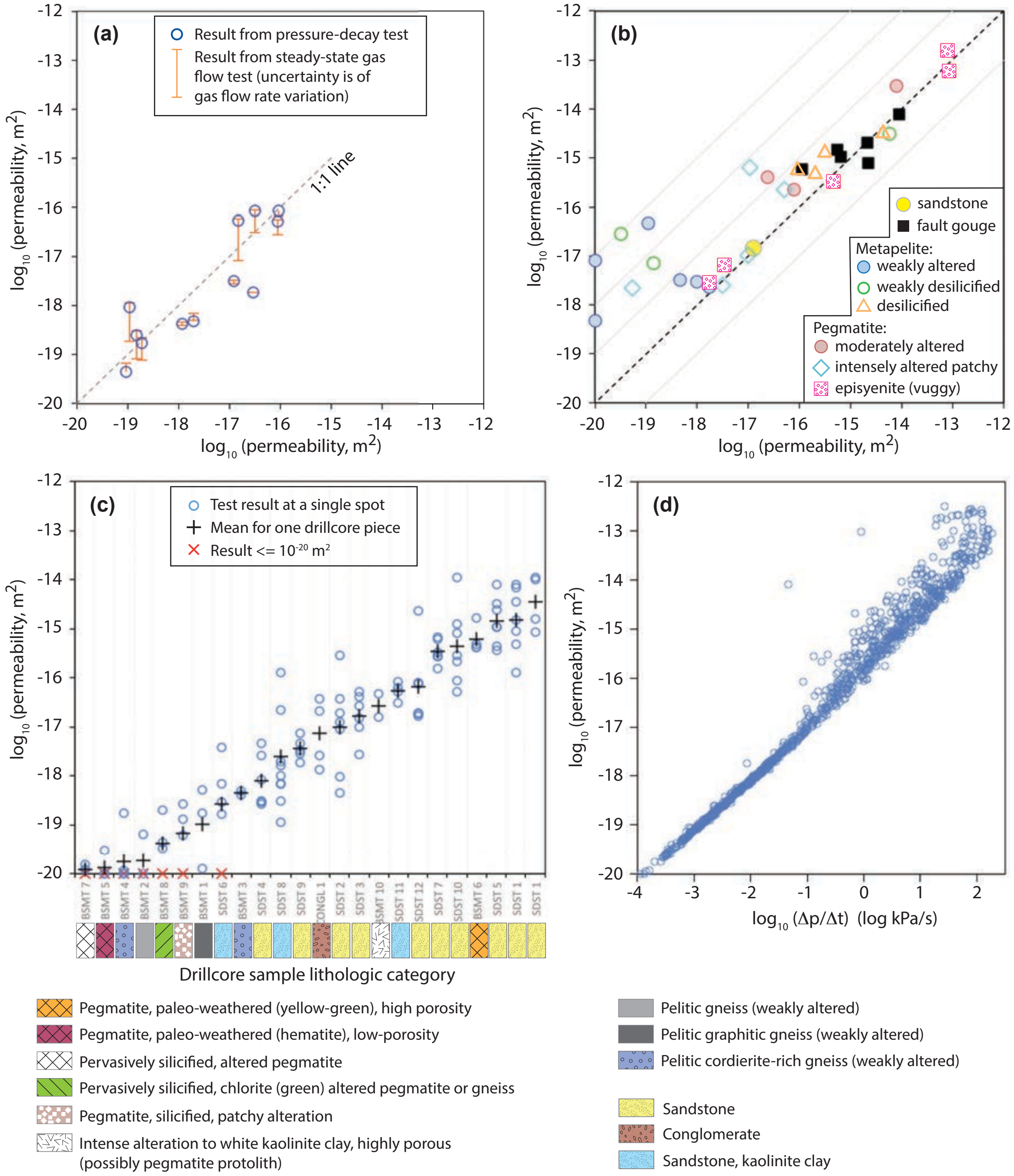

Figure 7-7 Comparing the matrix permeability log values of various samples from the Gryphon fault zone: (a) pressure-decay vs. steady-state gas flow tested on the same samples, (b) samples at ambient moisture content vs. the same samples oven dried, (c) comparing permeabilities at multiple spots on one drillcore piece and the median value, tested on different rock types and sorted by permeability median value, (d) scatter in results of about 1200 tests graphed as permeability vs. log of change in pressure over time in the analysed segment of the pressure-decay curve.

7.8 Results

7.8.1 Site-wide statistics

The most complete transect was along the WR-665 drillhole, where 275 valid tests were analysed. The 172 tests from WR-668 drillhole are also shown on this figure because the uranium-mineralized and faulted intervals below the G-fault were tested at the exploration site, from a freshly drilled hole, before the rocks were cute and crushed. These data were not available from WR-665 because the portion of fault zone containing uranium had been already crushed and sampled and could not be tested. Other drillholes were also tested for fault rocks, alteration zones, or fractures, to supplement the database. These include WR-671-D1 (48 tests), and WR-507-D2 (133 tests). The descriptive statistics for the permeability distributions are shown as boxplots in Figure 7-8 for metapelite, pegmatite, their fractured or altered samples, and the fault rocks. The statistics were calculated on $\log_{10}$ permeability values because permeability has approximately log-normal distribution.

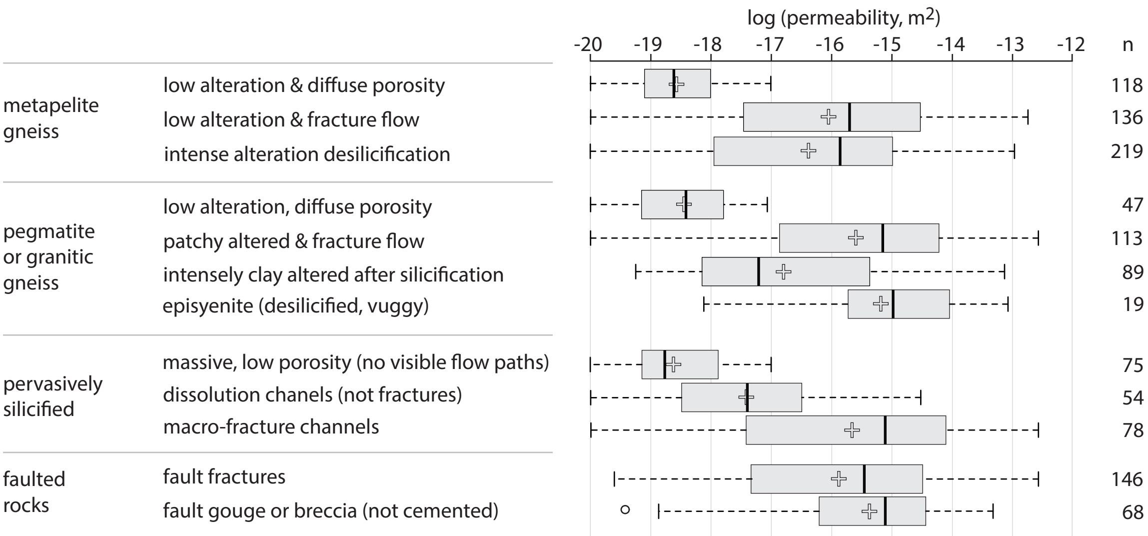

Figure 7-8 Summary statistics of matrix permeability by rock lithology and alteration categories, at the Gryphon fault zone and deposit.

The protolith metapelite and pegmatite (low alteration intensity), where the gas flow during tests was not visibly discharging from the macroscopic fracture channels (if present), but diffusively flowing slowly through microfractures and pores, has the lowest mean permeability of 3×10^{-19} m^2. On the transect graph, such value forms the base level of samples with the lowest permeability. The fractured gneisses and strongly desilicified gneisses are clearly more permeable on average (9 and 4 $\times10^{-17}$ m^2 respectively), and reach maximum values between 10^{-13} and 10^{-12} m^2. The fractured pegmatites, where the flow is through fracture channels, is more permeable ($\approx 3x10^{-16}$ m^2) than the fractured gneiss. Rock alteration strongly affected the porosity and permeability in the Gryphon fault zone. The alteration types and results will be discussed in the next sections.

7.8.2 Expected pressure sensitivity of the protoliths

In crystalline metamorphic and plutonic rocks, porosity in the form of microfractures is also sensitive to pressure. Meglis et al. (1991) tested the Precambrian mylonitised metasediments in Ramapo fault zone, in New Jersey. There, the microfracture component of porosity in amphibolite and granitic gneiss is about 0.35 to <0.2% below 600m depth, it apparently increases with depth due to crack opening due to sample depressurization. At the Lac du Bonnet granite, AECL's underground laboratory, the microcrack stress-relief was detected through sample geotechnical testing between depths 200 and 420 m below ground surface (Eberhardt et al. 1999), although a shallow-dipping thrust fault complicates the tectonic stress distribution at that location. However, at Forsmark, Sweden, drillcore samples from 700 m depth did not have anomalous stress-train responses or evidence of significant microcracking (Martin, 2007), while at Mizunami, Japan, the apparent uniaxial strength of granite was correlated with in situ rock stress ratio (horizontal/vertical), suggesting that a 20 to 30% strength loss occurred during drilling and sample extraction (Lanaro et al. 2008).

From theoretical calculations of elastic properties of mineral grains in biotite gneiss, in research on the super-deep Kola drillhole in Russia, Gorbatsevich 2003 estimated that the effect of stress release on grain-boundary microfractures should be negligible at depths less than 1000 m. However, a half-order of magnitude decrease in permeability is typical over 0 to 1km depth range effective pressure. Morrow and Lockner (1994) described tests data from pelitic and amphibolite gneisses and granite from the KTB drillhole at 1252 m depth, matrix permeability $2x10^{-19}$ m^2 at 5 to 10 MPa effective confining pressure (confining pressure - pore pressure). From 0 to 10 MPa, the permeability decreased by a factor of about 0.5. In granitic rocks at the Cajon Pass drillhole, permeability changed only slightly between 5 and 10MPa effective pressure, from $8x10^{-19}$ to $6x10^{-19}$ m^2. In the Kola drillhole, the drop in permeability was about half an order of magnitude in this pressure range. In the UPH3 drillhole in granite at 750 m depth, the permeability decreased from 0 (projected) to 10 MPa by a factor of 0.3 to 0.2 in these low porosity rocks (Morrow and Lockner (1997). Weathered granite showed even less pressure sensitivity at low confining pressure (Morrow 1999).

In granitic rocks, mylonitic shear zones were studied at Grimsel underground laboratory, 400m below ground surface by drilling and testing resin-impregnated and other samples (Schild et al. 2001). Over 10 MPa pressure range, the measured values are ≈ 10^{-18} m^2, compared to 1 to 3 x10^{-18} m^2 matrix permeability at 10's meters scale along tunnel measured by evaporative water discharge from unfractured tunnel surface, thus the effects of unloading/sample preparation were not significant at these depths. Extrapolating from 10 to 0 MPa, the unconfined sample overestimates the in-situ permeability by factor of 1.5 to 2, but that this overestimate actually fits the in-situ result in this case. Permeability tests on drillcore samples of gneiss and granite are routinely done on unconfined samples using water and gas fluids at Olkiluoto research site in Finland, that is located at a few hundred meters depth (Kuva et al. 2015).

7.8.3 Expected pressure sensitivity of fault rocks

At the Gryphon fault zone, the drillcore was extracted from about 400 to 700 m vertical depth, where the lithostatic pressure is about 10 MPa (assuming average rock density 2600 kg/m^3 and subtracting the hydrostatic pressure for water density 1000 kg/m^3). The permeability from the unconfined drillcore samples will have some systematic error of overestimate of matrix permeability because of rock sample depressurization, but the question is how much?

The phenomenon of pressure sensitivity of drillcore rock samples (matrix permeability and porosity decreasing with sample confining pressure in triaxial apparatus) is well known and has been studied since the 1970's (e.g. David et al. 1994, Morrow and Lockner 1994). The permeability of porous rock sample decreases with increasing confining pressure, usually in an exponential form such as Equation 12:

$$k_2 = k_1 exp(-\gamma \Delta P_c) \qquad [12]$$

where k_1 and k_2 are the initial and final permeabilities in the pressurizing step, such that $k_2 < k_1$ during the pressurizing path of permeability, ΔP_c is the confining pressure increase in this step, and γ is the pressure sensitivity coefficient. This equation will be used later in the last figure to re-calculate permeability from a the Median Tectonic Line in Japan (Wibberley and Shimamoto 2003) to compare to the Gryphon fault zone.

In porous rocks such as sandstones, the permeability and porosity decrease from 0 to 20 MPa is relatively small, and up to 200 MPa is required to decrease in permeability by an order of magnitude or two, but with enough pressure, the porosity structure collapses irrecoverably and the permeability doesn't recover after depressurization. However, unlike many structural studies, here we do not attempt to compress the fault rock samples to theoretical seismogenic depths near the brittle-ductile transition zone in the crust, and only aim to estimate the permeability at the in-situ drilled depth. The fault zone structure and fault rock type is not known at larger depths at this location, the fault gouge mineralogy may differ, the fault architecture is also unlikely to appear the same as at the drilled depth. In the following discussion, the problem of fault rock decompression and permeability is reviewed from the published geoscientific literature.

Fault gouges compact easily and irreversibly at high confining pressure to collapse the pore space from unconfined values in 30 - 60% range to much lower porosities 2 to 5% at 100 to 200 MPa confining pressures (e.g. Faulkner and Rutter 2000). Consequently the matrix permeability also decreases sharply by several orders of magnitude in the 0 to 200 MPa range. Tests at high confining pressure attempt to simulate the conditions at seismogenic depths near the brittle-ductile transition, as 100 to 200 MPa roughly corresponds to effective depth 10 to 20 km. However, this is below the expected depth of fault gouge formation in faults according to conceptual model of Sibson (1977), where cataclasites are expected. In this study, the in-situ depth of fault zone, at present geologic time, is 600 to 800m, thus the low effective pressure range 5 to 8 MPa is of interest. At low pressures the decrease from unconfined sample to about 5 or 10 MPa is small, less than half order of magnitude, as can be shown from the published geoscientific literature on fault rock tests in the following list.

1) San Andreas fault - granitic, sedimentary and metamorphic protolith:

- gouges from outcrops and shallow drillholes, initial permeability was $5x10^{-19}$ to 10^{-20} m^2 at various pressures, but a few samples were tested at 5 to 15 MPa, showing permeability decrease by a small factor ($4x10^{-20}$ to $1.5x10^{-20}$ m^2) (Morrow et al. 1984)
- SAFOD drillhole (Morrow et al. 2014): foliated gouge from 2.5 km depth below ground (high content of Mg-clay, 7% porosity), permeability decreased from 10^{-21} to $5x10^{-22}$ m^2 (10 and 40 MPa), and at low pressure form 10^{-19} to 10^{-20} m^2 (5 to 10 MPa); cataclastic, porosity 4 to 5%, permeability $k = 5x10^{-19}$ to 10^{-20} m^2 at 40 MPa.

2) Median Tectonic Line, Japan - mylonite and pelititc schist protolith:

- very fine gouges ($8x10^{-16}$ m^2), foliated gouges (2 to 4 $x10^{-15}$ m^2), coarse gouges (7x10-

^{15} to $2x10^{-14}$ m^2), at 30 MPa confining pressure (20 MPa pore pressure, 10 MPa effective pressure) (Wibberley 2002)

- extrapolating back to 20 MPa (0 effective pressure), the permeabilities could have decreased in the first 10 MPa by a factor of 0.2 to 0.5, by 2 to 5 times from unconfined samples (Wibberley 2002)
- cataclasite (cemented) and mylonite from outcrop had as low permeability that varied from outcrop to outcrop and samples, 10^{-20} to 10^{-18} m^2 at 80 MPa pressure (some samples as low as $2x10^{-22}$ m^2), lower than the pelitic schist protolith, and much more permeable sandy gouges even at 80 MPa effective pressure (10^{-14} to 10^{-16} m^2) and up to 10^{-13} m^2 at 5 MPa (Uehara and Shimamoto 2004)

3) Nojima fault, Japan - granite protolith:

- fault rock (gouge to cataclasite) porosity 0.2 to 5.7% (Surma et al. 2003), in GSJ drillhole at 750 m depth, estimated matrix permeability $2x10^{-19}$ to $5x10^{-18}$ m^2 at 50MPa (Lockner et al. 2000), and estimated in-situ permeability at 750 m depth is 10^{-17} to $2.5x10^{-16}$ m^2,
- cataclasite or healed gouge at 1800 m depth (NIED drillhole), 10^{-19} m^2 at 50 MPa, ≈ 10^{-18} m^2 at drilled depth (Lockner et al. 2000),
- fault breccia from outcrops, 10^{-12} to 10^{-16} m^2 at 5 MPa, depending on location and sample, wide variability (Mizoguchi et al. 2000, 2008).

4) Carboneras fault, Spain - schist and various protoliths

- Faulkner and Rutter 2000 tested the fault gouges taken from outcrops of 50m wide fault core zones; the gouge permeability to Argon gas, before compaction and at the lowest effective pressure (70 – 40 = 30 MPa or ≈ 3 km depth), had matrix permeability parallel to fabric (maximum) of 10^{-17} to 10^{-18} m^2, but the unconfined gouges are likely much more permeable than 10^{-17} m^2 because of high porosity ≈ 27%
- Faulkner (2004) also proposed a power-law function of effective pressure and temperature for the permeability of clay-rich fault gouges

7.8.4 Fault rocks

There were 68 tests done on uncemented porous fault gouges and breccias, resulting in a mean permeability 4.3×10^{-16} m^2 . The standard deviation is 1.3, or just over one order of magnitude about the log permeability mean value of -15.4. The most permeable gouges and breccias (5×10^{-14} m^2, or log value -13.3) are as permeable as the most altered or desilicified protoliths, or most of the macro-fractured rocks in the damage zone. The porous weak gouges and breccias in the fault cores are clearly good fluid conduits to gas and water at present time, compared to the protolith. The permeability is on average as high as the damage zone, but the damage zone is much wider than the fault core, and it also contains strongly altered rocks that add to the transmissivity of the zone. The least permeable spots on fault rocks are about as low as the unfractured protolith. Only a few cataclasites were tested and they were uniformly of low permeability, as these are strongly cemented old fault rocks that formed at seismogenic depths below the depth where the incohesive, and likely younger, fault gouges may have formed. Elsewhere in the fault zone, the cataclasites occur as relatively narrow zones, where as the incohesive fault gouges and breccias reach larger widths in drillcore. The age of the rocks is not known here.

One example of fault core and damage zone is shown in Figure 7-9 from the G fault, a major splay fault in the Gryphon fault zone. The permeability data are from WR-668-D2 and -D3 holes. The D stands for "daughter" drillhole, drilled from the same main hole casing and branched out when already near the deposit depth. The D2 and D3 holes are in the same area and are useful for comparing the heterogeneity of the fault strand and fault rocks. In WR-668-D3, the fault core is about 1.7m wide, and contains gouge and breccia in various proportions. The main slip surface is located near 619.3m depth along the hole, between test spots 34 and 35. A competent wall rock of metapelitic gneiss sharply bounds fault gouge. There is no visible fracturing or alteration of the wall rock, suggesting a slip against low-strength material in the fault core and no significant damage recently to the wall rock. There are smaller fault core strands near 623m and before 625m depth damage zone. In the adjacent drillhole -D2, the main fault core width is also about 1.7m wide, but fracturing pattern is different. Fracture density is large in the downhole direction from the fault core, between the central deformation zone near 620m and the splay faults near 623m. The damage zone and fault core distribution is asymmetric, but not greatly so. In the footwall, the damage zone is at least 1 meter wide, and might be a few meters wide if the fractures are related to this fault and above the background fracturing, but are definitely part of the wider Gryphon fault zone. The protolith is visibly undeformed, except regional fabric and ductile deformation. On the hanging wall (at shallower depths), the damage appears most intense and distributed. This is where the splay faults occur. The width of fractured damage zone was not mapped but likely extends a few meters.

The permeability of fault gouges and breccias is in most samples between $5x10^{-16}$ and 10^{-13} m^2, the median about 10^{-15} m^2. Intensely fractured damage zone (e.g. test spot #9) has similarly high permeability of the fracture mesh (or network). A few fractured samples had low permeability because of sealing minerals (e.g. in fault core near 616m in -D2 drillhole). Gneiss rock without visible macro-fractures in samples had a uniformly low matrix permeability about 10^{-19} m^2, close to the mean value for the whole site. Other protolith samples were leached by fluids near fractures (e.g. test spot #2), and generally experienced desilicification, leaving a porous mass of biotite and other minerals. These rocks retain most of the protolith fabric and do not show the comminution and rotation of grains found in fault gouges. The desilicified gneiss is locally as permeable as the fault gouges or the fractured rock. Clay-rich desilicified gneiss is much less permeable, similar to the protolith. In summary, the fault rocks in fault core of this strand of G fault are conduits to fluid flow at present time, and 3 to 5 orders of magnitude more permeable than the protolith. Rock alteration increases the rock permeability locally and acts to increase the width of the transmissive zone.

Coarse fault gouges at a few hundred meters depth and at outcrops can reach the permeability 10^{-15} to 10^{-14} m^2 (Wibberley and Shimamoto 2003, Bossart and Mazurek 1991) (Table 7-2), similar to fault rocks observed in G-Fault and other fault cores at the Gryphon fault zone. Fine clay-rich foliated gouges, with 3 to 8% effective porosity, have a wider range of permeability and lower minimum values down to 10^{-20} m^2 at low confining pressure (e.g. Morrow et al. 2014).

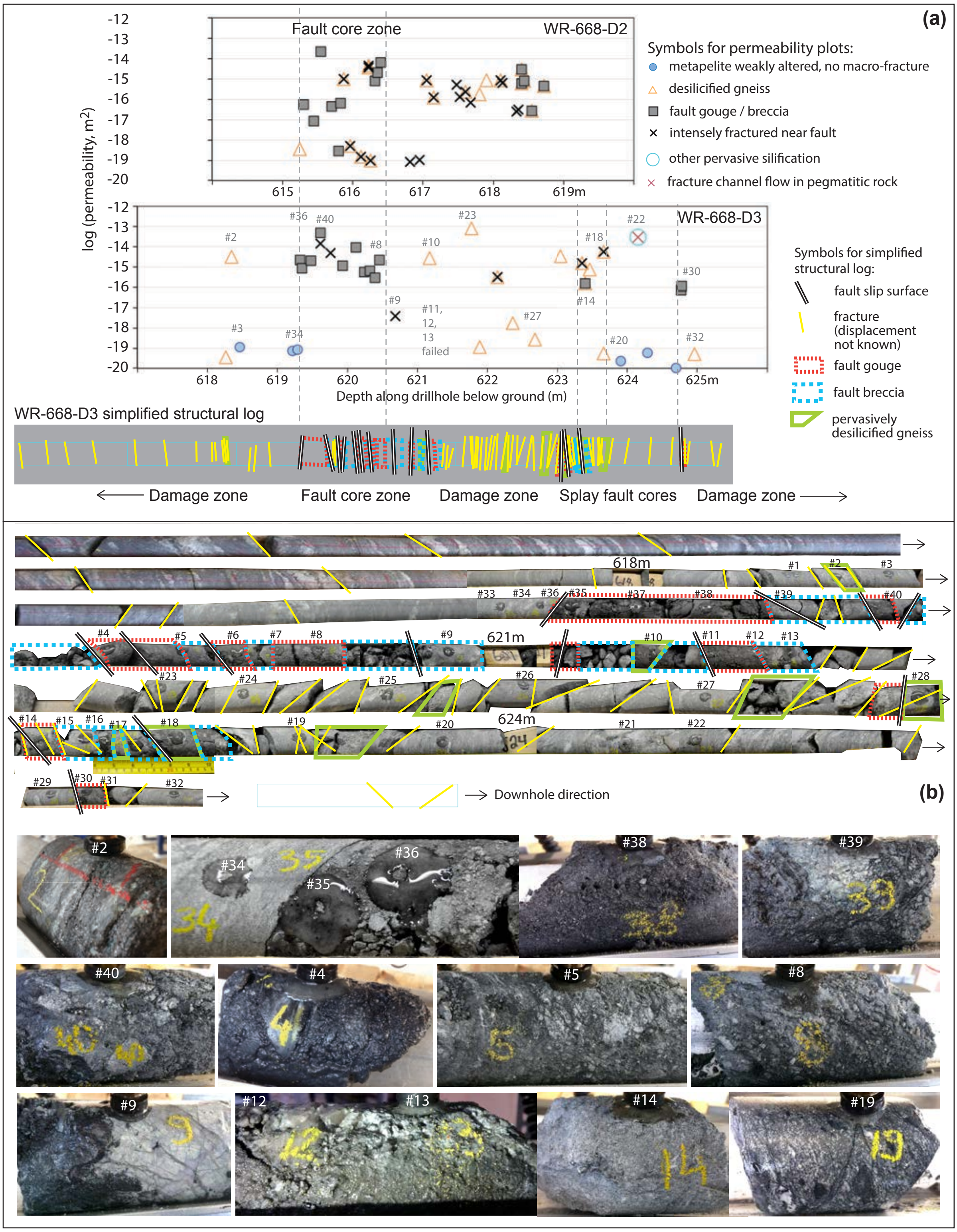

Figure 7-9 G-Fault in Gryphon fault zone, permeability testing in WR-668-D2 and -D3 drillholes: (a) matrix permeability transect of both drillholes and a simplified structural log for -D3 hole, (b) interpreted simplified structural features of the fault core and damage zone, overlayed on the photographic mosaic of the drillcore from -D3 hole, and examples of test spots on fault rocks.

Table 7-2 Porosity and matrix permeability of metasedimentary, granitic, and fault rocks from geoscientific literature review. Values are at shallow crustal depths <1km in most cases, outcrops, and tested at low effective confining pressures (as noted).

Rock type	Permeability of rock matrix (m^2)	Porosity (total or effective)	Research site	Ref.
metapelite gneiss, granitic gneiss, amphibolite gneiss				
various gneiss	@ 1 - 1.5km depths	1 -- 1.4 %	NAGRA drillholes, N Switzerland	1
various gneiss	$4x10^{-20}$ -- $4x10^{-19}$ @<0.5km	0.2 -- 1 %	Romuvaara, and Olkiluoto, Finland	2, 3
veined pelitic gneiss	10^{-20} -- $5x10^{-18}$	0.19 -- 1 %,	Olkiluoto, Finland	4
granitic gneiss	$6x10^{-19}$ -- $9x10^{-17}$	0.44 -- 0.63 %	Olkiluoto, Finland	4
gneiss (silimanite-garnet)	$9x10^{-19}$	0.9 %	various sites in USA	7
amphibolite gneiss	10^{-22} -- 10^{-17} @1 to 9km	1 % +/-0.4	KTB drillhole, Germany	6
metapelitic schist	$2x10^{-16}$ -- 10^{-18}		Median Tectonic Line (MTL), Japan	13
altered metapelite				
clay altered pelitic gneiss		6 -- 10 %	NAGRA drillholes, N Switzerland	1
pelitic gneiss (altered)	$7x10^{-18}$	2.9 -- 3.3 %	Olkiluoto, Finland, & sites in the USA	5, 7
greywacke, quartzite				
metagreywacke	$5x10^{-20}$ -- $5x10^{-21}$	1.9 -- 2.2 %	The Geysers, California	5, 9
quartzite	$3x10^{-20}$ -- $4x10^{-18}$	0.7 -- 1.9 %	various sites in USA	7, 8
granite				
granite (albitized)		0.23 -- 0.5 %	Forsmark, Sweden	11
granite	$7x10^{-21}$ -- $3x10^{-20}$	0.5 -- 0.8 %	Ploemeur site, France	12
granite	10^{-18} -- 10^{-17}		Olkiluoto, Finland	2
pegmatitic granite	$6x10^{-19}$ -- $6x10^{-18}$	0.44 -- 0.63 %	Olkiluoto, Finland	4
granite	$2x10^{-21}$ -- $8x10^{-19}$		Äspö HRL, Sweden	22

Table 7.2 (continued)

Rock type	Permeability of rock matrix (m^2)	Porosity (total or effective)	Research site	Ref.
fault gouge				
fine & foliated gouge	$8x10^{-16}$ -- 4 $x10^{-15}$ @30MPa		MTL, Japan	17
fine & foliated gouge	$2x10^{-17}$ -- $1x10^{-14}$ @50MPa ($P_{effective}$ 30 MPa)	6 -- 8 % eff. porosity	MTL, Japan	13
coarse gouge	$7x10^{-15}$ -- $2x10^{-14}$	10 -- 30 %	Grimsel, Switzerland	16
fine clayey fault gouge	$2x10^{-19}$ -- $5x10^{-18}$		Nojima fault (GSJ/NIED holes), Japan	14
sandy gouge (outcrops)	10^{-14} -- 10^{-16} @80MPa, 10^{-13} @5MPa		MTL, Japan	18
foliated gouge (@2.5km)	10^{-19} -- 10^{-20} @10MPa	2.8 -- 6.7 %	San Andreas fault, SAFOD site	14, 15
cataclasite				
cataclasite (@1.8km)			Nojima fault, NIED drillhole, Japan	19
cataclasite (outrops)	10^{-18} -- 10^{-20} @80MPa		MTL, Japan	18
cataclasite (outcrops)	2 -- 7 $x10^{-16}$ cemented, 10^{-15} incohesive @50MPa		MTL, Japan	13
cataclasite (@2.5km)	$5x10^{-19}$ -- 10^{-20} @40MPa	4 -- 5 %	San Andreas fault, SAFOD site	14
mylonitic shear zones				
shear zone, (granodiorite)	2 -- 7 $x10^{-19}$ @0.4km	0.96 -- 1.6 %	Grimsel, Switzerland	20, 21

References for table:

1 - Mazurek (1998), 2 - Hartikainen and Hartikainen (1998), 3 - Autio et al. (2003), 4 - Kuva et al. (2015), 5 - Lockner et al. (1982), 6 - Huenges et al. (1997), Berckhemer et al. (1997), 7 - Johnson (1983), 8 - Shabelansky et al. (2014), 9 - Persoff and Hulen (2001), 10 - Hirose and Hayman (2008), 11 - Waber et al. (2009), 12 - Geraud et al. (2010), 13 - Wibberley and Shimamoto (2003), 14 - Morrow et al. (2014), 15 - Janssen et al. (2011), 16 - Bossart and Mazurek (1991), Tilch (1992), 17 - Wibberley (2002), 18 - Uehara and Shimamoto (2004), 19 - Lockner et al. (2000), 20 - Bradbury (1989), 21 - Schild et al. (2001), 22 - Maaranen et al. (2001)

7.8.5 Transects across the fault zone

The matrix permeability has large variation across the fault zone in (Figure 7-10). On the plot, the WR-668 is shown shifted with depth along hole by -65m to project onto the fault zone. WR-668 and WR-665 were nearly parallel but offset by about 150 to 200m in plan view, thus the depths at fault contacts do not correspond directly and require re-projection. This has been done approximately and variation of 10 to 20m is expected, but this does not affect the overall data trend for the purpose of this illustration. In the presentation we refer to positions as drillhole meters along the drillhole trace, not a true depth due to the drillhole inclination and curvature. The permeability varies from sample to sample, and the moving average trend varies strongly over 10's of meters distance, between 10^{-19} and 10^{-14} m^2. The mean (and also the median) value for the whole transect from these two drillholes is approximately $2x10^{-17}$ m^2, but the protolith is clearly of lower average than the locally fractured damage zone, fault core, and strongly altered rocks.

<u>Graphitic metapelite block:</u>

The Offset faults contain many fault core strands, with a clear permeability peak (near drillhole meter 550m). However, some of the rock appears locally silicified (low permeability), and then partially desilicified (higher permeability), and cause large variation in the resulting test values from 10^{-20} to 10^{-13} m^2. The moving average decreases gradually, and irregularly, from the unconformity and into the middle of the graphitic metapelite faulted block toward the G fault. The local highs are where the rock is has open fracture channels or pervasive desilicification porosity, as will be explained in the section about rock alteration later.

The G fault strands near 650m reach permeability of 10^{-14} m^2, but most of the graphitic metapelite has average permeability 10^{-17} to 10^{-18} m^2, and this includes the effects of weak alteration and microfracturing. For the whole site (all drillholes and samples), the descriptive statistics for pelitic gneiss, pegmatite, and fault gouges from the whole site. The pelitic gneiss showing the lowest degree of alteration, considered "fresh" rock, at depth 100 to 300m below the unconformity has a mean matrix permeability about $2.6x10^{-19}$ m^2 (log k = -18.6). Pegmatite anatectite within the pelite is often visibly more altered and desilicified than the host pelite, but the relatively fresh pegmatite has about the same permeability as the pelite ($3.6x10^{-19}$ m^2). The fractured gneiss and pegmatite, on fracture channels tested directly in drillcore pieces, are about two orders of magnitude enhanced in permeability compared to the rock matrix (mean of 10^{-16} m^2 in pelite and 2.6x10^{-16} m^2 in pegmatite). The slicken-sided small tightly sealed fractures in graphitic metapelite were not tested. From our review of other published reports, the bulk permeability of faulted shales with slicken-sided fractures, is low, according to in-situ slug tests by the USGS (Carol et al. 1997), where the bulk permeability was 4x10^{-17} to 6x10^{-20} m^2.

Pegmatite/metapelite block:

In the footwall of the G-Fault, and cut by Linkage faults and the Basal fault, the pegmatite-rich rocks consist of alternating metapelite and pegmatite, both partially or pervasively silicified, desilicified, and otherwise altered. The rock mass is better described as pegmatite-rich gneiss, although the alteration often obscures the fabrics. The least altered pelitic gneisses and pegmatites at Gryphon are similar to and can be compared to those at the radioactive repository site at Olkiluoto, Finland. The "veined gneiss" at that site refer to pelitic gneiss containing neosome (anatectite) inclusions of pegmatitic rock. In the upper 1km depth, these gneisses have minimum permeability above 10^{-20}m^2, and the typical range is 5x10^{-19} to 10^{-16} m^2, and the mean near 10^{-18} m^2, all that is consistent with our results. the porosity varied from 0.2% to 2.5% for permeability values of about 10^{-18} to 5x10^{-21} m^2 in the unaltered (or least altered) samples. The porosity of pelitic and semi-pelitic gneisses, in the form of microfractures at grain boundaries and inter-grains, and in clays and other minerals lining or partly filling the microfractures is as low was 0.2 to 0.4% in unaltered rock (Siitari-Kauppi et al. 2010, Sammaljärvi et al. 2017), but a more typical porosity is 0.5 to 1% because of various alteration and microfracturing (e.g. sericite alteration of plagioclase, illite clay patches, preferential alteration of cordierite grains to clays, and kaolinite clay growing between biotite grains (Sammaljärvi et al. 2017). Foliated rocks such as gneiss have anisotropic matrix permeability that is highest parallel to foliation of the fabric, by about two orders of magnitude compared to perpendicular to foliation fabric, due to shape of pores and orientation of microcracks (Brosch et al. 2000, Heikamp and Nover 2003). The porosity of relatively unaltered ("fresh") granite is as low as for pelitic gneiss (<1%) (Waber et al. 2009, Geraud et al. 2010). Pegmatite (aplite and other coarse grained rocks) is 1 to 2% (Mazurek 1998), and about 0.5% in neosome granite within metapelite (Siitari-Kauppi et al. 2010). The % differences in porosity from sample to sample are explained by the degree of hydrothermal alteration and fractures.

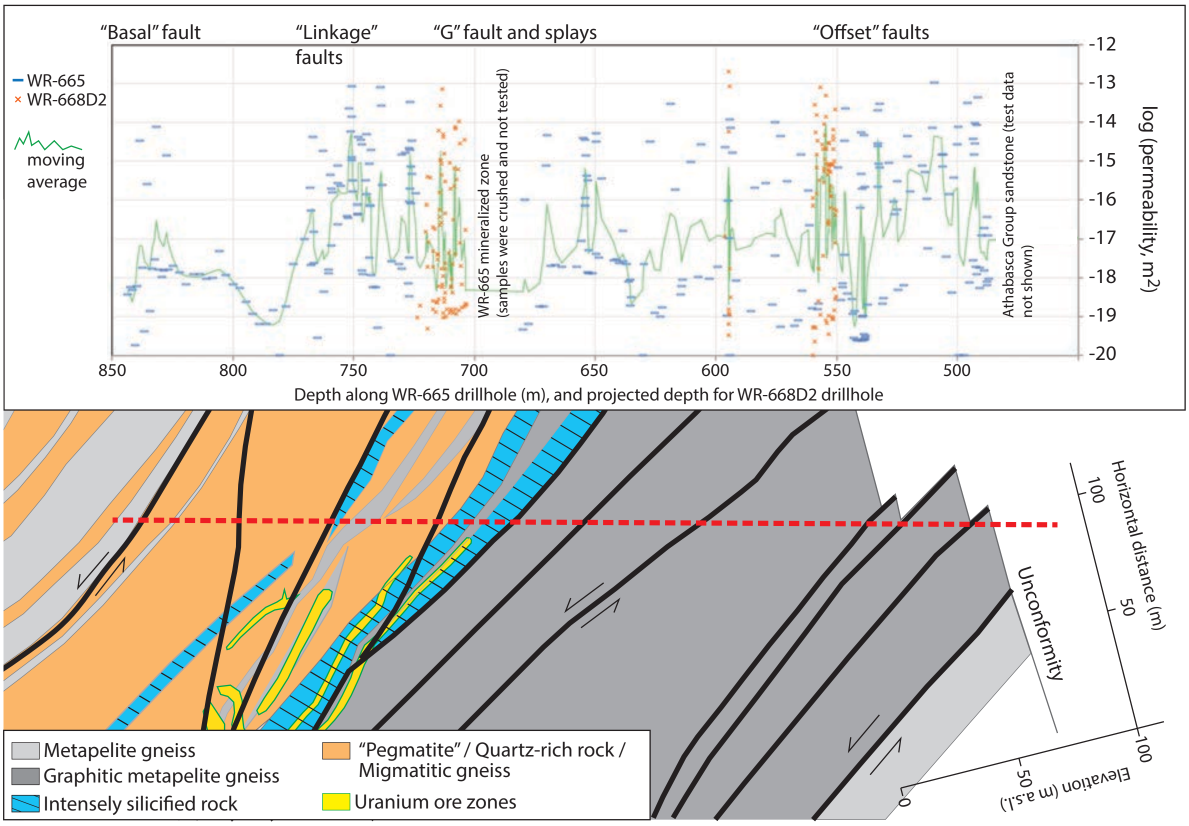

Figure 7-10 Permeability transect across the Gryphon fault zone along drillhole WR-665 and WR-668-D2, shown in rotated cross-section.

7.8.6 Rock alteration and permeability changes

Rock alteration can be pervasive (fluids permeated the whole rock matrix) or fracture-controlled (fluids diffused from discrete flow paths along fractures and affected only small volume of rock matrix). Porosity increases at single mineral grain scale (patches, pits) (Wark and Watson 1998), and entering the grains (e.g. plagioclase) and aggregates through new microfractures, causing sequential process of mineral dissolution and replacement (Nishimoto and Yoshida 2010). Macroscopic fractures and fracture zones channel the fluids the wall rocks are the most intensely altered there, although most of the fractures are partly or completely filled by hydrothermal minerals when sampled by drilling (Sausse et al. 2006). In active and young hydrothermal flow systems, crystalline rocks of low matrix permeability remain unaltered except for fracture walls and fracture mineral fills (Cox and Browne 1998). The density of fractures that provide the initial fluid access, their connectivity, and duration of fluid flow events, fluid and rock geochemical properties will affect the alteration intensity of the rock matrix.

The natural porosity and permeability of rocks are correlated, from nano to >10cm scale, and both depend on the scale, and also to the method of measurement to some extent (Anovitz and Cole 2015). At the mineral-grain scale, the nano-meter sized pits and patches can have local porosity 4.5% (Worden et al. 1990), while the whole sample has measurable porosity less than 1%. Nano-scale local intrinsic permeability can be large (Price et al. 2006), but because of very small apertures, the transmissivity is very small and the fluids during the test over short duration may not reach most of the pores. Over longer geologic times, most of the porosity can be reached by fluids.

7.8.7 Hydrothermal desilicification and silicification

Metapelitic and pegmatitic gneiss that is pervasively silicified (locally called metaquartzite) was tested in 75 drillcore pieces. The mean matrix permeability (on log permeability values) is $2.5\text{x}10^{-19}$ m^2 (Figure 7-8). This mean value is for the largest porous channels in that silicified rock found by the probe to access the N_2 gas into the rock sample, and locally the drillcore walls are glassy and have much lower permeability below our detection limit, perhaps at non-pore size only. Where the silicified rock was leached by fluids to form desilicification porous networks or 1 to 5mm patches (e.g. see Figure 7-5**c**), filled with secondary minerals such as tourmalines, illites that incompletely fill the pore spaces (e.g. Wang 2016 at the Phoenix deposit, and Mercadier 2010), the permeability of those desilicification pore spaces is $4\text{x}10^{-18}$ m^2. Where fractured (10's to 100's micro-meter apertures), the permeability of the fracture channels was tested directly by the probe in 78 samples and the mean value was $2.2\text{x}10^{-16}$ m^2.

Along the permeability transect on samples from WR-665 and WR-668-D2 drillholes (Figure 7-11), the pervasive silicified gneiss (upper graph panel) occurs locally in the hanging wall block above the G fault, and more extensively in the footwall block below the G fault, between the Basal fault. The original block model of the exploration site does not define rock properties by porosity or permeability, and does not map the smaller silicified zones or pervasively silicified zones where the rock fabric is still recognizable as pegmatite or gneiss (block model maps the original lithology). Only narrow silicified zones around the uranium deposit are mapped. In this study, the silicified zones were added along the transect as observed. The metapelitic blocks are also more heterogeneous and contain more pegmatite locally than in the block model. The pegmatite patches were added as conceptual symbols of pegmatite lens-shaped bodies (not implied actual shape) to the section. In the lower graph panel in Figure 7-11**b**, the samples that showed desilicification porosity over-printing the silicified rock. These occur sporadically in the silicified rocks. There are likely more desilicified spots not shown here because not all drillcore pieces were tested for permeability. Desilicified gneiss was found in many samples adjacent to the uranium-mineralized deposit, collaborating the evidence of past fluid flow there (near 720m on log in Figure 7-11**a**). In other areas, desilicified gneiss is only found in or near fault core zone of major fault strands in Offset faults, as was previously described in Figure 7-9.

When more drillhole data are added to the section, from WR-507 and WR-671, more of the silicified and desilicified alteration zones and their corresponding permeability distributions are mapped (Figure 7-12). In the fault damage zone, fractured silicified rock is locally highly permeable, as permeable as the fractured and faulted rock (graph panel a in the figure). There is also more evidence for higher permeability of porous desilicification in the rock matrix (graph panel b in the figure) in the damage zone in G fault and Offset fault. The porous clay-filled patches formed by partial desilicification have permeability 10^{-19} to 10^{-15} m^2.

The range of permeability is wide (10^{-19} to 10^{-13} m^2) in intensely altered pegmatite. The alteration appears to follow previous silicification and is gradational on 1 to 10m length scale. The mean permeability is $1.6x10^{-17}$ m^2, about the same as for desilicified gneiss. The later clay alteration (e.g. illite and kaolinite) pervasively fills the pore spaces and controls the permeability of the altered rock. 10^{-17} m^2 is in the lower range for pure kaolinite clay and in the upper range for illite clay (Mesri and Olson 1971). Pegmatite patches within the metapelite were found and tested in many drillcore pieces, but the dataset here only presents a sample of the actual distribution of pegmatite in metapelite. Where silicified, the pegmatite was of the same permeability as the metapelite gneiss. Where fractured, it was also as variable permeable as fractured gneiss. Sparse fractures in the damage zone in the silicified rock are as permeable as the intensely fractured rock near faults containing gouges and having well-defined slip surfaces. A small proportion of the fractured samples had low permeability near the protolith mean value.

7.8.8 Episyenite zones

Episyenites are vuggy highly porous rocks that were previously pervasively silicified and then partly desilicified. Episyenisation can involve pervasive desilicification of granitic rocks (Cathelineau 1986). The major difference between pegmatite and gneiss was in the argillic alteration zone below the G fault, where the pegmatitic rock was completely desilicified to form episyenites (near section point 750m in WR-665). The conceptual section in Figure 7-11 shows interpreted elongated narrow (1 - 10m) bodies of episyenite that are mostly disconnected. A few smaller episyenite zones were detected along the upper G fault and the lower main strand of Offset fault, detected in WR-507 and 671 (Figure 7-12). The graphitic metapelite contains relatively few pegmatite bodies or patches, thus most of the desilicification occurs in gneiss. As only a few drillholes were tested for permeability, despite more than 700 valid tests completed, the conceptual model underestimates the distribution of episyenites, silicified and desilicified rocks away from the mapped transects. The depth below the unconformity of these altered rocks is also not known.

In episyenite rock, the vugs and connected pore spaces have identical volume as the original quartz minerals in granite, but lost the quartz through hydrothermal leaching and Na or K metasomatism, at temperatures 250 to 450^{o}C and pressures 0.3 to 1.5kbar. Through fracture networks, fluids mobilize the silica and deposit it elsewhere, with some evidence of quartz dissolution and deposition in fractures (Cathelineau et al. 1996). The porosity of episyenites in the St. Sylvestre Massif, France, is 12 to 33% (Dahlkamp 1993), 9 to 13% near Forsmark, Sweden (Waber et al. 2009), The euhedral quartz and silicified zones may be sourced from the desilicified rocks. From outcrop studies, the porosity of episyenites is about 30%, and it matches the thickness of quartz veins where it was deposited (Rossi et al. 2005). The removal of quartz creates a highly permeable structure, where the area exposed to interaction with the hydrothermal fluid successively increases as the episyenite expands, and an increase in fluid salinity promotes the quartz dissolution (Petersson et al. 2012, Ballouard et al. 2017). The resulting shapes of episyenite vuggy zones are elongated tubular sub-vertical or steeply dipping columns, 0.1m to ~70m wide, following faults or fault intersections (Stephens et al. 2007, Ballouard et al. 2017). The process may occur rapidly, according to work by Nishimoto et al. 2014 in Toki Granite at Mizunami, Japan. There, an interval of desilicified episyenite (35% porosity) was found in one drillhole in otherwise sparsely fractured granite at 950m drilled depth. They estimated that the episyenization was relatively rapid, < 6Ma, in granite that was emplaced only 76 Ma ago.

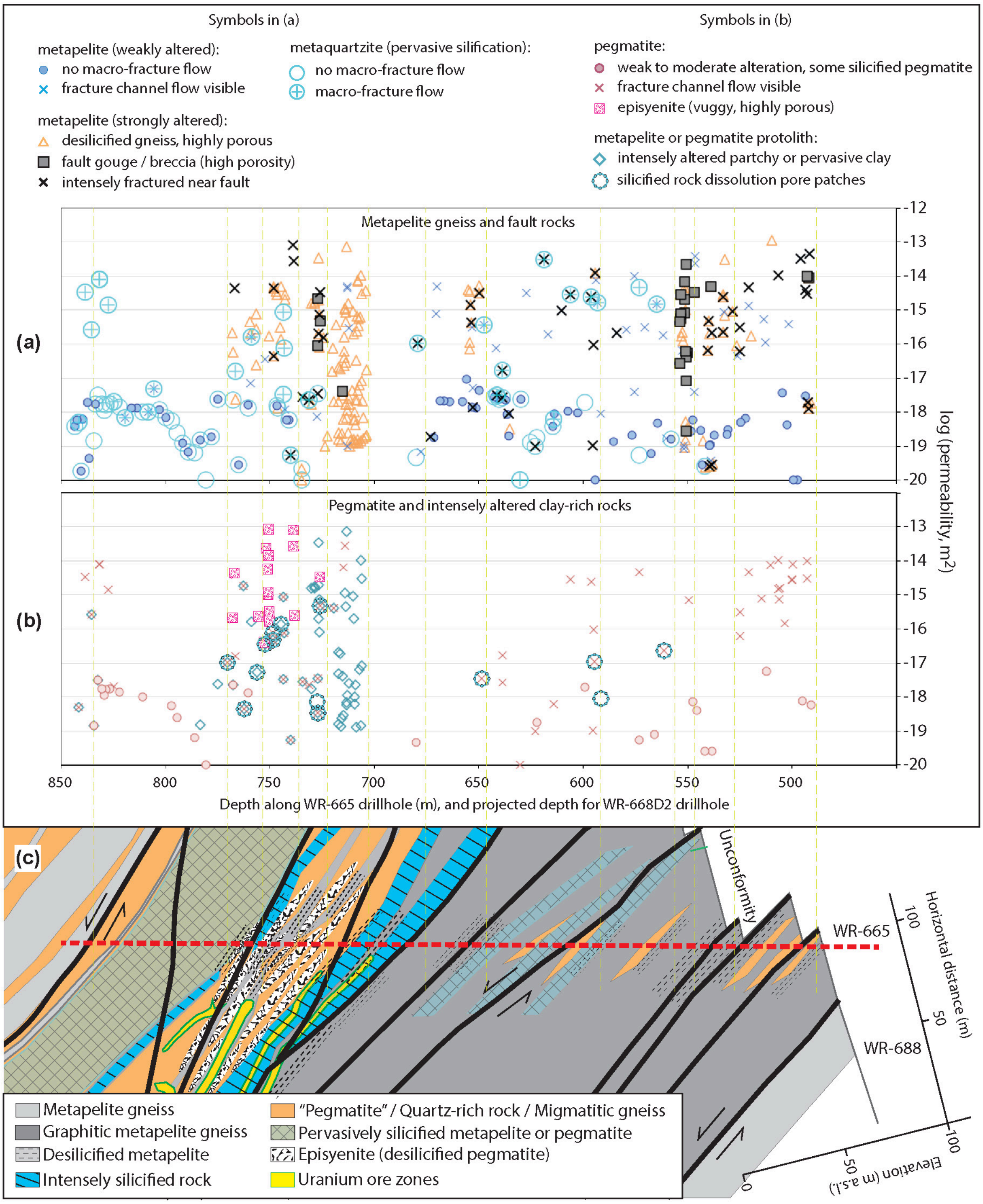

Figure 7-11 Permeability transect for different categories of permeable samples (by lithology, alteration, fracturing), across the Gryphon fault zone along drillhole WR-665 and WR-668-D2, shown in rotated cross-section.

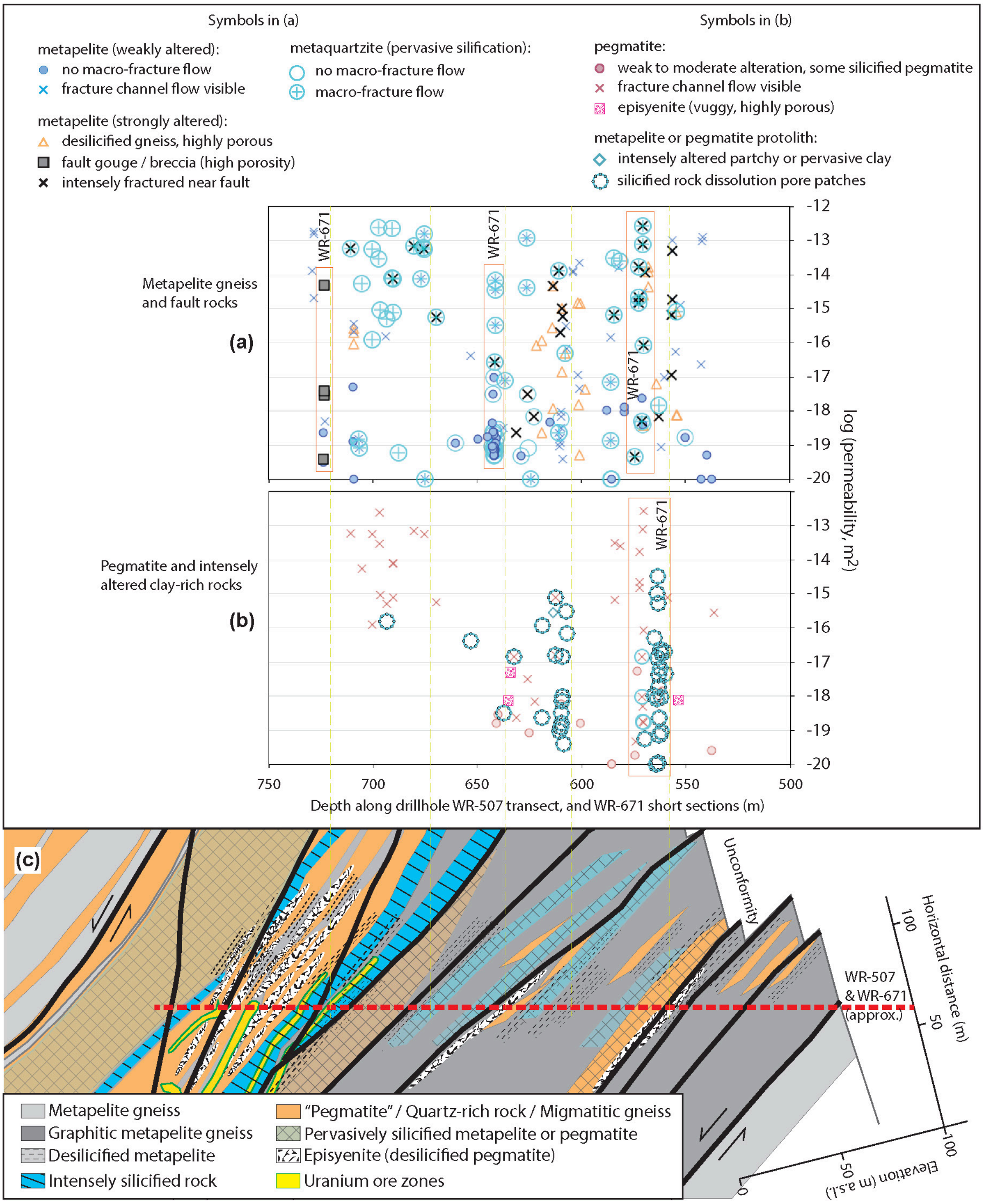

Figure 7-12 Permeability transect for different categories of permeable samples (by lithology, alteration, fracturing), across the Gryphon fault zone along drillhole WR-507 and WR-671, shown in rotated cross-section.

In the Athabasca Basin, episyenites occur in a fault zone and at outcrop in granites at the Gunnar deposit in Beaverlodge area (Ashton 2010). A somewhat similar fault hosted uranium deposit below the unconformity to the Gryphon deposit, was described by Wilde and Wall (1987) at the Nabarlek deposit in northern Australia, in the Alligator River area. It is hosted in a reverse fault zone (dip about 50 degrees) offsetting Archean amphibolite gneisses with dolerite and schists, and main mineralization dated to about 1590Ma. The higher grade ore (>1%) bodies are present along the Nabarlek fault in elongated strings, in the fault breccia that is desilicified, and surrounded by an envelope of disseminated lower grade ore (0.1%) in the intensely altered rocks and as small veins in fractures. The inner altered zone is locally completely desilicified in elongated narrow zones along the fault, and the zone within 50m has pervasive alteration to clays and chlorite, white mica, hematite. The silica was deposited in the outer halo, also along the branching faults.

The intensely altered pegmatite varies in average permeability depending on the clay infill in the vugs and pores, from an average $2x10^{-17}$ m^2 for silicified and clay altered rock (some in argillic alteration zone mapped by infrared spectrometers), and the average permeability of episyenites of approximately $7x10^{-16}$ m^2, and local maxima to 10^{-13} m^2. The multi-meter width and probably 10's to 100's meters length of these zones makes them a large contribution to the transmissivity of the fault zone, although at present the connectivity is low from evidence of low transmissivity values in interval injection tests and no losses of drilling fluids during drilling (unpublished data by Denison Mines).

7.8.9 Transmissivity of Gryphon fault zone

The intensely fractured rock near fault cores in pelite or pegmatite is about as permeable as the sparse fractures away from the fault core, but the total transmissivity of the zone is likely greater in the damage zone than the fault core because more fractures contribute to flow over a wider zone. Fractures in the damage zone appear the most effective at increasing permeability in the silicified (brittle) rocks, and are difficult to observe in clay-altered rocks during the N_2 gas injection tests into samples. The brittleness of rocks control on fracture permeability has been discussed by Ishii (2017) with examples from data collected in test holes in metamorphic and plutonic rocks.

The transmissivity of the fault zone can be estimated by the product matrix permeability (k) of drillcore sample and thickness or width (h) of tested zone in the sample (Table 7-3). As most of the tests affected a few cm of the sample, for simplicity we assume 5cm width of rock that is represented by the tested permeability. This is not the actual aperture of flow paths, but the width of rock that, if tested repeatedly in many spots, might have the measured permeability. This is approximately true for the samples that were tested at many spots in one drillcore piece. The same rock categories (lithological-alteration-structural) were used as in Figure 7-8. Within each lithological/alteration/structural rock category (Table 7-3), the sample permeability was multiplied by 5cm, and all sample kh summed up for the category. The total thickness of tested rock is simply the number of samples multiplied by 5cm per sample. The kh values must be scaled from the sample widths to the whole fault zone, by the proportion of the rock category zonal width (d) in the whole 360m wide fault zone, estimated roughly from inspection of our permeability transects in the available drillholes. The proportional kh values and their % proportions of the total can be compared.

Table 7-3 Estimation of permeability thickness of components of fault zone, by lithological-alteration-structural categories of rocks.

Lithological-alteration-structural category	Part of fault zone (note 1)	kh, (m^3)	n * 0.05m, (m)	d, (m)	kh * d/(n*0.05m), (m^3)	% of total kh
metapelite gneiss protolith	P	5.0×10^{-18}	5.9	100	8.5×10^{-17}	0.0%
metapelite gneiss (fracture flow in damage zone)	DZ	7.1×10^{-14}	6.8	50	5.2×10^{-13}	29.6 %
metapelite gneiss (intense alteration)	PA	2.8×10^{-14}	10.95	30	7.7×10^{-14}	4.4%
pegmatite of various alteration	P	3.3×10^{-18}	2.35	25	3.5×10^{-17}	0.0%
pegmatite (fracture flow)	DZ	7.0×10^{-14}	5.65	30	3.7×10^{-13}	21.0 %
pegmatite intensely altered to clay	PA	1.1×10^{-14}	4.45	30	7.7×10^{-14}	4.4%
episyenite (vuggy)	DZ	1.2×10^{-14}	0.95	10	1.3×10^{-13}	7.4%
pervasively silicified rock	P	3.2×10^{-18}	3.75	15	1.3×10^{-17}	0.0%
silicified rock (dissolution porosity)	PA	3.6×10^{-16}	2.7	15	2.0×10^{-15}	0.1%
silicified rock (fracture flow)	DZ	8.2×10^{-14}	3.9	15	3.2×10^{-13}	17.9 %
fault fractures (inner damage zone)	DZ	5.4×10^{-14}	7.3	30	2.2×10^{-13}	12.7 %
fault gouge or breccia (fault core zone)	C	1.5×10^{-14}	3.4	10	4.4×10^{-14}	2.5%
Total					1.8×10^{-12}	100%

note 1: P = protolith, PA = intensely altered protolith, DZ = fault damage zone, C = fault core

The different structural zones of the Gryphon fault zone were compared (Table 7-4). The fault core is the uncemented fault gouge and breccia. The fault damage zone includes the categories of samples that were fractured, and also the highly porous episyenites because of their correlation with major faults. The protolith consists of not visibly fractured metapelite gneiss, pegmatite, and pervasively silicified rock that may have been either gneiss or pegmatite. The altered protolith is the strongly altered rock where the porosity is pervasive and the gas flow during tests was not observed to be dominated by fractures. The fault core zone thickness in all fault strands was given an optimistic high estimate of 10m because not all fault strands were tested and the logged fault gouge/breccia width is at least 5m in the major fault strands. The total kh for the fault zone is here about 1.8×10^{-12} m^3, and the fault damage zone accounts for 67% of the kh value and potential fluid flow rate per unit area of the rock. The fault core only accounts for 2.5% of the kh. The second largest kh contribution, almost 30% is from the strongly altered protolith due to hydrothermal alteration. The unaltered or weakly altered (no large porosity enhancement) protolith has no significant kh contribution in this assessment, but this value can be larger if the background fractures are included in the protolith that were assigned to the damage zone. In this sense, the damage zone kh is probably overestimated and the protolith kh underestimated. The probe tests did not distinguish between the local disconnected macro-fractures and more connected fractures. Only a fraction of the tested fractures in drillcores samples might be connected at larger scale. The same argument might be said for the fault core zone and the fault gouges. The fluid flow is undoubtedly complex and involves both the damage zone and the fault core, and over time modifies the protolith matrix through rock alteration. It is also clear that the fault zone permeability distribution changed as a result of hydrothermal alteration, that on average caused a large increase in matrix permeability and porosity of the rock.

Table 7-4 Estimation of permeability thickness in fault damage zone, fault core, protolith, and strongly altered protolith.

Structural zone	kh (m^3)	% total
fault damage zone (fractured)	1.7×10^{-12}	67.6%
fault core	4.4×10^{-14}	2.5%
protolith (low alteration)	1.3×10^{-16}	0.0%
protolith (strong alteration)	5.3×10^{-13}	29.8%
Total	1.8×10^{-12}	100%

7.8.10 Conceptual model of permeability structure

The permeability distribution of the Gryphon fault zone can be compared to other major fault zones. One is the longest major fault zone in Japan, the Median Tectonic Line (MTL). One of the outcrops in Mie Prefecture was studied (Wibberley and Shimamoto 2005, Wibberley and Shimamoto 2003), and observation wells were installed and tested at ITA Observatory site nearby (Shigematsu et al. 2012). The sketches in Figure 7-13**f** illustrate the fault geometry. The Gryphon fault zone and the MTL are shown on the same scale, both horizontally and vertically. The Nojima fault is shown at the same horizontal scale as the other faults, but the vertical scale has been compressed to fit the figure on the page.

<u>Gryphon fault zone, Athabasca Basin:</u>

In the Gryphon fault zone, the fault core (zone) component of matrix permeability shown in Figure 7-13**a**, compared to the not visibly fractured and not strongly altered protolith. The protolith permeability (mean $3x10^{-19}$ m^2) varies from about 10^{-17} m^2 to the detection limit at 10^{-20} m^2. The fault core is a conduit to fluid flow that is 1 to 4 orders of magnitude more permeable than the protolith. There is little ambiguity in this result. Next, the fractured damage zone (Figure 7-13**b**) has a wide range of permeability at any location, from mostly sealed fractures that are little more permeable than the protolith, to highly permeable fracture channels. The upper limit of permeability is below 10^{-12} m^2 for each sample, and has a slight trend of decreasing away from the middle of the fault zone, but the outer damage zone has not been tested yet at this site and the full width of the damage zone cannot be estimated. The damage zone is as permeable on average as the fault core zone and more permeable by several orders of magnitude, on average, than the protolith. These are the standard fault zone permeability structural components. However, the newly added hydrothermally altered protolith and damage zone (Figure 7-13**c**) has a pervasive enhanced porosity and permeability of the rock matrix, in addition to any fractures that may have existed and are now obscured by the alteration minerals. Both the metapelites and pegmatites have highly permeable altered rocks, and less permeable altered rocks. This hydrothermal alteration component greatly modifies the permeability distribution of the fault zone and increases the overall transmissivity. It may on average increase the connectivity of different fractures in the fault damage zone, and also seal some fracture networks by clays and other hydrothermal products, and still retain above-protolith permeability.

Median Tectonic Line, Japan:

At the MTL fault zone, Wibberley and Shimamoto 2003 tested the outcrops and their data are plotted in Figure 7-13**d**. The fault core is tens of meters wide in this fault and contains foliated gouges, incohesive and cemented cataclasites, bounded by protolith of granitic mylonite and metapelitic schist. The authors tested the outcrop samples in confining pressurizing paths and unconfining paths after sample compression to nearly 200MPa (~20km effective depth), as the objectives there were to understand the conditions at seismogenic depths and not the in-situ conditions of the outcrop or at shallow depth. The grey squares and trend line are for samples in first pressurizing step at confining pressure of 50MPa, and pore pressure of 20MPa. This gives an effective pressure of 30MPa that corresponds to a depth of about 3km, assuming hydrostatic conditions. The authors also provided the pressure sensitivity coefficients for permeability values from nearly unconfined sample to this first confining pressure step. For this analysis, the pressure coefficients (unique for each sample) from Wibberley and Shimamoto 2003 were used to estimate the matrix permeability at shallow depth of 0.7km, at 7MPa effective pressure, 20MPa pore pressure (as tested). From Equation 11 solved for k_2, with k_1 as the permeability at 50MPa confining pressure, ΔP_c = 50MPa - 7MPa = 43MPa, the k_2 is estimated in reverse direction of the confining path of the first pressurizing confining step. This is plotted as blue dots and blue line the figure. The 0.7km depth was chosen to compare to the Gryphon fault zone. At the estimated 0.7km effective depth, the MTL outcrop course and foliated gouges are approximately as permeable as the coarse gouges in Gryphon fault strands, although a few samples from MTL are more permeable, up to $10^{-12}m^2$. This may be partly explained by surficial weathering of the outcrop, compared to the not weathered fault rocks at Gryphon fault, covered by 500m of remnant of Athabasca Basin.

The bulk permeability values were estimated through in-situ injection tests in two observation drillholes reported in Matsumoto and Shigematsu 2018, and also matrix permeability of the protolith from drillcore samples. The bulk permeability is in the damage zone near the main MTL fault and one of the smaller branching faults. This bulk permeability is similar in magnitude to the average fractured rock permeability in the damage zone at Gryphon fault zone. The protolith metapelite schist in the MTL is also very close to the mean value in metapelites at Gryphon site. The MTL is similarly oriented to the Gryphon fault and is of similar width of the damage zone, although the fault core is wider and centralized. The much more numerous tests at the Gryphon fault zone, at depths not affected by surficial weathering, show much more variation in tested values, and the additional hydrothermal alteration permeability than the sparsely tested MTL.

Nojima fault zone, Japan:

The second example is from the Nojima fault zone, an active fault that was drilled and studied on Awaji Island, south of Kobe city, Japan, and was the site of the 1995 Nambu earthquake, during which the fault slipped visibly (Koketsu et al. 1998). At one of the research sites, Hirabayashi locality, two drillholes were logged and tested, one by Geological Survey of Japan and another by NIED institute (Tanaka et al. 2001), in addition to three other drillholes by another institute at Kyoto University, installed in a branching fault off Nojima fault to the south of Hirabayashi (Ando et al. 2001). The fault cuts granodiorite and porphyry protoliths. The drillholes intercepted the Nojima fault central slip surface and damage zone, between depths approximately 700 and 1350m, and one deeper older and less permeable fault strand near 1800m depth (Locker et al. 2000), and it has been corrected to in-situ depths, but the samples were tested at higher confining pressures of a few km effective depth. Fracture frequency is higher in the damage zone than in the protolith, thus the damage zone is defined to be about 300m wide in the GSJ drillhole (Ito and Kiguchi 2005). The interpretation of the damage zone by Lockner et al. 2009 shows a relative narrow damage zone, and most of the macroscopic fractures are sealed. The micro-fractured and deformed rock in the inner damage zone has permeability 10^{-17} to ~$5x10^{-15}m^2$, and comparable the median permeability of the fractured damage zone at Gryphon. The fault gouges are less permeable than most of the samples from Gryphon or MTL, but half of the samples (form NIED drillhole) are from larger depths than at Gryphon, although only 700m deeper. The gouge samples were effectively compressed during the first pressurizing step to 50MPa. Some of the fault rocks are cataclasites that are fractured and tend to be less permeable than the incohesive gouges. Overall, the Nojima fault permeability structure closer to the classic fault barrier-conduit permeability model of Caine et al. 1996, and appears as a relatively simple and narrow structure in cross-section at this location. The Gryphon fault zone is more complex and wider, "distributed conduit" similar to the MTL, in its present explored depth and location, but we could speculate that the Nojima fault gives one example what the Gryphon fault might look like at larger depth.

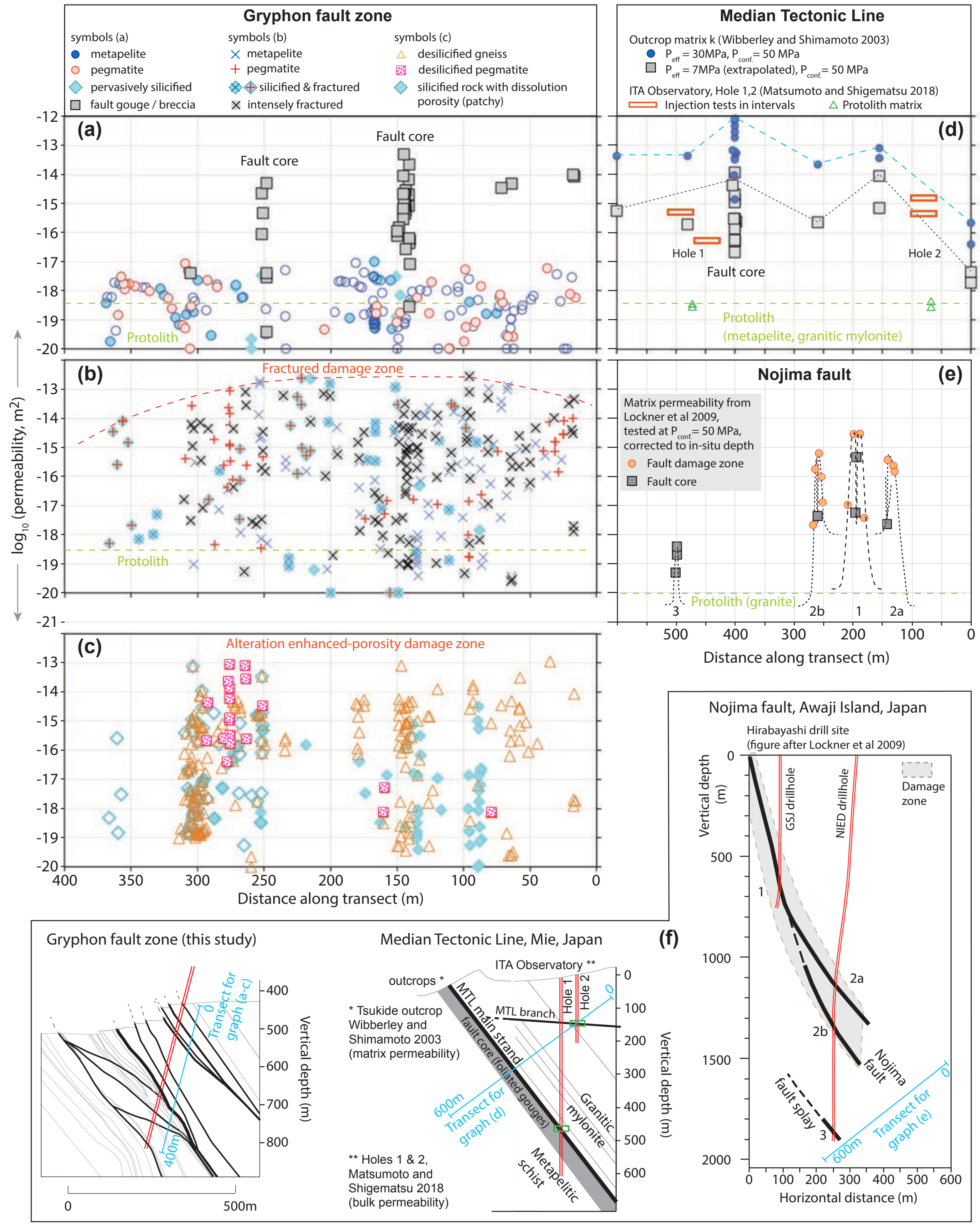

Figure 7-13 Permeability distribution in Gryphon fault zone, separated into components (a) fault core and protolith, (b) fractured damage zone, (c) strongly altered porous rock in the damage zone or in the protolith (strong porosity enhancing alteration component to permeability), (d) permeability data for transect across the MTL (Wibberley and Shimamoto 2003), (e) permeability transect through Nojima fault zone (Lockner et al. 2009), (f) fault zone geometry, drillholes, and transect sketches.

7.9 Conclusions

The large number of permeability tests in many transects across the fault zone provided new insights into the permeability structure of the fault zone. The permeability distributions can be separated into components, one for the relatively intact protolith, one for the fault core zone, one for fractured damage zone and background protolith fracturing (not distinguishable here), and one for the permeability attributable to the hydrothermal alteration of rocks. The protolith has relatively low matrix permeability (10^{-17} to 10^{-20} m^2) that is typical for metapelite rocks at depth of a few hundred meters. From transmissivity calculations of individual tests on samples, and the widths of the various zones, the fractured fault damage zone accounts for most of the transmissivity (67%), an overestimate, because there is "background" level of fracturing in the protolith that is difficult to separate from the fault damage. The outer damage zone has not been tested adequately at this location yet, although drillcore is available from outside of the fault zone and this will be done in the next part of research. The fault core is a permeable conduit here but it only accounts for 2.5% of the transmissivity. However, the surprising finding is that up to 30% of transmissivity appears to be from strongly hydrothermally altered protolith and damage zone. This enhanced porosity from rock alteration acts to magnify the conduit of the damage zone. Locally, it is largest conduit in the fault zone. The fractures in the damage zone appear the most effective at increasing permeability in the silicified (brittle) rocks, and are difficult to observe in clay-altered rocks.

The rocks found in fault core in the Gryphon fault zone strands consisted of relatively permeable and apparently highly porous coarse gouge and gouge/breccia mix. The permeability of the coarse gouges and the damage zone and the protolith was within the same order of magnitude at the Gryphon fault zone and at the Median Tectonic Line in Japan, a similarly wide and oriented, although more active fault zone. The high permeability of the relatively inactive Gryphon fault zone may be surprising, but the fault has not been affected by surficial weathering and is also below the paleo-weathering zone from pre-Athabasca Basin exposure.

7.10 References:

Aaltonen, I., Engstrom, J., Front, K., Gehor, S., Kosunen, P., Karki, A., Paananen, M., Paulamaki, S., & Mattila, J. (2016) Geology of Olkiluoto. Posiva Report 2010-70, Posiva Oy, Helsinki, Finland

Aaltonen, I., Heikkinen, E., Paulamäki, S., Säävouri, H., Vuoriainen, S., & Öhma, I. (2009) Summary of Petrophysical Analysis of Olkiluoto Core Samples 1990 – 2008. Working Report 2009-11

Alexandre, P., Kyser, K., Thomas, D., Polito, P., & Marlat, J. (2009) Geochronology of unconformity-related uranium deposits in the Athabasca Basin, Saskatchewan, Canada and their integration in the evolution of the basin. *Mineralium Deposita*, 44, 41–59

Ando, M. (2001) Geological and geophysical studies of the Nojima Fault from drilling: An outline of the Nojima Fault Zone Probe. *The Island Arc*, 10, 206–214

Annesley, I.R., Madore, C., & Portella, P. (2005) Geology and thermotectonic evolution of the western margin of the Trans-Hudson Orogen: evidence from the eastern sub-Athabasca basement, Saskatchewan. *Canadian Journal of Earth Sciences*, 42, 573–597

Annesley, I.R., & Madore, C. (1994) A geological study of the Wollaston–Mudjatik domain boundary in the Wollaston Lake area, Hearne Province, Saskatchewan. Saskatchewan Research Council, Publication R-1230–6-C-94, 162 p.

Annesley, I.R., Madore. C., Kusmirski, R.T., & Bonli, T. (2000) Uraninite-bearing granitic pegmatitic, Moore Lakes, Saskatchewan: Petrology and U-Th-Pb chemical ages: in Summary of Investigations 2000, Volume 2. Saskatchewan Gcological Survey, Saskatchewan Ministry of Energy and Mines, Misc. Rep. 2000-4.2

Ashton, K.E. (2010) The Gunnar mine: an episyenite-hosted, granite-related uranium deposit in the Beaverlodge uranium district. In: Summary of Investigations 2010, Vol. 2, Saskatchewan Geological Survey, Saskatchewan Ministry of Energy and Resources, Misc. Report 2010-4.2, Paper A-4, 21p.

Atomic Energy Control Board (1986) A compilation of subsurface hydrogeologic data, Volume I - Main Report. Research Report by GTC Geologic Testing Consultants to Atomic Energy Control Board, INFO-0203-2, Ottawa, Ontario, Canada

Autio, J, Hjerpe, T., & Siitari-Kauppi, M. (2003) Porosity, Diffusivity and Permeability of

EDZ in Crystalline Rock and Effect on the Migration in a KBS-3 Type Repository. Conference paper

Autio, J. (1996) Characterization of the excavation disturbance caused by boring of the experimental full scale deposition holes in the Research Tunnel at Olkiluoto. Report POSIVA 96-09, Posiva Oy, Helsinki, Finland

Ballouard, C., Poujol, M., Mercadier, J., Deloule, E., Boulvais, P., Baele, J.M., Cuney, M., & Cathelineau, M. (2017) Uranium metallogenesis of the peraluminous leucogranite from the Pontivy-Rostrenen magmatic complex (French Armorican Variscan belt): the result of long-term oxidized hydrothermal alteration during strike-slip deformation. *Mineralium Deposita*, 53(5), 601–628

Baudemont, D., & Fedorowich, J. (1996) Structural Control of Uranium Mineralization at the Dominique-Peter Deposit, Saskatchewan, Canada. *Economic Geology*, 91, 855–874

Baudemont, D., Piquard, J.P., Ey, F., & Zimmerman, J. (1993) The Sue uranium deposits. Saskatchewan, Canada. *Exploration Mining Geology*, 2(3), 179–202

Bear, J. (1972) Dynamics of Fluids in Porous Media. Dover Publications, New York

Becker, C.J. , Overton, M.D., Johnson, K.S., & Luza, K.V. (1997) Geologic and hydraulic characteristics of selected shaly geologic units in Oklahoma. U.S. Geological Survey Water-Resources Investigations Report 96-4303

Belghoul, A. (2007) Caracterisation petrophysique et hydrodynamique du socle cristallin. PhD Thesis. Universite Montpellier. HAL archives-ouvertes Id: tel-00444175, [https://tel.archives-ouvertes.fr/tel-00444175; Chapter 4: Characterization of fractured crystalline basement from downhole measurements and images; example from Stang Er Brune experimental site (Ploemeur, France)]

Berckhemer, H., Rauen, A., Winter, H., Kern, H., Kontny, A., Lienert, M., Noever, G., Pohl, J., Popp, T., Schult, A., Zinke, J., & Soffel, C. (1997) Petrophysical properties of the 9-km-deep crustal section at KTB. *Journal of Geophysical Research*, 102(B8), 18337–18361

Bickford, M., Collerson, K., Lewry, J., & Orrell, S. (1992) Pegmatites and leucogranites as probes of crust beneath allochthonous orogenic rocks in the Glennie and La Ronge domains. In: Summary of Investigations 1992, Saskatchewan Geological Survey, Sask. Energy and Mines, Miscellaneous Report 92- 4, 124–129

Bickford, M.E., Collerson, K.D., Lewry, J.F., Van Schmus, W.R., & Chiarenzelli, J.R. (1990) Proterozoic collisional tectonism in the Trans-Hudson Orogen, Saskatchewan. *Geology*, 18, 14–18

Blaise, J.R. (1997) The McClean Lake uranium project. In: IAEA, Assessment of uranium deposit types and resources — a worldwide perspective. Proceedings of a Technical Committee Meeting organized by the International Atomic Energy Agency and the OECD Nuclear Energy Agency and held in Vienna, 10–13 June 1997

Bongiolo, E.M., Bongiolo, D.E., Sardini, P., Mexias, A.S., Siitari-Kauppi, M., Gomes, M.E.B., & Formoso, M.L.L. (2007) Quantification of porosity evolution from unaltered to propylitic-altered granites: the 14C-PMMA method applied on the hydrothermal system of Lavras do Sul, Brazil. *Anais da Academia Brasileira de Ciências*, 79(3), 503–517

Borrelli, L., Perri, F., Critelli, S., & Gullà, G. (2014) Characterization of granitoid and gneissic weathering profiles of the Mucone River basin (Calabria, southern Italy). *Catena*, 113, 325–340

Bossart, P., & Mazurek, M. (1991) Grimsel Test Site – Structural geology and water flow paths in the migration shear zone. Nagra Tech. Report NTB 91-12. Nagra, Wettingen, Switzerland

Brace, W.F. (1980) Permeability of Crystalline and Argillaceous Rocks. *International J. Rock Mechanics and Mining Sciences & Geomechanics Abstracts,* 17(5), 241–251

Brace, W.F., Walsh, J.B. & Frangos, W.T. (1968) Permeability of granite under high pressure. *Journal of Geophysical Research,* 73, 2225–2236

Bradbury, M.H. (1989) Grirnsel Test Site: Laboratory investigations in support of the migration experiments, Nagra Technical Report NTB 88-23, Nagra, Wettingen, Switzerland

Brosch, F.J., Schachner, Blümel, K.M., Fasching, A., & Fritz, H. (2000) Preliminary investigation results on fabrics and related physical properties of an anisotropic gneiss. *Journal of Structural Geology*, 22(11-12), 1773–1787

Brown, S., & Smith, M. (2013) A transient-flow syringe air permeameter. *Geophysics*, 78(5), D307–D313

Browne, P.R.L. (1978) Hydrothermal alteration in active geothermal systems. *Annual Reviews of Earth and Planetary Sciences*, 6, 229–250

Bruneton, P. (1993) Geological environment of the Cigar Lake uranium deposit. *Canadian Journal of Earth Sciences*, 30(4), 653–673

Bucher K., & Frey M. (2002) Metamorphism of Pelitic Rocks (Metapelites). In: Petrogenesis of Metamorphic Rocks. Springer, Berlin, Heidelberg

Caine, J.S., Evans, J.P., & Foster, C.B. (1996) Fault zone architecture and permeability structure. *Geology*, 24, 1025–1028

Caine, J.S., Johnson, R.H., & Wild, E.C. (2011) Review and Interpretation of Previous Work and New Data on the Hydrogeology of the Schwartzwalder Uranium Mine and Vicinity, Jefferson County, Colorado. Open-File Report 2011–1092, US Geological Survey, Reston, Virginia

Cameco Corp. (2012) McArthur River Operation Northern Saskatchewan, Canada. National Instrument 43-101 Technical Report, November 2, 2012. McArthur River Operation, Northern Saskatchewan, Canada

Card, C. (2014) Altered pelitic gneisses and associated “quartzite ridges” beneath the southeastern Athabasca Basin: alteration facies and their relationship to uranium deposits along the Wollaston-Mudjatik transition; in Summary of Investigations 2013, Volume 2, Saskatchewan Geological Survey, Saskatchewan Ministry of the Economy, Miscellaneous Report 2013-4.2, Paper A-4, 23p.

Card, C.D., & Noll, J. (2016) Host-rock protoliths, pre-ore metasomatic mineral assemblages and textures, and exotic rocks in the western Athabasca Basin: ore-system controls and implications for the unconformity-related uranium model; in Summary of Investigations 2016, Volume 2, Saskatchewan Geological Survey, Saskatchewan Ministry of the Economy, Miscellaneous Report 2016-4.2, Paper A-8, 19p.

Card, C.D. (2012) The origins of anomalously graphitic rocks and quartzite ridges in the basement to the southeastern Athabasca Basin. In: Summary of lnvestigations 2012, Volume 2, Saskatchewan Geological Survey, Saskatchewan Ministry of the Economy, Miscellaneous Report 2012-4.2, Paper A-6, l5p.

Cassiaux, M., Proust, D., Siitari-Kauppi, M., Sardini, P., and Leutsch, Y. (2006) Clay minerals formed during propylitic alteration of a granite and their influence on primary porosity: A multi-scale approach. *Clays and Clay Minerals*, 54, 541–554

Cathelineau, M. (1986) The hydrothermal alkali metasomatism effects on granitic rocks; quartz dissolution and related subsolidus changes. *Journal of Petrology*, 27(4), 945–965

Cathelineau, M., Banks, D., Ayt Ougougdal, M., Boiron, M.C., & Poty, B. (1996) Fluid Penetration and Faulting in Alpine Granites (Mont Blanc and Aar Massifs): A Multidisciplinary Study of Fluid Inclusions and Their Chemistry . Proceedings of PACROFI VI, Pan-American Current Research On Fluid Inclusions, May 30 - June 1, University of Wisconsin-Madison

Chambefort, I., Buscarlet, E., Wallis, I.C., Sewell, S., and Wilmarth, M. (2016) Ngatamariki Geothermal Field, New Zealand: Geology, geophysics, chemistry and conceptual model. *Geothermics*, 59, 266–280

Chandler, F.W. (1978) Geology of part of the Wollaston Lake Fold Belt, north Wollaston Lake, Saskatchewan. Geological Survey of Canada, Bulletin 277, 25p.

Chester, F.M., & Logan, J.M. (1986) Implications for mechanical properties of brittle faults from observations of the Punchbowl Fault Zone, California. *PAGEOPH*, 124(1/2), 79–106

Chigira, M., Kanaori, Y., Wakizaka, Y., Yoshida, H., & Miyata, Y. (2016) Engineering geology. In: Moreno, T., Wallis, S., Kojima, T., Gibbons, W. (Eds.), The Geology of Japan. Geological Society, London

Choi, J-H., Edwards, P., Ko, K., & Kim, Y-S (2016) Definition and classification of fault damage zones: A review and a new methodological approach. *Earth-Science Reviews*, 152, 70–87

Cloutier, J., Kyser, K., Olivo, G.R., & Alexandre, P. (2010) Contrasting Patterns of Alteration at the Wheeler River Area, Athabasca Basin, Saskatchewan, Canada: Insights into the Apparently Uranium-Barren Zone K Alteration System. *Economic Geology*, 105, 303–324

Cloutier, J., Kyser, K., Olivo, G.R., and Alexandre, P., & Halaburda, J. (2009) The Millennium Uranium Deposit, Athabasca Basin, Saskatchewan, Canada: An Atypical Basement-Hosted Unconformity-Related Uranium Deposit. *Economic Geology*, 104, 815–840

Corbett, P., Potter, D., Mohammed, K., & Liu, S. (2001) Forget better statistics - concentrate on better sample collection. Proceedings of the 6th Nordic Symposium on Petrophysics, 15-

16 May 2001, NTNU, Trondheim, Norway

Cox, M.E., & Browne, P. (1998) Hydrothermal alteration mineralogy as an indicator of hydrology at the Ngawha Geothermal Field, New Zealand. *Geothermics*, 27(3), 259–270

Craw, D., & Upton, P. (2014) Graphite reaction weakening of fault rocks, and uplift of the Annapurna Himal, central Nepal. *Geosphere*, 10(4), 720–731

Cumming, G.L., & Krstic, D. (1992) The age of unconformity-related uranium mineralization in the Athabasca Basin, northern Saskatchewan. *Canadian Journal of Earth Sciences*, 29, 1623–1639

Dahlkamp, F.J. (1993) Uranium ore deposits. Springer-Verlag Berlin Heidelberg 1993, 1st edition. doi:10.1007/978-3-662-02892-6

David, C., Wong, T-f., Zhu, W., & Zhang, J. (1994) Laboratory measurement of compaction-induced permeability change in porous rock: implications for the generation and maintenance of pore pressure excess in the crust. *Pure and Applied Geophysics,* 143, 425–456

Davies, J.R. (1998) The origin, structural style, and reactivation history of the Tabbernor Fault Zone, Saskatchewan. Canada. MSc thesis, McGill University, Montreal

Davis, J.M., Wilson, J.L., & Phillips, F.M. (1994) A portable air-minipermeameter for rapid in-situ field measurements, *Ground Water,* 32(2), 258–266

Dill, H. (2015) Pegmatitic Rocks and Their Geodynamic Setting in the Central European Variscides. In: The Hagendorf-Pleystein Province: the Center of Pegmatites in an Ensialic Orogen, pp.55-110. Verlag: Springer International Publishing. doi:10.1007/978-3-319-18806-52

Dinwiddie, C.L., Molz, III, F.J., & Castle, J.W. (2003) A new small drill hole minipermeameter probe for in situ permeability measurement: Fluid mechanics and geometrical factors. *Water Resources Research*, 39(7), 1178

Eberhardt, E., Stead, D., & Stimpson, B. (1999) Effects of sample disturbance on stress-induced microfracturing characteristics of brittle rock. *Canadian Geotechnical Journal,* 36, 239–250

Elliott, C.G. (1994) Structural relationships across the Tabbemor Fault. Nielson Lake area, Trans-Hudson Orogen, Saskatchewan. In: Current Research 1994-C, Geological Survey of Canada, 113–120

Facca, G., & Tonani, F. (1967) The self-sealing geothermal field. IAV International Symposium on Volcanology (New Zealand) Nov. 1965. *Bulletin Volcanologique*, 30(1), 271–273

Faulkner, D.R. (2004) A model for the variation in permeability of clay-bearing fault gouge with depth in the brittle crust. *Geophysical Research Letters*, 31, L19611

Faulkner, D.R., & Rutter, E.H. (2000) Comparisons of water and argon permeability in natural clay-bearing fault gouge under high pressure at 20 ^{o}C. *Journal of Geophysical Research*, 105(B7), 16415–16426

Faulkner, D.R., Jackson, C.A.L., Lunn, R.J., Schlische, R.W., Shipton, Z.K., Wibberley, C.A.J., & Withjack, M.O. (2010) A review of recent developments concerning the structure, mechanics and fluid flow properties of fault zones. *Journal of Structural Geology*, 32, 1557–1575

Fayek, M., & Kyser, T.K. (1997) Characterization of multiple fluid-flow events and rare-earth-element mobility associated with formation of unconformity-type uranium deposits in the Athabasca Basin, Saskatchewan. *The Canadian Mineralogist*, 35, 627–658

Fisher, A.T. (1998) Permeability within basaltic oceanic crust. *Reviews of Geophysics*, 36(2), 143–182

Front, K., & Paananen, M. (2006) Hydrothermal Alteration at Olkiluoto: Mapping of Drill Core Samples. POSIVA Working Report 2006-59, Posiva Oy, Olkiluoto, Finland

Galan, E., & Ferrell, R.E. (2013) Genesis of Clay Minerals. Chapter 3, In: Developments in Clay Science, Vol. 5A. Elsevier Ltd. doi:10.1016/B978-0-08-098258-8.00003-1

Geraud, Y., Caron, J.-M., & Faure, P. (1995) Porosity network of a ductile shear zone. *Journal of Structural Geology*, 17, 1757–1769

Geraud, Y., Rosener, M., Surma, F., Place, J., Le Garzic, E., & Diraison, M. (2010) Physical properties of fault zones within a granite body: Example of the Soultz-sous-Forêts geothermal site. *Comptes Rendus Geoscience*, 342, 566–574

Goggin, D.J. (1993) Probe permeametry: is it worth the effort? *Marine and Petroleum Geology*, 10, 299–308

Goggin, D.J., Thrasher, R.L., & Lake, L.W. (1988) A theoretical and experimental analysis of minipermeameter response including gas slippage and high velocity flow effects. *In Situ,* 12(1 & 2), 79–116

Gomila, R., Arancibia, G., Mitchell, T.M., Cembrano, J.M., & Faulkner, D.R. (2016) Palaeopermeability structure within fault-damage zones: A snap-shot from microfracture analyses in a strike-slip system. *Journal of Structural Geology*, 83, 103–120

Gorbatsevich, F.F. (2003) Decompaction mechanism of deep crystalline rocks under stress relief. *Tectonophysics*, 370, 121–128

Grare, A., Benedicto, A., Lacombe, O., Trave, A., Ledru, P., Blain, M., & Robbins, J. (2018) The Contact uranium prospect, Kiggavik project, Nunavut (Canada): Tectonic history, structural constraints and timing of mineralization. *Ore Geology Reviews*, 93, 141–167

Grare, A., Lacombe, O., Mercadier, J., Benedicto, A., Guilcher, M., Trave, A., Ledru, P., & Robbins, J. (2018) Fault zone evolution and development of a structural and hydrological barrier: the quartz breccia in the Kiggavik Area (Nunavut, Canada) and Its Control on Uranium Mineralization. *Minerals*, 8, 319

Guffey, S.D. (2017) 3D Lithogeochemical Footprint of the Millennium-Mcarthur River Unconformity-Type Uranium Deposits, Saskatchewan, Canada. MSc thesis, Memorial University of Newfoundland, Canada

Habler, G., & Thöni, M., (2001) Preservation of Permo-Triassic low-pressure assemblages in the Cretaceous high-pressure metamorphic Saualpe crystalline basement (Eastern Alps, Austria). *Journal of Metamorphic Geology*, 19, 679–697

Haines, S.H., & van der Pluijm, B.A. (2012) Patterns of mineral transformations in clay gouge, with examples from low-angle normal fault rocks in the western USA. *Journal of Structural Geology*, 43, 2–32

Hakala, M., & Haikkila, E. (1997) Summary report - Development of laboratory tests and the stress-strain behaviour of Olkiluoto mica gneiss. POSIVA-97-04, Posiva Oy, Helsinki, Finland

Halvorsen, C., & Hurst, A. (1990) Principles, practice, and applications of laboratory minipermeametry. In: Advances in Core Evaluatton (ed. by P.F. Worthington), pp. 495-520. Gordon and Breach, New York

Harper, C.T. (1983) Iron Ores of Northern Saskatchewan. Saskatchewan Geological Survey Report 220, Saskatchewan Energy and Mines

Hartikainen, K., & Hartikainen, J. (1998) Posiva's site investigations in Olkiluoto, Kivetty, Romuvaara and Hästholmen by He-gas methods in 1997. Working Report 98–17e, Posiva Oy, Helsinki, Finland

Hartikainen, K., & Hartikainen, J. (1998) Posiva's site investigations in Olkiluoto, Kivetty, Romuvaara and Hästholmen by He-gas methods in 1997. Posiva Working Report 98–17e, Posiva Oy, Helsinki, Finland

Heikamp, S., & Nover, G. (2003) An integrated study on physical properties of a KTB gneiss sample and marble from Portugal: Pressure dependence of the permeability and frequency dependence of the complex electrical impedance. *Pure and Applied Geophysics*, 160, 929–936

Henley, R.W., & Ellis, A.J. (1983) Geothermal systems, ancient and modern. *Earth Science Reviews*, 19, 1–50

Hirose, T., & Hayman, N.W. (2008) Structure, permeability, and strength of a fault zone in the footwall of an oceanic core complex, the Central Dome of the Atlantis Massif, Mid-Atlantic Ridge, 30 N. *Journal of Structural Geology*, 30, 1060–1071

Ho, C.K., & Webb, S.W. (2006) Gas Transport in Porous Media . Theory and Applications of Transport in Porous Media, Vol. 20, Springer, The Netherlands. ISBN-10 1-4020-3962-X

Hobbs, W., Griggs, A.B., Wallace, R.E., & Campbell, A.B. (1965) Geology of the Coeur d'Alene District Shoshone County Idaho. US Geological Survey Professional Ppaer 478, Washington, D.C.

Hoeve, J., & Quirt, D. (1987) A stationary redox front as a critical factor in the formation of high-grade, unconformity-type uranium ores in the Athabasca basin, Saskatchewan, Canada. *Bulletin of Mineralogy* (Societe francaise de Mineralogie et de Cristallographie, Paris), 110, 157–171

Howard, J.J. (1992) Influence of authigenic clay minerals on permeability. In: Origin, Diagenesis and Petrophysics of Clay Minerals in Sandstones. SEPM Special Publication No. 47, Society for Sedimentary Geology. ISBN 0-918985-95-1

Hull, J. (1988) Thickness–displacement relationships for deformation zones. *Journal of Structural Geology*, 10, 431–435

Hunt, A. G., & Sahimi, M. (2017) Flow, transport, and reaction in porous media: Percolation scaling, critical-path analysis, and effective medium approximation. *Reviews of Geophysics*, 55, 993–1078

Ingebritsen, S.E., & Manning, C.E. (2010) Permeability of the continental crust: dynamic variations inferred from seismicity and metamorphism. *Geofluids*, 10, 193–205

Isaacs, A.J., Evans, J.P., Song, S-R, & Kolesar, P.T. (2007) Structural, Mineralogical, and Geochemical Characterization of the Chelungpu Thrust Fault, Taiwan. *Terrestrial, Atmospheric, and Oceanic Sciences*, 18(2), 183–221

Ishii, E. (2017) Preliminary assessment of the highest potential transmissivity of fractures in fault zones by core logging. *Engineering Geology*, 221, 124–132

Ishikawa, T., Hirono, T., Matsuta. N., Kawamoto, K., Fujimoto, K., Kameda, J., Nishio, Y., Maekawa, Y., & Honda, G. (2014) Geochemical and mineralogical characteristics of fault gouge in the Median Tectonic Line, Japan: evidence for earthquake slip. *Earth, Planets and Space*, 66, 36

Ito, H., & Kiguchi, T. (2005) Distribution and properties of fractures in and around the Nojima Fault in the Hirabayashi GSJ borehole. In: Harvey, P.K., Brewer, T.S., Pezard, P.A., and Petrov, V.A. (Eds.), Petrophysical Properties of Crystalline Rocks. Geological Society, London, *Special Publications*, 240, 61–74

Jeanneret, P., Goncalves, P., Durand, C., Trap, P., Marquer, D., Quirt, D., & Ledru, P. (2016) Tectono-metamorphic evolution of the pre-Athabasca basement within the Wollaston–Mudjatik Transition Zone, Saskatchewan. *Canadian Journal of Earth Sciences*, 53, 231–259

Jefferson, C. W., Thomas, D. J., Gandhi, S. S., Ramaekers, P., Delaney, G., et al. (2007) Unconformity-associated uranium deposits of the Athabasca Basin, Saskatchewan and Alberta. EXTECH IV: Geology and Uranium EXploration TECHnology of the Proterozoic Athabasca Basin, Saskatchewan and Alberta (Jefferson, C.W. and Delaney, G., eds.). *Geological Survey of Canada, Bulletin*, 588, 23–68

Jensen, J.L., Glasbey, C.A., & Corbett, P.W.M. (1994) On the interaction of geology, measurement, and statistical analysis of small-scale permeability measurements. *Terra Nova* 6, 397–403

Johnson, G.R. (1983) Rock property measurements and analysis of selected igneous, sedimentary, and metamorphic rocks from world-wide localities. Open-File report 83-736, U.S. Geological Survey

Johnstone, G.S., & Mykura, W. (1989) Migmatites, early igneous activity within the Caledonides, Northern Highlands of Scotland. In: British regional geology: Northern Highlands of Scotland. 4th edition. Keyworth, Nottingham: British Geological Survey (http://earthwise.bgs.ac.uk/index.php/Migmatites,earlyigneousactivitywithintheCaledonides, NorthernHighlandsofScotland)

Johri, M., Zoback, M.D., & Hennings, P. (2014) A scaling law to characterize fault-damage zones at reservoir depths. *AAPG Bulletin*, 98(10), 2057–2079

Jones, F.O., & Owens, W.W. (1980) A Laboratory Study of Low-Permeability Gas Sands. *Journal of Petroleum Techology*, September 1980, 1631–1640

Jones, S.C. (1972) A rapid, accurate, unsteady-state Klinkenberg permeameter. *SPE Journal*, October 1972, 383–397

Jones, S.C. (1992) Unsteady-state profile permeameter - method and apparatus. United States Patent # 5237854, Aug 24, 1993

Jones, S.C. (1997) A technique for faster pulse-decay permeability measurements in tight rocks. *Journal of SPE Formation Evaluation*, 12, 19–26

Karasaki, K., Onishi, T., Doughty, C., Conrad, M., Gasperikova, E., Cook, P., & Ulrich, C. (2012) Development of a Hydrologic Characterization Technology for Fault Zones. Report LBNL-5862E, Lawrence Berkeley National Laboratory. Available on www since 2014 from University of California [http://escholarship.org/uc/item/3j52x603]

Kerr, W.C. (2010) The discovery of the Phoenix Deposit; a new high-grade, Athabasca Basin unconformity-type uranium deposit, Saskatchewan, Canada. *Society of Economic Geologists Special Publications*, 15, 703–728

Klinkenberg, L.J. (1941) The permeability of porous media to liquids and gases. Americal Petroleum Institute, Drilling and Productions Practices, 200–213

Kobayashi, K., Hirano, S., Arai, T., Ikeda, R., Omura, K., Sano, H., Sawaguchi, T., Tanaka, H., Tomita, T., Tomida, N., Matsuda, T., & Yamazaki, A. (2001) Distribution of fault rocks in the fracture zone of the Nojima fault at a depth of 1140 m: Observations from the Hirabayashi NIED drill core. *The Island Arc*, 10, 411–421

Koketsu, K., Yoshida, S., & Higashihara, H. (1998) A fault model of the 1995 Kobe earthquake derived from the GPS data on the Akashi Kaikyo Bridge and other datasets. *Earth Planets Space*, 50, 803–811

Kotzer, T.G., & Kyser, T.K. (1995) Petrogenesis of the Proterozoic Athabasca Basin, northern Saskatchewan, Canada, and its relation to diagenesis, hydrothermal uranium mineralization and paleohydrogeology. *Chemical Geology*, 120, 45–89

Kristensen, T.B., Rotevatn, A., Peacock, D.C.P., Henstra, G.A., Midtkandal, I., & Grundvåg, S-A. (2016) Structure and flow properties of syn-rift border faults: The interplay between fault damage and fault-related chemical alteration (Dombjerg Fault, Wollaston Forland, NE Greenland). *Journal of Structural Geology*, 92, 99–115

Kuva, J., Voutilainen, M., Kekäläinen, P., Siitari-Kauppi, M., Timonen, J., & Koskinen, L. (2015). Gas phase measurements of porosity, diffusion coefficient and permeability in rock samples from Olkiluoto bedrock, Finland. *Transport in Porous Media*, 107(1), 187–204

Lanaro, F., Sato, T., & Nakama, S. (2009) Depth variability of compressive strength test results of Toki Granite from Shobasama and Mizunami Construction Sites, Japan. *Rock Mechanics and Rock Engineering*, 42(4), 611–629

Lechler, B.J. (2002) Gas permeameters: operation, modification, and design. MSc thesis, New Mexico Institute of Mining and Technology

Lee, Y-J. (1991) Slickenside petrography: slip-sense indicators and classification" (1991). Geology Theses and Dissertations. 52. State University of New York at Albany, NY (http://scholarsarchive.library.albany.edu/casdaesgeologyetd/52)

Lenhard, R.J., & Parker, J.C. (1987) A model for hysteretic constitutive relations governing multiphase flow: 2. Permeability-saturation relations. *Water Resources Research*, 23, 2197–2206

Lewry, J. F., & Sibbald, T. (1977) Variation in lithology and tectonometamorphic relationships in the Precambrian basement of northern Saskatchewan. *Canadian Journal of Earth Sciences*, 14, 1453–1467

Li, K., & Horne, R.N. (2001) Gas Slippage in Two-Phase Flow and the Effect of Temperature. Society of Petroleum Engineers Inc., ppaer SPE 68778 presented at Bakersfield, California, 26–30 March 2001

Li, Z., Bethune, K.M., Chi, G., Bosman, S.A., & Card, C.D. (2015) Topographic features of the sub-Athabasca Group unconformity surface in the southeastern Athabasca Basin and their relationship to uranium ore deposits. *Canadian Journal of Earth Sciences*, 52, 903–920

Liang, Y., Price, J.D., Wark, D.A., & Watson, E.B. (2001) Nonlinear pressure diffusion in a porous medium: Approximate solutions with applications to permeability measurements using transient pulse decay method. *Journal of Geophysical Research*, 106(B1), 529–535

Lockner, D., Tanaka, H., Ito, H., Ikeda, R., Omura, K., & Naka, H. (2009) Geometry of the Nojima Fault at Nojima-Hirabayashi, Japan – I. A Simple Damage Structure Inferred from Borehole Core Permeability. *Pure and Applied Geophysics*, 166, 1649–1667

Lockner, D.A., Naka, H., Tanaka, H., Ito, H., & Ikeda, R. (2000) Permeability and strength of core samples from the Nojima fault of the 1995 Kobe earthquake. In: Ito et al. (eds) Proceedings of the Internal Workshop on Nojima Fault Core and Borehole Data Analysis, November 22-23, 1999 Tsukuba, Japan. USGS Open-file Report 00-129. GSJ Interim Report No.EQ/00/1

Lockner, D.A., Summers, R., Moore, D., & Byerlee, J.D. (1982) Laboratory Measurements of Reservoir Rock from the Geysers Geothermal Field, California. *International Journal of Rock Mechanics and Mine Sciences & Geomechanics Abstracts*, 19, 65–80

Maaranen, J., Lehtioksa, J., & Timonen, J. (2001) Determination of porosity, permeability and diffusivity of rock samples from Äspö HRL using the helium gas method. Äspö Hard Rock Laboratory, International Progress Report IPR-02-17, Svensk Kärnbränslehantering AB, Stockholm, Sweden

MacDonald, C. (1985) Mineralogy and geochemistry of the sub-Athabasca regolith near Wollaston Lake. MSc thesis, University of Saskatchewan

Mark, G., Phillips, G.N., & Pollard, P.J. (1998) Highly selective partial melting of pelitic gneiss at Cannington, Cloncurry district, Queensland. *Australian Journal of Earth Sciences*, 45(1), 169–176

Martin, C.D. (2007) Quantifying In-Situ Stress Magnitudes and Orientations for Forsmark, Forsmark Stage 2.2. SKB R-Report R-02-27. Swedish Nuclear Fuel and Waste Management Co., Stockholm, Sweden

Martin, C.D. & Stimpson, B. (1994) The effect of sample disturbance on laboratory properties of Lac du Bonnet granite. *Canadian Geotechnical Journal*, 31, 692–702

Mathieu, L. (2018) Quantifying Hydrothermal Alteration: A Review of Methods. *Geosciences*, 8, 245

Matsumoto, N., & Shigematsu, N. (2018) In-situ permeability of fault zones estimated by hydraulic tests and continuous groundwater-pressure observations. *Earth, Planets and Space*, 70(13), 1–12

Mazurek, M. (1998) Geology of the crystalline basement of northern Switzerland and derivation of geological input data for safety assessment models. Nagra, Technical Report 93-12, Wettingen, Switzerland

McGill, B.D., Marlat, J.L., Matthews, R.B., Sopuk, V.J., Homeniuk, L.A., & Hubregtse, J.J. (1993) The P2 North uranium deposit, Saskatchewan, Canada. *Exploration and Mining Geology*, 2(4), 321–331

McKeough, M.A., Lentz, D.R., McFarlane, C.R.M., & Brown, J. (2013) Geology and evolution of pegmatite-hosted U–Th ± REE–Y–Nb mineralization, Kulyk, Eagle, and Karin Lakes region, Wollaston Domain, northern Saskatchewan, Canada: examples of the dual role of extreme fractionation and hybridization processes. *Journal of Geosciences*, 58, 321–346

Meglis, I.L., Engelder, T., & Graham, E. (1991) The effect of stress-relief on ambient microcrack porosity in core samples from the Kent Cliffs (New York) and Moodus (Connecticut) scientific research boreholes. *Tectonophysics,* 186, 163–173

Meier, D.B., Waber, H.N., Gimmi, T., Eichinger, F., & Diamond, L.W. (2015) Reconstruction of in-situ porosity and porewater compositions of low-permeability crystalline rocks: Magnitude of artefacts induced by drilling and sample recovery. *Journal of Contaminant Hydrology,* 183, 55–71

Mercadier, J., Cuney, M., Cathelineau, M., & Lacorde, M. (2011) U redox fronts and kaolinisation in basement-hosted unconformity-related U ores of the Athabasca Basin (Canada): late U remobilisation by meteoric fluids. *Mineralia Deposita*, 46, 105–135

Mercadier, J., Richard, A., & Cathelineau, M. (2012) Boron-and magnesium-rich marine brines at the origin of giant unconformity-related uranium deposits: d11B evidence from Mg-tourmalines. *Geology*, 40(3), 231–234

Mercadier, J., Richard, A., Cathelineau, M., Boiron, M-C., Annesley, I.R., & Cuney, M. (2014) From sources to deposits: Recent advances about the unconformity-related U deposits.

Mesri, G. & Olson, R.E. (1971) Mechanisms controlling the permeability of clays. *Clays and Clay Minerals*, 19, 151–158

Milord, I., Sawyer, E.W., & Brown, M. (2001) Formation of diatexite migmatite and granite magma during anatexis of semi-pelitic metasedimentary rocks: an example from St. Malo, France. *Journal of Petrology*, 42, 487–505

Mitchell, T.M., & Faulkner, D.R. (2012) Towards quantifying the matrix permeability of fault damage zones in low porosity rocks. *Earth and Planetary Science Letters*, 339–340, 24–31

Mizoguchi, K., Hirose, T., Shimamoto, T., & Fukuyama, E. (2008) Internal structure and permeability of the Nojima fault, Southwest Japan. *Journal of Structural Geology*, 30, 513–524

Molz, F.J., Dinwiddie, C.L., & Wilson, J.L. (2003) A physical basis for calculating instrument spatial weighting functions in homogeneous systems. *Water Resources Research,* 39(4), 1–14

Mondol, N.H., Bjørlykke, K., Jahren, J., & Høeg, K. (2007) Experimental mechanical compaction of clay mineral aggregates—changes in physical properties of mudstones during burial. *Marine and Petroleum Geology*, 24, 289–311

Money, P.L. (1968) The Wollaston Lake fold-belt system, Saskatchewan-Manitoba. *Canadian Journal of Earth Sciences*, 5, 1489–1504

Morikiyo, T. (1986) Hydrogen and carbon isotope studies on the graphite-bearing metapelites in the northern Kiso district of central Japan. *Contributions to Mineralogy and Petrology*, 94, 165–177

Morrow, C., Lockner, D., & Hickman, S. (1994) Effects of lithology and depth on the permeability of core samples from the Kola and KTB drill holes. *Journal of Geophysical Research*, 899, 7263–7274

Morrow, C.A. (2000) Permeability of Deep Drillhole Core Samples. In: Ito, H., Fujimoto, K., Tanaka, H., and Lockner, D. (Eds.), Proceedings, International Workshop on the Nojima Fault Core and Borehole Data Analysis, Nov. 22-23, 1999, Tsukuba, Japan.

Morrow, C.A., & Lockner, D.A. (1994) Permeability differences between surface-derived and deep drillhole core samples. *Geophysical Research Letters*, 21(19), 2151–2154

Morrow, C.A., Lockner, D.A., Moore, D.E., & Hickman, S. (2014) Deep permeability of the San Andreas Fault from San Andreas Fault Observatory at Depth (SAFOD) core samples. *Journal of Structural Geology*, 64, 99–114

Morrow, C.A., Shi, L.Q., & Byerlee, J.D. (1984) Permeability of fault gouge under confining pressure and shear stress. *Journal of Geophysical Research*, 89, 3193–3200

National Research Council (1996) Rock Fractures and Fluid Flow: Contemporary Understanding and Applications. Committee on Fracture Characterization and Fluid Flow / U.S. National Committee for Rock Mechanics / Geotechnical Board / Board on Energy and Environmental Systems / Commission on Engineering and Technical Systems. National Academy Press, Washington, D.C. ISBN: 0-309-56348-8, 568 pp.

Nishimoto, S. , Yoshida, H., Asahara, Y., Tsuruta, T. Ishibashi, M., & Katsuta, N. (2014) Episyenite formation in the Toki granite, central Japan. *Contributions to Mineralogy and Petrology*, 167(960), 1–12

Nishimoto, S., & Yoshida, H. (2010) Hydrothermal alteration of deep fractured granite: Effects of dissolution and precipitation. *Lithos*, 115, 153–162

Niwa, M., Shimada, K., Tamura, H., Shibata, K., Sueoka, S., Yasue, K-I., Ishimaru, T., & Umeda, K. (2016) Thermal constraints on clay growth in fault gouge and their relationship with fault-zone evolution and hydrothermal alteration: case study of gouges in the Kojaku granite, central Japan. *Clays and Clay Minerals*, 64(2), 86–107

North, F. K. (1985) Petroleum Geology. Allen & Unwin, London, 607 p.

Numelin, T., Marone, C., & Kirby, E. (2007) Frictional properties of natural fault gouge from a low-angle normal fault, Panamint Valley, California. *Tectonics*, 26. TC2004

Ogata, K., Senger, K., Braathen, A., Tveranger, J., & Olaussen, S. (2014) Fracture systems and mesoscale structural patterns in the siliciclastic Mesozoic reservoir-caprock succession of the Longyearbyen CO2 Lab project: Implications for geological CO2 sequestration in Central Spitsbergen, Svalbard. *Norwegian Journal of Geology*, 94, 121–154

Olsen, H.W. (1960) Hydraulic flow through saturated clays. *Clays and Clay Minerals*, 11, 131–161

Parslow, G.R., Brandstätter, F., Kurat, G., & Thomas, D.J. (1985) Chemical ages and mobility of U and Th in anatectites of the Cree Lake Zone, Saskatchewan. *Canadian Mineralogist*, 23, 543–551

Pattison, D.R.M. (2006) The fate of graphite in prograde metamorphism of pelites: An example from the Ballachulish aureole, Scotland. *Lithos*, 88, 85–99

Peacock, D.C.P., Dimmen, V., Rotevatn, A., & Sanderson, D.J. (2017) A broader classification of damage zones. *Journal of Structural Geology*, 102, 179–192

Pennacchioni, G., Ceccato, A., Fioretti, A.M., Mazzoli, C., Zorzi, F., & Ferretti, P. (2016) Episyenites in meta-granitoids of the Tauern Window (Eastern Alps):unpredictable? *Journal of Geodynamics*, 101, 73–87

Persoff, P., & Hulen, J.B. (2001) Hydrologic characterization of reservoir metagraywacke from shallow and deep levels of The Geysers vapor-dominated geothermal system, California, USA. *Geothermics*, 30, 169–192

Petersson, J., Stephens, M.B., Mattsson, H., & Möller, C. (2012) Albitization and quartz dissolution in Paleoproterozoic metagranite, central Sweden — Implications for the disposal of spent nuclear fuel in a deep geological repository. *Lithos*, 148, 10–26

Plumper, O., & Putnis, A. (2009) The Complex Hydrothermal History of Granitic Rocks: Multiple Feldspar Replacement Reactions under Subsolidus Conditions. *Journal of Petrology* 50(5), 967–987

Potter, E.G., & Wright, D.M. (2015) TGI-4 Unconformity-related Uranium Deposits Synthesis: Tools to Aid Deep Exploration and Refine the Genetic Model, in Targeted Geoscience Initiative 4: unconformity-related uranium systems, (ed.) E.G. Potter and D.M. Wright. Geological Survey of Canada, Open File 7791, 1–13

Price, J.D., Wark, D.A., Watson, E.B., & Smith, A.M. (2006) Grain-scale permeabilities of faceted polycrystalline aggregates. *Geofluids*, 6, 302–318

Putnis, A., & Austrheim, H. (2010) Fluid-induced processes: metasomatism and metamorphism. *Geofluids*, 10, 254–269

Rabiei, M., Chi, G., & Normand, C. (2015) Field and petrographic investigations of the Maw Zone REE deposit, Athabasca Basin, Saskatchewan; in Summary of Investigations 2015, Volume 2, Saskatchewan Geological Survey, Saskatchewan Ministry of the Economy, Miscellaneous Report 2015-4.2, Paper A-7, 16p.

Rainbird, R.H., Stern, R.A., Rayner, N., & Jefferson, C.W. (2007) Age, provenance, and regional correlation of the Athabasca Group, Saskatchewan and Alberta, constrained by igneous and detrital zircon geochronology. In EXTECH IV Geology and Uranium EXploration TECHnology of the Proterozoic Athabasca Basin, Saskatchewan and Alberta. Edited by C.W. Jefferson and G. Delaney. Geological Survey of Canada, Bulletin, 588 (also Saskatchewan Geological Society, Special Publication 17; Geological Association of Canada, Mineral Deposits Division, Special Publication 4)

Ramaekers, P. (1990) Geology of the Athabasca Group (Hehkian) in Northern Saskatchewan: Saskatchewan Energy and Mines, Saskatchewan Geological Survey, Report 195, 49 p.

Ramaekers, P. (2004) Development, stratigraphy and summary diagenetic history of the Athabasca Basin, early Proterozoic of Alberta and its relation to uranium potential. EUB/AGS Special Report 62, Alberta Energy and Utilities Board, Edmonton, Alberta

Ramaekers, P., Jefferson, C.W., Yeo, G.M., Collier, B., Long, D.G.F., Drever, G., McHardy, S., Jiricka, D., Cutts, C., Wheatley, K., Catuneanu, O., Bernier, S., Kupsch, B., R.T., & Post, R.T. (2007) Revised geological map and stratigraphy of the Athabasca Group, Saskatchewan and Alberta. Geological Survey of Canada, Bulletin 588, 155–190

Renac, C., Kyser, T.K., Durocher, K., Dreaver, G., & O'Connor, T. (2002) Comparison of diagenetic fluids in the Proterozoic Thelon and Athabasca Basins, Canada: implications for protracted fluid histories in stable intracratonic basins. *Canadian Journal of Earth Sciences*, 39, 113–132

Renard, P., & Allard, D. (2013) Advances in Water Resources. *Advances in Water Resources*, 51, 168–196

Rice, J. (1992) Fault stress states, pore pressure distributions, and the weakness of the San Andreas Fault. In: Evans, B., Wong, T.-f. (Eds.), Fault Mechanics and Transport Properties of Rocks. Academic Press, San Diego, CA. 69-88

Rogiers, B., Beerten, K., Smeekens, T., Mallants, D., Gedeon, M., Huysmans, M., Batelaan, O., & Dassargues, A. (2014a) The usefulness of outcrop analogue air permeameter measurements for analyzing aquifer heterogeneity: quantifying outcrop hydraulic conductivity and its spatial variability. *Hydrological Processes*, 28, 5176–5188

Roscoe Postle Associates Inc. (2016) Technical Report On The Rook I Property, Saskatchewan, Canada. NI 43-101 Report. Prepared by Mathisen, M.B., and Ross, D.A., April 13, 2016, Toronto, Ontario

Rossi, M., Rolland, Y., Vidal, O., & Cox, S.F. (2005) Geochemical variations and element transfer during shear-zone development and related episyenites at middle crust depths: insights from the Mont Blanc granite (French – Italian Alps). In: Bruhn, D. and Burlini, L. (eds), High-Strain Zones: Structure and Physical Properties. Geological Society, London, *Special Publications*, 245, 373–396

Ruth, D.W., & Kenny, J. (1989) The unsteady-state gas permeameter. *Journal of Canadian Petroleum Technology*, 28, 67–72

Sahimi, M. (2011) Flow and Transport in Porous Media and Fractured Rock, From Classical Methods to Modern Approaches. 2nd Edition, WILEY-VCH Verlag GmbH & Co. KGaA, Weinheim, Germany

Sammaljärvi, J., Lindberg, A., Voutilainen, M., Voutilainen, M., Ikonen, J., Siitari-Kauppi, M., Pitkänen, P., & Koskinen, L. (2017) Multi-scale study of the mineral porosity of veined gneiss and pegmatitic granite from Olkiluoto, Western Finland. *Journal of Radioanalytical and Nuclear Chemistry*, 314(3), 1557–1575

Sampath, K., & Keighin, C. (1982) Factors affecting gas slippage in tight sandstones of cretaceous age in the Uinta basin. *Journal of Petroleum Technology*, 34(11), 2715–2720

Sausse, J., & Genter, A. (2005) Types of permeable fractures in granite. In: Harvey PK, Brewer TS, Pezard PA, Petrov VA (eds.) (2005) Petrophysical Properties of Crystalline Rocks. Geological Society, London, *Special Publications*, 240, 1–14

Schild, M., Siegesmund, S., Vollbrecht, A., & Mazurek, M. (2001) Characterization of granite matrix porosity and pore-space geometry by in situ and laboratory methods. *Geophysical Journal International*, 146, 111–125

Scholz, C.H. & Anders, M.H. (1994) The permeability of faults. p.247-253, In: Hickman, S.H., Sibson, R., Bruhn, R. (Eds.), *The Mechanical Involvement of Fluids in Faulting*. Open File Report 94-228, U.S. Geological Survey

Scibek, J. (2019 submitted - a) Multidisciplinary database of permeability of fault zones and surrounding protolith rocks at world-wide sites. Submitted to *Scientific Data*

Scibek, J., Gleeson T., & McKenzie J.M. (2016) The biases and trends in fault zone hydrogeology conceptual models: global compilation and categorical data analysis.

Geofluids, 16, 782–798

Scibek, J., Gleeson, T., Ingebritsen, S., & McKenzie, J. (2019 submitted - b) The bulk permeability of fault rocks and protolith in Earth's brittle crust: Insights from statistical analysis of the first global database. Submitted to *Journal of Geophysical Research*

Shabelansky, A.H., Bernabe, Y., Mok, U., & Evans, J.B. (2014) Temperature influence on permeability of Sioux quartzite containing mixtures of water and carbon dioxide. *International Journal of Rock Mechanics & Mining Sciences*, 70, 546–551

Shanks III, W.C.P. (2012) Hydrothermal alteration in volcanogenic massive sulfide occurrence model. U.S. Geological Survey Scientific Investigations Report 2010–5070–C, chapter 11, 12 p.

Sharp Jr, J.M., Fu, L., Cortez, P., & Wheeler, E. (1994) An electronic minipermeameter for use in the field and laboratory. *Groundwater*, 32(1), 41–46

Shigematsu, N., Fujimoto, K., Tanaka, N., Furuya, N., Mori, H., & Wallis, S. (2012) Internal structure of the Median Tectonic Line fault zone, SW Japan, revealed by borehole analysis. *Tectonophysics*, 532-535, 103–118

Sibbald, T.L.L. (1985) Geology and genesis of the Athabasca Basin uranium deposits; in Summary of Investigations 1985. Saskatchewan Geological Survey; Saskatchewan Energy and Mines, Miscellaneous Report 85-4

Sibson, R.H. (1977) Fault rocks and fault mechanisms. *Journal of the Geological Society of London*, 133, 191–213

Sibson, R.H. (1986) Earthquakes and rock deformation in crustal fault zones. Annual *Reviews of Earth and Planetary Sciences*, 14, 149–175

Sibson, R.H. (2000) Fluid involvement in normal faulting. *Journal of Geodynamics*, 29, 469–499

Sibson, R.H., Robert, F., & Poulsen, K.H. (1988) High-angle reverse faults, fluid pressure cycling and mesothermal gold-quartz deposits. *Geology*, 16, 551–555

Siitari-Kauppi, M., Ikonen, J. & Kauppi, I., & Lindberg, A. (2010) Investigation of Porosity and Pore Structure Adjacent to Fractures by PMMA Method; Samples Taken from Drill Cores at Olkiluoto. Working Report 2010-66, Posiva Oy, Eurajoki, Finland

Solum, J.G., Van der Pluijm, B.A., Peacor, D.R., & Warr, L.N. (2003) Influence of phyllosilicate mineral assemblages, fabrics, and fluids on thebehavior of the Punchbowl fault, southern California. *Journal of Geophysical Research*, 108(B5), 2233

Sopuck, V.J,, de Carla, A., Wray, E.M., & Cooper, B. (1983) The application of lithogeochemistry in the search for unconformity-type uranium deposits, Northern Saskatchewan, Canada. *Journal of Geochemical Exploration*, 19, 77–99

Spear, F.S., Kohn, M.J., & Cheney, J.T. (1999) P-T paths from anatectic pelites. *Contributions to Mineralogy and Petrology*, 134, 17–32

SRK Consulting Inc. (2015a) Structural Review of the Gryphon and Phoenix deposits. Report Prepared for Denison Mines Corp. June 7, 2016 version. (unpublished consulting report)

SRK Consulting Inc. (2015b) Gryphon alteration study. Report prepared for Denison Mines Corp. (eds.) Fonseca, A., Siddorn, J., Toronto, Ontario. July 12, 2015 (unpublished consulting report)

SRK Consulting Inc. and RPA Inc. (2018) technical report with an updated mineral resource estimate for the Wheeler River property. March 15, 2018. Report to Denison Mines Corp. by SRK Consulting (Canada) Inc., and Roscoe Postle Associates Inc. Published online as: SEC Info - Denison Mines Corp. - ‘6-K’ for 3/16/18 - ‘EX-99.2’

Stephens, M.B., Fox, A., Simeonov, A., Isaksson, H., Hermanson, J., and Öhman, J. (2007) Geology Forsmark. Site Descriptive Modelling. Forsmark Stage 2.2. Report SKB R-07-45, Svensk Kärnbränslehantering AB, Sweden

Stober, I., & Bucher, K. (2007). Hydraulic properties of the crystalline basement. *Hydrogeology Journal*, 15, 213–224

Surma, F., Geraud, Y., & Pezard, P. (2003) Porosity Network of the Nojima Fault Zone in the Hirabayashi Hole (Japan). EGS – AGU – EUG Joint Assembly, Abstracts from the meeting held in Nice, France, 6–11 April 2003, abstract #12946

Sutherland, W.J., Halvorsen, C., Hurst, A., McPhee, C.A., Robatson, G., Whattler, P.R., & Worthington, P.F. (1993) Recommended practice for probe permeametry. *Marine and Petroleum Geology*, 10(4), 309–317

Takagi, H., Takahashi, K., Shimada, K., Tsutsui, K., Miura, R., Kato, N., & Takizawa, S. (2012) Integrated estimates of the thickness of the fault damage zone in granitic terrain based on penetrative mesocracks and XRD analyses of quartz. *Journal of Structural Geology*, 35, 64–77

Tanaka, H., Fujimoto, K., Ohtani, T., & Ito, H. (2001) Structural and chemical characterization of shear zones in the freshly activated Nojima Fault, Awaji Island, Southwest Japan. *Journal of Geophysical Research*, 106, 8789–8810

Tanikawa, W., & Shimamoto, T. (2006) Klinkenberg effect for gas permeability and its comparison to water permeability for porous sedimentary rocks. *Hydrological and Earth Systems Science Discuss*ions, 3, 1315–1338

Tartakovsky, D.M., Moulton, D.J., & Zlotnik, V.A. (2000) Kinematic structure of minipermeameter flow. *Water Resources Research*, 36(9), 2433–2442

Thomas, D., Aubin, A., Brisbin, D., Mukwakwami, J., Yang, H., & Zaluski, G. (2014) Fault Architecture, Associated Structures and Uranium Mineralization, Eastern Athabasca Basin. Cameco Corp., SGS Open House Dec 2014, Presentation report. 31pp. (http://publications.gov.sk.ca/documents/310/95089-4_Thomas_Open_House_2014.pdf)

Tidwell, V.C. and Wilson, J.L. (1997) Laboratory method for investigating permeability upscaling. *Water Resources Research*, 33(7), 1607–1616

Tidwell, V.C., Gutjahr, A.L., and Wilson, J.L. (1999) What does an instrument measure? Application of linear filter theory to characterize minpermeameter tests. *Water Resources Research*, 35, 43–54

Tourigny, G., Wilson, S, Breton, G, and Portella, P. (2001) Structural control and emplacement of uranium mineralization at the Sue C deposit, McClean Lake operation, northern Saskatchewan. In: Summary of Investigations 2001, Vol. 2, Saskatchewan Geological Survey, Saskatchewan Ministry of Energy and Resources, Misc. Report 2010-4.2

Tourigny, G., Quirt, D.H., Wilson, N.S.F., Wilson, S., Breton, G., and Portella, P. (2007) Geological and structural features of the Sue C uranium deposit, McClean Lake area, Saskatchewan; in EXTECH IV: Geology and Uranium EXploration TECHnology of the Proterozoic Athabasca Basin, Saskatchewan and Alberta, (ed.) C.W. Jefferson and G. Delaney; Geological Survey of Canada, Bulletin 588, p. 229–247 (also Saskatchewan Geological Society, Special Publication 18; Geological Association of Canada, Mineral Deposits Division, Special Publication 4)

Townend, J., and Zoback, M.D. (2000) How faulting keeps the crust strong. *Geology*, 28, 399–402

Tran, H.T. (2001) Tectonic evolution of the Paleoproterozoic Wollaston Group in the Cree Lake Zone, Northern Saskatchewan, Canada. Ph.D. Thesis, University of Regina, Regina, Canada

Tremblay, LP. (1982) Geology of the uranium deposits related to the sub-Athabasca unconformity, Saskatchewan, Canada. Geological Survey of Canada, Paper 81-20, 56p.

Tuisku, P., and Karki, A. (2010) Metamorphic Petrology of Olkiluoto. Working Report 2010-54, June 2010, Posiva Oy, Olkiluoto, Finland

Tullborg, E-L. and Larson, S.A. (2006) Porosity in crystalline rocks – A matter of scale. *Engineering Geology*, 84, 75–83

Volkert, R.A., and Drake, A.A., Jr. (1999) Geochemistry and stratigraphic relations of Middle Proterozoic rocks of the New Jersey Highlands. In Geologic studies in New Jersey and eastern Pennsylvania. Edited by A.A. Drake, Jr. United States Geological Survey, Professional Paper 1565-C

Volkert, R.A., Johnson, C.A., and Tamashausky, A.V. (2000) Mesoproterozoic graphite deposits, New Jersey Highlands: geologic and stable isotopic evidence for possible algal origins. *Canadian Journal of Earth Sciences*, 37, 1665–1675

Voutilainen, M., Myllys, M., and Timonen, J. (2009) Structural and Transport Properties of Illitized Samples from Drillhole OL-KR12 in Olkiluoto: Porosity, Diffusion Coefficient, Permeability and Tomographic Imaging. Working Report 2009-80. Posiva Oy, Eurajoki, Finland

Waber, H.N., Gimmi, T., and Smellie, J.A.T. (2009) Porewater in the rock matrix Site descriptive modelling SDM-Site Forsmark. SKB Report R-08-105, Swedish Nuclear Fuel and Waste Management Co., Stockholm, Sweden

Waber, H.N., Gimmi, T., and Smellie, J.A.T. (2009) Porewater in the rock matrix Site descriptive modelling SDM-Site Forsmark. SKB Report R-08-105, Swedish Nuclear Fuel and Waste Management Co., Stockholm, Sweden

Waber, H.N., Gimmi, T., and Smellie, J.A.T. (2011) Effects of drilling and stress release on transport properties and porewater chemistry of crystalline rocks. *Journal of Hydrology,* 405, 316–332

Wallace, A.R., and Karlson, R.C. (1985) The Schwartzwalder uranium deposit, I: Geology and structural controls on mineralization. *Economic Geology*, 80(7), 1842–1857

Wallis, R.H. (1971) The geology of the Hidden Bay area, Saskatchewan. Department of Mineral Resources, Geological Sciences Branch, Report No. 137

Wang, K. (2016) A Study of Petrography, Fluid Inclusions and Graphite Alteration of the Phoenix Uranium Deposit, Athabasca Basin, Northern Saskatchewan, Canada. MSc Thesis, University of Regina, Regina, Saskatchewan

Wark, D.A., and Watson, E.B. (1998) Grain-scale permeabilities of texturally equilibrated, monomineralic rocks. *Earth and Planetary Science Letters*, 164, 591–605

Wibberley, C.A.J., and Shimamoto, T. (2003) Internal structure and permeability of major strike-slip fault zones: the Median Tectonic Line in Mie Prefecture, Southwest Japan. *Journal of Structural Geology*, 25, 59–78

Wilde, A.R. and Wall, V.J. (1987) Geology of the Nabarlek Uranium Deposit, Northern Territory, Australia. *Economic Geology*, 82, 1152–1168

Woodcock, N.H., and Mort, K. (2008) Classification of fault breccias and related fault rocks. *Geological Magazine*, 145(3), 435–440

Worden, R.H., F. Walker, F.D., Parsons, I., and Brown, W.L. (1990) Development of microporosity, diffusion channels and deuteric coarsening in perthitic alkali feldspars. *Contributions of Mineralogy and Petrology*, 104, 507–515

Wu, F.T., Robertson, H.E., Wang, C-Y., and Mao, N.H. (1979) Fault zones, gouge and mechanical properties of clays under high pressure. In: Proceedings of Conference VIII - Analysis of Actual Fault Zones in Bedrock. U.S. Geological Survey Open-File Report 79-1239 (https://pubs.usgs.gov/of/1979/of79-1239/Chapters/CH2-04.PDF)

Xue, L., Li, H.B., Brodsky, E.E., Xu, Z.Q., Kano, Y., Wang, H., Mori, J.J., Si, J.L., Pei, J.L., Zhang, W., Yang, G., Sun, Z.M., and Huang, Y. (2013) Continuous permeability measurements record healing inside the Wenchuan Earthquake Fault Zone. *Science*, 340(6140), 1555–1559

Yamamoto, H., Terabayashi, M., Oasa, H., Kaneko, Y., Anma, R. (2004) Competence contrast between pelitic schist and silicified pelitic schist in the Iwakuni-Yanai area of the Ryoke Belt, southwest Japan. *Journal of Geological Society of Japan*, 110(2), 119–122

Yamashita, T., and Tsutsumi, A. (2018) Involvement of Fluids in Earthquake Ruptures. Field/Experimental Data and Modeling. Springer Japan KK 2018. DOI 10.1007/978-4-431-56562-8

Yeo, G.M., and Delaney, G. (2007) The Wollaston Supergroup, Stratigraphy and Metallogeny of a Paleoproterozoic Wilson Cycle in the TransHudson Orogeny, Saskatchewan. In: Jefferson, C.W. and Delaney, G. (Eds.), EXTECH IV: Geology and Uranium Exploration Technology of the Proterozoic Athabasca Basin, Saskatchewan and Alberta. *Geological Survey of Canada Bulletin*, 588, 89–117

Zhang, G., Wasyluk, K. and Pan, Y. (2001) The characterization and quantitative analysis of clay minerals in the Athabasca Basin, Saskatchewan: Application of shortwave infrared reflectance spectroscopy. *The Canadian Mineralogist*, 39, 1347–1363

Zoback, M.D., and Byerlee, J.D. (1975) The effect of microcrack dilatancy on the permeability of Westerly granite. *Journal of Geophysical Research*, 80(5), 752–755

8 Conclusion and summary

From the bulk permeability values, mostly from *in situ* drillhole tests, the depth-distribution of permeability was described. The trends of decreasing permeability with depth are weak (low correlation) in the metamorphic/plutonic rocks. In the upper few kilometres of the crust, fault zones serve as fluid conduits (bulk permeability $>10^{-17}$ m^2 threshold).

The distribution of world-wide values, when compared to the geothermal-metamorphic curve that represents the trend for time-averaged metamorphic fluid fluxes, is consistent with the trend over depth in fault zone permeability. It is not consistent with the protolith permeability alone, which also has a decreasing trend with depth. This finding implies that fault zones control and serve as large-scale fluid conduits through the metamorphic crust in tectonically active regions at least. The conduit magnitude of a fault zone can be expressed as the ratio of permeability of fault damage zone (or fault zone in general) to the protolith. This ratio value is on average +2 to +3 orders of magnitude, and peaks at shallow depths 0-3 km in the available data. The patterns raise questions about permeability-maintenance processes at different depths, and the role of cool meteoric waters in the upper 3km depth.

My research found a significant and relatively good correlation (r^2 = 0.5 to 0.8) between the bulk permeability of fault zone (mostly the damage zone) and the surrounding protolith in most rock types considered here, but not in coarse siliciclastics (e.g. sandstone filled basins). Such empirical relationship may be used to predict the permeability of fault zones from the permeability of the protoliths and depth in the brittle crust, in absence of other data. Over 50% of the variation can be predicted, according to the data presented here.

In the field-tested fault zone under the Athabasca Basin there was a large variability of results, but also clear differences in value ranges and mean values for the fault damage zone, fault core zone and the protolith. The fractured fault damage zone accounts for most of the transmissivity (67%), and another large component (30%) is attributed to hydrothermally altered matrix of host rock in the wide damage zone. This enhanced porosity from rock alteration acts to magnify the conduit of the damage zone. In total, the relatively permeable fault core zone (multiple strands of faults) are now, and have been in the past, a conduit to fluid flow, but in total account only for 2.5% of the transmissivity in the fault zone.

The ability to separate the permeability and transmissivity into components within highly heterogeneous fault zone is a step forward in understanding the permeability structure, but it requires a large number of tests, such as presented here. A small number of tests, as is usually published at other research sites, may seriously underestimate the transmissivity of the fault zone and not capture the variability of permeability distribution, at least not enough to define statistical distributions. The testing of fault zones at 500 to 1000 m depths is particularly advantageous, in that the effects of surficial weathering are avoided. The drillcore samples can be tested without confinement without large loss of accuracy of results to produce large number of measurements rapidly and affordably, the heterogeneity of fault zone can be adequately tested from 10 cm to km scale. Another advantage is the macroscopic dominant flow paths and porous features can be tested directly, without further coring and damage to the drillcore, and not biasing the results on only the most competent rock samples. It is also important that the drillcore can be extracted using small mineral exploration drill rigs, and that the hundreds or thousands of kilometres of exploration drillcore that is produced annually may be used for research on fault zone hydrogeology.

The Gryphon fault zone is an ancient fault zone that experienced peak activity, presumably, hundreds of millions of years ago and formed at several kilometres deeper than is found at present. The fault rocks and the damage zone appear remarkably preserved under the 500 m cover of the remaining sedimentary rocks in the once deeper basin. The permeability distribution is also very similar to the sparsely tested Median Tectonic Line, one of the largest active faults in Japan at present, of similar geology and damage zone width, and similar permeability distribution. This result suggests that present-day permeability of fault zones, where adequately "preserved", offers insights into past fluid flow, and paleo-permeability, directly.

9 References

The reference list here is for the introductory chapters 1 and 2, and not the individual articles. Separate reference lists are given within each journal article in chapters 3 to 7.

Achtziger-Zupancic, P., Loew, S. & Mariéthoz, G. (2017) A new global database to improve predictions of permeability distribution in crystalline rocks at site scale. *Journal of Geophysical Research Solid Earth,* 122(5), 3513–3539

Annesley, I. R., Madore, C., & Portella, P. (2005) Geology and thermotectonic evolution of the western margin of the Trans-Hudson Orogen: evidence from the eastern sub-Athabasca basement, Saskatchewan. *Canadian Journal of Earth Sciences*, 42, 573–597

Atomic Energy Control Board (1986) A compilation of subsurface hydrogeologic data, Volume I - Main Report. Research Report by GTC Geologic Testing Consultants to Atomic Energy Control Board, INFO-0203-2, Ottawa, Ontario, Canada

Balsamo, F., & Storti, F. (2010) Grain size and permeability evolution of soft-sediment extensional sub-seismic and seismic fault zones in high-porosity sediments from the Crotone basin, southern Apennines, Italy. *Marine and Petroleum Geology*, 27, 822–837

Becker, K., Morin, R.H., and Davis, E.E. (1994) Permeabilities in the Middle Valley hydrothermal system measured with packer and flowmeter experiments. Chapter 39 In: Mottl, M.J., Davis, E.E., Fisher, A.T., and Slack, J.F. (Eds.), 1994 Proceedings of the Ocean Drilling Program, Scientific Results, 139, 613-626

Bickford, M.E., Collerson, K.D., Lewry, J.F., Van Schmus, W.R., & Chiarenzelli, J.R. (1990) Proterozoic collisional tectonism in the Trans-Hudson Orogen, Saskatchewan. *Geology*, 18, 14–18

Bodvarsson, M. G. & Benson, M. (1982) Well Test Data From Geothermal Reservoirs. Report LBL-13295, Lawrence Berkeley Laboratory, Berkeley, California

Bossart, P., & Mazurek, M. (1991) Grimsel Test Site – Structural geology and water flowpaths in the migration shear zone. Nagra Tech. Report NTB 91-12. Nagra, Wettingen, Switzerland

Brace, W. F. (1980) Permeability of Crystalline and Argillaceous Rocks. *International Journal of Rock Mechanics and Mining Sciences & Geomechanics Abstracts,* 17(5), 241–251

Bryan, K. (1919) Classification of springs. *The Journal of Geology*, 27(7), 522–561

Caine, J. S., Evans, J. P. & Foster, C. B. (1996) Fault zone architecture and permeability structure. *Geology*, 24, 1025–1028

Chester, F. M. & Logan, J. M. (1986) Implications formechanical properties of brittle faults from observations of the Punchbowl fault zone, California. *Pure and Applied Geophysics*, 124, 80–106

Choi, J-H., Edwards, P., Ko, K., & Kim, Y-S (2016) Definition and classification of fault damage zones: A review and a new methodological approach. *Earth-Science Reviews*, 152, 70–87

Curewitz, D. & Karson, J. A. (1997) Structural settings of hydrothermal outflow: Fracture permeability maintained by fault propagation and interaction. *Journal of Volcanology and Geothermal Research*, 79, 149−168

Denison Mines (2018) Pre-feasibility Study for the Wheeler River Uranium Project, Saskatchewan, Canada. NI 43-101 Technical Report for the Wheeler River project, October 30, 2018. www.sec.gov/edgar.shtml

Engelder, J.T. (1974) Cataclasis and the generation of fault gouge. *Geological Society of America Bulletin*, 85, 1515−1522

Evans, J.P. (1988) Deformation mechanisms in granitic rocks at shallow crustal levels. *Journal of Structural Geology*, 10(5), 437−443

Evans, J.P., Forster, C.B., Goddard, J.V. (1997) Permeability of fault-related rocks, and implications for hydraulic structure of fault zones. *Journal of Structural Geology*, 19(11), 1393−1404

Faulkner, D.R., Jackson, C.A.L., Lunn, R.J., Schlische, R.W., Shipton, Z.K., Wibberley, C.A.J., & Withjack, M.O. (2010) A review of recent developments concerning the structure, mechanics and fluid flow properties of fault zones. *Journal of Structural Geology* , 32, 1557–1575

Fisher, A.T. (1998) Permeability within basaltic oceanic crust. *Reviews of Geophysics*, 36(2), 143–182

Flodin, E.A. (2003) Structural Evolution, Petrophysics, and Large-Scale Permeability of Faults in Sandstone, Valley of Fire, Nevada. Ph.D. Thesis, Stanford University, California

Gleeson, T., Smith, L., Moosdorf, N., Hartmann, J., Durr, H.H., Manning, A.H., van Beek, L.P.H., & Jellinek, A.M. (2011) Mapping permeability over the surface of the Earth. *Geophysical Research Letters*, 38, L02401

Gomila, R., Arancibia, G., Mitchell, T. M., Cembrano, J. M., Faulkner, D. R. (2016) Paleopermeability structure within fault-damage zones: A snap-shot from microfracture analyses in a strike-slip system. *Journal of Structural Geology* , 83, 103–120

Howald, T., Person, M., Campbell, A., Lueth, V., Hofstra, A., Sweetkind, D., Gable, C.W., Banerjee, A., Luijendijk, E., Crossey, L., Karlstrom, K., Kelley, S., & Phillips, F.M. (2015) Evidence for long timescale (>10^3 years) changes in hydrothermal activity induced by seismic events. *Geofluids*, 15, 252–268

Ingebritsen, S.E., & Manning, C.E. (2010) Permeability of the continental crust: dynamic variations inferred from seismicity and metamorphism. *Geofluids*, 10, 193–205

Jeanneret, P., Goncalves, P., Durand, C., Trap, P., Marquer, D., Quirt, D., and Ledru, P. (2016) Tectono-metamorphic evolution of the pre-Athabasca basement within the Wollaston–Mudjatik Transition Zone, Saskatchewan. *Canadian Journal of Earth Sciences*, 53, 231–259

Johri, M., Zoback, M. D. & Hennings, P. (2014) A scaling law to characterize fault-damage zones at reservoir depths. *AAPG Bulletin*, 98(10), 2057–2079

Jolley, S. J., Fisher, Q. J., Ainsworth, R. B., Vrolijk, P. J. & Delisle, S. (Eds.) (2010) Reservoir Compartmentalization. Geological Society Special Publication 347

Karasaki, K., Onishi, T., Doughty, C., Conrad, M., Gasperikova, E., Cook, P., & Ulrich, C. (2012) Development of a Hydrologic Characterization Technology for Fault Zones. Report LBNL-5862E, Lawrence Berkeley National Laboratory. Available on www since 2014 from University of California [http://escholarship.org/uc/item/3j52x603]

Kassoy, D. R. & Zebib, A. (1978) Convection fluid dynamics in a model of a fault zone in the earth's crust. *Journal of Fluid Mech*anics, 88(4), 789–792

Kerrich, R. (1986) Fluid infiltration into fault zones: chemical, isotopic, and mechanical effects. *PAGEOPH*, 124(1/2), 225–268

Kitagawa, Y., & Kano, Y. (2016) Changes in permeability of the Nojima fault damage zone inferred from repeated water injection experiments. *Earth, Planets and Space*, 68, 185-194

Lockner, D., Tanaka, H., Ito, H., Ikeda, R., Omura, K., & Naka, H. (2009) Geometry of the

Nojima fault at Nojima-Hirabayashi, Japan – I. A simple damage structure inferred from borehole core permeability. *Pure and Applied Geophysics*, 166, 1649–1667

Louderback, G. D. (1950) Faults And Engineering Geology. In: Application of Geology to Engineering Practice, Vol. 1, 125–150, Geological Society of America, Berkeley

Manning, C. E. & Ingebritsen, S. E. (1999) Permeability of the continental crust: The implications of geothermal data and metamorphic systems. *Reviews of Geophysics*, 37, 127–150

Ingebritsen, S. E. & Manning, C.E. (2010) Permeability of the continental crust: dynamic variations inferred from seismicity and metamorphism. *Geofluids*, 10, 193–205

Masset, O. & Loew, S. (2010) Hydraulic conductivity distribution in crystalline rocks, derived from inflows to tunnels and galleries in the central Alps, Switzerland. *Hydrogeology Journal*, 18, 863–891

Matonti, C., Lamarche, J., Guglielmi, Y., Marie, L. (2012) Structural and petrophysical characterization of mixed conduit/seal fault zones in carbonates: Example from the Castellas fault (SE France). *Journal of Structural Geology,* 39, 103–121

Meinzer, O.E. (1923) The Occurrence of Ground Water in the United States with a Discussion of Principles. Ph.D. Dissertation, reprinted from USGS Water Supply Paper 489. The University of Chicago Libraries, Illinois

Michie, E.A.H. & Haines, T.J. (2016) Variability and heterogeneity of the petrophysical properties of extensional carbonate fault rocks, Malta. *Petroleum Geoscience*, 22, 136–152

Mitchell, T. M. & Faulkner D. R. (2012) Towards quantifying the matrix permeability of fault damage zones in low porosity rocks. *Earth and Planetary Science Letters,* 339–340, 24–31

Mizoguchi, K., Hirose, T., Shimamoto, T., & Fukuyama, E. (2008). Internal structure and permeability of the Nojima fault, Southwest Japan. *Journal of Structural Geology*, 30, 513–524

National Research Council (1996) Rock Fractures and Fluid Flow: Contemporary Understanding and Applications. Committee on Fracture Characterization and Fluid Flow / U.S. National Committee for Rock Mechanics / Geotechnical Board / Board on Energy and Environmental Systems / Commission on Engineering and Technical Systems. National

Academy Press, Washington, D.C. ISBN: 0-309-56348-8, 568 pp.

Newhouse, W. H. (1942) Ore Deposits As Related To Structural Features. Princeton University Press, Princeton, N. J.

Okubo, C. H. (2012) Spatial distribution of damage around faults in the Joe Lott Tuff Member of the Mount Belknap Volcanics, Utah: A mechanical analog for faulting in pyroclastic deposits on Mars. *Journal of Geophysical Research,* 117, E08003

Pope, E. C., Bird, D.K., Arnorsson, S. & Giroud, N. (2016) Hydrogeology of the Krafla geothermal system, northeast Iceland. *Geofluids,* 16, 175–197

Ranjram, M., Gleeson, T. & Luijendijk, E. (2015) Is the permeability of crystalline rock in the shallow crust related to depth, lithology or tectonic setting? *Geofluids*, 15, 106–119

Rice, J. (1992) Fault stress states, pore pressure distributions, and the weakness of the San Andreas Fault. In: Evans, B. & Wong, T-f. (Eds.), *Fault Mechanics and Transport Properties of Rocks*. Academic Press, San Diego, California, p.69–88

Rowland, J. V., & Simmons, S. F. (2012) Hydrologic, magmatic, and tectonic controls on hydrothermal flow, Taupo Volcanic Zone, New Zealand: implications for the formation of epithermal vein deposits. *Economic Geology*, 107, 427–457

Rutqvist, J. (2017) Fractured rock stress–permeability relationships from in situ data and effects of temperature and chemical–mechanical couplings. *Geofluids*, 15, 48–66

Savage, H. M., and Brodsky, E. E. (2011) Collateral damage: Evolution with displacement of fracture distribution and secondary fault strands in fault damage zones. Journal of Geophysical Research, 116, B03405

Scholz, C. H. & Anders, M. H. (1994) The permeability of faults. In: Hickman, S.H., Sibson, R., Bruhn, R. (Eds.), The Mechanical Involvement Of Fluids In Faulting. Open File Report 94-228, U.S. Geological Survey, p.247–253

Seeburger, D.A. (1981) Studies of natural fractures, fault zone permeability, and a pore space-permeability model. Ph.D. Thesis (reprinted from Stanford Rock Physics Report #11), Stanford University, California

Seeburger, D.A. and Zoback, M.D. (1982) The distribution of natural fractures and joints at depth in crystalline rock. *Journal of Geophysical Research*, 87(B7), 5517–5534

Shigematsu, N., Fujimoto, K., Tanaka, N., Furuya, N., Mori, H., Wallis, S. (2012) Internal structure of the Median Tectonic Line fault zone, SW Japan, revealed by borehole analysis. *Tectonophysics*, 532-535, 103–118

Shipton, Z. K., Evans, J. P., Robeson, K. R., Forster, C. B., Snelgrove, S. (2002) Structural heterogeneity and permeability in faulted eolian sandstone—implications for subsurface modeling of faults. *AAPG Bulletin*, 86, 863–883

Sibson R. H. (1981) Fluid Flow Accompanying Faulitng: Field Evidence And Models. In: Earthquake Prediction: An International Review, American Geophysical Union, p.593-603

Sibson, R.H. (2000) Fluid involvement in normal faulting. *Journal of Geodynamics*, 29, 469–499

Snow, D. T. (1965) *A Parallel Plate Model of Fractured Permeable Media*. Ph.D. Thesis, University of California, Berkeley

Snow, D.T. (1970) The frequency and apertures of fractures in rock. *International Journal of Rock Mechanics and Mining Sciences*, 7, 23–40

Stimac, J., Nordquist, G., Suminar, A., & Sirad-Azwar, L. (2008) An overview of the Awibengkok geothermal system, Indonesia. *Geothermics*, 37, 300–331

Stober, I. & Bucher, K. (2007) Hydraulic properties of the crystalline basement. *Hydrogeology Journal,* 15, 213–224

Thomas, D., Aubin, A., Brisbin, D., Mukwakwami, J., Yang, H., Zaluski, G. (2014) Fault architecture, associated structures and uranium mineralization, Eastern Athabasca Basin. Cameco Corp., SGS Open House Dec 2014, Presentation report. 31pp. (http://publications.gov.sk.ca/documents/310/95089-4_Thomas_Open_House_2014.pdf)

Townend, J. & Zoback, M. D. (2000) How faulting keeps the crust strong. *Geology*, 28, 399–402

Tran, H.T. (2001) Tectonic evolution of the Paleoproterozoic Wollaston Group in the Cree Lake Zone, Northern Saskatchewan, Canada. Ph.D. Thesis, University of Regina, Regina, Canada

Tuisku, P., and Karki, A. (2010) Metamorphic Petrology of Olkiluoto. Working Report 2010-54, June 2010, Posiva Oy, Olkiluoto, Finland

Wibberley, C.A.J., and Shimamoto, T. (2003) Internal structure and permeability of major strike-slip fault zones: the Median Tectonic Line in Mie Prefecture, Southwest Japan. *Journal of Structural Geology*, 25, 59–78

Wenning, Q.C., Madonna, C., de Haller, A., and Burg, J-P. (2018) Permeability and seismic velocity anisotropy across a ductile–brittle fault zone in crystalline rock. *Solid Earth*, 9, 683-698

Woodcock, N.H., and Mort, K. (2008) Classification of fault breccias and related fault rocks. *Geological Magazine*, 145(3), 435–440

Yamashita, T., & Tsutsumi, A. (2018) Involvement of fluids in earthquake ruptures. Field/experimental data and modeling. Japan: Springer. doi:10.1007/978-4-431-56562-8

Zoback, M.D., & Byerlee, J.D. (1975) The effect of microcrack dilatancy on the permeability of Westerly granite. *Journal of Geophysical Research*, 80(5), 752–755

Appendix 1

Appendix 1 contains the "Data Records" section from the journal article. The database columns (or fields) store the values for text, labels, categorical and numerical variables. The database is one MS Excel spreadsheet.

9.1 Data records

The database is available as a Microsoft Excel spreadsheet file or a text tab-delimited file (.txt). The data records are organized in rows in two spreadsheet tables, and the attributes are in columns (fields). There are two tables: dataset table, and references table. The first table contains site name and location information, short reference list, summary of geology and structure, test methods, and the representative permeability values. The second table contains bibliographic references of the most relevant publications related to the permeability datasets, and those that were mentioned in other text fields in comments about methods and results.

9.2 Dataset table

9.2.1 Dataset number, site name, and location information:

1. **Dataset number** - is the identification number of a permeability dataset. It increases by integer numbers between sites at different geographic locations, and by first decimal digit (incremented by 0.1) for different datasets at the same study site. The dataset ID number acts as one primary key (relational database format) and the same ID number is used in the first field of the references table. Because the whole database is subdivided into five sections (see Table 3-1), the records for data sites are sorted separately within each data source section. The sorting is alphabetical by country name and site name. This sorting determines the ordering of the site ID numbers.
2. **Site name** - is a short text string that matches the commonly used name for a particular study site. For multiple datasets in one general location, site names were created from the names of major faults or other information such as sector, depth, or distance along a tunnel. Some of the attributes may then repeat (e.g. lithology, country, region names, etc.), but the information specific to the dataset will be unique (e.g. depths, permeability values, test methods, results, notes).
3. **Country** is a text string with a country name (e.g. Japan, USA, etc.).

4. **Administrative Region** - is a text string that holds the name of the largest administrative regions within a country. This can be a state, province, prefecture, etc.

5. **Locality Name** - is the name of the nearest locality to the study site, such as a town, village, mountain, lake, etc. Many site names originate with a locality name.

6. **Geologic Region** - is the name of geological area such as sedimentary basin, mountain massif, volcanic area, or tectonic plate boundary.

7. **Geographic Region** - is the name or short description of a geographic area (e.g. island, river valley, mountain, or sector of larger region).

8. **Latitude** - location coordinate on Earth in degrees and with decimal degrees fraction, in WGS84 geographic coordinate system. Positive values are in the northern hemisphere and negative values in southern hemisphere. The coordinates of latitude and longitude in the database given an approximate location of sites on web-based mapping tools and are not meant for detailed mapping at site-scale. The coordinate values are taken directly from other databases or publications, without any verification of position accuracy. Where coordinates were not listed in the paper but shown on a figure, the locations were found by comparing published maps in reports and journal papers, digitized and geo-referenced maps from original journal papers. In some cases the locations are of the nearest locality as named in a report or shown on regional maps. In some cases the coordinates are at the drill pads if a site consists of individual drillholes, where these could be positively located during the review.

9. **Longitude** - location coordinate on Earth in degrees and with decimal degrees fraction, in WGS84 geographic coordinate system. Positive values are to the east of 0 meridian and negative values to the west. In some cases the coordinates are at the drill pads if a site consists of individual drillholes, where these could be positively located during the review.

10. Elevation of ground at site - average elevation in meters above sea level (in areas below sea level on land, the values are negative), rounded off to nearest 10m, or to nearest 5m near the sea shore. In areas where the exact coordinates were not found during the review, a location in general area is given, with ground elevation is rounded off to between 20 and 50m, depending on steepness of local topography, and elevations from Google, Google Earth application.

11. **Depth to sea floor at site** - depth to sea floor in meters, as reported. Values are positive in meters.

12. **Site location uncertainty** - text noting the location data source or uncertainty.

9.2.2 Lithologic and structural information summary:

The lithologic categories and some rock deformation categories are coded with "blank or no value" or integer number 1, to facilitate data sorting and statistical analysis by those categories. The fields are not exclusive and more than one can be flagged for each dataset. However, for the main lithological categories, one dominant lithology was selected in nearly all the cases to avoid data repetition.

13. **siliciclastic (coarse)**
14. **siliciclastic (fine, "mudrocks")**
15. **carbonate**
16. **volcaniclastic**
17. **volcanic igneous**
18. **plutonic**
19. **metamorphic**
20. **intrusive dikes in volcanic rocks**
21. **unlithified siliciclastic sediments**
22. **deformation bands** (not part of mapped fault core or damage zone)
23. **mylonite**
24. **Lithology** - is a text describing briefly the main geological or lithological units at the site that match the permeability datasets. For example, some locations have complex geology and many lithological units, thus this brief summary is for the entered permeability dataset.
25. **Structures** - is a text describing very briefly the fault structure at the site.

9.2.3 Permeability test methods and result categories:

26. **Permeability test methods** - a brief text summary of hydraulic or laboratory test methods of rock permeability used at a study site.
27. **Permeability values** - a brief text summary of permeability, transmissivity, hydraulic conductivity or storativity values, organized by references to papers or reports.
28. **Flow model** (not in-situ) - category that indicates where the permeability dataset is from model parameters
29. **Initial review pass** - this category is flagged "1" after the initial review if the bulk or matrix permeability was measured at a site in a fault zone. The database contains some

records where it was not possible to not obtain a meaningful representative fault zone permeability dataset, but other data may exist at that site and further review is needed.

30. **Reference list** - is shortlist of authors from publications that are the most relevant to the fault zone permeability dataset. The full reference text is given in a separate table.

Category of test data location (fault outcrop at ground vs. in-situ below ground surface): Categorical values are "1" or blank.

31. **Outcrop** - this category indicates that the test site has a rock outcrop at ground surface where rock samples were tested or extracted from and tested in laboratory. This may be in addition to any other in-situ data from depth.

32. **Outcrop data** - category flagging that the outcrop permeability data were entered as matrix permeability in this database.

33. **Downhole in-situ tests data** - category for tests performed in drillholes in-situ over some test interval

9.2.4 Depth of tested zone relative to the ground surface:

34. **Maximum depth below ground** - value in km. For borehole test intervals, this would be the "TO depth". The outcrop depth was entered as 1m (0.001 km) to represent the upper 1m of the rock outcrop and mainly to allow plotting of outcrop permeabilities on graphs with logarithmic depth values.

35. **Minimum depth below ground** - value in km. For borehole test intervals, this would mean the "FROM depth". For outcrops, the minimum depth was left blank.

36. **Average depth below ground** - value in km. For borehole test intervals, this would mean the "midpoint" depth. In cases of one depth reported only, or one already averaged depth, it is entered both as the maximum depth and as the average depth.

9.2.5 Depth of tested zone relative to the top of metamorphic or plutonic basement rock:

This depth is applicable where the in-situ depth interval is in basement rock that is covered by unlithified or lithified sediments in a sedimentary basin. Otherwise enter no value (empty). The value in km calculated from the difference (depth below ground) - (depth of top of basement rock).

37. **Depth of top of basement rock** - value in km below ground surface.
38. **Maximum depth below top of basement rock** - is the value in km.
39. **Minimum depth below top of basement rock** - is the value in km.
40. **Average depth below top of basement rock** - is the value in km.

9.2.6 Elevation of tested zone relative to mean sea level:

This is useful for plotting regional or continental cross-sections of multiple site data. For intervals tested in drillholes that were below the sea floor, the elevation is negative and it is the sum of the depth to the sea floor and the depth below sea floor to the test zone. For ground surface rock outcrops (0 depth), the depth was entered as 1m (0.001 km) to represent the upper 1m of the rock outcrop, and to allow plotting of outcrop permeabilities on graphs with logarithmic depth scales. For outcrops, the minimum depth was left blank.

41. **Maximum elevation of test zone** - value in km above mean sea level.
42. **Minimum elevation of test zone** - value in km above mean sea level.
43. **Average elevation of test zone** - value in km.

9.2.7 Confining pressure and effective depth (matrix samples only):

Confining pressure of laboratory tests on rock samples (testing the matrix permeability), and the estimates of effective depth that correspond to the matrix permeability values:

44. **Maximum confining pressure on rock samples** - value in MPa from permeability tests on matrix samples under confining pressure conditions performed in a laboratory. The value is usually taken from graphs or tables of the reports and may be approximated to nearest 5 or 10 MPa.
45. **Minimum confining pressure on rock samples** - value in MPa from permeability tests on matrix samples under confining pressure conditions performed in a laboratory.
46. **Confining pressure on rock samples for effective depth calculation** - value in MPa of the lowest confining pressure test series on rock samples, closest to the effective pressure at original depth of the rock sample.
47. **Effective depth -** is a value in km, estimated from the confining pressure on matrix sample, applicable only to rock matrix samples.
48. **Confining P >> P at sample depth** - category that indicates where the rock sample was

tested at confining pressure that was greater than in-situ confining or ambient pressure at depth or outcrop where the sample was extracted from. This category is not flagged if the test pressure was approximately the same as the in-situ effective pressure.

9.2.8 Permeability values:

All permeability values are in (m2) units. Matrix permeability refers to small rock samples that usually exclude macroscopic open fractures or fracture channels. Bulk permeability refers to downhole in-situ test intervals that sample a larger rock volume that includes macroscopic fracture networks and the rock matrix together.

Data from fault core (zone):

49. **matrix k** - matrix permeability of the fault core rock
50. **matrix k low estimate** - low estimate of representative matrix permeability of the fault core rock,
51. **bulk k** - bulk permeability of the fault core (zone),
52. **bulk k low estimate** - low estimate of representative bulk permeability of the fault core (zone),

Data from fault damage zone:

53. **matrix k** - matrix permeability of fault damage zone,
54. **matrix k low estimate** - low estimate of representative matrix permeability of the fault damage zone,
55. **bulk k** - bulk permeability of fault damage zone,
56. **bulk k low estimate** - low estimate of representative bulk permeability of the fault damage zone,

Data from protolith (host rock):

57. **matrix k** - matrix permeability of the protolith (host) rock
58. **matrix k low estimate** - low estimate of representative matrix permeability of the protolith,
59. **bulk k** - bulk permeability of the protolith,
60. **bulk k low estimate** - low estimate of representative bulk permeability of the protolith

9.2.9 Ratios of permeability values:

The logarithm of ratio of permeability values of fault damage zone (FDZ) to the permeability of protolith, and a ratio of fault core (FC) to the permeability of protolith, was calculated for matrix and bulk permeability data separately. In some cases, the permeability values were not given in the original publication, only the permeability ratios.

Ratios of FDZ/Protolith, where only ratio values were provided in publications:

61. ratio = log matrix k FDZ / log matrix k Protolith,
62. ratio = log matrix low k FDZ / log matrix low k Protolith,
63. ratio = log bulk k FDZ / log bulk k Protolith,
64. ratio = log bulk low k FDZ / log bulk low k Protolith,

Ratios of FDZ/Protolith, where permeability values were available:

65. ratio = log matrix k FDZ / log matrix k Protolith,
66. ratio = log matrix low k FDZ / log matrix low k Protolith,
67. ratio = log matrix geometric mean k FDZ / log matrix geometric mean k Protolith,
68. ratio = log bulk k FDZ / log bulk k Protolith,
69. ratio = log bulk low k FDZ / log bulk low k Protolith,
70. ratio = log bulk geometric mean k FDZ / log bulk geometric mean k Protolith,

Ratios of FC/Protolith, where only ratio values were provided in publications:

71. ratio = log matrix k FC / log matrix k Protolith,
72. ratio = log matrix low k FC / log matrix low k Protolith,

Ratios of FC/Protolith, where permeability values were available:

73. ratio = log matrix k FC / log matrix k Protolith,
74. ratio = log matrix low k FC / log matrix low k Protolith,
75. ratio = log matrix geometric mean k FC / log matrix geometric mean k Protolith,
76. ratio = log bulk k FC / log bulk k Protolith,
77. ratio = log bulk low k FC / log bulk low k Protolith,
78. ratio = log bulk geometric mean k FC / log bulk geometric mean k Protolith

9.3 References table:

The references table contains the following fields:

1. **Dataset number** (same as in dataset table),
2. **Site name**
3. **References** - full reference text for journal papers or reports.

Appendix 2

10 Supporting information for article in Chapter 5

Table S1 (spreadsheet and text file in Appendices) contains the paired bulk or matrix permeabilities for fault damage zone (FDZ), fault core zone (FCZ), and protolith (Protolith), in different lithologic categories. All values are logarithms ($\log_{10}$) of permeability values (m^2 units). All values are logarithms ($\log_{10}$) of ratios of permeability values (m^2 units). This is equivalent to difference in $\log_{10}$ permeability values between the fault damage zone and the protolith. The boxplot statistics are summarized in Table 10-1 and Table 10-2.

Table 10-1 Box plot statistics for permeability values from Table S1

Zone	Rocky type	Upper whisker	3rd quartile	Median	1st quartile	Lower whisker	Nr. of data	Mean
FCZ	plut. & metam.	-10.46	-14	-15.3	-17	-19.15	13	-15.25
Protolith	metamorphic	-11.22	-14.85	-16	-17.3	-19.15	56	-15.85
FDZ	metamorphic	-9.4	-12.4	-13.26	-15	-18.6	86	-13.69
Protolith	plutonic	-11.7	-14.7	-15.7	-17	-19.32	71	-15.83
FDZ	plutonic	-10.22	-12.15	-13.3	-14.7	-18.23	105	-13.53
Protolith	volc igneous	-13.3	-14	-14.7	-15	-16	26	-14.43
FDZ	volc igneous	-11	-12.4	-13.03	-13.52	-14.7	62	-13.04
Protolith	volcaniclastic	-10.64	-11.87	-14.07	-15.15	-17	12	-13.8
FDZ	volcaniclastic	-9.92	-11.7	-12.6	-13	-14.52	21	-12.42
Protolith	carbonate	-11.4	-12.4	-13.14	-14.3	-17	14	-13.54
FDZ	carbonate	-10	-11.15	-12.15	-12.7	-14	21	-12.04
Protolith	mudrocks	-14.7	-17	-18.22	-19.5	-21	11	-18.15
FDZ	mudrocks	-12.22	-14	-14.9	-17.11	-19.52	13	-15.56
FCZ	sedimentary	-13.1	-13.55	-14.05	-14.85	-16	11	-14.16
Protolith	silicilcastic	-10.3	-12.5	-13.4	-14.18	-15.4	19	-13.35
FDZ	silicilcastic	-11	-12.52	-13	-13.6	-15.05	25	-13.12
FCZ	low k fault rock	-13.3	-16.15	-17	-19.94	-21.7	29	-17.67
FCZ	drilled breccia-gouge	-12.15	-14.52	-15.1	-16.3	-17.7	33	-15.71
FCZ outcrops (lower k)	gouge-cataclasite	-12.4	-14.3	-16	-17	-20	26	-15.88
FCZ outcrops (higher k)	breccia-gouge	-10	-12.05	-14.25	-15	-17.7	33	-13.99
Protolith matrix		-9.92	-11.15	-12	-14	-18	34	-12.75
FDZ matrix		-10	-11.59	-12.3	-14	-17	26	-12.78

Table 10-2 Box plot statistics for permeability values from Table S2

Zone	Rocky type	Upper whisker	3rd quartile	Median	1st quartile	Lower whisker	Nr. of data	Mean
bulk k FDZ / bulk k Protolith	plutonic and metamorphic	5.5	3	2	1	0	125	2.2
	metamorphic	5.5	3.12	2.06	1	0	56	2.21
	plutonic	4.7	3	2	1	0.22	69	2.19
	volc igneous	3.6	2.3	1.89	1.3	0.09	35	1.77
	volcaniclastic	2.83	2.18	1.79	1.3	0.52	26	1.8
	Carbonate	3.15	2.3	1.89	0.79	0.09	12	1.65
	mudrocks	3	2	1.98	1.24	0.6	14	1.76
	sedimentary	3.95	3	2.39	1.39	0.18	11	2.15
	silicilcastic	2.7	1.77	0.9	0.5	0	15	1.13
matrix k FDZ / matrix k Protolith	silicilcastic	1.3	0.4	-0.05	-0.58	-1.3	22	0

10.1 Additional estimates of bulk permeability of fault zones from groundwater inflow rates to tunnels

In the cases of tunnels with inflow rates from fault zones, we performed calculations of bulk permeability of fault zones using the Goodman et al. (1965) formula, but only for sites where such calculations had not been published in the literature. The tunnel sites and our results of calculations are summarized and included in Table 10-3.

All references are listed in the article in Chapter 5.

Table 10-3 Bulk permeability of fault zones calculated from groundwater inflow rates to selected tunnels.

Site Name	Q (m^3/s)		H_0 (m)	w (m)	r (m)	K (m/s)		bulk k (m^2)	
	high	low	(m)	(m)	(m)	high	low	high	low
Mont Blanc Tunnel (at PM 5000-F m)	0.081		2000	280	3	2.E-07		1.E-14	
Malgovert Tunnel	0.25		305	10	3	7.E-05		7.E-12	
Enasan Tunnel (faults in welded tuff)	0.067	0.008	500	10	3	1.E-05	1.E-06	1.E-12	1.E-13
Enasan Tunnel (faults in granite)	0.83	0.005	1000	10	3	9.E-05	5.E-07	9.E-12	5.E-14
Kurobe Tunnel	0.66	0.38	274	80	2.5	3.E-05	1.E-05	3.E-12	1.E-12
Taupo Volcanic Zone water tunnels in Greywacke	0.1		400	10	3	2.E-05		2.E-12	
Taupo Volcanic Zone water tunnels in sedimentary	0.01		200	10	3	4.E-06		4.E-13	
Cleuson-Dixence Hydroelectric Gallery (faults at PM 3100-3300m)	0.007	0.004	650	100	2.9	1.E-07	6.E-08	1.E-14	4.E-15
rock around the faults at PM 3100-3300m	0.001		650	100	2.9	1.E-08		1.E-15	
Eklutna Tunnel (fault zones)	0.63		700	30	1.37	3.E-05		3.E-12	
	0.24		300	100	1.37	8.E-06		8.E-13	
San Jacinto Tunnel	1.1	0.47	335	10	3	3.E-04	1.E-04	2.E-11	8.E-12

Q = inflow rate from fault zone
H0 = saturated depth to tunnel below water table
w = fault zone width in tunnel
r = tunnel radius
K = hydraulic conductivity from Goodman et al. 1964 formula
bulk k = bulk permeability

Mont Blanc Tunnel (at PM 5000-F m):

Maréchal (1998) reported the average permeabilities of many tunnel sections in the Alps using an analytical solution for unsteady flow to tunnels, and reported data on one large fault zone at PM 7932-F and 8536-F in the Mont Blanc Tunnel (included in our database). At another fault zone near PM 5000-F, the inflows were provided but a local transmissivity was not calculated. There, the inflow occurred from two faults: 16 I/s and 50 l/s at PM 5000-F. A third fault discharged 15 l/s at PM 5280-F. The total from the major faults was 81 l/s. We assumed a zone length of 280 m, and our calculation resulted in hydraulic conductivity $2\text{x}10^{-7}$ m/s and bulk permeability $1\text{x}10^{-14}$ m^2 (water viscosity at 30^{o}C).

Malgovert Tunnel:

Goodman et al. *(*1964) provided a summary of inflow rate of 8.9 ft^3/s (0.25 m^3/s) for faults in schist at a depth of 305 m. This case was also described in Jaeger (1979). After a tunnel roof failure in swelling clay-rich rocks, within a fault zone containing highly deformed shale, a water inflow occured (0.25 m^3/s). We estimated a hydraulic conductivity of $7x10^{-5}$ m/s and bulk permeability of $7x10^{-12}$ m^2.

Enasan Tunnel:

Many inflow points from faults were documented in the Enasan tunnel (Yano et al., 1978). In welded tuff, inflows from 8 fault zones at depths of approximately 500 m were measured (maximum 0.067 m^3/s, minimum 0.008 m^3/s and geometric mean 0.023 m^3/s). The resulting hydraulic conductivity from the Goodman formula is 10^{-12} to 10^{-13} m^2. For fault zones in granite at depths of about 1000m, inflows ranged from 0.83 to 0.005 m^3/s with a geometric mean of 0.52 m^3/s. The calculated hydraulic conductivities range from ~ $9x10^{-5}$ to $5x10^{-7}$ m/s (bulk permeabilities of $9x10^{-12}$ to $5x10^{-14}$ m^2).

Kanden (Omachi) tunnel to Kurobe Dam:

A summary was provided in Haga (1961). The tunnel crossed a 80m wide fault zone in granite at 1691m from portal, where cold water inflow occurred at 660 l/s, with high pressure measured ahead of the tunnel, slowing down the exavation for 7 months. A major film was made about this event and the now cemented fault zone is a tourist attraction at present. Goodman et al. (1964) listed the inflow to this tunnel as 13.5 ft^3/s (0.38 m^3/s) at a depth of 900 ft (274 m), although we could not review the references. Using the higher inflow rate of 0.66 m^3/s yields a hydraulic conductivity of $3x10^{-5}$ m/s and a bulk permeability of $3x10^{-12}$ m^2.

Taupo Volcanic Zone water tunnels:

Seebeck et al. (2016) presented fault permeability values for tunnels in Taupo Volcanic Zone and estimated a very high value of $10^{-9}m^2$. This is orders of magnitude greater than bulk permeability typically calculated for fault zones with much larger inflow rates. The calculations were not included in the doctoral dissertation (Seebeck, 2016) or the paper, thus we could not verify. Applying the Goodman formula to the inflow data yields bulk permeability values in the range of $2x10^{-12}$ to $2x10^{-13}$ m^2, similar to results in other tunnels with similar inflow rates. For fault zones in Miocene sediments, we obtained bulk lower permeability of $2x10^{-13}$ to $2x10^{-15}$ m^2. These values match the regional geothermal well permeabilities discussed in Seebeck et al. (2016).

Cleuson-Dixence Hydroelectric Gallery (faults at PM 3100-3300m):

Maréchal (1999) calculated average transmissivity and hydraulic conductivity values for the Cleusson-Dixence tunnel in lot B at a depth of 460 m (250 l/s inflow) and lot C at depth 250 (80 l/s inflow). The average hydraulic conductivities (including fault zones and unfaulted rock) for 8.2 km and 7.6 km of tunnel were $1.6x10^{-7}$ m/s and $9x10^{-8}$ m/s. A figure in Maréchal (1999) shows inflow rates per 100 m tunnel intervals over the entire tunnel. In the fault zones (the paper uses the term Kakirites for rocks with fault gouges/breccias) at tunnel locations PM3100-3300, inflow rates were about 4 and 7 l/s over 100 m intervals. The tunnel diameter was 5.6 to 5.8 m (Strozzi et al., 2011). From the Goodman formula and Maréchal's data we estimated the hydraulic conductivity to be $6x10^{-8}$ to $1x10^{-7}$ m/s and bulk permeability to be $4x10^{-15}$ to $1x10^{-14}$ m^2. The rock surrounding the fault zones had inflow rates per 100 m of about 1 l/s, implying bulk k ~$1x10^{-15}$ m^2.

Eklutna Tunnel:

This hydroelectric water tunnel passes through faulted greywacke, argillite and slate. A cumulative inflow rate for the entire tunnel was 1.1 m^3/s (Goodman et al., 1964). A U.S. Geoogical Survey report by Logan et al. (1964) has much more detail, and shows the tunnel cross-section and water conditions (inflow rate bar graphs) at approximately 30 m spacing along the tunnel. A fault zone more than 30 m wide had a 0.7 m wide fault gouge (Station 208+75), and a fault zone in greywacke rock (Stations 220 to 250) included at least 3 large inflow points and had a total width of about 100 m. The first fault zone produced groundwater at a rate of 0.6 m^3/s and the second wider fault zone produced about 0.24 m^3/s. We calculated the hydraulic conductivity for the two fault zones to be $3.3x10^{-5}$ and $7.7x10^{-6}$ m/s and bulk permeability to be $3x10^{-12}$ and $8x10^{-13}$ m^2.

San Jacinto Tunnel:

Inflow rates reported by Goodman et al. (1964) were 1.12 m^3/s from one fault at 640 m depth and 0.47 m^3/s from another fault at 248 m depth. The tunnel diameter averaged 5.9m (Kaneshiro et al., 2007). Using the Goodman formula, our estimate of hydraulic conductivity is 1 to $3x10^{-4}$ m/s and bulk permeability is $8x10^{-12}$ to $2x10^{-11}$ m^2 (water at 30°C).

10.2 Summary of bulk permeability of fault zones at EGS/HDR/rock laboratory sites

The following are notes from our review of published scientific work on at 21 research sites associated with Enhanced Geothermal System (EGS), Hot Dry Rock (HDR), or underground hard rock laboratories. The text describes the geology, structures, hydraulic test methods, and bulk and matrix (where applicable) permeability of faults or other fracture zones, before and after injection stimulation. Table 10-4 contains the summary that was used to plot Table 10-3a in the main manuscript. All references are listed in the article in Chapter 5.

Rock fracturing/faulting/fluid flow research sites (<0.5km depth):

Falkenberg test site, Germany:

At Falkenberg, 8 boreholes were drilled to depths of about 300-500 m in granite, and in one or more of these boreholes high pressure water injection was done to extend sub-vertical fractures found at depths near 250 m, producing a dipping fracture plane that intersected multiple boreholes (Kappelmeyer & Jung, 1987; Jung, 1989). The fracture is not a fault zone, and its displacement, if any, is not known. We include this site, assuming that the fracture does represent a small-scale fault. The tests were done on 4 new drillholes and 2 uranium-exploration drillholes where the granite is altered. The hydraulics of the tests, and fracture orientation in the stress field, suggested that pre-existing fractures were present, though not previously identified from core inspections or logs (Baumgartner et al., 1987; Gaumgartner et al., 1986). For a fracture in granite over a 4.7 m long packer interval, extending tens of meters, the estimated transmissivity was ~1 to 10 Darcy*m (10^{-12} - 10^{-11} m^3) at low injection pressure and up to 100 Darcy*m (10^{-10} m^3) at higher pressures corresponding to fracture progation and temporary dilation (Jung, 1989). Regardless of the aquifer's effective thickness, or fracture network extent, the permeability-increase ratio was approximately 1 order of magnitude here.

LSBB underground laboratory, France:

The LSSB (Le Laboratoire Souterrain à Bas Bruit) at Rustrel, France, has faults cutting a protolith of carbonate grainstone and thin mudstone layers, and the bulk permeability varies over 2 to 3 orders of magnitude. There are alternating high and low permeability stratigraphic units (Jeanne et al., 2012). The fault zone was mapped on gallery walls and outcrops and in vertical drillholes ~20 m deep. The fault core contains highly deformed porous rock, <4 to <30 cm wide clay lenses, surrounded by cracked angular breccia and a 20 m wide damage zone. From rock-quality (geotechnical) empirical laws, the hydraulic conductivity was estimated as 10^{-7} m/s (Jeanne et al., 2012). In a short vertical hole (17.5 m), low-pressure injections were performed and modeled. The bulk permeability ranged from 1.8 $x10^{-12}$ to $1.7x10^{-15}$ m^2 (we entered a representative value of $5x10^{-12}$ m^2). The permeability contrast (damage zone / protolith) is greater than one order of magnitude in low-porosity fractured layers near the fault core (10^{-14} m^2 / 10^{-15} m^2). In less fractured rock, the permeability contrast was lower (bulk permeability 10^{-16} m^2).

A fault shear/dilation experiment was done in a vertical well at a depth of 282 m, in 1.5 m long interval isolated by packers (Guliermi et al., 2013; Guliermi et al., 2015). The fault was strike-slip with a normal component, >500 m long with a few meters of slip. The damage zone includes smaller faults <10 m long and thin brecciated zones. The bulk permeability of protolith is 1 to 4 $\times10^{-13}$ m^2 and the average bulk permeability of the fault damage zone (fracture network) is 10^{-12} m^2 to 7×10^{-12} m^2 (the latter value being from a more recent estimate). The fault slip initiated at 1.5 MPa, by shear failure, producing microsesismic events a few meters away from the injection point. A hydromechanical flow model was calibrated to observed pressures. During the aseismic period, the bulk permeability increased by factor of 14, from 0.07 to 1 $\times10^{-10}$ m^2 , with a total increase by a factor of 20 during the experiment (to $1.4x10^{-10}$ m^2).

<u>Fjällbacka test site, Sweden:</u>

Fjällbacka is a rock fracturing test site with 3 boreholes, the deepest to 500m. Hydraulic stimulation was done at 460 m depth, producing a sub-horizontal fracture (Eliasson et al. 1987). The hydraulic tests were done between packer intervals as described by Sundquist et al. (1988) and more briefly by Jupe et al. (1992) and Wallroth et al. (1999). The protolith was fractured at all depths, with fracture spacing typically 2 to 8 per meter, and hydraulic characterization showed that the presently open fracture networks are compartmentalized and have different pressures and water salinities (Sundquist et al., 1988). The shallow-depth protolith contained highly permeable sub-horizontal fracture zones near 205 m depth (K ~ 10^{-4} to 10^{-7} m/s), unrelated to the fault. However, near the fault zone at 475 m depth in Well Fjb1, the protolith was much less permeable, with hydraulic conductivity less than 10^{-11} m/s (bulk permeability < 10^{-18} m^2) – still much higher than the protolith matrix hydraulic conductivity of 10^{-14} m/s (matrix permeability 10^{-21} m^2).

At this test site it was difficult to distinguish small-scale fractures from small fault planes. The hydraulically stimulated fracture zone at 475.1 m depth was a fault, 8 cm wide and showing slip striations, with 1 to 2 mm thick clay and chlorite fill containing smectite clays (Eliasson et al., 1990). Before stimulation, hydraulic conductivity was 10^{-10} m/s (bulk permeability 10^{-17} m^2). The injection experiment produced a microseismic cloud that was confirmed to coincide with enhanced fracture permeability. The final stimulated hydraulic conductivity over the depth interval of 455-472 m was 10^{-7} m/s (bulk permeability 10^{-14} m^2). Transmissivity increased from $6x10^{-8}$ to $8x10^{-6}$ m^2/s for a 30 m long interval.

Grimsel Underground Laboratory, Switzerland:

The Grimsel laboratory, near Grimsel Lake in the Bernese Alps, is in granitic rock that contains major structures: shear zones (formed under ductile conditions), brittle faults overprinting the shear zones, fracture zones along the rock fabric, and igneous dikes (Davey et al., 1989). The protolith consists of granite and granodiorite (for the brittle structures), and zones of mylonite (in shear zones). Many different hydrogeological experiments have been done in the research tunnels (Alexander et al., 2009). The recently performed in situ stimulation of fault permeability and circulation experiment involved water injection into a 0.2 m wide shear zone (now a brittle fault) to cause shear movement at scale of about 20 m (Amann et al., 2018). Jalali et al. (2017) reported that short-packer-interval hydraulic tests (e.g. pulse tests) showed that, before the injection experiment, the median transmissivity was about $2.5x10^{-12}$ m^2/s, the hydraulic conductivity about $3.5x10^{-12}$ m/s, and bulk permeability about $3x10^{-19}$ m^2. After injection stimulation, the largest values of transmissivity were 1 to $9x10^{-10}$ m^2/s, hydraulic conductivity $1.3x10^{-9}$ m/s, and bulk permeability 10^{-17} to 10^{-16} m^2.

Geothermal research/operating sites (0.5 to 2.5km depth):

Ogachi HDR, Japan:

At Ogachi the protolith granodiorite in a Neogene caldera is faulted into horst/graben blocks, some with 1000 m of vertical displacement (Suenaga et al., 2000). The fault zone contains slip surfaces with slickenside and thin gouge (<2 to 5 mm width). Minor faults with 3cm displacement cut anhydrite veins and andesite dikes (Ito, 2003). Two hydraulic stimulation experiments were performed in 1991 and in 1992. The injection well was drilled to a depth of 1000 m with a 10 m long open section. Fluid injection in 1991 created a fractured zone 200 m thick and 500 m wide, as outlined by the distribution of microseismicity (Kaieda et al. 1992). In 1992, a second fractured zone was stimulated between depths of 711 and 719 m. Before fault stimulation, the upper fracture zone had bulk permeability $1.0x10^{-16}$

m^2 and after stimulation permeability had increased to $1.0x10^{-14}$ m^2 (Hori et al. 1994). Using the diffusion rate from microseismicity, Audigane et al. (2002) estimated the mean pre-stimulation bulk permeability for the 1992 experiment as $2.0x10^{-16}$ m^2 to $1.4x10^{-15}$ m^2. In 1995 additional hydraulic tests were done. Permeability increased by a factor 10 to 100 at both open sections compared to pre-stimulation values (Ito, 2003). Kaieda (2012) found that permeability increased to 1.0×10^{-13} m^2 in the lower reservoir and 1.0×10^{-14} m^2 in the upper reservoir.

Hijiori HDR, Japan:

The Hijiori HDR project is in northern Honshu Island in the Tohoku volcanic region, in central Yamagata Prefecture to the south of Akinomiya (Kaieda et al. 1990). The geological setting is the rim of Hijiori caldera. The sediment fill in the caldera consists of alluvium, volcaniclastics and basaltic lava. Faulted granodiorite bedrock is found at 1460 m depth (Kitani & Tezuka 1999, Sasaki & Kaieda 2002).

In 1986 well SKG-2 was tested before stimulation in the depth interval 1788 to 1802 m using low rate injection. The estimated bulk permeability was 10^{-15} to 10^{-16} m^2 (Kobayashi et al. 1987). In a 1988 injection experiment, the caldera ring faults were reactivated, as seen from microseismicity distribution (Sasaki, 1998). The hydraulic diffusivity was approximately 0.1 m^2/s and the bulk permeability was roughly 10^{-16} m^2, assuming other parameters such as compressibility and porosity. A NIED 1992 report listed apparent post-stimulation bulk permeability values of 10^{-10} to 10^{-13} m^2, based on an injection test between SKG-2 and HDR-1 wells. We could not obtain the actual report and entered the more conservative value of 10^{-13} m^2 for the fault damage zone, consistent with the other tests at that site. The protolith bulk permeability is not known, but the matrix permeability of granodiorite is low, 10^{-19} to 10^{-21} m^2, from core speciments drilled obtained at 1650-2200 m depth (at effective confining pressure 29.4 MPa and temperature 100 to 300^{o}C). More details can be found in Yamaguchi et al. (1992), Tenma et al. (1994), Tenma et al. (1996), and Takada et al. (1997).

Desert Peak EGS, Nevada, USA:

The Desert Peak geothermal reservoir was developed in the 1980s, partly in metamorphic basement rock at depths of 1 to 2.3 km (argillite, quartzite, phyllite, some metavolcanic) and partly in fracture zones in the overlying Tertiary volcanic rocks. A deeper granodiorite unit contains fault zones (Yeamans, 1983; Goyal et al., 1983). One EGS study at Desert Peak was initiated in well DP 23-1 in the faulted granodiorite. Hydraulic tests were described in Sanyal et al. (2003) and in Robertson-Tait et al. (2005). Circulation losses occurred while drilling between 2533 and 2586 m and continued to at least 2809 m depth. Natural state conditions were tested in interval 2438 to 2939 m (500 m long) and yielded a transmissivity of 4000 md-ft (bulk permeability $2.4x10^{-15}$ m^2). Another EGS study was done in Tertiary rhyolitic rocks in well DP 27-15, in a segment of Rhyolite Ridge fault zone. Hydraulic interference tests were done in the "shallow reservoir" in several wells (Stacey et al., 2010) and yielded a permeability thickness (kh) product of 5600 md-ft ($1.7x10^{-12}$ m^3). For well 27-15, the pre-stimulation kh = 60 mD-ft (bulk permeability $1.2x10^{-16}$ m^2). A coupled geomechanical-flow model including a discrete fracture network was developed (in FLAC), and model calibration yielded a bulk permeability of $1.8x10^{-16}$ m^2 in the direction of maximum permeability, with permeability characterized as a three-dimensional tensor (Benato et al., 2013; Benato et al., 2016). The simulations estimated that the rock formation near well 27-15 and the "shearing target fault" increased from a pre-stimulation value of about $1.2x10^{-16}$ m^2 to a post stimulation value of about $1.1x10^{-14}$ m^2 (Benato et al., 2016), an enhancement of 2 orders of magnitude.

Raft River EGS, Idaho, USA:

The Raft River fractured geothermal reservoir was developed in the 1980s in Proterozoic schist and quartzite and underlying adamellite. A postulated "Narrows structure" was considered the source of upflowing hot water (Covington, 1980). The fractured upper part of the metamorphic rock reservoir was permeable and productive. An EGS project was done in well RRG-9 ST-1 at a depth of 1808 m in quartzite (Diek et al. 2012, Bradford et al. 2013; Plummer et al. 2014, Bradford et al. 2017). Televiewer logs showed a dominant fracture zone at 1719 to 1725 m depth, and the modeled pre-stimulation bulk permeability from flow metering was $2.0x10^{-13}$ m^2. Post-stimulation pressure fall-off tests in 2015 suggested a bulk permeability of $1.2x10^{-12}$ m^2 (Bradford et al. 2015) an increase of one order of magnitude. A model by Bradford et al. (2017) adjusted fracture zone permeability near the injection point from 2 to 15 mD during the stimulation but did not change the permeability of the larger Narrows fault zone.

Rosemanowes Quarry HDR, England:

This research drilling project is in Carnmenellis granite. Experiments were done in 1982 and described by Pine (1983), Pine et al. (1983), and Pine and Batchelor (1984). The fracture hydrogeology was also reviewed by Heath (1985). Review papers were written more recently by Richards et al. (1994), Watkins (2003), McClure (2012), and Hirschberg et al. (2015). At shallow depths, mining exploration mapped faults with small shear displacements (few to 10s of meters) containing collapse breccia, clays, silica, quartz, iron oxides and other low-temperature alteration. At greater depths there is pervasive hydrothermal mineralization in fractures (Pine and Batchelor 1984). McClure (2012) pointed out that some fractures have slickensides but no gouge or cataclasite, and small (mm-scale) displacements. Hydraulic tests done before the experiment at low pressures yielded average bulk permeability of 1 to 10 micro-Darcy, increasing to 60 micro-Darcy at 5MPa overpressures (Pine & Batchelor, 1984). We use a bulk permeability of 10^{-18} to 10^{-17} m^2 for "undisturbed jointed granite"; the matrix permeability of granite is about 10^{-23} m^2. The bulk permeability of natural fractures and fracture zones before the stimulation was 10 to 100 micro-Darcy (10^{-17} to 10^{-16} m^2). During injection stimulation in 1982, microseismicity occurred over a depth range of 1.5 to 3.5 km, along sub-vertical zones originating at at the point of injection at 2 km depth. The bulk permeability increased from less than 100 micro-Darcy to greater than 5 mD ($5x10^{-15}$ m^2) (Pine, 1983). The conceptual model invoked an inner zone at 0.5 to 5 mD that is up to 0.6 km long; we accept this value as the bulk permeability (0.5 to 5 $x10^{-15}$ m^2) for the fault damage zone. The outer stimulated zone had a permeability of 100 to 500 micro-Darcy (1 to 5 $x10^{-16}$ m^2). The surrounding non-stimulated zone had a permeability of 10 to 100 micro-Darcy ($1x10^{-17}$ to $1x10^{-16}$ m^2).

Geothermal EGS sites (>3km depth):

The NW Geysers EGS, California, USA:

The Northwest Geysers is divided into horst blocks bounded by north-west trending strike-slip faults and antithetic northeast trending normal faults which may have some minor strike-slip offset. The local geology and structure and fracturing was described in Sternfeld (1989), Persoff and Hulen (2001), and Altmann et al. (2013). The crystalline basement includes graywacke and contact metamorphosed biotite hornfels in metagraywacke, bounded above by very low-permeability formations. Granitic intrusions exist at approximately 4000 m depth. Well P-32 was cased to 1863 m and open to 3396 m. Pre-stimulation pressure-build up tests yielded permeability thickness ~ 6.7 Darcy-m ($6.7x10^{-12}$ m^3) (Garcia et al. 2016). In comparison, permeability thickness values at the The Geysers main reservoir range from 5000 to 400,000 md-ft ($1.2x10^{-10}$ m^3). The stimulation experiment in 2012 (Jeanne et al. 2014 and 2015) provided some estimates of permeability thickness, and the results suggested that it had increased from 6.6 to 12.7 Darcy-m ($1.3x10^{-11}$ m^3). The bulk permeability after stimulation is about $2.0x10^{-14}$ m^2, similar to the estimate from numerical models by Jeanne et al. (2015). The estimated bulk permeability of the host rock was 2.0×10^{-15} m^2, and the "N130 shear zone" had values of 1.0×10^{-13} to 5.0×10^{-15} m^2 (Jeanne et al. 2014). Jeanne et al. (2015) estimated an average bulk permeability of 2.8×10^{-14} m^2 for a volume extending up to 1212 m from the injection point. The ratio of stimulated fault permeability / initial fault permeabilty varied in space and time. The largest enhancement factor was about 12 at the injection well, 50 to 100 days after the beginning of experiment at maximum injection rate, but longer-lasting permeability changes were only a factor of 5.

Fenton Hill HDR, New Mexico, USA:

Fenton Hill is located near the Valles Caldera. Precambrian basement rock begins at 730 m depth, gneiss and schist occur to 2600 m depth, granodiorite, gneiss, and schist near 3000 m depth, and then metavolcanic rock, granodiorite and granite at 3700 to 4500 m depth (Laughlin et al., 1983). The first phase of the test program has been described in many reports (e.g. Zyvoloski 1981; Dash et al. 1983, Duchane and Brown 2002). In 1975 experiments were done at a depth of 2900 m. Pressure-transient tests (Fisher & Tester, 1979; Fisher & Tester, 1980) implied a large area of dilated fracture of 1 to 2 mm effective (average) aperture and an effective permeability of $2x10^{-17}$ m^2 within a protolith with low matrix permeability (10^{-19} to 10^{-20} m^2 in core samples). In 1984 massive hydrofracturing was done to connect the wells and previously formed fractured reservoirs at depths of about 3500 m (Dash et al. 1985). A tracer test was done after this stimulation and, assuming a low porosity matrix ($2x10^{-4}$), the permeability was $1.1x10^{-15}$ m^2 (Birdsell and Robinson 1988). Seismological analysis of previously recorded microseismic events (Fehler, 1989) provided an estimate of hydraulic diffusivity and, with several assumptions, yielded an estimate of maximum bulk permeability in the range of ~$2x10^{-17}$ to $2x10^{-16}$ m^2 (Shapiro et al. 2003). More flow testing work was done between 1992-1995 (Brown and DuTeaux 1997), and a numerical model by Yamamoto et al. (1998) was calibrated to a near-injection permeability value of $6.7x10^{-14}$ to $3.3x10^{-13}$ m^2. In the model, the the two lowest-permeability zones were 10^{-17} to 10^{-16} m^2.

Habanero EGS, Australia:

Located in the northeast corner of South Australia, in the central part of the continent, the Habanero EGS reservoir was created in shallowly dipping fault zones in granite at depths of ~ 4200 to 4325 m under the shaly sediments of the Cooper Basin. In well Habanero 1, permeable fault zones were encountered at 4209 m and 4254 m depth. In Habanero-2, fault zones at 4170, 4224 and 4325 m depth caused mud losses during drilling, and flow tests demonstrated along-fault connectivity between wells. A third well found only one permeable fracture zone at 4181 m (Chen and Wyborn 2009). During injection stimulation in 2003, microseismicity defined a zone up to 2 km long and <50m thick along two parallel structures (Baisch et al. 2006, Holl and Barton 2015). Llanos et al. (2015) built a numerical model (using TOUGH2) and assigned a bulk permeabilty of 1 to 5 $x10^{-14}$ m^2 to the fault zone. The mean effective flow aperture was less than 40 micro-meters in a discrete fracture model. The protolith permeability was assumed to be 10^{-22} m^2. After stimulation, the numerical model simulations were calibrated to a fault zone bulk permeability of $8x10^{-13}$ m^2 along the fault plane, with a surrounding zone at $2.8x10^{-14}$ m^2.

Pohang EGS, South Korea:

The Pohand project is located near Busan, South Korea (Lee et al. 2015). The basement rock consists of granodiorite, first encountered at a depth of ~2350 m under Tertiary sediments. A nearby outcrop of the Yangsan strike-slip fault was mapped by Kim et al. (2016). Well PX-1 was drilled to 4127 m (casing to 2391 m) and crossed a dike at 3596-3726 m (Song et al., 2015). Well PX-2 crossed a steeply dipping major fault at 4348 m. The injection stimulation was done on this pre-existing fault over a 140 m open section (Park et al. 2017). Before the stimulation experiment, the estimated bulk permeability, tested at low pressure, was 10^{-16} m^2. The estimated permeability at the highest pressure, based on increased injectivity, was $9.4x10^{-14}$ m^2 (Park et al. 2017).

Urach-3 EGS, Germany:

The geothermal well Urach-3 is located at Bad Urach in the Black Forest Mountains, southern Germany. Stober (2011) reviewed the long and complex testing history at this well. The lithology is dominated by granite and gneiss. There are pre-existing fractures and brittle faults at frequency of 2 to 8 per meter. The structures include shears and cataclastic faults (Genter 1994, Tenzer et al. 2000). McClure (2012) reviewed the evidence for cataclastic fault zones in core logs and cuttings in Urach-3. Small sections of recovered core (2% of total open drillhole length) contained cataclasite and ultracataclasite, and it is very likely that larger hydrothermally altered zones (10s of cm thick) were present. The section from 2500-3000 m depth appeared significantly geotechnically disturbed owing to fracture zones, hydrothermal alteration, and cataclastic rocks in faults. Heinemann et al. (1992) described hydraulic tests in the late 1970s and 1980s (pump tests, leak off tests, slug tests), interpreted and published by various authors. There are natural fracture zones at 3325 m depth and, from slug tests, the average transmissivity immediately adjacent to the well was $1.5x10^{-6}$ m^2/s. Injection tests over a 34 m interval yielded transmissivities of 2.3 to 3.5 $x10^{-7}$ m^2/s and bulk permeability 3 to $4x10^{-16}$ m^2 after adjustment for fluid properties (Heinemann et al. 1992, Stober 2011). The protolith transissivity was tested over many small intervals, and a long-interval pump test over 1808 to 3334 m gave results fitted by a transmissivity value of $6x10^{-8}$ m^2/s (Stober, 2011) (bulk permeability 10^{-18} m^2). Injection experiments caused temporary dilation of the fracture zone at pressures above 170 bar, with transmissivity increasing from $3.5x10^{-7}$ m^2/s to 3 $x10^{-6}$ m^2/s (Heinemann et al., 1992) (maximum bulk permeability about $4x10^{-17}$ m^2). In 1992, the well was deepened to 4444 m. A subsequent massive injection experiment did not cause fault shear, but dilated the fracture network, with an estimated transmissivity of $1.3x10^{-6}$ m^2/s (2.9x greater than before stimulation). After the long-duration pump tests, the transmissivity decreased to the original pre-stimulation value. McDermott et al. (2005) modeled the fractured reservoir with anisotropic permeability ($1.5x10^{-15}$ m^2 maximum value, $6x10^{-16}$ m^2 minimum value).

Basel EGS, Switzerland:

The Basel geothermal well was drilled through sedimentary rocks to a depth of 2411 m, through siltstone and weathered granite between 2411 and 2507 m, and through granite of the Black Forest plutonic massif to a total depth of 5000 m (Häring et al. 2008). Evidence for fault zones was clearly seen in cuttings that contained cataclasite fault rock (Kaeser et al. 2007, and a structural review by McClure 2012). With downhole logs, nearly 1000 steeply dipping fracture planes were mapped, and cuttings from fault zones between 4629 to 5000 m (at 4700 and 4835 m) contained argillic alteration. There are numerous publications describing the 2006 injection experiment, and particularly the seismological analysis of hypocentres (Tarekawa et al. 2012, Deichman et al. 2014, and a review in Cox 2016). Steeply dipping fault zones were clearly defined by microseismicity, with many small and variously oriented slip surfaces. A flow-meter device monitored the hole above 4682 m during the experiment and indicated that, at 4671 m, a fault zone absorbed 50% of the injected flow (Ladner and Häring 2009). In 2009, low flow rate injection tests were run and the results confirmed that reservoir permeability increased to a bulk value of $6x10^{-15}$ m^2 irreversibly – a factor x400 compared to the pre-stimulation natural conditions (Ladner and Haring 2009). Before the stimulation experiment, hydraulic tests yielded a permeability thickness product of $5x10^{-15}$ m^3 over a 371 m length interval (Häring et al. 2008, Ladner and Häring 2009), implying bulk permeability of about 10^{-17} m^2. A numerical model was created and calibrated based on the coupled diffusive process observed during the 2006 injection experiment (Miller, 2015). The bulk permeability of faulted reservoir increased temporarily to 10^{-13} m^2, and on average (more definitely) to $3.2x10^{-15}$ m^2.

Soultz-sous-Forêts EGS, France:

The Upper Rhine Graben is filled by sedimentary rock to about 1.4 km depth, underlain by granite. Normal faults cut sediments and granite to at least 5km depth. Four geothermal exploration drillholes (GPK-1 to -4) were tested, in addition to deepened petroleum wells such as EPS-1 (to 2227 m). Each fault zone contains many permeable sections. Three geothermal reservoirs were defined by clusters of fracture zones in faulted granite (Dezayes et al. 2010, Genter et al. 2015) below the faulted sedimentary aquifer (Vidal et al. 2015).

Upper reservoir, 1.2 to 2.5km depth (fracture zone cluster I):

The upper 300 to 400 m of the granite has experienced paleoemersion (paleoweathering) and exhibits subhorizontal joints, inferred to be from isostatic unloading under oxidizing conditions. The water-conducting "open" fractures are only partially open, often filled by geodic or drusy secondary quartz (Genter and Traineau 1996). The fracture cements are iron oxides, quartz, calcite, and clay. Fault damage zones have medium to high hydrothermal alteration intensity, are steeply dipping, and most are sealed by hydrothermal minerals. About 25% of fractures are faults with movement indicators, containing cataclastic fault rocks (breccia, cataclasite) and also protomylonite. The thickest filled fracture is a 25 cm thick quartz vein at 2175 m in a highly fractured zone that produced hot water during coring (Genter and Traineau 1996). One hydrothermally altered fault zone occurs at 2069-2074 m depth. The fault core has intense fracturing, breccias, and some protomylonitic textures. Many fractures are sealed by vuggy quartz veins up to 20 cm thick. There is an intermediate zone of strongly altered but less fractured granite and "cataclastic granite" and argiilized zones and an outer zone with few fractures but intensely altered granite protolith. The damage zones had porosities of 5% to 25% (Genter et al. 2000) and could explain the large volume of water storage during injection experiments, but the permeability distribution in fault zones is not clear (McClure et al. 2011).

A test program in GPK-1 in 1988-1989 was described in Jung (1991) and Jung (1992). In the 580 m open interval, 90% of flow was from one fault-associated fracture. The bulk permeability was reported as <35 micro-Darcy (<$3.5x10^{-17}$ m^2). In well GPK-2, drilled in 1995, a fault zone at 2100 m depth was tested by injection and yielded a permeability-thickness of 50 Darcy-m (Baumgartner et al., 1996). The matrix permeability of unfractured granite was also tested on core samples from GPK-1 (Rummel, 1992). Values were 10^{-17} to 10^{-16} m^2 at atmospheric pressure and 10^{-17} to 10^{-19} m^2 at 100 MPa confining pressure (summary in McClure et al. 2011). Matrix permeabilities from EPS-1 drillhole interval 1420-2161 m were reported in Geraud et al. (2010): 10^{-20} m^2 in the fresh granite and 10^{-15} m^2 in the fault core.

<u>Intermediate reservoir, 3.4 to 3.6km depth (fracture zone cluster II):</u>

Fracture networks and their connections to fault zones have been mapped and tested extensively between depths of 2850 and 3500 m. Clusters of permeable fracture channels ("flow tubes") match the observed pressure responses and are associated with hydrothermal alteration zones (Evans et al. 2005, Sausse and Genter 2005). Petrographic and geochemical work showed a correlation between fracture permeability and alteration intensity, because fluid flow through the granite matrix results in dissolution of some primary minerals and precipitation of secondary phases (Sausse et al. 2008). However, fluid-rock interactions are complex and not completely understood, and alteration mapping from washed drill cuttings does not always match the inferences from in-situ hydraulic tests.

The sequence of tests in 1993 in GPK-1 has been described in many papers and reports, and here we provide a summary mainly from Evans et al. (2005) and Sausse et al. (2006), and the primary literature cited in those papers. The pre-stimulation pump test on August 19 1993 was done on depth interval 3560-3590 m and resulted in a bulk permeability of 1.5×10^{-17} m^2 (Jung, 1993). The interval was opened to 2850 m depth for the stimulation.

1st major stimulation (September 1, 1993)

- This experiment was designed to target the rock section at 2850-3400 m above the known fracture zone at 3500 m; the bottom of the drillhole section was temporarily plugged with sand.
- During the stepped injection process, high pressure at the lowest step indicated that the interval was "tight prior to stimulation", and had natural pre-stimulation permeability-thickness (transmissivity) of 0.014 Darcy-m over 550 m open-hole section, implying a bulk permeability value of 25 micro-Darcy (2.5×10^{-17} m^2) (Jung et al. 1995).
- After stimulation, the bulk permeability was 3×10^{-16} m^2 (Jung et al. 1995), or 20x larger than under natural conditions
- In a 2D flow model fitted to a flow meter profile over various depth intervals, the

equivalent bulk permeability varied from 10^{-15} to 10^{-17} m^2, with most values between 10^{-17} and 10^{-16} m^2 (Sausse et al. 2006).

- Microseismicity was observed to migrate over time, and interpreting this migration in terms of hydraulic diffuvisity provided bulk permeability estimate of 5.2×10^{-17} m^2 (in the maximum direction of the tensor) (Shapiro et al., 1999). This value was later determined to represent pre-stimulation rock conditions that limited the diffusive process; it agrees with the result of a pre-stimulation pump test.

2nd major stimulation (October 11, 1993)

- This experiment was performed on the 2850-3590 m depth interval, targeting the fault zone at 3490 m (this zone could not be further isolated due to packer failure; thus the test on a longer interval).
- Jung et al. (1995) reported that during the drilling operations, the mud loss into the fracture zone at 3480-3490 m was partly controlled by plugging with a mixture of "bentonite and nutshells", and that 90% of outflow was into this zone.
- After the stimulation, when the hole was open over a long interval, spinner logs were done during injection and determined that most of the inflow was now into the upper interval at 2850-2900 m depth, with only 10% into the fracture zone at 3480-3490 m; thus the permeability was much greater at the shallower depth (Jung et al. 1995).
- After stimulation, the bulk permeability was 3×10^{-15} m^2 (Jung et al. 1993) or within a range of 1.6 to 2.4 $\times 10^{-15}$ m^2 (Sausse et al. 2006), representing an increase by a factor of 200x relative to pre-stimulation conditions.
- From interpretations of microseismicity migration as a diffusive process, the inferred pre-stimulation bulk permeability was 4.1×10^{-16} m^2 (maximum direction of a tensor) or 6×10^{-17} to 5.7×10^{-16} m^2 (isotropic bulk value) (Audigane et al. 2002);

Tests in the GPK-2 well 1994-1995:

- During the 1995 stimulation, the pre-stimulation bulk permeability was inferred to be 7×10^{-17} m^2 from microseismicity diffusion (Shapiro et al. 1998, Sausse et al. 2006), a 10x increase compared to natural conditions (Shapiro et al. 1999).
- After the stimulation, Kohl et al. (1996) reported on a 2D model calibrated to a 1995 pump test that yielded a bulk permeability of 2.6×10^{-16} m^2.
- Another hydraulic test using an oscillation method resulted in a bulk permeability of 8.1×10^{-15} m^2 (reported in Audigane et al. 2002).
- After the 1995 stimulation, the bulk permeability was 4.5×10^{-15} m^2, as reported in

Audigane et al. (2002) based on other references.

- From microseismicity diffusion, the inferred pre-stimulation bulk permeability was 2.8×10^{-16} m^2 in the maximum direction of the tensor and 2.8×10^{-16} to 2.0×10^{-15} m^2 as an isotropic value (Sausse et al. 2006)

<u>Lower reservoir, >4.5km depth (fracture zone cluster III):</u>

Wells GPK-2 (to 5093 m), GPK-3 (to 5100 m) and GPK-4 (to 5240 m) were tested and logged. A fault zone occurs near 4775-4780 m in wells 2 and 3 and is associated with a very high fracture frequency. This zone is a lithological boundary between two granite facies and took approximately 65 to 80% of the fluid during hydraulic stimulation (Davatzes et al. 2010). There are several other permeable zones near 5025 m and down to 5135 m, but there is still uncertainty as to the associated hydraulic properties and fluid circulation. The fault zones differ between wells in terms of fracture network permeability. The deepest well GPK4 has more diffuse and smaller connections, with more calcite found in cuttings, suggesting more sealing of fracture zones (Ledesert et al. 2010). Hydraulic tests were done before the stimulation experiment (slug, production and injection tests) and yielded a transmissivity value of about 0.06 Darcy-m (6×10^{-14} m^3) (Weidler et al. 2002). After the stimulation, technical problems caused poor hydraulic test data quality and the permeability enhancement could not be precisely estimated.

The 2003 injection experiment took place in GPK-3 (4500-5000 m) (Weidler et al. 2002, Genter et al. 2015). In GPK-2, the stimulation resulted in 20-fold increase in productivity along a narrow fault zone defined by microseismicity, but there was little change in GPK-3. The enhancement of permeability was correlated with the density (distribution) of microseismicity (Michelet and Toksoz 2007). Results of a long-term tracer-circulation test in 2005 between three wells (Sanjuan et al. 2006) were modeled numerically by Kosack et al. (2011). The average bulk permeability in most of the deep reservoir was 10^{-15} m^2, embedded in rock that was statistically estimated to have a permeability of 10^{-18} to 10^{-16} m^2 (mean about 10^{-17} m^2). However, a highly permeable connection between wells GPK-2 and GPK-3 was inferred to have a bulk permeability of 10^{-13} m^2. Vogt et al. (2012) developed a stochastic model in which the most extensive fracture zone had bulk permeability in the range of 10^{-15} to 10^{-16} m^2, and the most permeable part of the fractured zone (of smaller extent) had bulk permeability of 10^{-14} to 10^{-12} m^2 (mean estimate of 10^{-13} m^2). A discrete fracture network model was also built (Gentier et al. 2010) to match the structural model of the area (Valley et al. 2007), and other modeling studies are ongoing.

Deep scientific drillholes:

<u>KTB, southern Germany:</u>

The KTB project is described by Emmermann and Lauterjung (1997) and Zimmermann et al. (2000), among others. The pilot drillhole reached 4km and the main drillhole 9.1km. The drillholes were located at the western margin of the Bohemian Massif, in lithology dominated by metabasites and gneisses. Hirschmann et al. (1997) described the structural geology. The Nottersdorf fault zone occurs at 600 to 1600 m, and the Waldeck-Klobenreuth fault zone (also called the SE-2 seismic reflector) is part of the major regional Franconian lineament. The most faulted intervals were between 3500 and 3600 m, with faults following the regional rock fabric. The deeper Altenparkstein fault zone (the SE-1 reflector), the main part of the Franconian lineament, has a reverse component with 3 to 6 km displacement and was encountered at depths of 6850-7300 m.

Our database contains permeabilities for several fault zones based on KTB observations. At the intermediate level, the faulted rocks were pumped for a year in 2002 and bulk permeability determined to be about $2x10^{-15}$ m^2 (Stober and Bucher 2005, Grasle et al. 2006). Injection and pumping tests determined that the fracture zone linking two wells at a depth of about 4000m had a hydraulic diffusivity of about 0.12 m^2/s and a transmissivity of about $2.3x10^{-13}$ m^3 (Kessels and Kuck 1995). At the bottom of the drillhole near 9.1 km depth, no major fault zones were mapped, but the presence of a fault was inferred from an injection experiment. This fault has brittle open fractures aligned with present day stress conditions such that they are critically stressed, and only small pressure perturbation (i.e. ~ 1% of ambient hydrostatic pressure) results in fault slip and microseismicity generation (Harjes et al. 1997). Huenges et al. (1997) described a drill-stem test over the short interval 9030-9101 m. This tested only a small rock volume, or the "skin" of the well. A pressure build-up test was also done, and yielded a bulk permeability of $8x10^{-18}$ m^2. The matrix permeability was tested on a large number of samples of drilled core, and all values represent the protolith. The geometric mean of the matrix permeabilitiy is $7.4x10^{-20}$ m^2 (median $7x10^{-20}$ m^2) and most values range from $2x10^{-19}$ to 10^{-20} m^2. However, at 8 km depth the two deepest samples had values of 10^{-18} m^2. The bulk permeability is not well-characterized at depth below 7 km.

In 1994, a short-term injection experiment was done on the 9030-9101 m depth interval and induced almost 400 microearthquakes in a spatial domain extending 500-700 m laterally from the borehole in the depth range 7500-9000 m (Zoback and Harjes 1997). Pressure diffusion along a fault zone (assumed 100 m wide) was modeled to match the hypocenter locations of microearthquakes. The 1994 data provided estimates of hydraulic diffusivity (0.3 to 2 m^2/s) and bulk permeability ($2.5x10^{-15}$ to 1.0×10^{-16} m^2) (Shapiro et al. 1997, Shapiro et al. 2006). Zoback and Harjes (1997) also estimated a permeability of 10^{-16} m^2 by assuming a 100 m wide fault zone between the borehole and the observed clusters of microseismic events. The permeability tensor has a strong anisotropy and is aligned with the SE-1 reflector (Altenparkstein fault zone).

The 2000 injection experiment lasted for several months and is described in Baisch et al. (2002). About 50 microseismic events were detected near 9.1 km, but a larger cloud of events was detected at 5.4 km depth. Analysis of the diffusive process near 9.1 km depth yielded a value of hydraulic diffusivity of 0.05 to 0.2 m^2/s (Rothert et al. 2003). In 2004, following a long term pump test in the main hole, fluid was injected into the pilot hole near and parallel to the main hole. Observed microseismicity clustered near 4 to 5 km depth at the SE-2 structure and the hydraulic diffusivity 0.01 to 0.02 m^2/s (Shapiro et al. 2006).

Active fault observatories:

Nojima-Ogura fault observatory, Japan:

The Nojima-Ogura Fault is an active fault that is part of the Rokko-Awaji fault system. The fault was drilled and tested to depths of less than 2 km following the 1995 Hyogo-ken Nanbu earthquake (Hyogo-ken is the prefecture name). There are two drill sites on Awaji Island and several governmental and research organizations were involved (Ando, 2001). Most of the hydraulic testing and other related work was summarized by Ito et al. (2000). At outcrops, the fault zone is up to 63 m wide and contains many different deformation zones (Mizoguchi et al. 2008). At depth, the fault zones were characterized by downhole logs, geophysical surveys, hydraulic tests, and laboratory tests on samples. Zones of intense damage, inferred from enhanced permeability, are 20 to 30 m wide and probably located within a broader damage zone (Lockner et al. 2009). The protolith is granodiorite, weathered to 260 m depth and highly fractured to about 400 m depth. The fault core contains gouge with low matrix permeability, whereas the fractured damage zone is many orders of magnitude more permeable than either the surrounding protolith or the clay-rich fault core (Morrow, 2000).

The Kobe earthquake and its aftershocks were at seismogenic depths in this fault zone (a few km to <20 km) - Zhao et al. (1996) - and at shallow aseismic depths creep occurs in a fault core containing abundant incohesive gouge. The exhumed cohesive fault rocks (excepting the gouges) formed at seismogenic depths, and the overall permeability structure also originated at those depths and has experienced a long history of sealing and disturbance by seismic waves and fault movements. Mizoguchi et al. (2008) noted that although the outcrop samples can be tested at various pressures, it is not yet proven that those samples represent the conditions at depth.

Hydraulic tests were done in the fault zone under natural conditions at the Hirabayashi site:

- In the GSJ drillhole, pumping tests were done at 625 m depth (Roeloffs and Matsumoto 2000, Moore et al. 2009), in a narrow zone (1 to 2 m) with an extent of about 500 m. This zone was intended to represent the fracture network of the damage zone. The transmissivity from pumping test was 1.5×10^{-5} m^2/s, hydraulic conductivity was 1.5×10^{-5} to 7.5×10^{-6} m/s (bulk permeability 1.5×10^{-12} to 7.5×10^{-13} m^2), and protolith matrix permeability ~ 1.0×10^{-19} m^2.
- In the NIED drillhole, water injection was done in the depth interval 1596-1671 m. Shimazaki et al. (1998) reported results of hydraulic tests for the "inner damage zone" (~ 1.0×10^{-13} m^2), although the fault core of lower permeability was also included. Kiguchi et al. (2001) reported transmissivity of 1.5×10^{-5} m^2/s over a width of 1 to 2 m, so that the hydraulic conductivity would be 2.0×10^{-5} m/s and the bulk permeability about 2.0×10^{-12} m^2.
- We use the results of repeated injections that were done to estimate the natural change of bulk permeability over time, since the last major disturbance.
- Tadokoro (2000) compared the time lag of migrating seismicity due to injection in 1997 and 2000 to estimate that the permeability decreased by 40% over those three years. The bulk permeability was estimated from hydraulic diffusivity determined from microsesimicity migration, yielding bulk permeability 10^{-14} to 10^{-15} m^2.
- Water injection experiments were conducted in 1997, 2000, 2003, 2004, 2006, 2009, and 2013. From 1997 to 2009, water was injected at the top of a 1800m borehole. Kitagawa (2002) reported 7 injections, 3 in 1997 and 4 in 2000. Kitagawa and Kano (2016) presented new results, using a 2D numerical model and assuming a constant specific storage value. Fault width was assumed to be 50m. The hydraulic conductivity ranged from 2.4×10^{-6} m/s in 1997, to 1.4×10^{-6} m/s in 2006, and most of the change had occurred by the year 2000 (value of 1.6×10^{-6} m/s).

Table 10-4 Enhanced fracture and fault zone permeability at EGS/HDR sites.

Site Name	Structure	Lithology	Depth below ground surface (km)			bulk permeability after stimulation		bulk permeability before stimulation		permeability enhancement ratio: log(k before/k after)	
			From	To	bsmt	high	low	high	low	high	low
Falkenberg hydrofracturing test site, Germany (1987)	fractures (no major structures)	granite	0.26	0.25	0.00	3.0E-11		3.0E-12	3.0E-13	1.0	
LSBB galleries laboratory, France (2012-2013)	fault zone outcrop	limestone	0.28		0.00	1.4E-10		7.0E-12		1.3	
Fjällbacka EGS, Sweden (1986)	strike-slip fault/reverse fault, and sub-horizontal fracture zones	granite	0.47		0.00	1.0E-14		1.0E-17		3.0	
Grimsel underground lab, Switzerland (2017, ISC experiment)	shear zones formed in ductile conditions, overprinted with brittle fractures	granodiorite	0.48		0.00	1.3E-16	1.0E-17	5.4E-19	3.0E-19	2.4	1.5
Ogachi HDR, Japan ("shallow" reservoir)	faults related to horst block in caldera structure	granodriorite	0.72	0.71	0.30	1.0E-14		1.0E-16		2.0	
Ogachi HDR, Japan ("deep" reservoir)	recent faulting occurred along andesite dykes	granodriorite	1.00	0.99	0.30	1.0E-13		3.0E-15		1.5	
Desert Peak EGS, USA (2010-2012, Wells 27-15 and 22-22)	segment of fault zone	rhyolite	1.07	0.91	2.14	2.6E-13		4.3E-15		1.8	
Nojima-Ogura fault injections, Japan (1997, 2000)	major active fault zone	granodiorite	1.67	1.48	0.00	1.0E-14	1.0E-15	4.0E-15	4.0E-16	0.4	0.4
Raft River EGS, USA (2015, Well RRG-9 ST-1)	fault zone at shallow depth below top of metamorphic rock surface below sedimentary cover	quartzite	1.80		1.45	1.2E-12		2.0E-13		0.8	
Hijiori HDR, Japan (1986)	caldera ring-fault of a caldera, at shallow depth below the top of granititc rock surface, covered by volcanics	granodriorite	1.80	1.79	1.46	1.0E-13		1.0E-15	1.0E-16	2.0	
Soultz-sous-Forêts EGS, France (GPK1, 1988)	steeply dipping fault zone related to graben structure, near the top of granitic bedrock, below sedimentary cover	granite	1.99	1.97	1.42	2.0E-14	2.0E-15	3.0E-17		2.8	
Rosemanowes Quarry hydrofracturing test site, England (1982)	pre-existing sub-vertical minor faults with slickensides (no gouge or cataclasite)	granite	2.19	2.16	0.00	5.0E-15	5.0E-16	1.0E-16	1.0E-17	1.7	1.7
The NW Geysers EGS, USA (2012, Well P-32)	horst blocks bounded strike-slip faults and normal faults	greywacke	3.00	2.60	0.10	2.8E-14	2.0E-14	1.1E-14	1.1E-14	0.4	0.3
Fenton Hill HDR, USA (1970s-1990s)	fractures or minor faults (no major structures)	granodiorite	3.00	2.60	0.73	1.0E-15	1.0E-16	1.0E-17		2.0	
Soultz-sous-Forêts EGS, France (GPK1, 1993)	steeply dipping fault zone related to graben structure	granite	3.48		1.42	3.0E-15		1.5E-17		2.3	
Habanero EGS, Australia (2003-2005)	shallow-dipping fault zones at shallow depth below top of granite below sedimentary basin	granite	4.30	4.20	3.67	8.0E-13	3.0E-14	5.0E-14	1.0E-14	1.2	0.5
Pohang EGS, South Korea (2016)	fracture zone related to major fault zone	granite	4.35	4.21	2.35	9.4E-14		1.0E-16		3.0	
Urach-3 EGS, Germany	sparse fracture zones, dilated (not sheared) during the experiment (no major structures)	gneiss	4.44	3.32	1.60	5.0E-17	2.0E-17	8.0E-18		0.8	
Basel EGS, Switzerland (2006)	fault zone containing cataclasite	granite	4.67		2.51	6.0E-15	3.0E-15	1.0E-17		2.8	
Soultz-sous-Forêts EGS, France (GPK2, 2004-2005)	steeply dipping fault zone related to graben structure	granite	4.78		1.42	1.0E-13	1.0E-15	1.3E-16	5.0E-17	2.9	1.3
KTB, Germany (1994)	microearthquakes clustered along strike-slip planes (the nearest major fault zone was 1700m above this depth)	gneiss, amphibolite	9.10	9.03	0.00	1.0E-16	2.5E-17	8.0E-18	5.0E-18	1.1	0.7

10.3 Regional seismicity-depth distributions

The list of regions,datasets, and references is in Table 10-5. The seismicity-depth distributions were summarized from various regions from published seismological literature, and are included in Table 10-6. There was no reanalysis done and the counts of earthquakes in depth bins are as reported. The completeness magnitude, M_C, of catalogs was between 1 and 3, excluding events with local magnitude (M_L) below the threshold defined by the M_C. The hypocentral depth uncertainty was typically 1 to 2 km for individual events.

All references are listed in the article in Chapter 5.

Table 10-5 List of regions and datasets and references.

#	Region	Years	References
1	Nojima fault area, Honshu, Japan	1998 - 2014	Japan Meteorological Agency (2017)
2	Atotsugawa fault, central Honshu, Japan	1998 - 2014	Japan Meteorological Agency 2017, Niwa et al. 2011
3	Tohoku volcanic region, Honshu, Japan	1998 - 2015	Japan Meteorological Agency 2017
4	Taupo Volcanic Zone, New Zealand	1995	Sherburn et al. 2003
5	southern Iceland	1991 - 2013	Panzera et al. 2016
6	San Francisco Bay area, California, USA	1975 - mid. 2013	Tal and Hager 2015
7	southern California, USA	1981 - 2011	Tal and Hager 2015
8	western Great Basin, USA	1974 - 1981	Ryall and Vetter 1983
9	area near Yucca Mountain, Nevada, USA	1992 - 1994	Smith et al. 2007
10	southern Rhine Graben, Germany/France	1976 - 1992	Bonjer 1997
11	The Alps, Switzerland / France	1975 - 2012	Wiemer et al. 2016
12	Provence, southern France	1963 - 1997	Baroux et al. 2001
13	Armorican Massif, France	1962 - 2002	Mazabraud et al. 2005
14	Gulf of Corinth, Greece	mid. 1991	Rigo et al. 1996
15	central Apennines, Marsica area, Italy	2003 - 2004	Chiaraluce et al. 2009
16	south-eastern Sweden	2003 - 2011	SKB 2017
17	central Fennoscandian Shield, Finland	1965 - 1997	Kaikonen et al. 2000
18	south-central Canada	1980 - 2004	Ma and Atkinson 2006

Table 10-6 Earthquake counts at depth intervals for regional seismicity-depth histograms.

Region:	Reference:	Depth category (km)	0-1	1-2	2-3	3-4	4-5	5-6	6-7	7-8	8-9	9-10	10-11	11-12	12-13	13-14	14-15	15-16	16-17	17-18	18-19	19-20
		Mid depth for histogram	0.5	1.5	2.5	3.5	4.5	5.5	6.5	7.5	8.5	9.5	10.5	11.5	12.5	13.5	14.5	15.5	16.5	17.5	18.5	19.5
		Dataset region or extent:																				
southern California	Tal and Hager 2015	Southern California region, USA	0.01	0.01	0.02	0.05	0.08	0.10	0.09	0.09	0.10	0.10	0.08	0.06	0.05	0.04	0.03	0.03	0.02	0.02	0.01	0.01
		San Francisco Bay region, California, USA	0.01	0.03	0.04	0.07	0.11	0.13	0.14	0.13	0.10	0.07	0.04	0.03	0.02	0.02	0.02	0.01	0.01	0.01	0.01	0.00
western Great Basin	Vetter and Ryall 1983	western Great Basin and eastern Sierra Nevada, 1970-1981	0.01	0.01	0.02	0.04	0.03	0.07	0.10	0.15	0.15	0.12	0.10	0.07	0.04	0.03	0.02	0.02	0.01	0.01	0.00	0.00
	Smith et al. 2007	vicinity of Yucca Mountain	0.01	0.01	0.03	0.02	0.05	0.05	0.07	0.10	0.08	0.13	0.16	0.12	0.10	0.05	0.01	0.00	0.00	0.00	0.00	0.00
New Zealand, TVZ	Sherburn et al. 2003	central Taupo Volcanic Zone, New Zealand	0.00	0.01	0.06	0.13	0.27	0.28	0.20	0.05	0.00	0.01	0.00	0.00								
Japan	Niwa (2011), pers. comm (2017)	Atotsugawa Fault, Japan (<1km from fault trace)	0.01	0.00	0.01	0.04	0.02	0.03	0.05	0.08	0.08	0.14	0.23	0.17	0.08	0.04	0.00	0.00	0.00	0.00	0.00	0.00
	Japan Meteorological Agency (2017), and Ito et al. 1990	central Honshu including Nojima FZ area, 1998-2014		0.00	0.00	0.01	0.01	0.02	0.05	0.07	0.08	0.10	0.15	0.15	0.15	0.11	0.06	0.02	0.01	0.00		
	Japan Meteorological Agency (2017)	Tohoku volcanic region between Latitutde 38.7 to 40, and Longitude 140.5 to 141 (1998 to 2015)	0.00	0.00	0.02	0.04	0.07	0.10	0.14	0.19	0.15	0.09	0.08	0.05	0.03	0.01	0.00	0.00	0.00	0.00	0.00	0.00
The Alps	Wiemer et al. 2016	Alpine Region, Switzerland (1975-2012)	0.04	0.04	0.08	0.08	0.09	0.09	0.14	0.13	0.08	0.10	0.07	0.00	0.02	0.01	0.02	0.00	0.00	0.00	0.00	0.00
southern Rhine Graben	Plenefisch and Bonjer 1997	southern Rhine Graben (1976-1992)	0.00	0.00	0.00	0.00	0.00	0.06	0.08	0.02	0.00	0.10	0.08	0.10	0.10	0.08	0.00	0.02	0.04	0.04	0.18	0.06
southern France	Baroux et al. 2001	Provence, southern France	0.00	0.00	0.07	0.00	0.12	0.15	0.20	0.08	0.08	0.08	0.10	0.05	0.00	0.00	0.05	0.00	0.00	0.00	0.00	0.00
SE Canada	Ma and Atkinson 2006	Western Quebec, Southern Ontario, and Northern New York	0.01	0.01	0.01	0.02	0.07	0.05	0.04	0.07	0.05	0.07	0.07	0.14	0.04	0.04	0.10	0.04	0.04	0.03	0.04	0.03
Sweden	SKB quarterly reports on seismicity in Sweden	Swedish National Seismic Network, 2003-2011	0.00	0.07	0.04	0.06	0.03	0.04	0.04	0.03	0.03	0.03	0.04	0.03	0.02	0.03	0.03	0.02	0.03	0.06	0.06	0.06
northern Finland and NE Sweden	Kaikkonen et al. (2000)	central Fennoscandian Shield (N Finland, NE Sweden)	0.02	0.04	0.05	0.05	0.08	0.06	0.07	0.10	0.08	0.05	0.06	0.05	0.05	0.03	0.03	0.04	0.02	0.01	0.01	0.01
southern Iceland	Panzera et al. 2016	South Iceland revised catalogue	0.01	0.01	0.04	0.11	0.18	0.23	0.16	0.13	0.08	0.04	0.02	0.01	0.00	0.00	0.00	0.00	0.00	0.00	0.00	0.00

western France	Mazabraud et al. 2005	Depth (km), middle of bin on histogram	**0**	**3**	**5**	**8**	**10**	**13**	**15**	**18**	**20**	**23**	**25**	**28**	**30**	**33**	**35**	**38**	**40**	**43**	**45**						
		area near Lorient earthquake zone, Armorican Massif, Western France	0.01	0.04	0.07	0.10	0.12	0.17	0.15	0.11	0.09	0.06	0.04	0.02	0.01	0.00	0.00	0.00	0.01	0.00	0.00						
central Italy	Chiaraluce et al. 2009	Depth (km), middle of bin on histogram	**0**	**1**	**2**	**3**	**4**	**5**	**5**	**6**	**7**	**8**	**9**	**10**	**10**	**11**	**12**	**13**	**14**	**15**	**15**	**16**	**17**	**18**	**19**	**20**	**20**
		C: Marsica (Central Apennines, near Gran Sasso area)	0.02	0.02	0.04	0.05	0.09	0.12	0.06	0.05	0.03	0.05	0.05	0.04	0.05	0.05	0.05	0.07	0.03	0.03	0.03	0.01	0.03	0.01	0.02	0.00	0.01

Appendix 2

11 Permeability of drillcore samples at Gryphon site

The electronic database of samples is in Excel spreadsheet format and in text file format. The data fields are:

- Drillhole
- Test #
- Test location, Date, Time in notes, start time (computer), end time (computer)
- Matrix permeability to N2 (m^2), log permeability (log m^2)
- Depth (depth marker, distance from depth marker, depth along hole) (m)
- Seal quality
  - good, small leak (not dominant), poor (large leak)
  - no epoxy (rubber only), inject into small vug
  - fracture vented quickly beside epoxy seal or rock fractured during test - ignore
- Seal notes
- Final QA Use data for analysis (1 or 0)
- Load on probe (lb)
- Water spray absoprtion by matrix (high, moderate, low, very low / not apparent)
- Dryness of rock (saturated - just drilled, moist, dry from storage)
- Athabasca group Sandstone
  - sandstone (coarse+gravel, coarse, med-fine)
  - conglomerate
  - paleo-weathered, silicified conglomerate at unconformity
  - silicified, altered
  - well cemented
  - dissolution channels/vugs present
  - brecciated/fractured after silification
  - hematite
  - clay filled / altered
  - test along dark thin sediment bands
  - test along coarse grain bands/deformation
- Paleo-weathered (regolith - silicified, altered, hematite, green, orange-brown)
- Porous weathered pegmatite
- Gneiss (pelitic, cordierite, migmatitic, unknown due to pervasive alteration)
  - quartz vein
  - intensely altered porous, desilicified + clays
  - moderately altered gneiss (increased porosity along fabric, channels)
  - weak green-grey alteration (quartz replaced by clays)
  - weak green-grey
  - greenish illite along fractures
  - graphite, pyrite, U-mineralization, redox front
- Silicified rock with alteration or dissolution
  - metaquartzite (large pegmatitic sized grains)
  - silicified (migmatitic gneiss fabric)

- silicified (minor gneiss fabric)
  - silicified grey + patchy white replaced by sericite or clay
  - some kaolinite or dravite (patches)
  - dissolution channels
  - grey-bluish fine alter.
  - moderately altered whittish
  - intensely altered whittish clayey
  - intensely desilicified vuggy or coarse grained
- Pegmatite
  - pegmatite/migmatite
  - most feldspars pink
  - some pink feldspars still visible
  - early silicification, white-grey-green patches
  - strongly silicified
  - grey-green pervasive
  - partly desilicified (porous)
  - green sudoite after subhedral feldspars
  - green sudoite or other mineral replacing quartz in fractures and veins
  - hematite alteration prominent of some grains
  - garnet porphyroblasts
  - illitisation (light green) and enhanced porosity
  - paleo-weathering
  - fault gouge notes
- Structure
  - fault gouge/breccia (weak)
  - breccia/gouge (cemented)
  - fault slip surface wall
  - fault fractured rock matrix
  - cataclasite
  - fracture sealed with minerals (not known if fault)
  - pseudotachylite or cataclasite vein
  - vein
- Fracture type (II fabric, x-cut, sub-verical, fine mesh (hairline, random)

Table 11-1 Comparing the permeability of drillcore samples tested on October 5, 2016 after owen-drying at Wheeler River site, and the same samples tested previously in 2016 (air dried in ambient storage conditions or partly saturated for some samples).

		owen dried		air dried outside	
Drillhole #	Test #	k (m^2)	log k	k (m^2)	log k
		fault gouges			
WR-668-D3	4 trial 1	7.8x10-15	-14.1	9.0x10-15	-14.0
WR-668-D3	5	1.5x10-15	-14.8	5.6x10-16	-15.3
WR-668-D3	8 trial 1	2.0x10-15	-14.7	2.1x10-15	-14.7
WR-668-D3	6 trial 1	1.0x10-15	-15.0	6.5x10-16	-15.2
WR-668-D3	31	5.8x10-16	-15.2	1.1x10-16	-15.9
WR-665	183 trial 2	7.9x10-16	-15.1	2.2x10-15	-14.7
		strongly desilicified porous gneiss			
WR-665	208	1.4x10-15	-14.9	3.2x10-16	-15.5
WR-665	213	3.6x10-15	-14.4	4.4x10-15	-14.4
WR-665	181	5.2x10-16	-15.3	2.0x10-16	-15.7
WR-665	182	6.2x10-16	-15.2	9.0x10-17	-16.0
		metapelite (moderately altered, more porous)			
WR-665	84	7.2x10-18	-17.1	1.4x10-19	-18.8
WR-665	68	2.8x10-17	-16.6	3.2x10-20	-19.5
WR-668-D3	19	3.1x10-15	-14.5	5.6x10-15	-14.2
		desilicified vuggy clayey rock (episyenites)			
WR-665	196	1.6x10-13	-12.8	8.0x10-14	-13.1
WR-665	188	2.8x10-18	-17.5	1.8x10-18	-17.8
WR-665	219 trial 1	5.9x10-14	-13.2	8.7x10-14	-13.1
WR-665	176	3.3x10-16	-15.5	4.7x10-16	-15.3
WR-665	184	6.5x10-18	-17.2	3.4x10-18	-17.5
		intensely altered bleached			
WR-665	197	2.2x10-18	-17.6	5.4x10-20	-19.3
WR-665	226	2.2x10-16	-15.7	5.1x10-17	-16.3
WR-665	246	1.0x10-17	-17.0	1.0x10-17	-17.0
WR-665	272 spot 3	2.5x10-18	-17.6	3.1x10-18	-17.5
WR-665	115	6.3x10-16	-15.2	1.1x10-17	-17.0
		other pemgatites			
WR-665	98	4.0x10-16	-15.4	2.4x10-17	-16.6
WR-665	216	2.2x10-16	-15.7	7.7x10-17	-16.1
WR-665	26	3.0x10-14	-13.5	7.9x10-15	-14.1
		metapelite (weakly altered)			
WR-665	121	3.0x10-18	-17.5	9.8x10-19	-18.0
WR-665	95	3.2x10-18	-17.5	4.7x10-19	-18.3
WR-665	25	7.9x10-18	-17.1	1.0x10-20	-20.0
WR-665	75	4.6x10-17	-16.3	1.1x10-19	-19.0
WR-665	273	2.3x10-18	-17.6	1.7x10-18	-17.8
WR-668-D3	29	4.8x10-19	-18.3	1.0x10-20	-20.0
		sandstone			
WR-665	10	1.4x10-17	-16.8	1.3x10-17	-16.9